City Research Online

City, University of London Institutional Repository

MICRO- AND MACRO-MECHANICAL PROPERTIES OF AEROSPACE COMPOSITE STRUCTURES AND THEIR DYNAMIC BEHAVIOUR

PHD THESIS

JAMES A. K. NJUGUNA

SEPTEMBER 2006

City University
London

School of Engineering and Mathematical Sciences

PhD Thesis

Micro- and Macro-Mechanical Properties of Aerospace Composite Structures and their Dynamic Behaviour

by

James A. K. Njuguna

A PhD thesis submitted to the School of Engineering and Mathematical Sciences in partial fulfilment of the requirements for the degree of

DOCTOR OF PHILOSOPHY IN AERONAUTICAL ENGINEERING

September 2006

Supervisor: Professor J. R. Banerjee
Co-Supervisor: Dr. C.W. Cheung

Content

List of Figures

Schematic Diagrams

List of Tables

Acknowledgement

To

My wife Agnieszka,

For her constant love and patience

Declaration

This is to grant powers of discretion to the University Librarian to allow the thesis to be copied in whole or in part without further reference to the author. This permission covers only single copies made for study purposes, subject to normal conditions of acknowledgement.

Abstract

The research presented in this thesis focuses on the micro- and macro-mechanical properties of aerospace composite structures, and their buckling, free vibration, and flutter behaviour. The first part of the thesis concentrates on fundamental experimental research into prediction and enrichment of polymers composites with nanoparticles with particular emphasis on polyurethane and polyaniline. To this end, a conducting thermoplastic elastomer is developed and characterised using physiochemical methods for thermo-mechanical properties. Consequently, a sophisticated new polyurethane nanocomposite elastomer with improved mechanical and thermal properties is developed.

The second part of the thesis is a development of an accurate dynamic stiffness matrix for a three-layered sandwich beam of asymmetric cross-section using the Timoshenko beam theory, Hamiltonian mechanics and symbolic computation. The resulting dynamic stiffness matrix is used to investigate the free vibration characteristics of a number of sandwich beams examples and their results are validated by experiment. Next, a detailed analysis is carried out to establish the rigidity properties (stiffnesses) of fibre reinforced composite structures with particular emphasis on solid rectangular and thin-walled box section. The effect of ply orientation on rigidity properties and the consequent coupling between various modes of deformation is studied. Buckling analysis is carried out to provide an estimate of the stiffnesses. Free vibration investigations on flat and box carbon fibre-reinforced composite beams are then carried out to gain important insights into the material-geometrical coupling effects, and modal interchange in bending-torsion coupled behaviour. Although the dynamic stiffness method is primarily used in the analyses, some complementary finite element analysis and experimental modal analysis using an Impulse Hammer Kit were performed to confirm the predictable accuracy of the dynamic stiffness method. A few carefully designed composite beams were fabricated for the experimental work. Flutter behaviour of swept and unswept wing is also investigated. The results are discussed with significant conclusions drawn. A scope for further work is outlined.

Abbreviations

12COOH - 12-aminolauric acid

AEAPS - Aminoethylaminopropyltrimethoxysilane

APES - Aminopropyltrimethoxysilane

APTS - 3-aminopropyltriethoxysilane

APU - Amphiphilic urethane precursor

AUA - Aminoundecanoic acid

AUN - Urethane acrylate nonionomers

AUNV- UV-cured AUN

BD - 1,4-butanediol

BZD - Benzidine

CNT – Carbon nanotubes

CTAB - Cetyltrimethyl ammonium bromide

CVD - Chemical vapour deposition

DMAc - N,N-dimethylacetamide

DMF - N,N'- dimethylformamide

DMPA - Dimethyl propionic acid

DOCA - Deoxycholic acid

ESCA – Electron spectroscopy for chemical analysis

HBP - Hyper-branched polyesters

HDI - Hexamethylene diisocyanate

ICP ES – Inductively coupled plasma emission spectrometry

IPDI - Isophorone diisocyanate

IPN - Interpenetrating polymer networks

MDI- 4,4'-diphenylmethane diisocyanate

MMT - Montmorillonite

MPP - Modified polyether polyol

TMI - Isopropenyl-α,α'-dimethylbenzyl isocyanate

MWNT- Multi-walled nanotubes

NMP - 1-methyl-2-pyrrolidinone

OLS - Organically layered silicate

OMLS - Organically modified layered silicate

PAMPSA -Poly(2-acrylamido-2-methyl-1- propanesulfonic acid)

PANI –Polyaniline

PBA- Poly(butylene adipate)

PCL - Poly(ε-caprolactone)

PDHB – 3-phenyl-3,4-dihydro-2H-1,3-benzoxazine

PDMS - Poly(dimethylsiloxane)

PEO - Polyethylene oxide

PIB - Poly(isobutylene)

POHSS - Polyhedral oligo-hydrido-silsesquioxanes

POSS - Polyhedral oligosilsesquioxanes

PPG - Poly(propylene glycol)

PSSA - Poly(styrenesulfonic acid)

P(S-DVB) - Styrene-divinylbenzene copolymer

PTMG -Poly(tetramethylene glycol)

PTMO - Poly(tetramethylene oxide) glycol

PTU - Polythiourethane

PU – Polyurethane

PUU - Poly(urethane urea)

Q_8M_8/TMI–Octakis(m-isopropenyl-α,α'dimethylbenzyl isocyanatodimethylsiloxy)octasilsesquioxane

SWNT- Single-walled nanotubes

TDI - Toluene diisocyanate

TEOS - Tetraethoxysilane

TG - Thermogravimetry

Principal Notations

$A_1- A_9$ = non-dimensional sandwich beam parameters, see Appendix B

$a - z$ = non-dimensional sandwich beam parameters, see Appendix A

$C_1 - C_9$ = non-dimensional sandwich beam parameters, see Appendix B

$D_1 - D_7$ = non-dimensional sandwich beam parameters, see Appendix B

E_1A_1, E_2A_2, E_3A_3 = axial or extensional rigidities of layers 1, 2 and 3 respectively

E_1I_1, E_2I_2, E_3I_3 = bending or flexural rigidities of layers 1, 2 and 3 respectively

F_1, F_3 = amplitudes of axial forces in layers 1 and 3, respectively

h_1, h_2, h_3 = thicknesses of layers 1, 2 and 3 respectively

i = $\sqrt{-1}$, also used as a dummy integer variable

K = dynamic stiffness matrix

$k_1A_1G_1$, $k_2A_2G_2$, $k_3A_3G_3$=shear rigidities of layers 1, 2 and 3 respectively

L = length of sandwich beam, Lagrangian

M_1, M_3= amplitudes of local bending moments in layers 1 and 3 respectively

P_j, Q_j, R_j, S_j, T_j=sets of constants used in the general solution

T = total kinetic energy of sandwich beam

U = total strain energy of sandwich beam

U_1, U_3 = amplitudes of axial displacements of the mid-planes of layers 1 and 3, respectively

u_1, u_3 = axial displacements of the mid-planes of layers 1 and 3 respectively

W = amplitude of bending (or flexural) displacement of sandwich beam

w = bending (or flexural) displacement of sandwich beam

x, y, z = rectangular Cartesian co-ordinate system for sandwich beam

α_i, β_i, γ_i, η_l = parameters showing relationships between constants, see Eqs. (38)

$\mu_1 - \mu_5$= coefficients of the governing differential equation, see Eq. (31)

θ_1, θ_2, θ_3 = local bending rotation of layers 1, 2 and 3, respectively

Θ_1, Θ_2, Θ_3 = amplitudes of local bending rotation of layers 1, 2 and 3, respectively

ω = angular (or circular) frequency

1 General Introduction

1.1 Introduction

Composites are multiphase materials obtained by combination of different materials, so as to attain properties that the individual components by themselves cannot attain. Such materials can be tailored to give high strength coupled with relatively low weight, high corrosion resistance to chemicals and offer long-term durability under severe environmental conditions. In this respect, macro-nanophase polymer materials are fundamental to a number of modern technological applications, including aerospace, automobiles, polymer blends or alloys, biomaterials for drug delivery systems, electro-optic and luminescent devices, coatings, powder impregnation of inorganic fibres in composites, and are also critical in polymer-supported heterogeneous catalysis [1.1-1.3].

Laminated composites are widely used in high performance aerospace applications. This owes to weight saving advantages but also due to aeroelastic benefits. However, it should be recognised that the weight savings advantage has been challenged by metals such as aluminium due to recent developments in metal technology. Importantly, composite research has shown that a careful choice of lay-up and design variables leads to a desirable bending, torsional and coupling rigidities, with the provision of an efficient approach when achieving a maximum flutter and/or divergency speed with a minimum mass of a composite wing. The research described in this thesis explores qualitatively the feasibility of further enhancements in material properties for high performance aerospace applications. Special emphasis is placed on aerospace structural applications in airframes.

Primarily, aerospace laminated composites are manufactured using carbon fibre reinforced with high performance epoxy resins. However, the widespread use of the epoxy-thermosets is limited in many high-performance applications because of their inherent brittleness, delamination, fracture toughness and temperature limitations. The development of improved high performance composites based on epoxy-thermosets can only be achieved by simultaneously improving resin, fibre and interface properties. A judicious approach to enhance these properties involves development of sandwich composite structures that incorporate elastomeric and thermoplastic phases into the matrix, which results in a multiphase polymeric system.

1

1.2 Study problem and key objectives

It is well recognised that the application of advanced composite materials can have profound influence in the design aerospace structures. Since composite materials are multiphase materials that are tailored for specific applications, their static characteristics vary considerably as well as their dynamic ones and the end results is either beneficial or detrimental. In particular, civil and military airplane wings are designed to carry heavy loads along their span. Depending on their magnitude and location, drastic changes in natural eigenfrequencies and eigenmodes are experienced. These changes can be beneficial but can also result in a deterioration of the dynamic response to time-dependent excitations and thus precipitate in the occurrence of flutter or divergency instability.

The thesis has been aimed towards a better understanding of micro- and macro-mechanical properties of aerospace composite structures of their dynamic behaviours and exploitation of their characteristics for aeroelastic benefits. The investigation is interdisciplinary in nature lying broadly with field of material science and aerostructures and combining different but related subjects. A significant path of the work is directed towards the investigation of aircraft composite wings using the numerical methods and validation of results by experiment and computational approaches.

The key objectives of this thesis are:
> - to fabricate thermoplastic rubber-like (elastomer) materials from (i) polyurethane polymer and (ii) polyanilne polymer
> - to develop conducting thermoplastic elastomers – blending of polyurethane and polyaniline polymers to produce an electricity conducting rubber (elastomer)
> - to reinforce polyurethane thermoplastic elastomers with nanoparticles (organic clay, montmorillonite)
> - to develop a refined sandwich beam theory for three-layered composite beams and validate it by experiment and finite element analysis
> - to predict the rigidity properties of flat and box composite beams using classical lamination theory
> - to investigate the vibration properties of flat and box composite by studying in particular the beam effects of ply orientation, the use of Timoshenko theory on natural frequencies and mode shapes changes in bending-torsion coupling

> ➤ to carry out critical buckling analysis of composite columns

> ➤ to investigate the aeroelastic behaviour of composite wings by studying the effect of ply orientation on flutter and divergency speeds

1.3 Motivation

The main motivation behind the research performed is the urge to develop intelligent multifunctional thermoplastic and/or other composite structures that could be employed in aerospace design. Such structures would have enhanced damping, toughness and elastic behaviour and more opportunity to assist in aeroelastic active control system design leading to the alleviation of aeroelastic flutter, reduction of gust loading, increased fatigue life of structural components, diminished cabin noise and improved manoeuvrability and handling thus expanding the aerospace design limits. A multifunctional structure may involve conducting polymers since they have potential for aerospace applications in antistatic coatings, sensors, actuators, multifunctional conducting films etc with improved stability. Appreciably, such a structure can also be a vehicle health system even with the possibilities of self-healing system functionality. The research performed has also established that such a multifunctional intelligent structure can also serve as energy storage as well as a delivery system simultaneously such as lubrication and fuel cells thus adding to its advantages. Altering the damping in structural systems also hold the potential for improving the tracking and pointing characteristics and therefore the accuracy of weapon systems mounted on aircraft and land systems.

On the other hand, convectional carbon fibre reinforced plastic (CFRP) composites are prone to moisture absorption and the composite structures generally get heavier in wet conditions. Studies on nanocomposites on polyurethane nanocomposites for example, have shown good mechanical, thermal and water resistant properties that could be used in coatings, adhesives, foams, etc for aerospace uses. The fact that the composite structures have undergone major developments in terms of fabrication and manufacture, it means that the structural analysis and vibration control is a key issue in their applicability in various industries, especially when the electronic equipment are integrated within structures.

Recent advances in convectional processing techniques aiming at high modulus polymers and advanced reactive processing techniques such as resin transfer moulding, reactive

extrusion, and reaction injection moulding have been deployed with success. This means that skin-like structures can now be produced by use of automatic lay up machines and automatic cutting machines enabling much more complex structures to be produced economically. Furthermore, progress in current research on reinforced polymer nano-composites (PNC) suggest that optimum levels of nanomaterials loading, e.g. in high temperatures reinforced polymers are in the range of 10-20% by weight. As can be seen in Table 1.1, the reinforced PNC are predicted to possess 20% of the theoretical properties of nanomaterials, although processing methods are still in their very early stages. Molecular level control of nanomaterials distribution and interaction with the matrix material is extremely demanding so as to obtain optimal properties and performance. There is also need to develop an affordable and reproducible method to make large quantities of nanomaterials with controlled size, geometry, chirality and purity [1.3]. Shall these difficulties be overcome; the reinforced polymer nano-composites stand a good chance particularly in the aerospace advanced structural and propulsion structural systems [1.4-1.12].

Table 1.1 **Carbon fibre reinforced composites in comparison with other materials (Specific Modulus refers to specific strength which is equals to Young's modulus divided by density)**

	Tensile strength (GPa)	Tensile modulus (GPa)	Elong-ation (%)	Density (g/cm³)	Specific strength	Specific Modulus	Thermal Conductivity (W/mK)	Use Temp. (°C)
Aluminium 2219-T87 [1.10, 1.11]	0.46	73	10	2.83	0.16	26	121	150
Inconel 718 [1.11]	1.03	190	14	8.2	0.13	23	15	650
Carbon fibre IM7 [1.5]	5.6	300	1.8	1.77	3.0	170	50	-
SWNT single crystal [1.6, 1.7]	180	1200	6	1.2	170	1000	<5000	~1200
CFRP Q-I M46J/7714A [1.8, 1.9]	0.7	86	-15	1.64	0.42	52	5	120
CFRP Q-I IM7/8552 [1.9, 1.10]	1.3	58	1.0	1.59	0.80	36	5	120
PNC Q-I composite [1.12]	2.5	240	1.59	0.98	2.5	240	5	120

1.4 Approaches

In order to meet the above objectives, the following subjects were studied and the knowledge obtained was applied in this work:

> polymer thermoplastics elastomers and nanocomposites

> ➤ thermal degradation of polymeric materials
> ➤ aircraft structures including adaptive structures
> ➤ Composite materials
> ➤ structural dynamics
> ➤ aeroelasticity

The layout of the thesis is influenced by the following systematic approach: a thorough literature survey; fabrication and characterization of a series of thermoplastic polymeric nanohybrid elastomers; comprehensive study of simple aircraft wing models; dynamic stiffness approach; modal analysis and experiments; and finite element approach. A high aspect ratio aircraft wing can be modelled as a beam and therefore the words 'wing' and 'beam' are used interchangeably throughout the thesis.

1.5 Thesis structure

Chapter 1 attempts to familiarise the reader with the thesis by giving relevant background information in objectives, approaches, motivation and the thesis structure. Key emphasis is on structural properties of polymer composites and in particular the relationship between the nano-micro-macrostructural properties, which is the one of main concerns of this work. The study problems, motivation and approaches are discussed. Typical applications relevant to the study are presented to emphasize the importance of current work in aerospace industry. Chapter 2 is a comprehensive literature review concerned with the current work. Polymer nanocomposites, theoretical and computational composite modelling, free vibration analysis, tailoring of composite beams, flutter investigations, aerothemoelastic behaviours, buckling problem determination, adaptive composite structures and flutter analyses of actively controlled composite structures are covered and commented on.

Chapter 3 is concerned with synthesis of polyurethane and polyaniline thermoplastic elastomers. It has been found that the intrinsic properties of the components of the blends are different from primary polymers. Sometimes, the properties are enhanced but for the most part, they were diminished. The key characteristics for polyurethane (PU) and polyaniline (PANI) are investigated independently. Chapter 4 aims at combining the beneficial properties of the two polymers (PU and PANI) i.e. tensile strength, thermal properties and

compatibility. PU/PANI conducting thermoplastic elastomers with good mechanical properties and processability (associated with high conductivity or electrochromism) were prepared, characterised and experimented on. In Chapter 5, polyurethane/organically modified montmorillonite (MMT) nanocomposites (PU/unmodified MMT and PU/organically modified MMT (OMMT)) were prepared and experimented. In particular, thermal properties of PU/MMT and PU/OMMT nanocomposites with intercalated structure, as evidenced by scanning electron microscope (SEM) data, prepared by prepolymer method, were studied. This work paves the way for further investigations to exploit the unique properties for technological considerations. The key interest in the current work is the potential of the prepared thermoplastics applications as the core materials in sandwich composites. The computational and experimental investigations reported herein verify these beneficial issues without undermining the outlined compatibility difficulties mentioned herein.

Chapter 6 reports on the free vibration of a three-layered sandwich beam. To start with, theoretical work of Banerjee [1.13, 1.14] is extended and an advanced dynamic stiffness theory for a three-layered sandwich beam is developed in order to investigate its free vibration characteristics. This is followed by experimental measurement of the free vibration characteristics, (natural frequencies and mode shapes), of sandwich beams by using an impulse hammers kit and associated computer software. In order to achieve this, a number of specimens of three-layered sandwich beams are manufactured using rubber as the core and aluminium as the face materials. By replacing aluminium by steel as face material, a few additional specimens are also made.

The macromechanical properties of composites form the background of the aeroelasticity of the composite wing. In particular, the rigidities (static) and other properties need to be known in advance as they are used as the basic design data. Chapter 7 is therefore committed to the determination of three important parameters, related to the flexural rigidity (EI), the torsional rigidity (GJ) and the material bending-torsion coupling rigidity (K). Parametric studies for flat and box beam models are carried out to study the effect of ply/fibre orientation onto these rigidities. For good estimate of stiffnesses, Chapter 8 looks into the buckling phenomenon and the results are corroborated with finite element analysis (FEA) using a commercially available software ANSYS for both metallic and epoxy carbon-fibre-reinforced composites

beams. The application of the dynamic stiffness matrix is demonstrated by numerical results for cantilever composite and metallic beams.

The effect of ply orientation on free vibration behaviour of laminated composite beams is investigated using an exact analytical method in Chapter 9 including the Timoshenko theory effects and those of bending-torsional couplings. Results are obtained for two different types of carbon-epoxy composite beams of which one is flat with solid rectangular cross-section whereas the other is a thin-walled box beam. The ply angles in the stacking sequence of these beams are varied and their subsequent effects on the free vibration characteristics are studied. Experimental modal analysis and finite element analysis are conducted to validate the theoretical results.

In Chapter 10, the effect of ply orientation on flutter speeds is carried out. The chapter intends to address the flutter phenomenon highlighting the associated issues, and to seek further insights on flutter speed characteristics of composite wings. A uniform flat and box-beam wing model are investigated to further understand the flutter behaviour of composite wings. The ply angles are varied against sweep angles to study the effects of ply orientation on flutter speed as applicable to convectional sweptback aircraft wings. The importance of aeroelastic coupling is particularly emphasised. The work summary and scope for further work are outlined in Chapter 11 followed by a personal profile and appendices.

2 Literature Review

2.1 Introduction

Today aircraft designers do have a considerable flexibility in design where a lighter wing with considerable strength is possible, due to the advent of advanced composite materials. In addition to the weight and strength advantage to conventional metals such as steel and aluminium, composite materials have directional properties that can be manipulated to achieve desirable aeroelastic and other effects on an aircraft wing. Free vibration and aeroelastic tailoring of composite beams or wings are just but some of the main beneficiaries from the success of composite modelling. It is with such understanding that the extensive study of composites' properties and behaviour characteristics have been attributed to. To start with, it is necessary to conduct a literature review in order to be up-to-date with the current research, particularly on works on aeroelasticity of the composite wings.

Researchers have been able to include various static and dynamic loads including the transverse shear loads found on composite beam that have been on some occasions a drawback in aerospace industrial use of composites. The research has gone a step further to the vital consideration of the *wash-in* and *wash-out* effects that can be advantageous from an aeroelastician point of view. Development of computer programs able to handle the large matrices involved in the analysis has speeded up the research on composites as reflected by the amount of work dedicated to composites in the last few decades. Both analytical approach and finite element approach have been covered in the relevant areas of interest in this study. The analytical approach solutions are exact although there are approximations, and their validations are destined to the work of experimental researchers. Conversely, the finite element method provides a comparative but useful measure to the analytical approach. Both approaches continue to develop and this has given confidence to the aircraft designers as they are able to predict the characteristics of composite structures.

The development of nanostructured materials on the other hand opens a new paradigm where composite matrix resins can be tailored to optimise properties of interest just as fibre orientation is used to optimize current advanced composites. The biggest challenge facing nanocomposites

is the assessment of the extent and efficiency of stress transfer through the interface between nanomaterials and polymers. Such knowledge could in turn be used for the determination and utilisation of Young's modulus and strength of polymer-nanocomposites and by taking full advantage of the results. Polymer nanocomposites (PNC) have received much attention over the past decade as scientists search for ways to enhance the properties of engineering polymers while retaining their processing ease. Unlike traditionally filled polymer systems, nanocomposites require relatively low dispersant loadings to achieve significant property enhancements, which make them a key candidate for aerospace applications. Some of these enhancements include increased modulus, improved gas barrier properties and atomic oxygen resistance, and better thermal and ablative performance.

Although this literature review concentrates mainly on composite beam modelling free vibration, and aeroelastic tailoring of composite beams, work has also been directed to other aspects of composite beams. Among them is on the active control (artificial intelligence) of the composite wings, which is a break through in the utilisation of composite structures. Others include delamination, development of new materials, wind tunnel model testing, computer modelling, advanced analysis and air-crashworthiness, just to mention but a few. In this work, the flutter characteristics have been addressed and associated effects have been commented on. All in all, the potential of composites is reflected by the capability to idealise the structures. The phenomenon is overwhelmingly and warmly welcomed by the aerospace industry.

2.2   Polymer nanocomposites (PNC)

Polymer nanocomposites may provide significantly increased modulus, gas barrier, thermal performance, atomic oxygen resistance, resistance to small molecule permeation and improved ablative performance when compared to typical traditional carbon-fibre-reinforced polymeric composites. This presentation gives a review of both theoretical and experimental investigations extracting valuable fundamental information including field emission, thermal stability, and electrical, optical and mechanical properties of polymer nanocomposites for aerospace applicability.

2.2.1 Modelling for properties

In order to facilitate the development of PNC, constitutive relationships must be developed to predict the mechanical properties of the composite as a function of molecular structure of the polymer, the nanomaterials, and the polymer/nanomaterials interface. Different models have been proposed to describe the relation between the orientation distribution of the basal planes and the elastic properties of carbon nanofibres: the unwrinkling model [2.1-2.3], the uniform strain model and the uniform stress model [2.1, 2.4]. In addition, several models (Cox [2.5], Kelly and Tyson [2.6], Lewis and Nielsen model [2.7] etc.) have been proposed and employed to investigate matrix-fibre transfer. It must be recognised that stiffness and strength can be increased at the expense of toughness and vice versa, demanding a balance line to be struck at early stages of the composite development and/or design.

Considerable attention has been given to measuring and modelling the principal Young's modulus of carbon nanotubes (CNT) [2.8-2.10]. Some of these studies assume a nanotube shell, but others on enclosed nanotube volume. These different geometry definitions have led to reported values differing by almost two orders of magnitude [2.8, 2.9]. For example, an experiment determining the Young's modulus of the single-walled nanotube (SWNT) from vibrational analysis, assumed in the data analysis a nanotube shell of 0.34 nm thickness resulting in a Young's modulus of 1.25 TPa for SWNT of 1.0-1.5 nm in diameter [2.11]. AFM deflection experiments, which included the entire cross-section of the nanotube in the analysis, measured a Young's modulus of 1.31 TPa for an array 3 nm in diameter with the modulus dropping to 67 GPa for an array 20 nm in diameter [2.12]. The average diameter of individual SWNT in this study was 1.4 nm. The geometrical dependence of the nanotube modulus has been confirmed with theoretical calculations. Non-orthogonal tight-binding calculations based on a nanotube shell at a thickness of 0.34 nm, but parameterized for any shell thickness, yield 1.22-1.26 TPa for SWNT of 0.8-2.0 nm in diameter [2.9]. When the entire nanotube cross-section is included, molecular dynamics simulations of nanotubes in compression that utilize the Tersoff-Brenner potential for the C-C bonds, yield a Young's modulus of 1.5 TPa at SWNT diameter of ~0.5 nm which reduces to 0.2 TPa at a SWNT diameter of 4.0 nm.

First principle total-energy (electronic structure) calculations for CNT and fullerenes using the density functional theory [2.13, 2.14] showed that hetero-nanotubes and hetero-sheets consisting

of boron and nitrogen in addition to carbon are nanoscale ferromagnets [2.15]. The norm-conserving pseudopotentials [2.16] are used to simulate nuclei and core electrons [2.17, 2.18]. Based on the quantitative values, the authors predict that the carbon fullerene is a new multicarrier one-dimensional metal being robust against lattice distortion, and that the zigzag carbon ribbons and CNT as well as the zigzag-bordered boron-nitrogen-carbon hetero-sheet and hetero-tubes have certain magnetic ordering, becoming nanoscale ferromagnets in some cases. Those surprising properties are closely related to electron states peculiar to tube-like structures and to hexagonally bonded networks. Further calculations using double-periodicity unit cells have revealed that the total energy for the anti-ferromagnetic state is lower than that of the non-magnetic state by 20 meV per unit cell [2.13].

2.2.2 Mechanical properties

2.2.2.1 Strength and stiffness properties

Nanofibres alignment has been an issue for poor experimental results on strength and stiffness parameters for PNC. Although polymer-organic nanocomposites also have a significantly higher modulus and strength than the unfilled polymer, reported results [2.19] are still far below those obtained from traditional carbon fibres. However, recent work seems very promising. For instance, fracture toughness for a 10 vol.% multi-walled nanotubes (MWNT)/alumina composite has been measured, indicating that it increased by 24% from 3.4 to 4.2 MPa/m^2 [2.20]. Experiments have been presented for carbon fibres that strongly favoured the uniform stress model [2.3]. In a recent work [2.4], different models were compared and a mosaic model was developed, which could explain the non-linearity of the stress–strain curve of the fibres, i.e. the increase in the Young's modulus during loading. Other such work by Lau and Shi [2.21] displayed rupture after extensive loading of 5-6 nm but the same PNC withheld better when heat-treated. By computing the stiffness of SWNT for different chiralities, it has been demonstrated that the Young modulus shows a small dependence on the tube diameter and chirality for the experimental range of nanotube diameters (between 1.3 and 1.4 nm). It has been predicted that carbon nanotubes have the highest Young's modulus of all the different types of composite tubes considered (BN, BC, BC N, C, N, CN, etc.) [2.11, 2.22]. Nonetheless, experimental results have shown Young's modulus value of around 1.25 TPa for both SWNT and MWNT are achievable.

The in-plane Young's modulus and the shear modulus of polyacrylonitrile (PAN) based fibres and mesophase-pitch based fibres, carbon nanocrystallites were investigated [2.23] during in-situ tension tests of single carbon fibres by X-ray diffraction using the shift of the 10 band in the meridional direction and the change in the azimuthal width of the 002 reflection. The limiting value for the Young's modulus was found to be 1140 GPa, which is higher than the value for graphite obtained from macroscopic specimens, but coincides with recent measurements on nanotubes. The research also found out that, the shear modulus evaluated using a uniform stress approach was found to increase with increasing disorientation of the crystallites. It turns out that both the in-plane Young's modulus and the shear modulus are not constant, but dependent on the orientation parameter. Poisson's ratio for SWNT obtained [2.11, 2.23] so far ranges around 0.14 to 0.28. It is worth noting that the computed Poisson's ratio values for SWNT are in all cases positive meaning the elongation of the tube reduces its diameter. Effects on the tube radius reflected a strong dependency with the nanotube chirality.

On CNT/poly (vinyl alcohol) composite films for mechanical characterisation [2.24], the tensile elastic modulus and damping properties of the composite films were assessed in a dynamic mechanical thermal analyser as a function of nanotube loading and temperature. On application of the short-fibre composite theory, a nanotube elastic modulus of 150 MPa was obtained from the experimental data that is far below the values reported for isolated nanotubes. On development of the high-temperature semicrystalline poly(ether ether ketone) nanocomposite, the authors [2.18] noted addition of low CNF contents lead to a linear increase in tensile and bending stiffness and tensile yield stress and strength without negatively affecting the matrix ductility at loadings up to 10 wt.%. The stiffness increase was more pronounced above the glass transition of the polymer. Though the success of this experiment showed the nanofibres could influence the polymer/matrix during crystallisation, the intrinsic stiffness was quite low and only applicable on delicate composite structures and films.

On characterisation of carbon nanotube/polystyrene composites [2.25] with the addition of only 1% nanotubes by weight (about 0.5 vol.%), the authors achieved between 36–42% increase in the elastic stiffness and a 25% increase in the tensile strength. They also used short-fibre composite theory to demonstrate that 10% by weight of carbon fibres (about 5 vol.%) obtained in a different work [2.26] would be required to achieve the same increase in elastic modulus with 1

wt.% of CNT. The latter [2.26] showed that the mechanical properties of vapour grown nanofibres for reinforced thermoplastics could be improved by ball-milling the fibres before blending them with the polymer matrix. This process breaks down the fibre clumps and increases the infiltration of the matrix material during high injection moulding. As such, the infiltration of fibres could be further improved by processing under high pressure. Further tensile, shear and strength tests on fibre reinforced composites exhibited their superiority to conventional short-fibre epoxy composites [2.27].

Strain-induced hardening observed in uniaxial elongational converging flow for a nanocomposite of 0.2 wt.% maleic anhydride modified PP and an organically modified montmorillonite is attributed, through TEM measurements, to the perpendicular alignment of the silicate layers to the flow direction [2.28]. The authors observed that Trouton's rule relating the shear and elongational viscosity failures. Small-angle X-ray scattering (SAXS) measurements by Medellin-Rodriguez *et al.* [2.29] showed that an end-tethered nanocomposite of nylon 6 and clay can be oriented at relatively low shears at temperatures slightly above the melting points. The orientation occurs by the 'normal' to the clay surface aligning along the flow direction through vortices during shear. The orientation increases with shear time and remains stable for fairly long times even in the molten state. Preserving the orientation below the nylon 6 melting points can be achieved by dynamic non-isothermal crystallisation. The formation of the oriented-type nylon 6 crystals is suggested [2.29] to be due to the previously oriented clay particles and not to the weak shear rates applied during crystallisation.

2.2.2.2   Toughness

Recent work on spherical nanoparticle titania filled epoxy has shown that the modulus, strength, strain-to-failure and scratch resistance can be increased simultaneously at a certain volume fraction of filler [2.30]. Layered silicate based nanocomposites, like other intrinsically anisotropic materials, exhibit the ability to orient the silicate layers in response to externally applied flow. This ability to orient, along with the quiescent mesoscale structure, appears to control the viscoelastic properties of such nanocomposites. The early studies on nylon 6 based end-tethered nanocomposites suggested that the silicate layers, upon injection moulding of the nanocomposites, exhibit substantial parallel alignment layer normal in the gradient. Similar

orientation for end-tethered poly (ε-caprolactone) montmorillonite nanocomposites subjected to prolonged large amplitude oscillatory shear has also been reported [2.31].

Another characterisation experiment was on hardness, fracture toughness and the tensile behaviour of spherical nanoparticle alumina filled poly(methyl methacrylate) (PMMA) [2.20]. The results showed a significant increase in strain to failure, averaging over 28%, in the 5 wt.% on filled samples. This represents an increase of 400% over that for neat PMMA tested at 25°C. A drop in modulus, ultimate strength, and scratch resistance accompanied a similar response observed for the strain-to-failure. A similar experiment was carried on CNT/PMMA composites [2.1, 2.25], whereby a free-radical initiator, AIBN, to open their π-bonds, initiated the nanotubes.

2.2.3   Storage modulus

The characterization of the WAXS, SAXS and TEM demonstrated that exfoliated nanocomposites can be formed from organoclay and epoxy [2.32]. Dynamic mechanical analysis (DMA) showed the storage modulus of this nanocomposite is higher than that of the pristine polymer. This was attributed to high aspect ratio and high strength of the nanoclay. The solvent uptake, such as acetone for the nanocomposite, was significantly reduced when compared with the pristine polymer as a result of the barrier effect of nanosheets of the clay.

Besides, polymetallic nanocomposites of aerospace relevance have been cited in the literature. Lukehart *et al.* [2.33] presented methods for preparing polymetallic precursors and for preparing improved nanocomposites formed from such precursors, which are useful in fuel cell catalyst compositions. The nanocomposites include a support and a plurality of polymetallic nanoparticles with a selected metal atomic ratio. The metals in the polymetallic precursors have a stoichiometric ratio that is approximately equal to the selected atomic ratio of metals in the nanoparticles such that stoichiometric control is provided for the resulting nanocomposite catalyst. Crystalline intermetallic or metal alloy nanoparticles form when a polymetallic precursor having a particular metal stoichiometry is contacted with a conductive support and the precursor is thermally degraded on the support leading to retention of the metal core of the precursor on the support. The polymetallic alloy nanoparticles that are formed have a selected metal atomic ratio, which is approximately equal to the stoichiometric ratio of metals in the

polymetallic precursor. Fuel cell catalysts comprising such nanocomposites have utility as either anode or cathode fuel cell catalysts, particularly in DMFCs and can be extended to other uses.

2.2.4 Dispersion and interfacial bonding

Improved dispersion and interfacial bonding of the nanotubes in an epoxy matrix appears to result in a 30% increase in elastic modulus with addition of 1 wt.% nanotubes [2.34]. The key factor in forming a strong interface is having a helical conformation of polymer around the nanotube. It has been suggested that the strength of the interface may result from molecular level chemistry [2.35]. As mentioned earlier on, investigation on SWNT/epoxy composite displayed a nearly constant value of Raman peak which the authors [2.36, 2.37] attributed this to tube sliding within the nanotube bundles resulting in to poor interfacial load transfer between the nanotubes [2.22]. Other reports [2.36] on investigations made by Raman spectroscopy found the effect modulus of SWNT dispersed in a composite could be over 1 TPa and that of MWNT about 0.3 TPa.

On the same pursuit, an examination was reported on MWNT-containing film, of approximately 200-μm thickness [2.10]. Stress-induced fragmentation of the film was observed and attributed to either process-induced stress resulting from curing of the polymer or tensile stress generated by polymer deformation and transmitted to the nanotube. On a different perspective [2.20], an investigation on compression and tension by Raman spectroscope showed the compressive modulus on MWNT/epoxy composite was found to be higher than the tensile modulus of the composites, while the Raman peak was found to shift only in compression, indicating poor interfacial load transfer in tension.

Work by Chenggang and Curliss [2.38] on organoclay epoxy nanocomposites proved that addition of clay to the resin did not significantly alter the viscosity or cure kinetics and that the modified resin would still be suitable for liquid composite moulding techniques such as resin transfer moulding. Differential scanning calorimeter (DSC) was performed to study the kinetics of the curing reactions in the modified resin. An in situ SAXS experiment was used to understand the structural development during cure. Based on the in situ SAXS data, structural changes were monitored in real time during cure and analysed. Results from wide-angle X-ray diffraction (WAXS), SAXS, and TEM of the polymer-silicate nanocomposites were used to

characterize the morphology of the layered silicate in the epoxy resin matrix. The glassy and rubbery moduli of the polymer-silicate nanocomposites were found to be greater than the unmodified resin due to the high aspect ratio and high stiffness of the layered silicate filler. The solvent methanol absorption was also slower for the polymer-silicate nanocomposites.

Conductive complex of polyaniline and sulfonated polyurethane (PANI-SPS), which is a template-synthesised form of PANI that produces a complex between the two polymers, PANI, and the strong acid polyelectrolyte, sulfonated polystyrene, were used to blend two forms of carbon nanotubes into thermoplastic elastomeric polyurethanes for processing into nanotube-containing nanofibres. The polyelectrolyte is presumed to provide the ionic doping of the templated PANI in the complex, and aids in plasma enhanced chemical vapour deposition prepared CNT (1-5 μm long and straight), and furnace chemical vapour deposition prepared carbon nanotubes (5-10 μm long, coiled and twisted). This sort of process could be valuable for the PANI/clay nanocomposites manufacturing [2.39]. As such, the PANI–clay nanocomposite particles, which can form columnar structure under an electric field, strongly enhance the mechanical rigidity of suspensions [2.25]. The maximum yield stress of the PANI/clay composite suspensions (15 wt.% in silicon oil) was 1.6 KPa at 3 kV/mm, while that of pure PANI was 300 Pa at the same electric field.

2.2.5   *Thermal stability*

Flame retardancy and thermal stability of nanocomposites have achieved considerable attention due to strict and stringent aerospace requirements. The complexity in achieving extended range of thermal stability can sometimes be related to the inadequacy of the numerical estimations currently in use. For example, nanofibres, like the vapour grown carbon fibres (VGCF), are composed of an annular geometry parallel to the fibre axis, the conductive properties along the fibre axis are very different from those in the transverse direction up to 2000 W/m K in the axial direction versus 10-110 W/m K in the transverse direction [2.40]. This makes it difficult to apply the existing models such as Cox's model or simple rule-of-mixture to VCGF due to their anisotropic characteristics, as well; the fibres are not perfectly aligned longitudinally. Hence, Kuriger *et al.* [2.40] predicted thermal conductivity by semi-theoretical Lewis and Nielsen model for uniaxially oriented fibres [2.7]. The results obtained here were considerably higher than those

previously reported by Dasch *et al.* [2.41] and Patton *et al.* [2.42] who had heat-treated their specimens to increase thermal properties.

Singh and Haghighat [2.43] developed a tetra phenyl phosphonium compound (with thermal stability in the range of 190-200 ^{0}C) to carry out cation exchange with the layered silicate reinforcement. The salt ions readily exchange with the cations on the surface of the inorganic phase attaching itself from the oxide surface and thus rendering the surface organophilic. That surface modified system lends itself to direct melt intercalation because tetraphenyl phosphonium is a high temperature organic moiety with thermal stability of 175-200^{0}C later extended to the use-temperature of the PNC to over 250^0 C. The thermal extension range was based on the innovative use of organically modified layered alumino-silicates that combine the layered silicate and the organic surfactant/compatibilizing agent in a single chemical compound. The organic surfactant groups are bonded to the structural Si atom through thermally stable Si-C bonds thus enhancing the thermal stability of the overall system. Therefore, those materials provide unique inorganic layered silicate reinforcements having markedly more thermally stable surfactants 'built-in' to the chemical structure.

Blumstein [2.44] showed PMMA inserted (*d* spacing increase of 0.76 nm) between the lamellae of montmorillonite clay, prepared by free radical polymerisation of methyl methacrylate, resisted thermal degradation under conditions that would otherwise completely degrade pure PMMA (refluxing decane, 215°C, N_2, 48h). Thermogravimetric analysis (TGA) reveals that both linear PMMA and cross-linked PMMA intercalated into Na^+ montmorillonite have a 40-50°C higher decomposition temperature. Improvement in thermal stability similar to that reported by Blumstein for both poly(dimethyl siloxane) (PDMS) and polyimide nanocomposites was also observed. In the case of PDMS, the nanocomposite was prepared by melt intercalation of silanol terminated PDMS into dimethyl to allow ammonium-treated montmorillonite [2.45, 2.46].

Despite the low clay content, the disordered-delaminated nanostructure shows an increase of 140°C in decomposition temperature compared to the pure PDMS elastomer. Gilman *et al.* [2.47] reported heat release rate's peak reduction by 50-75% for Nylon-6, PS, and polypropylene-*graft*-maleic anhydride nanocomposites. The experiment also found the type of layered silicate, level of dispersion, and processing degradation has an influence on the

magnitude of the flammability reduction. Triantafillidis *et al.* [2.48] work on an industrially purified Na^+-montmorillonite and Li^+-fluorohectorite clay, with a cation exchange capacity of 120 meq/100 g, which was converted to the H^+- and Li^+- exchanged forms by ion-exchange with dilute HCl or LiCl aqueous solutions, respectively, recorded the data in Table 2.1. These organic clays were prepared by ion-exchanging the inorganic clay with the diprotonated forms of Jeffamine diamines D2000, D400, and D230. All the other nanocomposite samples in Table 2.1 were prepared by direct addition of the clay additive to the epoxy resin curing agent mixture apart from D2000-PGW, which was prepared by pre-mixing of epoxy monomers with the organo clay. Pristine epoxy-B (star marked) was prepared by substitution of 4.0 mol.% D2000 (organic clay modifier) for D230 (curing agent) in the pristine. It has already been demonstrated that for high-use temperature, lightweight polymer/inorganic nanocomposite materials possess enhanced performance characteristics and thermal stability for long-term use-temperatures of 175-200 ^{0}C [2.43]. Beyer [2.49] synthesised a nanocomposite through melt-blending ethylene-vinyl acetate copolymer (EVA) with MWNT. Fire property measurements by cone calorimeter revealed that the incorporation of MWNT into EVA significantly reduced the peak heat release rates compared with the virgin EVA. Peak heat release rates of EVA with MWNT were slightly improved compared with EVA nanocomposites based on modified layered silicates. The char acted as an insulating and non-burning material reducing the emission of volatile products (fuel) into the flame area. There was also a synergistic effect by the combination of CNT and organoclays resulting in an overall more perfect closed surface with improved heat release values [2.49].

Table 2.1   Dynamic mechanical analysis and thermogravimetric data for pristine epoxy polymer and polymer/clay nanocomposites with Na$^+$-montmorillonite (PGW) and Li$^+$-fluorohectorite clay (FH) clay loading of 6 wt.% unless otherwise stated [2.48].

	Storage Modulus (E)		T_g (tan δ_{max})	Thermal stability, T=1.5%
Clay additives	At 40^{0}C GPa ($\pm$10%)	At 110^{0}C GPa ($\pm$10%)	^{0}C ($\pm 2^0$)	^{0}C
Pristine epoxy-A(0% clay)	2.9	18.4	82.6	373
Pristine epoxy-B(0% clay)	3.0	20.1	75.5	361
H$^+$-PGW	2.9	22.1	82.8	354
Li$^+$-PGW	2.7	19.9	82.3	356
Li$^+$-FH	3.1	25.2	85.2	351
D2000-PGW (1 wt% clay)	3.5	21.5	81.2	345
D2000-PGW (3 wt% clay)	3.6	22.1	76.8	341
D2000-PGW	3.8	21.5	69.8	336
D2000-PGW*	3.6	24.0	75.1	339
D400-PGW	3.6	23.2	84.2	346
D230-PGW	3.5	28.3	84.5	358
D2000-FH	3.9	30.5	73.7	323
D400-FH	3.9	32.1	79.1	340
D230-FH	4.0	45.4	84.7	345

2.2.6   Aerospace durability

Organic polymers with uniformly dispersed nanoscale inorganic precursors may enable polymeric materials to withstand the harsh space environment and be used as critical weight-reduction materials on current and future space systems. Lincoln *et al.* [2.50] speculated launch

vehicles would greatly benefit from appropriately designed nanocomposites that could provide improved barrier properties and gradient morphologies enabling linerless composite cryogenic fuel tanks. Self-rigidizing and self-passivating nanocomposite materials could be used to construct space vehicle components that are both highly resistant to space-borne particles and resistant to degradation from electromagnetic radiation, while reducing the overall weight of the spacecraft.

Nanocomposite materials also offer the unique opportunity for improved tailorability of physical and structural properties such as the coefficient of thermal expansion, which would be especially useful in constructing large aperture telescopes and antennas using inflatable membranes. Lake [2.51] observed nanofibre with a diameter in the order of 100 nanometers and a length of about 100 microns has a higher potential for low cost and large volume production. Methods for fabricating composites from these materials are under development, and show promise in a number of large volume applications.

Models describing the strength and modulus of other short fibre reinforced composites suggest that this form of fibre could be used to produce excellent engineering composites with modulus several times in excess of aluminium. This level of reinforcement implies that critical degrees of two-dimensional orientation are achievable, as well as a proper fibre/matrix interface. This premise, coupled with the prospect of a production cost comparable to that of glass fibres provides the basis of a potential revolution in the field of PNC.

2.3 Theoretical and computational composite modelling

2.3.1 Sandwich composite beams

The dynamic behaviour of sandwich beams is well researched and the literature has been around for nearly half a century. A sample of selected papers published in recent years is given, which review the state of the art and provide numerous cross references on the subject. One of the main reasons for conducting research in this area is due to the fact that sandwich constructions offer designers a number of advantages of which, perhaps the most important one is the high strength to weight ratio. This can be crucial, particularly in aerospace design, where weight saving is, as always, a major consideration. The published literature on the free vibration

analysis of sandwich beams deals mainly with three layered sandwich beams that are elastic (and some times viscoelastic), homogeneous and isotropic, but rigidly joined together, and for which the top and bottom layers are generally made of strong materials such as steel or aluminium whereas the core (i.e. the middle layer) is relatively soft, for example, rubber, so as to provide adequate damping and good energy absorption characteristics.

Di Taranto [2.52], Mead and Sivakumaran [2.53] and Mead and Marcus [2.54] are some of the earlier investigators who studied the free vibration problem of sandwich beams using the classical approach. They solved the governing differential equations of motion of a sandwich beam and imposed boundary conditions to obtain the natural frequencies and mode shapes. In later years, with the advent of digital computers, finite element based solutions became available [2.55-2.58]. One important feature of the published literature is that the value judgements made by various investigators when establishing the model accuracy of a sandwich beam have been interestingly, and often intriguingly, diverse. There is no doubt that there is considerable difficulty in obtaining an accurate analytical (mathematical) model for a sandwich beam. The difficulty arises from the very nature of the problem in which two or more structural components with different properties are joined together. For instance, in the case of a three-layered sandwich beam consisting of a (soft) core and two face materials, the difficulty in the formulation would appear when preserving equilibrium and compatibility conditions in the interfaces between the core and the face material. In the early eighties, Mead [2.54] made an objective assessment of various sandwich beam models that were used to investigate the free vibration characteristics. Basically, he compared the governing differential equations derived by various authors for free vibration analysis of sandwich beams. A relatively simple (but practically realistic) model assumes that the top and the bottom faces of a sandwich beam deform according to the Bernoulli–Euler beam theory whereas the core deforms only in shear. This model has been used by many [2.52, 2.54] and has provided an important basis for further development on the subject. Some authors [2.59-2.63] have extended this simple model by considering the core to be viscoelastic. (This has generally been achieved by simply assigning a complex value to the shear modulus of the core in the formulation.) Most of these investigations focus on the analysis of a single sandwich beam. There are, however, some finite element based solutions [2.55-2.58] that extend the general application of the work as they can cover an assembly of sandwich beams.

Sainsbury and Ewins [2.64] carried out a detailed vibration analysis of a machinery structure consisting of composite beams by using the mechanical impedance of component structures. Their method can at best be described as an approximation to the dynamic stiffness method.

A majority of the analyses reported, appear to have been carried out either by using the solution of the classical governing differential equations and thereby imposing the boundary conditions or by using the conventional finite element methods. However, in recent years, Banerjee [2.65], Banerjee and Sobey [2.66], and Howson and Zare [2.67] used a different approach which is that of the dynamic stiffness method. The authors of these papers have pointed out that there are many advantages of the dynamic stiffness method in that it is probably the most accurate method (often called an exact method) and unlike the finite element and other approximate methods, the model accuracy is not unduly compromised, as a result of using a small number of elements in the analysis. For instance, one single structural element can be used in the dynamic stiffness method to compute any number of natural frequencies to any desired accuracy. This is, of course, impossible in the finite element and other approximate methods. Earlier investigators of the free vibration analysis of sandwich beams using the dynamic stiffness method have had varying degrees of success. However, it is to be noted that during the developments of the dynamic stiffness method, especially for solving the sandwich beam vibration problem, there were considerable difficulties due to lack of knowledge and scarcity of literature on the subject. Thus, in the initial stages, simplifying assumptions were made and the choice of the allowable displacement was significantly restricted. This was probably justified at the time, particularly in view of the complexities involved in deriving as well as solving the governing differential equations in closed analytical form which are basic requirements in the dynamic stiffness method. For instance, Banerjee [2.65] in his earlier work assumed that the top and bottom layers of the sandwich beam behave according to the Bernoulli-Euler beam theory whereas the core deforms only in shear. This was no-doubt restrictive, but nevertheless, the theory worked well for certain classes of problems, particularly in the lower frequency range. A couple of years later, Banerjee and Sobey [2.66] improved the model substantially, by idealising the top and bottom layers as Rayleigh beams whereas the central core as a Timoshenko beam. This recent development which led to an eight order system as opposed to the sixth order one in the former, benefited very considerably from the use of symbolic computation when

manipulating the algebra. Without the application of symbolic computation the work would have been very difficult, and probably impossible. With the advent of symbolic computation, the research using the dynamic stiffness method to solve free vibration problems has no-doubt reached a certain degree of maturity, which partly motivated this work.

2.3.2 Composite beam modelling

Once the geometric idealization is made, a separate logical step in beam modelling consists of selecting the type of beam theory to be employed. Any beam theory is associated with introduction of variables, which depend only on the coordinate along the beam axis (Figure 2.1). For general deformation at least four such one-dimensional (1-D) variables have to be introduced: extensional, torsional, and two flexural variables corresponding to bending deformation along two orthogonal directions. The corresponding 1-D governing equations are uncoupled for isotropic beams with doubly symmetric cross sections and are given by the Euler-Bernoulli theory for extension and bending and the St. Venant theory for torsion. To extend this theory to composite beams, one must allow the governing equations to become coupled due to the appearance of off-diagonal terms in the cross-sectional stiffness matrix [2.68]. To take advantage of the beam geometric feature without loss of quality, one has to capture the behaviour associated with the two dimensions eliminated in the model. Together with elastic couplings among all the forms of deformation of a composite beam, the beam stiffness model is strongly affected by the in- and out-of-plane warping displacements [2.69]. For instance, a classical theory originating from variational asymptotic method (VAM) accounts for extension, torsion, and bending in two directions [2.70]. The theory is based on 3-D nonlinear theory, and provides the basis for both the (typically) linear, 2-D cross-sectional analysis and the 1-D nonlinear equations. The classical theory is limited to slender beams (beam that is not a thin-walled open section) and undergoes motions with large wavelength i.e., low-frequency modes of vibration. However, a refined theory is often required for high accuracy in other situations resulting in to the following refinements:

    i) The Timoshenko refinement, needed for short-wavelength modes associated with transverse shear effects,

ii) The Vlasov refinement, typically needed for thin-walled, open-section beams; and finally,

iii) A general refined theory, in which new degrees of freedom are chosen based on criteria that are problem dependent (high frequency vibrations and sandwich beams).
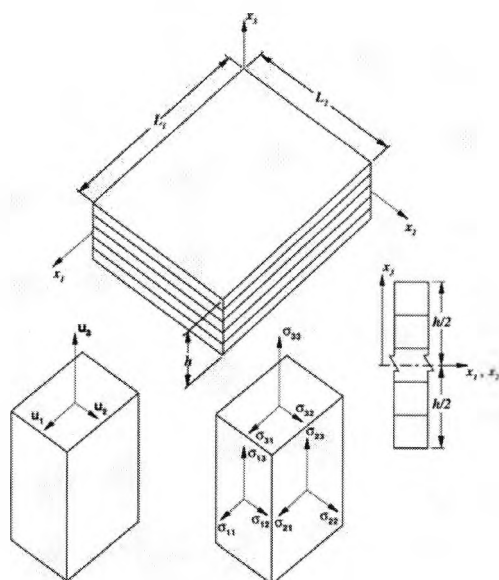
Figure 2.1   Laminated panel: geometry, coordinates axes, and sign convention for displacements and stresses

Few excellent reviews have been presented in recent times associated with composite beam modelling [2.68, 2.71, 2.72], and specialised works on pretwisted rotating beam theories have been reviewed [2.73]. To mention but a few, Patila and Hodges [2.74] presented theoretical development of a nonlinear aeroelastic analysis for high-aspect-ratio wings. The analysis coupled a geometrically exact beam theory with a nonplanar aerodynamic theory aiming to investigate the effects of geometrical nonlinearities on the aeroelastic behaviour of high-aspect-ratio wings.

In another development, Pandey *et al.* [2.75] presented work that attempted to address the potential of composites to improve the lateral-torsional stability of I-beams. The work was based on the composite I-beam theory of Bauld and Tzeng [2.76]. Further, the theory of Bauld and Tzeng has been shown to fail in certain situations by a comparison with numerical solutions and

with an asymptotically correct theory for composite I-beams developed by Volovoi *et al.* [2.77]. Recently, Hodges and Peters [2.78] considered lateral-torsional buckling of elastically coupled composite I-beams, and looked at closed-form approximate solutions that would be valuable in preliminary design. Using this comparison function, a formula for the buckling load as a function of the small parameters of the problem was found and validated. However, the load-offset parameter always appeared in the governing equations as multiplied by a ratio of stiffness, which become large, especially for composite I-beams - for this case, a special treatment was recommended.

2.3.3 Fibre and ply orientation

Fibre and ply orientation have substantial aeroelastic benefits. For instance, Sarigul-Klijn and Oguz [2.82] reported on the effect of aspect ratio and ply orientation on aeroelastic response of composite plates and they explored the importance of divergence and flutter behaviour in flight vehicles. Georghiades and Banerjee [2.79-2.81] examined the significance which *wash-out* can have on the flutter characteristics relating to swept and unswept aircraft composite wings. The coupling effect between the bending and twisting modes of structural deformation in flutter analysis was also investigated. Another work reported on the nonlinear effects of fibre orientations on the transonic and supersonic flutter characteristics of a composite missile wing model can be found in [2.83]. Free vibration of composite wings on the other hand has been extensively investigated [2.84, 2.85]. The lay-ups of some structural components may have a significant effect on the structural rigidities but may have little effect on flutter behaviour. In fact, a careful selection of initial lay-up and/or design variables may improve the optimisation efficiency. However, an unconstrained aeroelastic optimisation for maximum flutter speed might reduce the laminate strength of a composite wing structure. The strength set in the initial design can be regained without compromising the maximum flutter speed and the weight by optimising the wing structure in a constrained optimisation. Guo *et al.* [2.87] showed that a careful choice of initial lay-up and design variables leads to a desirable bending, torsional and coupling rigidities, with the provision of an efficient approach when achieving a maximum flutter speed with a minimum mass of a composite wing. An analytical study on optimisation of a thin walled wing box model made of laminated composite material showed that up to 18% increase in flutter

speed and 13 % reduction in weight can be achieved without compromising the strength. The work also reported that in comparison with the bending rigidity, both the torsional and the coupling rigidities have much more significant effects on the flutter speed of a composite wing. The torsional rigidity also played a relatively more dominant role in aeroelastic tailoring although the work failed to determine a clear trend of the coupling rigidity effect on the flutter speed.

2.4 Buckling problem

Elastic stability (or buckling) of beams, plates, and shells is one of the most important criteria in the design of any structure. Often, it is the critical design issue (even more than strength) in sizing certain structural elements. Because of this crucial role of elastic stability, it is extremely useful to have results of buckling analysis expressed in closed form, even if they are approximate, whenever possible for design analysis [2.75-2.77]. Although such approximate analyses cannot replace an over-all elastic stability analysis of the entire structure, the ease of implementation and the physical insight that such forms give allows valuable design tradeoffs to be made in the preliminary design phase; and that can lead to significant improvements in cost and performance of the structural design. On this line of interest, active buckling controls of laminated composite plates [2.88, 2.89], beams [2.90-2.92] and beam columns [2.93] with surface bonded or embedded piezoelectric sensors that are either continuous or segmented have been presented.

In a recent work, a procedure has been developed to produce and solve algebraic equations for any order aeroelastic systems, with and without frequency-dependent aerodynamics, to predict the Hopf bifurcation point [2.94]. Apparently, the estimation of the Hopf bifurcation point is an important prerequisite for the non-linear analysis of non-linear instabilities in aircraft using the classical normal form theory. For unsteady transonic aerodynamics, the aeroelastic response is frequency-dependent and therefore a very costly trial-and-error and iterative scheme, frequency-matching, is used to determine flutter conditions. Also, the standard algebraic methods have usually been used for systems not bigger than two degrees of freedom and do not appear to have been applied for frequency-dependent aerodynamics. In the proposed approach the computation

is performed in a single step using symbolic programming and does not require trial and error and repeated calculations at various speeds required when using classical iterative methods. The method has been evaluated via a Hancock two-degrees-of-freedom aeroelastic wing model and a multi-degree-of-freedom cantilever wing model [2.94]. Hancock experimental data was used for curve fitting the unsteady aerodynamic damping term as a function of frequency. As claimed, a fairly close agreement was obtained between the analytical and simulated aeroelastic solutions with and without frequency-dependent aerodynamics.

2.5   Free vibration analysis

The analytical approach to the vibration problem of the composite beams is an on going process with most researchers developing previous ideas and taking them a step further. Various works from over the years concerned with the free vibration of beams may be found from the literature since the design concepts of elastic tailoring in a wooden propeller design was invented in 1949 [2.95]. Over the years a number of stiffness models for composite beams have been developed and this study makes no attempt to cover each of the models. However, several of the famous models are described in this section. For instance, an investigation on the effects of laminate unbalance on the natural frequencies and mode shapes of cantilevered graphite/epoxy plates with bending-torsion stiffness coupling was conducted [2.96]. It involved performing a Rayleigh-Ritz analysis in order to determine the sensitivity of the accuracy for the predicted lowest three natural frequencies to the choice of assumed mode shapes. The study successfully co-related the predicted frequencies with experiments. The conclusion was that inclusion of chordwise bending is of vital importance even for configurations with a high aspect ratio. Otherwise the predicted torsional frequencies may not be reliable for plates with high bending-torsion stiffness coupling. In another case, a study was carried out on the calculation of natural frequencies and mode shapes but for non-rotating composite beams [2.97]. It was shown that predicted free-vibration characteristics of composite beams could be sensitive to the assumptions used in determining the stiffnesses.

A numerical study on the influence of the shear flexibility, due to either bending and/or warping, on the out-of-plane free vibration of continuous horizontally curved thin-walled beams

with both open and closed sections has been carried out [2.98]. A spectrally formulated element that has 3D (axial motion, transverse motion and rotation) per node for analysis of slender multiply connected composite beams under high-frequency impact loading was presented [2.99]. It was proposed that with this approach, a very large composite 2D beam network can be analyzed under high-frequency impact loading with much smaller system size and lower computational cost compared to time domain finite element method. Bassiouni *et al.* [2.100] worked on the dynamic behaviour for laminated composite beams using finite element method to obtain natural frequencies and mode shapes of the beam. Kim *et al.* [2.101] studied free vibration of a rotating tapered composite Timoshenko shaft. A mechanical model rotating at a constant speed about its axis was developed. This model represented an extended length-cutting tool intended for use in high-speed operations. In another development, analysis of the non-linear vibrations/post buckling analysis of laminated orthotropic beams/columns on two-parameter elastic foundation was performed [2.102]. The element was based on a consistency approach eliminating the shear-locking phenomenon for thin beam cases. The formulation accounted for transverse shear deformation, in-plane and rotary inertia terms, and highlighted the influences of different parameters on frequencies and buckling loads of laminated orthotropic beams. The nonlinear frequency/post-buckling load was obtained using an eigenvalue approach coupled with an iterative procedure. A different work carried out on the in-plane free vibration analysis of symmetric cross-ply laminated circular arches using both the Timoshenko and Bernoulli-Euler beam theories and derived free vibration equations based on the distributed parameter model while the transfer matrix method [2.103]. The study concluded that the dynamic problems of laminated composite circular arches must be solved considering the rotary inertia; axial and transverse shear deformation effects in the mathematical formulation.

Hidenori and Junya [2.104] studied the effect of constitutive coupling of stretching, bending, and transverse shearing on the free vibration of anisotropic cantilever beams as well as simply supported beams with narrow rectangular cross-sections. Song and Waas [2.105] investigated the effect of buckling and free vibration of stepped laminated composite beams using simple higher-order theory (SHOT), which assumes a cubic distribution for the displacement field through the thickness. The results showed that SHOT did not predict superior results than Timoshenko's shear theory even though SHOT was algebraically more complex. An additional investigation

was conducted on the free vibration of a stepped composite Timoshenko cantilever beam [2.106]. In an interesting development, Fein [2.107] successfully employed holographic interferometry, alternate methods that define actual data on the ground in a non-invasive environment to characterize the materials and behaviour of diverse types of structures under stress. This work followed the previous one on holographic interferometry applied to characterize the dynamic structure of an advanced graphite-epoxy polymer composite structure [2.108]. He *et al.* [2.109] presentation focused on a uniformizing method presented for the free vibration analysis of metal-piezoceramic composite thin plates, which are popular structures of thin plate-type ultrasonic motors. Sundaresan *et al.* [2.110] developed a general model based on Hamilton's principle and spectral analysis for non-linear free vibrations occurring at large displacement amplitudes of fully clamped beams and rectangular homogeneous and composite plates. The work concentrated on forced non-linear response of clamped-clamped (C-C) and simply-simply (S-S) supported beams and the model was derived using spectral analysis, Lagrange's equations and the harmonic balance method. The use of Padé approximants permitted considerable increase in the zone of validity of the solution obtained for very large vibration amplitudes. In another interesting work, study on skew fibre reinforced composite laminates considering a B-spline Rayleigh-Ritz method (RRM) has been presented [2.111]. It covers free vibration analysis of thin skew fibre reinforced composite laminates which may have arbitrary lay-ups, admitting the possibility of coupling between in-plane and out-of-plane behaviour and general anisotropy. The RRM has also been used on the calculation of natural frequencies of composite plates [2.112]. Similar work combined Ritz method with appropriate, complete bases of orthonormal polynomials and subsequently applied on the energy functional of the love-type version of a unified shear-deformable shell theory [2.113]. The accurate modelling of the interlaminar stress distribution may become a serious issue for further investigation, as it already is for the stress analysis of laminated composite structural elements.

Free vibration investigations have been researched from as many angles as the complexity of the composite beams. An actively developing field is 'vibration control'. Although this is not discussed further here, readers are directed elsewhere for further reading [2.114-2.118].

2.6   Flutter phenomenon investigations

2.6.1   Panel flutter

Panel flutter is a dynamic aeroelastic instability phenomenon resulting from the interactions between motions of an aircraft structural panel and aerodynamic loads exerted on that panel by air flowing past one of the faces. Recently, considerable research efforts have been expended to address panel flutter. For instance, a high-precision higher-order triangular-plate element that can be used to deal with transverse shear effects based on a simplified higher-order shear deformation plate theory (SDPT) and von Karman large deformation assumption has been developed for the nonlinear flutter analysis of composite laminates [2.119]. The transverse shear was found to have profound influence on the flutter boundary for a thick plate and under certain conditions it might change the plate motion from elastically buckled but dynamically stable to a limit-cycle oscillation.   On further developments, the finite-strip method [2.119] was later applied by the same authors to the flutter analysis of aircraft composite panels [2.120]. Elsewhere, following adaptive composites modelling and application in panel flutter plate, Suleman [2.121] concluded that it can be inferred that it is possible to achieve an increase in the flutter envelope using piezoceramics. However the application of the electromechanical adaptive composite plate concept is dependent on the mass to stiffness ratio and on the configuration and placement of the actuator patches.

Jinsoo and Younhyuck [2.122] developed a frequency-domain flutter analysis scheme for wings using an unsteady 3D panel method. The method was validated by comparing the generalized aerodynamic forces and the flutter points with other numerical results and measured data for various types of wings. In a corresponding work, a study on subsonic flutter suppression using self-straining actuators for the Goland wing model with torsion mode flutter has been reported [2.123]. The work revealed that while effective in increasing structure damping prior to flutter, self-straining controllers have little or no effect on the flutter speed.

2.6.2   Thrust induced flutter

Considering that engine thrust can be represented as a follower force, it is possible that thrust could lead to instability of an aircraft wing [2.124]. Even if the thrust force were not high enough

to induce instability on its own, it is quite likely that thrust could interact with other destabilizing mechanisms, for example, aeroelastic flutter. Even for propeller-driven aircraft, thrust could be important although, in the case of prop-whirl flutter, the thrust follows the propeller tip-path plane rather than the nacelle. For stiff propellers, however, it would nearly follow the nacelle. The effect of thrust on the flutter speed may be important, especially in the case of aircraft with very flexible wings. If thrust were to lead to a lowering of the aeroelastic flutter speed, one would certainly need to know about that in order to make appropriate adjustments in the design. Even if thrust were to increase the flutter speed, this could lead to an overly conservative design. In either case, the inclusion of thrust effects in flutter analysis should lead to a more complete analysis.

Kurnik and Przybyowicz [2.125] have studied an extended problem of the stability of Leipholz's slender column with rotation effect taken into account. The follow-up work examined a rotating cantilever column (slender shaft) subject to a tip-concentrated follower load and actively stabilised by piezoelectric elements [2.126]. The shaft was made of an active laminate - the piezoelectric fibre composite since such systems exhibit flutter-type instability as a result of energy transfer from rotation and to transverse motion of the shaft [2.127]. A velocity feedback was assumed in the system of active stabilisation. It was found out that shafts undergoing compression were particularly sensitive to such a stabilisation method; however, in the case of tensile loads the approach becomes ineffective since the system could be stabilised with respect to e.g. follower load but at the cost of angular velocity, the critical threshold of which dropped.
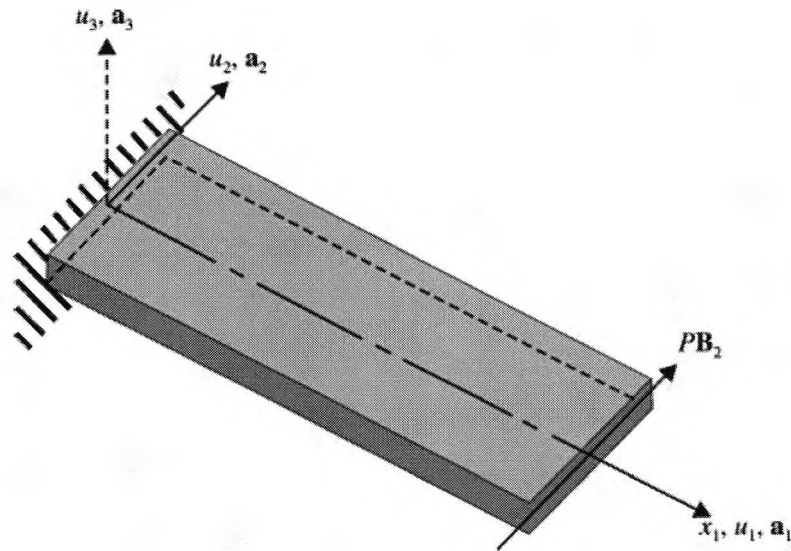
Figure 2.2   Schematic of wing showing co-ordinate systems and follower force [2.128].

In another interesting development, Hodges [2.128] focused on a uniform beam without bending-torsion coupling. In the model shown in Figure 2.2, three non-dimensional parameters that govern the dimensionless critical load were taken as the ratio of the cross-sectional mass centre offset from the elastic axis to the beam length (e) – (dashed lines), the ratio of the cross-sectional mass radius of gyration to the beam length (ϕ), and the ratio of the fundamental bending and torsional frequencies of an unloaded and uncoupled beam (r). Remarkably, when e = 0 the problem ceased to be dependent on ϕ, and the critical load depended only on r. And, when $e \neq 0$, there was a rich dependency of the critical load on both e and ϕ. The researcher suggested that bending-torsion elastic coupling of the beam, tip mass/inertia, and aeroelastic effects could be included in a more generalized approach. In a later work, the effect of thrust on the flutter of a high-aspect-ratio wing represented by a beam was investigated using a nonlinear mixed finite element method [2.124]. Aerodynamic forces were calculated using a finite-state, a 2-D unsteady aerodynamic model.

The effect of thrust was modelled as a follower force of prescribed magnitude. Parametric studies showed that the predicted stability boundaries are very sensitive to the ratio of bending stiffness to torsional stiffness. It was proposed that the effect of thrust can be stabilizing or

destabilizing, depending on the value of this parameter. An assessment whether or not the magnitude of thrust needed to influence the flutter speed in practice was also conducted for one configuration.

2.6.3 Wing/store type flutter

Within the context of aeroelastic tailoring, the influence of external stores attached to the wing structure has to be considered during the preliminary aircraft design phases. The mathematical model of aircraft structure for flutter analysis is usually symmetric. When different stiffness or mass properties exist between the left and right external stores, asymmetric configuration would be taken into account. For certain external store configurations, a small amount of structural asymmetry may increase the wing/store type flutter speed significantly. In this case, if feedback control is introduced to adjust automatically the stiffness of the external store on either side, then flutter can be suppressed effectively. The study of Liu *et al.* [2.129] study has shown feasibility of this flutter suppression scheme - suppressing aircraft flutter by means of disrupting the external stores symmetric state through some actuators driven by the structural-response signals. Gern and Librescu [2.130, 2.131] addressed structural and aeroelastic tailoring applied to advanced straight and swept aircraft wings' carrying external stores via a wing structure modelled as a laminated composite plate exhibiting flexibility in transverse shear and warping restraint effects. The results were found to be in good agreement with other published work highlighting the effects of underwing and tip stores on flutter instability [2.130]. Hu and Zhao [2.132] proposed a simple automatic control device that has been adopted to adjust the friction force of an electro-magnetic damper which is installed at the junction between the external store and the wing model (Figure 2.3). Since some wing/store (configuration) application of an impact damper can have significant effects on raising the flutter speed, the damping effects of the friction force was utilized to suppress the wing/store flutter. For the proposed model, when the electrical circuit is established, the armature was pressed to the yoke by the electro-magnetic attraction force proportional to which a friction force is introduced between the friction disc and the yoke. The attraction force was proportional to the square of the magnetic induction intensity which itself was proportional to the current intensity fed to the coil of the damper. When the damper was used to attenuate the rotational motion of a single-degree-of-freedom system, then

the frictional torque produced by the damper varied proportionally to the intensity squared of the current fed to the damper.
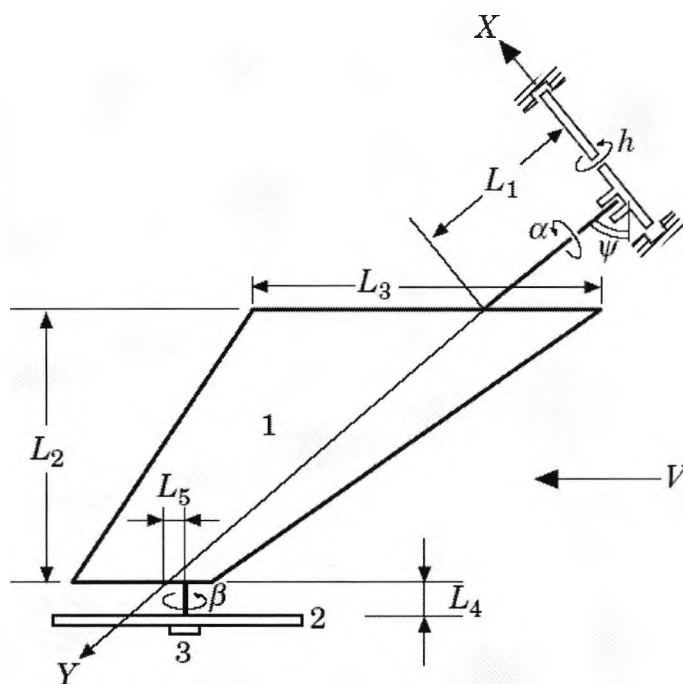
Figure 2.3   Sketch of wing/store model. 1 wing; 2 store; 3 electromagnetic friction damper [2.132].

2.6.4   Non-linear flutter

The next generation aeronautical and space vehicles are likely to feature increasing structural flexibility, operate in severe environmental conditions and feature greater manoeuverability capabilities than the present ones. In order to satisfy such contradictory requirements, an exhaustive exploitation of both the load carrying capacity of their structures and the associated manoeuverability capabilities should be used. The non-linear approach of the aeroelastic stability problem enables one to determine the conditions in which, due to the character of the influence of non-linearities that are inherently present in the aeroelastic system, the critical flutter velocity can be exceeded without an immediate failure of the structure as well as conditions in which undamped oscillations may appear at velocities below the critical flutter velocity [2.133-2.135]. Matching this behaviour with the post-buckling behaviour, the structures subjected to

compressive and/or lateral loads experience some features similar to that of the post-flutter response, in the sense of being benign that is mainly the behaviour of flat panels, or accompanied by a snap-through jump, in which case the failure is imminent (case that is proper for curved panels) [2.136]. These facts emphasize the considerable importance of at least two issues of including in the aeroelastic analysis the various non-linear effects - on the basis of which it is possible to gain a better understanding of their implications upon the character of the flutter boundary for benign or catastrophic effects. The importance of devising powerful methodologies based on both passive and active feedback control algorithms enables one not only to increase the flutter speed, but also to convert the catastrophic flutter boundary into a benign one. The desirability of using passive means based upon the use of directionality property of advanced composite materials and of active feedback control methodology appears to be an elegant approach.

Chandiramani *et al.* [2.137] examined the non-linear dynamic behaviour of a uniformly compressed, composite panel subjected to non-linear aerodynamic loading due to a high-supersonic co-planar flow. Meanwhile, Librescu *et al.* [2.136] have recently studied the benign and catastrophic characters of the flutter instability boundary of 2-D lifting surfaces in a supersonic flow field. The work based on the first Liapunov quantity was used to study the bifurcational behaviour of the aeroelastic system in the vicinity of the flutter boundary. It was demonstrated that the increase of non-linearities yielded an increase of the 'benign' portions of the flutter instability boundary; the opposite conclusion appeared for 'soft' non-linearities. Further, with the increase of the supersonic flight speed that resulted in an increase of aerodynamic non-linearities, an increase of the catastrophic portions of the flutter instability boundary was experienced (Figure 2.4 and 2.5).

The first order shear deformable plate and Timoshenko beam theories have been used for the finite element modelling of a skin panel and stiffeners considering von Karman non-linear strain-displacement relationships, and the nonlinear transient response of fluttering stiffened composite plates subject to thermal loads [2.138]. In a similar development, the thermal postbuckling and aerodynamic-thermal load analysis of cylindrical laminated panels has been performed using the finite element method in a follow-up work [2.139]. Again, the von Karman nonlinear displacement strain relationships based on layerwise theory are applied to consider large

deflections due to thermomechanical loads. The cylindrical arc-length method was used to take account of the snapping phenomena while panel flutter analysis of cylindrical panels subject to thermal stresses was carried out using Hans Krumhaar's supersonic piston theory [2.139].
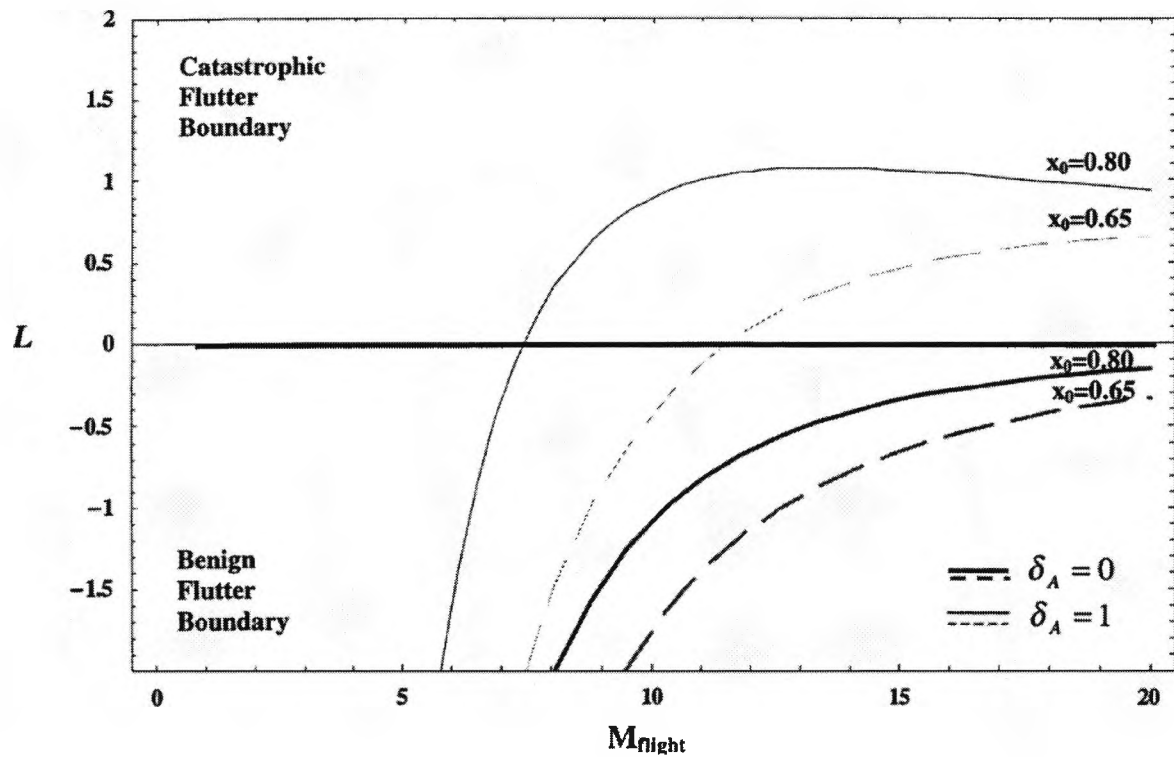
Figure 2.4 **Influence of the aerodynamic non-linearities and of the elastic axis position on the first Liapunov quantity, L, in the presence of physical non-linearities [2.136].**
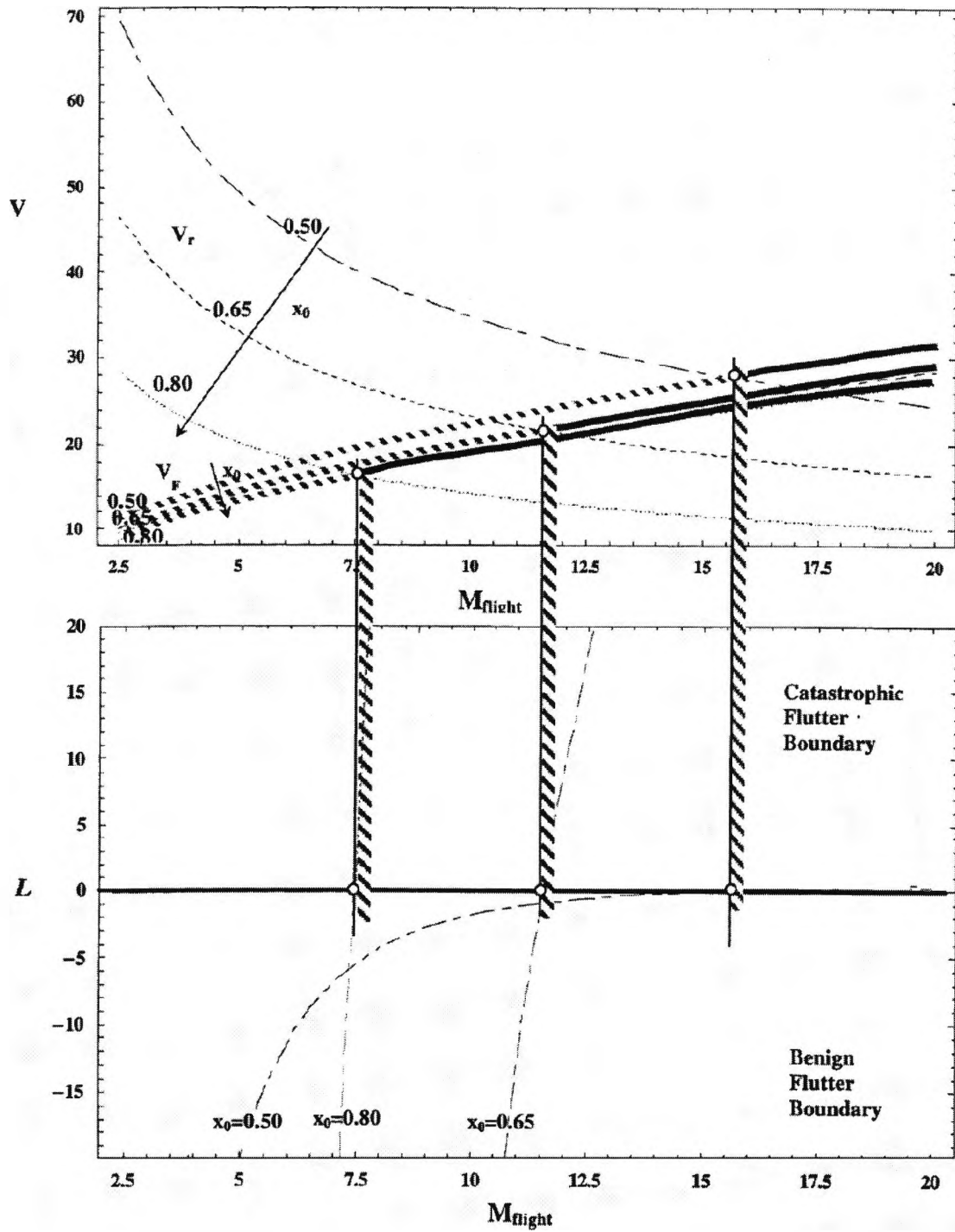
Figure 2.5   Benign and catastrophic portions of the flutter critical boundary as a function of the elastic axis position |2.136|.

Research has also been in progress in the field of passive suppression systems which are believed to be always more simple and robust than active control in practical operation. The feasibility of passively dissipating mechanical energy with electrical shunt circuits has been investigated. Such capabilities are likely to result in a tremendous increase in aircraft efficiency, range, speed, and manoeuverability rate as well as in higher payloads characteristics. Hagood and von Flotow [2.140] have recently formulated the equations of the mechanical and electrical characteristics with piezoelectric material shunted with electrical circuits for the case of a resistor alone and of an inductor-resistor resonant shunt to provide damping for the beam. Hollkamp [2.141] showed that multiple modes can be suppressed using a single piezoelectric patch connected to a multiple inductor-resistor-capacitor for a beam model. A finite element formulation has been presented for the nonlinear flutter suppression of an isotropic panel under uniform thermal loading by using the modal reduction scheme and LQR linear control [2.142]. Kim *et al.* [2.143] investigated a lag mode suppression of hingeless helicopter rotor blades with an L-R shunt circuit. Moon and Kim [2.144] presented a finite element formulation for a passive suppression scheme of nonlinear panel flutter using piezoelectric inductor-resistor series shunt circuit. However, since this approach is a fixed design, the damping would not be optimal when the system or operating conditions change.

Some studies have developed on active/passive hybrid control system, which integrates PZT actuators with an external voltage source and an inductor-resistor circuit in series. A systematic design/control method to ensure that the passive and active actions are optimally synthesized has been presented [2.145]. In a recent work, Moon and Kim[2.146], have proposed a new optimal active/passive hybrid control design for the suppression of nonlinear panel flutter, with piezoceramic actuators using finite element methods. The researchers claimed that this approach has the advantages of both active (high performance, feedback action) and passive (stable, low power requirement) systems. Elsewhere, Bauchau *et al.* [2.147] have presented a methodology for the analysis of backlash, freeplay and frictional effects in joints, within the framework of non-linear finite element multibody procedures and their applications, incorporating the effects of friction in joint elements together with effective computational strategy. A new strategy, based on the nonlinear phenomenon of saturation, has been proposed for controlling the flutter of a wing [2.148]. The results indicated that the aerodynamic nonlinearities alone can be

responsible for limit-cycle oscillations and that the saturation controller can effectively suppress the flutter oscillations of the wing when controller frequency is actively tuned. In still another development, Patil *et al.* [2.149] have looked at the effect of structural geometric nonlinearities on the flutter behaviour of high-aspect-ratio wings. Theoretical and experimental investigation of flutter and limit cycle oscillations using a nonlinear beam model and a stall model has been conducted by Tang and Dowell [2.150]. Hall *et al.* [2.151] presented the results obtained by using a 3-D geometrically exact (nonplanar) aerodynamic theory coupled with a linear structural analysis. The results that were based on free-wake aerodynamic analysis, also, illustrated that flutter instability speed was drastically reduced with wing curvature

In conclusion, there are many potential sources of non-linearities, which can have a significant effect on an aircraft's aeroelastic response. One essential limitation involving the linearized analysis is that it can only provide information restricted to the flight speed at which the aeroelastic instability occurs. Furthermore, the linearized analyses are restricted to cases where the transient aeroelastic response amplitudes are small. Often this assumption is violated prior to the onset of instability. Thus, to study the behaviour of aeroelastic systems either in the post-instability region or near the point of instability, the structural, physical and aerodynamic non-linearities must be accounted for [2.136, 2.152]. Nowadays, there is an increased attention to address the non-linearlity issues as highlighted here.

2.6.5 *Flutter of a damaged panel*

To meet the increased performance and standards for the existing aircraft as well as new generation of aerospace vehicles, engineers are using a combination of metallic and composite structures in their design. The repair structures may be skewed in shape and may develop cracks due to manufacturing process or fatigue loading during service. It is therefore, important to study the flutter behaviour of such panels caused by the complex interaction of aerodynamic, inertia and structural forces. Flutter takes place at a critical air speed and it is important to capture this instability accurately for arbitrary panel configurations as it might otherwise lead to catastrophic failure. Strganac and Kim [2.153] have also studied the aeroelastic behaviour of composite plates subject to damage growth and suggested that there is a need to develop damage as part of the flutter solution. Thus, Pidaparti and Chang [2.154] carried out an investigation of skewed and

cracked panels under supersonic flow using the general plate/shell finite element based on tensorial approach. Another work studied the supersonic flutter behaviour of isotropic thin cracked panels using the hybrid finite element method [2.155]. Recently, Lin *et al.* [2.156] studied the panel flutter problems of thin plate-like composite panels with patched cracks using a finite element method (FEM). They showed that flutter performance could be improved by isotropic patching. The flutter characteristics of 2-D delaminated composite panels at high supersonic Mach numbers were investigated by Shiau [2.157] and concluded that the presence of a delamination decreases the flutter boundary. A finite element method was also employed to investigate the free vibration and supersonic flutter analysis of arbitrary damaged composite panels [2.158]. The FEM employed 48 degrees of freedom (DOF) general plate element and used the classical lamination theory, microstructural continuum damage theory and linearized piston theory. Finite element results were obtained to illustrate the effect of damage on the eigenvalues and flutter boundaries. The results obtained further indicated that damage had a strong influence on both free vibration and flutter boundaries.

2.6.6   Flutter in compressible flow

With the advent of active control technology for flutter suppression and gust load alleviation, and with the increasing need for evaluating the time-dependent subcritical aeroelastic response of lifting surfaces, the time domain representation of unsteady aerodynamic loads becomes a necessary prerequisite toward achieving these goals [2.159]. This is in contrast to the flutter instability analysis in which context a frequency domain formulation is required. The accurate modelling of the unsteady aerodynamics plays a key role towards approaching the aeroelastic problems. By definition, an indicial function, also called indicial admittance, is the response to a disturbance generated by a step function [2.152]. The unsteady lift and aerodynamic moment in time and frequency domains in the compressible flight speed range are obtained by using the pertinent aerodynamic indicial functions. As is well-known, if the indicial function can be determined, then by using Duhamel superposition principle, these can be applied toward determination of the aerodynamic lift and moment in time or frequency domain, for any arbitrary variation in angle of attack (α) and/or inflow velocity. The representation of the unsteady aerodynamic loads in the time domain is necessary toward determination, in the subcritical flight

speed regime, of the dynamic response of aeroelastic systems exposed to arbitrary time-dependent pressure pulses. In addition, when a feedback control system is implemented, this representation of aerodynamic loads is essential toward determination of its closed-loop aeroelastic response [2.160]. In this context, both the open and closed loop dynamic responses of the aeroelastic system can be analysed. On the other hand, the representation of aerodynamic loads in the frequency domain is necessary toward determination of the flutter instability boundary [2.159]. Also, since the aircraft design is primarily based on the principle of thin-walled beams, it is desirable to investigate the aeroelastic instability and aeroelastic response directly within the framework of thin-walled beams [2.161].

Marzocca *et al.* [2.160] investigated the subcritical aeroelastic response of 2-D lifting surfaces in an incompressible flow field to gust and explosive type loadings, including that due to a sonic-boom pressure pulse employing the concept of the indicial functions to determine the unsteady aerodynamic loads for a 2-D lifting surface in various flight speed regimes that include the compressible subsonic, linearized transonic, supersonic and the hypersonic ones. In a later work, unified approach enabling one to obtain the unsteady lift and aerodynamic moment in the time and frequency domains for 2-D lifting surfaces was developed - the concept of the indicial functions was employed to determine the unsteady aerodynamic loads for a 2-D lifting surface in various flight speed regimes that include the compressible subsonic, linearized transonic, supersonic and the hypersonic ones [2.162]. Validation of the aerodynamic model, obtained by comparing the indicial aerodynamic functions with the ones based on other unsteady aerodynamic theories showed an excellent agreement. Moreover, the predictions of the subcritical aeroelastic response in subsonic compressible, transonic, supersonic and hypersonic flight speed regimes to external pulses, based on the aerodynamic models developed [2.162], revealed an excellent agreement with the ones generated via the application of other aerodynamic theories. The numerical simulations assessing the versatility of this approach enabled the researchers to treat both the subcritical aeroelastic response and flutter instability.

Plate-beam model has been used for investigating the implications of warping restraint and transverse shear on the static divergence, and flutter of aircraft wings [2.161]. Lately, the problems of aeroelastic instability and dynamic aeroelastic response of advanced aircraft wings modelled as anisotropic composite thin-walled beams in compressible subsonic flow and

exposed to a sharp-edged gust load have been approached using a unified approach. It was claimed that warping restraint effect had to be considered in the structural model of composite aircraft wings. Compared with the warping restraint effect, the influence of transverse shear appears to be much less significant. In yet another development, aeroelastic model was developed toward investigating the influence of directional property of advanced composite materials and non-classical effects such as transverse shear and warping restraint on the aeroelastic instability of composite aircraft wings [2.163].

As addressed earlier, for the prediction of aeroelastic response in the compressible flow it is necessary to express the lift and moment via the proper indicial functions expressed in time domain. For flutter problem in the subsonic compressible and supersonic flight speed regimes, an analogous procedure based on the generalized counterparts of Theodorsen's function for these flight speed regimes can be used [2.163]. Also, simple harmonic motions are normally interpreted as the forces on the imaginary axis in the complex ω-plane, Vepa's matrix Padé approximants of the aerodynamic forces, have been widely used in aeroelastic analyses [2.163-2.165]. Edwards [2.164] used the classical theories of Theodorsen and of Garrick and Rubinow for 2-D lifting surfaces, and obtained the corresponding ω-domain solutions for incompressible and supersonic flows. Ueda and Dowell [2.165] have generalized their doublet lattice method to the ω-domain for 3-D subsonic lifting surfaces and developed a simple method for calculating the unsteady aerodynamics on harmonically oscillating thin wings in subsonic compressible flow.

2.6.7 Flutter control via neural networks

There exists a great anticipation that artificial neural networks, once properly trained, can be used to significantly speed up the design and analysis process of aerospace systems by allowing rapid trade analysis as well as quick evaluation of potential impacts of design changes. However, training time is has not been generally included in this assertion [2.166]. It is envisaged that the training of networks can be done autonomously during off hours, so that they are made available to the designer/analyst when required. Nevertheless, there are certain drawbacks associated with neural networks that need to be addressed. These include the time-consuming nature of the

training process, training difficulties, such as optimisation problems, and a lack of a meaningful way to establish network accuracy.

One of the main advancements in neural networks (NN) approach is the match-point solution for robust flutter analysis. The computation of robust flutter speeds presents a significant advancement over traditional types of flutter analysis. In particular, μ-method analysis is able to generate robust flutter speeds that represent worst-case flight conditions with respect to potential modelling errors. Robust flutter speeds may be computed using a model formulation that has been previously presented but the formulation has limitations in its ability to generate a match-point solution. Of late, a model formulation has been introduced for which μ-method analysis is guaranteed to compute a match-point solution that is immediately realized by analysing a single model thus reducing the computation time significantly eliminating the normally required iterations [2.167]. The proposed model was claimed to be able to consider parametric uncertainty in any element. The match-point formulation is derived by properly treating the nonlinear perturbations and uncertainties that affect the equation of motion - the aerostructures test wing was used to demonstrate that the μ-method analysis computes match-point flutter speeds using this new formulation.

2.6.8 *Flutter analyses of actively controlled composite structures*

Smart structures sense external stimuli, process the sensed information, and respond with active control to the stimuli in real or near-real time. A response can consist of deforming or deflecting the structure or communicating the information to another control centre. Smart materials deform or deflect the structure by changing their physical properties when subjected to electric, magnetic or thermal loads. An extension of this is the intelligent, self-healing vehicle whose built-in redundancy and on-board self-inspection detects damage and responds with autonomous adjustments and repair. Further, smart structures may be time-variant and non-linear. It is a challenge to control such structures. Conventional active controller design methods, e.g., eigenstructure assignment and optimal control, require accurate mathematical models. But accurate models are almost impossible for smart structures, because of non-ideal behaviour, simplifications in modelling, manufacture error, parts wear, and environment change.

In this case, adaptive control may be an attractive alternative. There are two radically different adaptive control approaches: (i) adaptive feedback control and (ii) adaptive feedforward control. Adaptive feedforward control was originally used for noise control and then extended to vibration control. Up to now, it has been studied in large space structure control, civil structure vibration under seismic or wind excitation, helicopter vibration control, wing flutter suppression, and vibration reduction for automobiles [2.168, 2.169]. Its recursive capability makes it very suitable for digital signal processors (DSP). In the meantime, the rapid development of digital signal processors also expedites the application of this technology. However, adaptive feedforward control is not available to control the higher harmonic components in responses. This is just because the reference signal does not correlate with the higher harmonic components in these responses. In order to solve this problem, one idea that has been proposed is to introduce a non-linear functional block into the adaptive feedforward control strategy [2.169]. This non-linear functional block must be able to receives an input reference signal that only contains the fundamental component and its output contains both the fundamental and higher harmonic components, i.e., it can non-linearize the reference signal.

It is ironic that although much work has been carried out to study the fundamental problems in smart structures, there have been few experimental demonstrations of such active solutions, because the control algorithms are complex and require a significant processing power so that the signals can be calculated in real-time. Previous simulation work has indicated that the computing resources required for addressing the main problems are considerable, and hence attempts have been made to make major simplifications. Normally, this means that the modelling orders cannot be too high, and only the dominant modes can be included so that the computing resources are reduced; however, this inevitably leads to degradation in the accuracies that are achievable in practice. In control applications, model reduction is vital in order that real-time performances can be achieved especially in direct digital control (DDC) situations coupled with good overall accuracies. Published work in this area is rather scarce, since even with the reduced order models effective on-line control is difficult because uni-processor systems cannot achieve real-time performances. But such works are beginning to appear. Most recently Virk and Al-Dmour [2.170] successively demonstrated a good way of reducing the dimensionality of the control problem by deleting the modes that were the least controllable and observable dependent on

system configuration, i.e. the precise locations of the sensors and actuators. It was shown that the accuracy demanded by the nature of the problem needs to be balanced with the real-time data throughput that is practically achievable by the computer system available to perform the processing. Clearly, this trade-off need to be resolved for each situation but having a network of processing elements will increase the number of operations that can be performed, and hence lead to better solutions, assuming the parallel solutions are efficient.

2.7   Summary of the literature review

Aerospace industry is likely to be the main beneficially of the polymer nanocomposites developments as the nanotechnology evolves. Often the aerospace applications demand high performance materials durable for an extended period of time in volatile climatical conditions that traditional composite materials may struggle to meet. The literature survey revealed some of these expectations. It is well beyond any doubt that polymer nanocomposites (PNC) portray superior characteristics that can be tailored to meet most of these specific requirements. Nevertheless, nanotechnology is still in its early stages, only around a decade old, and there lays a lot of challenges ahead to procure the quality assurances for safe and economical applications before its full engagement in aerospace. Some applications are beginning to appear, nanotubes-manufacturing method is gearing towards mass production hence lowering the overall costs, macrostructures are gradually establishing, regulations and standardization procedures are being developed. Thus, the impetuous for the growth of the polymer nanocomposites is finally gaining its grounds.   Although this literature review concentrated mainly on free vibration, beam modelling and aeroelastic tailoring of composite beams, remarkable work has also been carried out in other aspects of composite beams. Amongst them is on the active control (artificial intelligence) of the composite wings, which is a really break through in the utilisation of composite structures. Others works include delamination, development of new materials, wind tunnel model testing, computer modelling, advanced analysis and air-crashworthiness, just to mention a few. In this work, the aeroelastic characteristics have been addressed and associated effects on real life aircraft wings accounted for. The potential of composites is reflected by the capability to idealise the structures. The phenomenon is without doubt overwhelming and warmly welcomed by the aerospace industry.

2.8 Scope of the present investigations

The present investigation involves polymer science, sandwich beams, laminated composite beam modelling, buckling analysis, free vibration analysis and aeroelasticity. In the following Chapters, PU and PANI key properties (mainly mechanical and thermal properties) are investigated independently. Samples of PANI and PU are prepared and tested using spectroscopy, microscopy, TGA and mechanical testing. PU/PANI conducting thermoplastic elastomers with good mechanical properties and processability are synthesed combining the beneficial properties of the two polymers i.e. tensile strength, thermal properties and compatibility. The computational and experimental investigations reported herein verify associated technological issues without undermining the outlined compatibility difficulties for such systems, as mentioned in the literature review. In the next stage of this development, an advance PU/montmorillonite (MMT) nanocomposites is prepared and characterised to demonstrate the special properties featuring in the literature review.

The follow-up work focuses on rigorous formulation of aircraft structures. The first part is theoretical in which a refined theory based on advanced dynamic stiffness theory for a three-layered sandwich beam is developed in order to investigate its free vibration characteristics. In this new development all three layers of the sandwich beam are assumed to behave according to the Timoshenko beam theory. A significantly improved model is realised. The focal point of the follow-up research is the experimental measurement of the free vibration characteristics, namely the natural frequencies and mode shapes, of sandwich beams by using an impulse hammer kit and associated computer software. In order to achieve this, a number of specimens of three-layered sandwich beams are manufactured using rubber as the core and aluminium and/or steel as the face materials.

The structural rigidities (static) need to be known in advanced stage for any composite wing design. This forms the next step of this thesis. Using classical lamination theory, the development leads to the establishment of the cross-coupling parameter, which is defined as a measure of bending–torsion coupling present in a structure, thus establishing trends, generalising the results and also underpinning the aeroelasticity of composite wings. Buckling analysis is carried out to confirm the wing stiffnesses. Simultaneous flexure and twist in a composite

column, caused by both geometric and material coupling terms, which are usually present in thin-walled cross-section are studied. After the properties evaluation, the composite wing can be safely applied to the real design. Therefore in the next phase, beams with cantilever end conditions are examined in detail for their free vibration characteristics. This is directly relevant in the context of composite aircraft wings. In particular the effect of the ply angle (θ) on the natural frequencies and mode shapes of composite beams are studied. The results highlight interesting features. Additionally, flutter analysis of composite wings is carried out. Additional insights have been gained into the composite wing flutter characteristics and to further understand the phenomenon better. The ply angles are varied to study the effects of ply orientation on flutter speeds as applicable to unswept and sweptback aircraft wings.

3 Synthesis of polyurethane and polyaniline thermoplastic elastomers

3.1 Introduction

The potential usage of conducting polymer blends includes electro-chromic and electro-optical devices, packaging materials, actuators, batteries, and catalysis. Such elastomers may also have applications as rollers used in electrostatic imaging, cables, EMI-shielding gasket materials, and, potentially, chemical and/or biological sensors [3.1-3.3]. Conducting polymers such as polyaniline, polythiophene and polypyrrole exhibit excellent electrical conductivities and outstanding thermal stability, while their chemical solubility and mechanical properties are poor leading to a reduced processability. To overcome these difficulties most research efforts found in the literature was focused on the chemical functionalization of such conducting polymers and on composites of conducting polymers with elastomers, with thermoplastic polyurethanes being one of the most important groups of materials. In the case of conducting polymers, the objective is to prepare polymeric materials with good mechanical properties and improve processability associated with high conductivity or electrochromism [3.4, 3.5]. Conductive polymers may be synthesised by any one or combination of the following techniques: chemical polymerisation, electrochemical polymerisation, photochemical polymerisation, metathesis polymerisation, concentrated emulsion polymerisation, inclusion polymerisation, solid-state polymerisation, plasma polymerisation, pyrolysis or soluble precursor polymer preparation [3.5, 3.6]. The incorporation of functional groups (e.g. carboxylic, sulfonic, phosphonic groups) in the polyurethanes (PU) backbone, able to react further covalently or non-covalently, leads to PU-ionomers with the improved characteristics such as adhesion, dyeability and ionic conductivity or polymers with special properties like haemocompatibility, polymers with shape memory effects and non-linear optic properties. It can be demonstrated that these polymers could be highly promising for many technological uses because of their chemical versatility, stability, processability and low cost. PU conducting composite/blends can be prepared in either chemical or electrochemical techniques with the aim of preparation for new materials combining synergistically the properties of the blend components.

Polyurethane thermoplastic elastomers are extremely chemical resistant for use in the harshest environments whereby specially formulated PU meet unique requirements that are necessary for electronic and other material engineering applications. Of great importance, PU is a unique material that offers the elasticity of rubber combined with the toughness and durability of metal. It is composed of a polyether or polyester soft segment and a diisocyanate-based hard segment, is a well-known tough material and is usually used as an additive to enhance toughness of brittle materials as well as thermal properties [3.1-3.3]. The most common diisocyanates are presented in Table 3.1 (below) along with that of schematic representation of segmented PU – see Scheme 3.1 below. Because of the incompatibility between the hard segments and the soft segments, PU undergoes microphase separation resulting in a hard-segment domain, soft-segment matrix, and urethane-bonded interphase. The hard-segment domains act as physical cross-links in the soft-segment matrix. The primary driving force for phase separation is the strong intermolecular interaction of the urethane units, which is capable of forming intermolecular hydrogen bonds. Owing to such interactions, interconnected or isolated hard segments remain distributed in the soft segment matrix, though the soft domain may contain some hard segments dissolved in it, which is evident from the hydrogen bonding of the urethane–NH groups with the oxygen of the ether or ester linkages [3.3]. These kinds of PU are utilized mainly as water dispersions (coatings, adhesives) and also as biomedical devices, temperature-sensing elements, polymer electrolytes, etc.
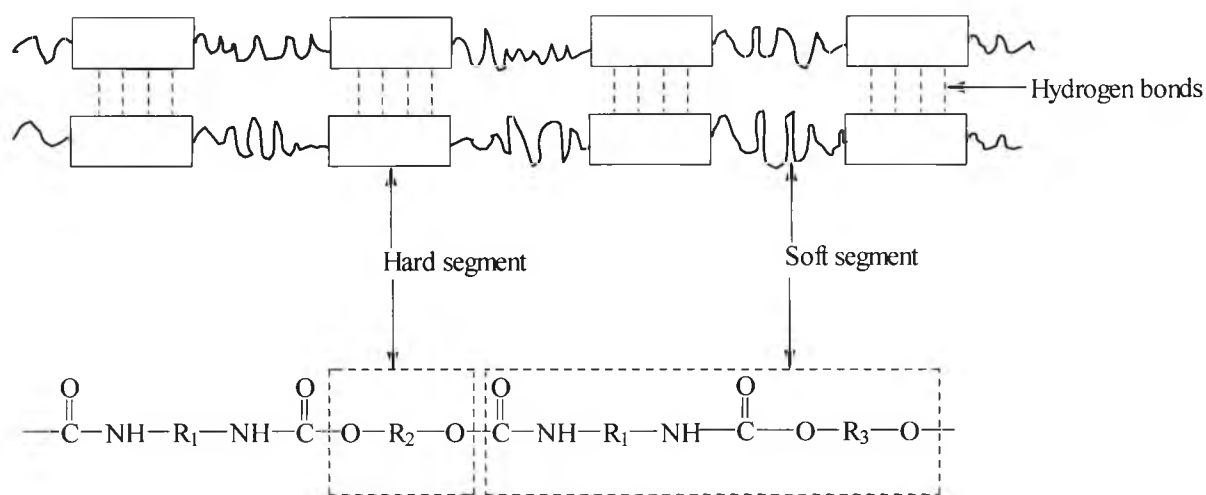
Scheme 3.1   Schematic structure of segmented polyurethane [3.3].

Table 3.1   Structure and molecular masses of selected diisocyanates.

Conducting polymer	Structural formula	Conductivity (S/cm)
Polyaniline		$10^{-9}-10^{5}$
Polypyrrole		600
Polythiophene		200
Poly-p-phenylene		500
Polyacetylene		10^{5}
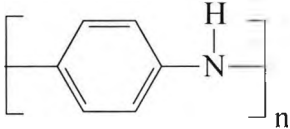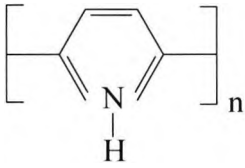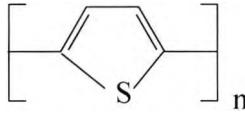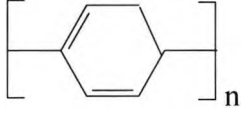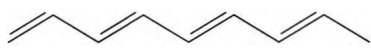
In the case of conducting polymers, the objective is the preparation of polymeric materials with good mechanical properties and processability associated with high conductivity or electrochromism. Polyaniline is one of the oldest conductive polymers known. Polyaniline (PANI) is one of the most investigated conducting polymers, due to its easy synthesis and good conductivity. However, its intractability resulting from the stiffness of the backbone and hydrogen-bonding interaction between adjacent chains limits not only industrial applications.

Electrically conductive polymers (ECP) are able to conduct electricity because of their conjugated π -bond system, which is formed by the overlapping of carbon π-orbitals and alternating carbon-carbon bond lengths. In some systems, such as polyaniline, nitrogen π-orbitals and C-rings are also part of the conjugation system. The conjugated double bonds permit easy electron mobility throughout the molecule because the electrons are delocalized. Delocalization is the condition in which π-bonding electrons are spread over a number of atoms rather than localized between two atoms. This condition allows electrons to move more easily, thus making the polymer electrically conductive. PANI exists in three forms of oxidation states: leucoemeraldine (fully reduced or only benzenoid amine structures), emeraldine (neutral or partially reduced and partially oxidized), and pernigraniline (fully oxidized or only quinoid imine structures). The emeraldine-based (EB) form of PANI was used for this research because only doped EB PANI is conductive among the three-oxidation states. The emeraldine-based form of PANI is also the most stable of the three states because leucoemeraldine is easily oxidized when exposed to air and pernigraniline is easily degraded.

Furthermore, PANI is the only conducting polymer whose electrical properties can be controlled suitably by charge-transfer doping and/or protonation. Due to its reversible electrochemical response during anodic oxidation and cathodic reduction, it is useful as a secondary electrode in rechargeable batteries and electrochromic display devices. However, two major limitations of conducting PANI are an inability to process it by conventional methods and its poor mechanical properties. These limitations can be overcome by preparing conducting PANI blends and composites, which possess the mechanical properties of the insulating host matrix and the electrical properties of the conducting PANI guest [3.4, 3.7]. Recently, PANI has been found to exhibit unusual chemical, electrical, and optical phenomena, both in insulating and conducting forms. Incorporation of conductive PANI into a hosting polymer substrate forming interpenetrated networks (IPN) has been a newly adopted method as an approach to combine electrical conductivity of PANI with desirable mechanical strength of insulating polymers. These unique properties make PANI useful in many applications, particularly in energy storage, electronics, photovoltaic devices, displays, and sensors, antenna material in cellular phone, as an antistatic paper roller in a printer, and as a fragile, preventive wrapping bag for packing electronic products [3.5]. The unique properties have led to an interest in the potential use of

PANI as a new class of conductors. This interest was generated due to the relative ease of synthesis, low cost, and the stability of PANI in air. In spite of all, the insulating form of PANI, polyaniline emeraldine base (PANI-EB), suffers from limited solubility in organic solvents. This difficulty was recently resolved by Cao *et al.* [3.8] by functionalising the dopant counter-anion with polar and non-polar analogs to increase solubility in organic solvents. The aniline polymers are also on beam light because of their environmental stability, controllable electrical conductivity and interesting redox properties associated with the chain nitrogen. These polymers also exhibit crystallinity and solution- or counterion-induced processability.

In much of the research done in PU/PANI blends, it has been found that the intrinsic properties of the components of the blends are different from the primary polymers. Sometimes, the properties are enhanced but for the most part, they were diminished. In this chapter, the investigations reported are designed to explore the key characteristics for PU and PANI independently. This work paves way into further investigations to exploit the unique properties for technological considerations. The computational and experimental investigations reported herein verify these beneficial issues without undermining the outlined compatibility difficulties mentioned earlier on.

3.2 Experiment

3.2.1 Materials

For synthesis of segmented polyurethanes, partially polymerised 4,4'-diphenylmethane diisocyanate (MDI, 31% of free isocyanate groups in relation to the pure diisocyanate) (Zachem Bydgoszcz, Poland) and 1,6-hexamethylenediisocyanate (HMDI) (Aldrich), polyoxypropylenediol (POPD, M=750, Rokita S.A., Brzeg Dolny, Poland), 1,2-propanediol (PD) (POCh, Gliwice, Poland) or 3-chloro-1,2-propanediol (CPD) (Aldrich), and 1-allyl-2-methylimidazole (catalyst) (Zachem) were used. Ethyl acetate (POCh) was purified by distillation and used as a solvent during polymerisation. Aniline (POCh Gliwice, Poland) was distilled under nitrogen prior to use; ammonium peroxydisulphate (POCh Gliwice, Poland) was used without further purification.

3.2.2 *Preparation for polyurethanes*

Segmented polyurethanes were prepared by a two-step (prepolymer) method, according to the general procedure: isocyanate and polyoxypropylene glycol were reacted at 65 °C for 2 h in a temperature-controlled reactor (Figure 3.1). The resulting prepolymer was dried under vacuum, and then subjected to further polymerisation with a mixture of diols in the presence of catalyst (0.5 wt.%). The reaction time was 30 min. The second set of polyurethanes were prepared by a one-step method (Figure 3.2), according to the general procedure: into a thermostated reactor first put isocyanate (MDI) and solvent (ethyl acetate); next, a mixture of diols (POPD and low-molecular chain extenders: PD or CPD) with catalyst was added dropwise under mixing within 30 min; temperature of the exothermal polyaddition did not exceed 60 °C. The obtained highly viscous polymer was placed into an open mould and dried for 7 days. Figure 3.3 and Figure 3.4 illustrates the experimental set up while Figure 3.5 shows the vacuum drier used throughout the experiments.
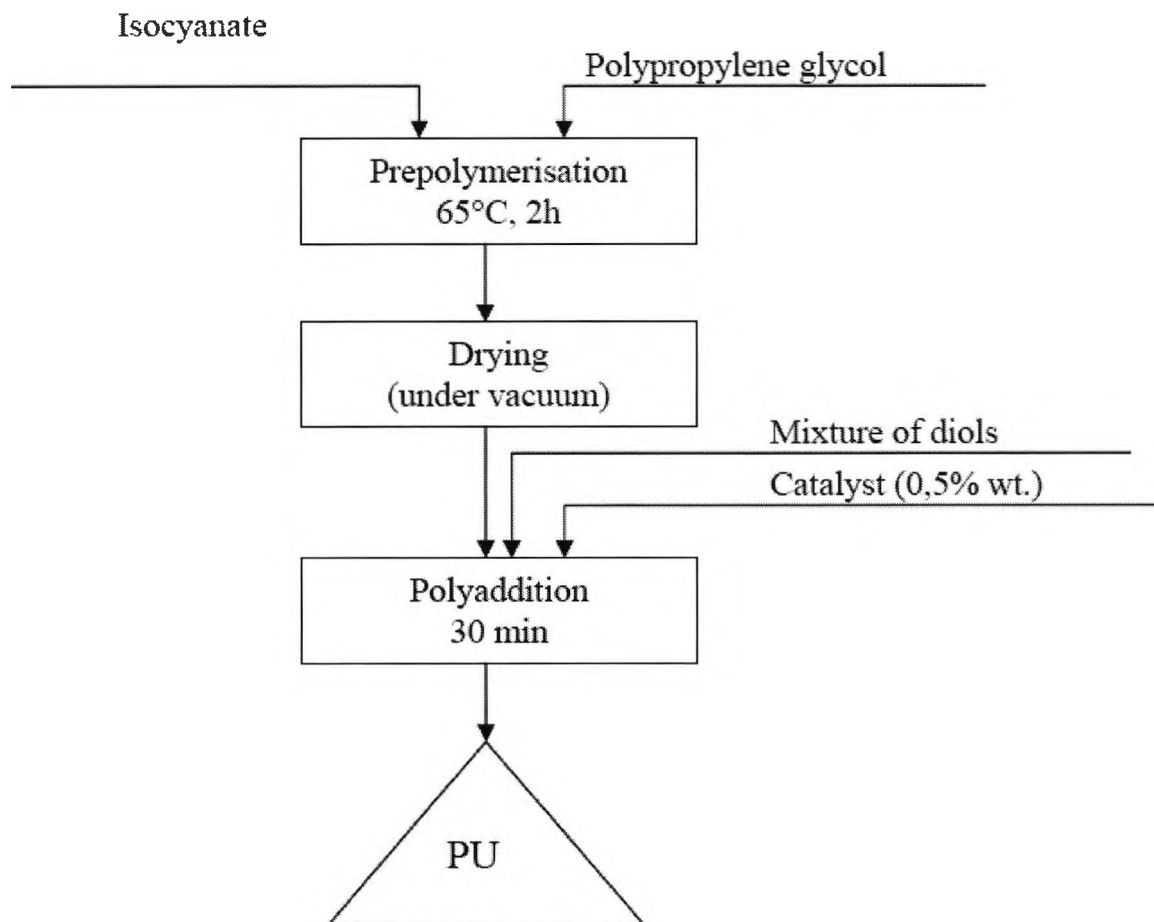
Figure 3.1   Schematic diagram showing the synthesis of PU films through two-step (prepolymer) method

Isocyanate

Solvent (ethyl acetate)

Mixing

Mixture of diols

Catalyst (0,5% wt.)

Polyaddition
(Mixing, added dropwise), 60°C

Cast into the mould

Drying
7 days

PU
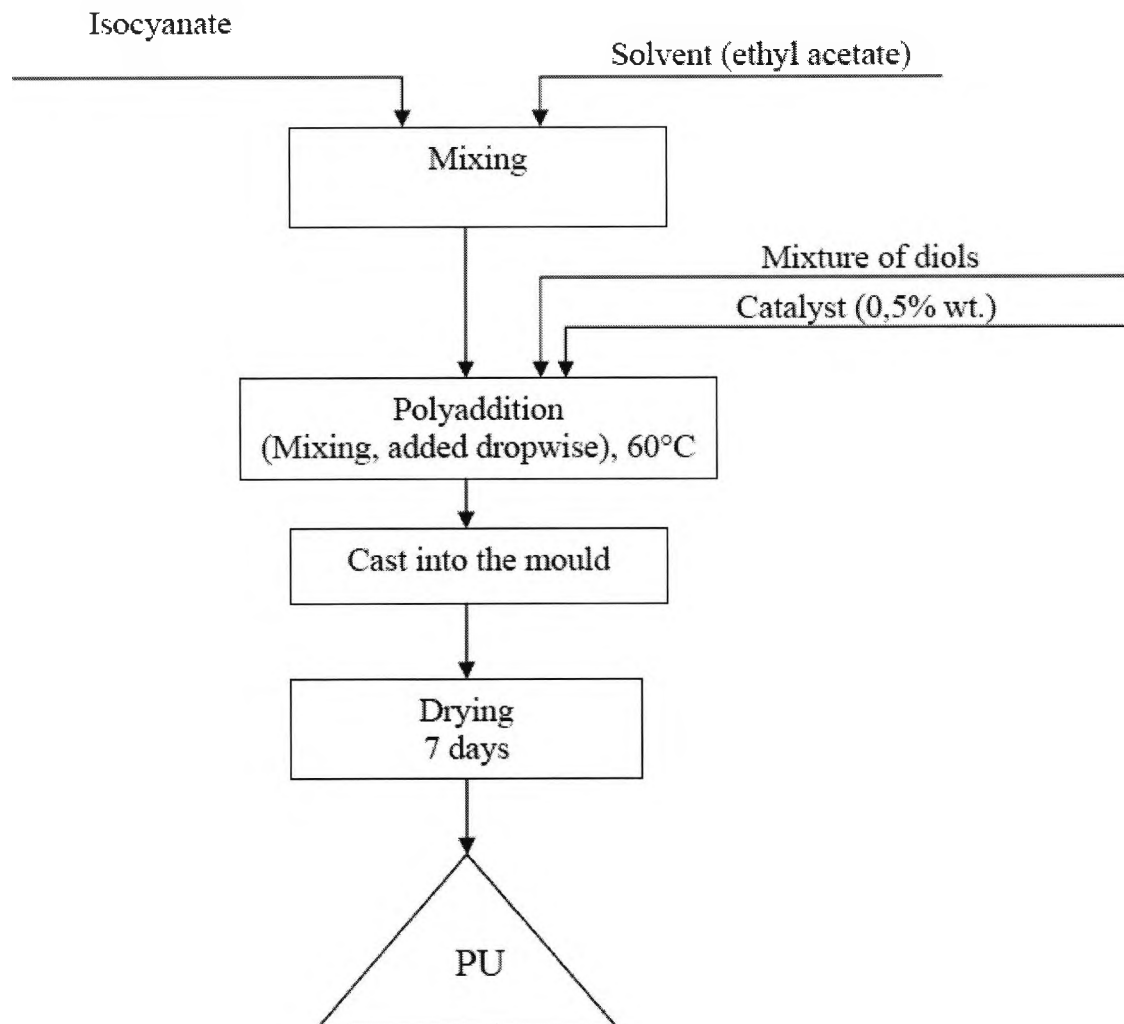
Figure 3.2   Polyurethane synthesis through one-step (prepolymer) method
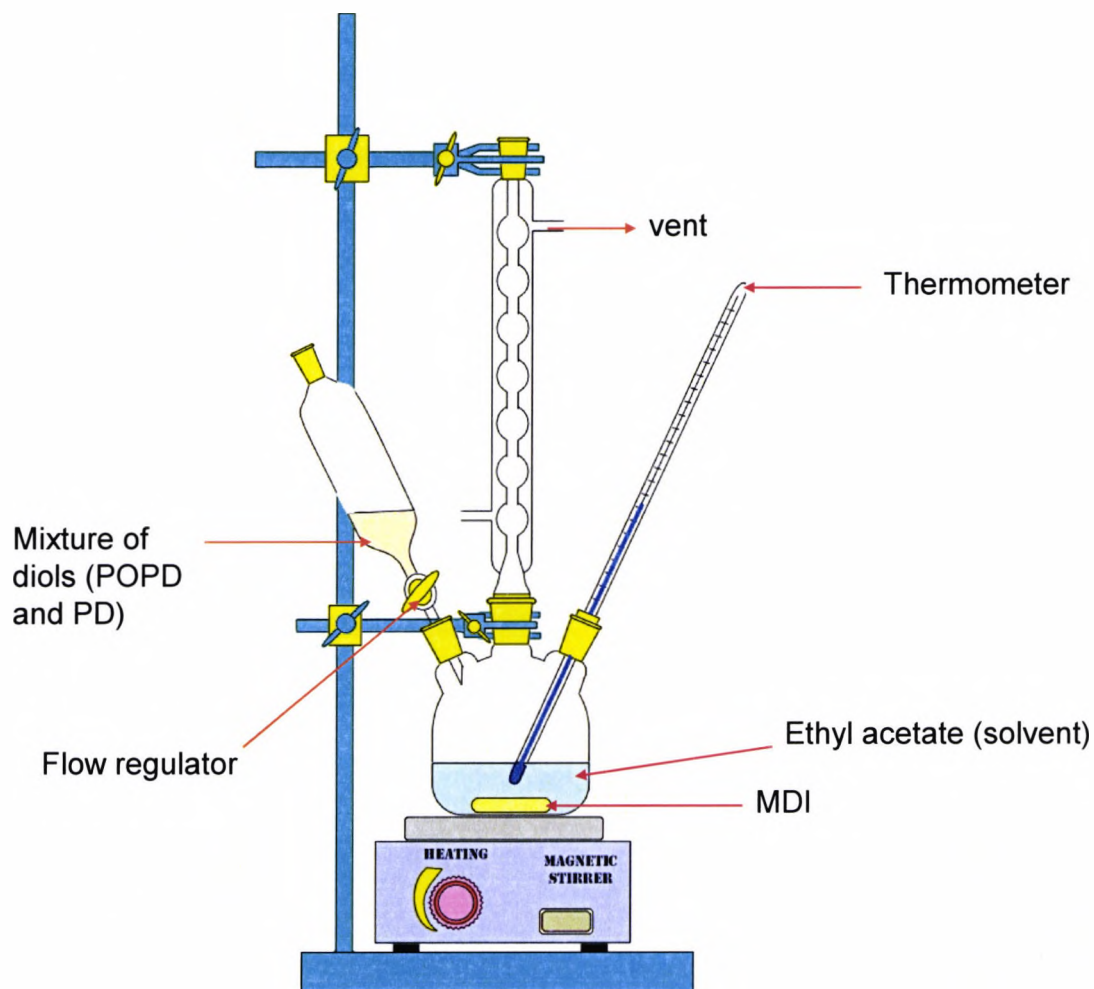
Figure 3.3   Diagrammatic set up of the synthesis of PU thermoplastic elastomers
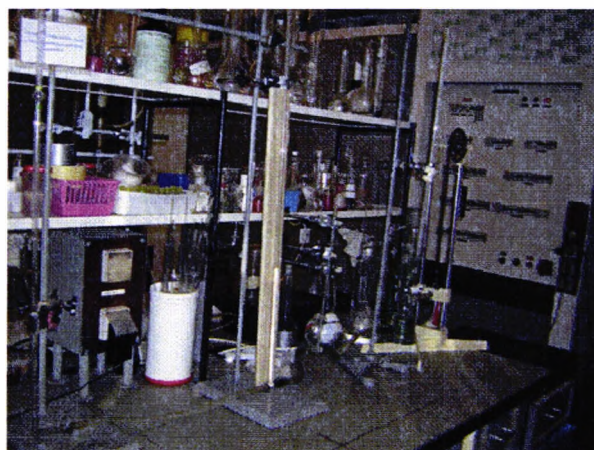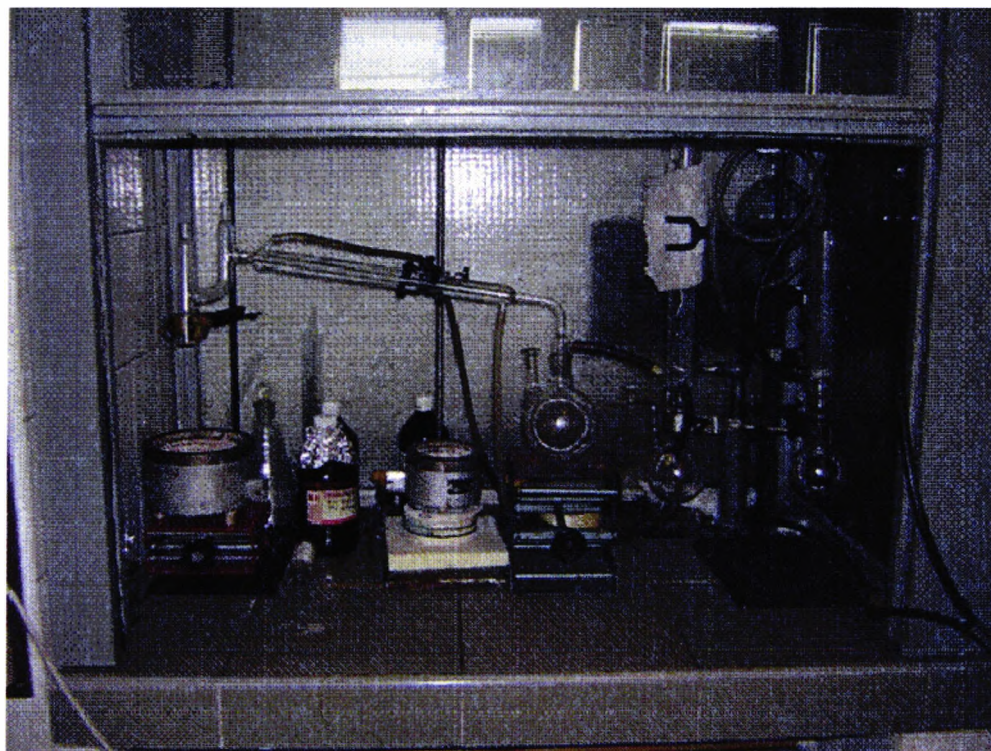
Figure 3.4 Typical experimental set up for the synthesis of PU, PANI, PU/PANI and PU/MMT
thermoplastic elastomers (top) and a selection some of the test equipment (below) used in the experiments

Figure 3.5   Vacuum drier used for the experiments

3.2.3   *Preparation for polyaniline*

Polyaniline was synthesized by chemical oxidation in an acidic medium following a previously described procedure [3.9].   In a typical synthesis (Figure 3.6), Camphor sulfonic acid doped polyaniline (PANI-CSA) at doped ratio of 2:1 - of two CSA molecules in one PANI repeating unit - was used. A mixture of m-cresol-chloroform (1:9) was used as the spreading solvent. The concentration of PANI-CSA solution was 1.0×10^{-3} g/ml. The substrates used in this work were all CaF_2 that had been pretreated by ultrasonic cleaning, sequentially with $CHCl_3$, C_2H_5OH and H_2O for 20 min. The casting film was prepared by adding the PANI-CSA solution on the substrate drop by drop. Surface pressure-mean molecular area isotherm determination and multilayer LB film deposition were carried out using $KSV^{@}$-5000 system. Deionized and double distilled water (pH 6.5) was used as the subphase.
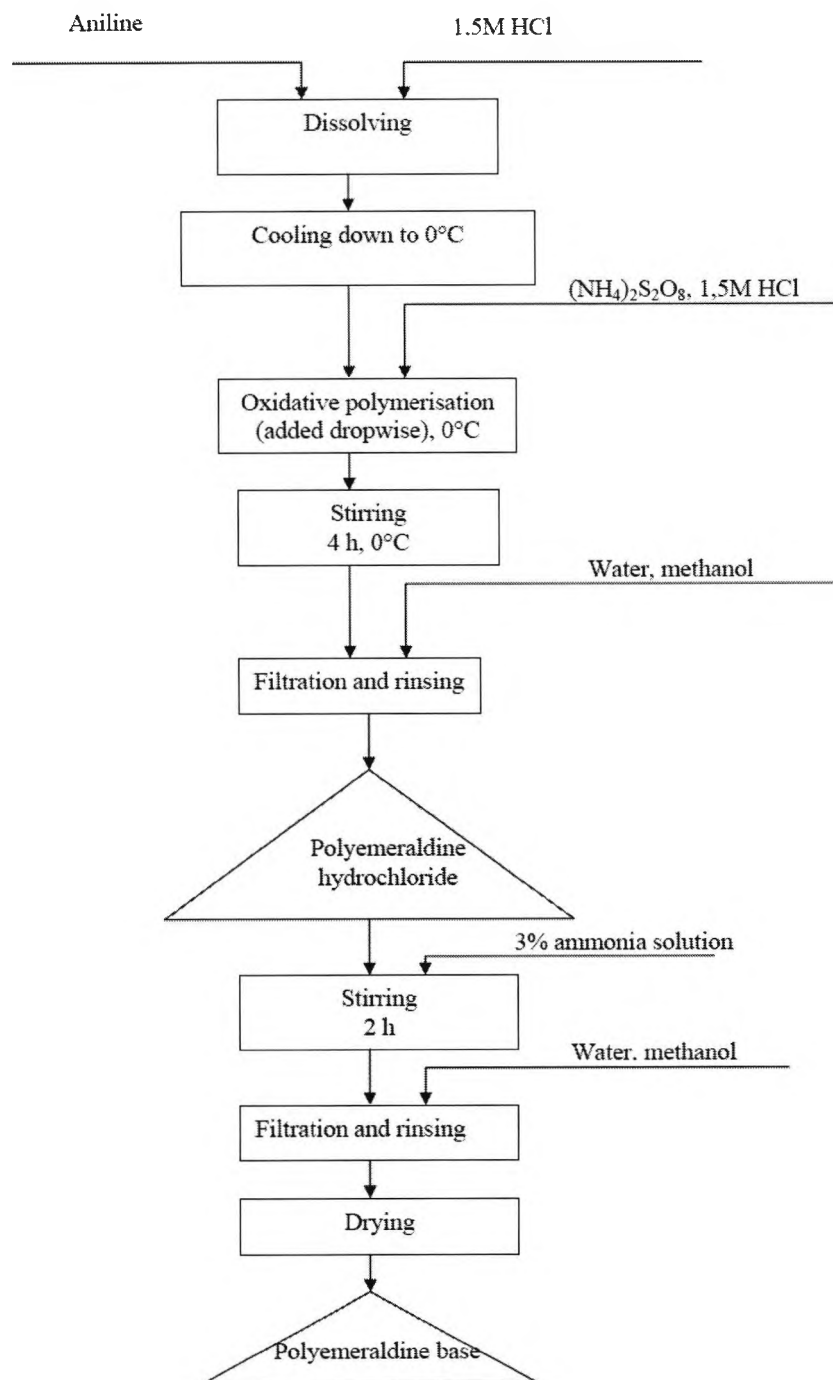
Figure 3.6   Schematic diagram showing the route for the synthesis of PANI films

3.3 Characterisation techniques

3.3.1 Thermogravimetry (TG)

Thermogravimetric analysis (TGA) for PU was performed on a Netzsch TG 209 thermal analyser, operating in a dynamic mode at a heating rate of 10 $Kmin^{-1}$ or in an isothermal mode for 150 min. The conditions were: sample weight - ~ 5 mg, atmosphere - argon, open α-Al_2O_3 pan. Thermogravimetric analysis of PANI was performed on a Derivatograph-C thermal analyser, operating in a dynamic mode at a heating rate of 1, 2.5, 5 and 10 K/min. The conditions were: sample weight - ~ 10 mg, atmosphere - argon or air, reference material - Al_2O_3. The raw data were converted to ASCII files and kinetic analysis was carried out using an in-house program and a Netzsch Thermokinetic Program (v. 6.65) on a Hewlett-Packard HP 486 Vectra computer.

Thermogravimetric analysis coupled with Fourier transform infrared spectroscopy (TG-FTIR) was carried out using a Mettler-Toledo TGA/SDTA 851 thermal analyser (heating rate=20 K min^{-1}, sample weight ca. 2 mg, nitrogen flow=50 cm^3 min^{-1}) and a JASCO 610 FTIR spectrometer. Thermogravimetric analysis coupled with mass spectroscopy (TG-MS) was performed with a TA Instruments DTA-TGA 2960 SDT and a Balzers ThermoStar quadrupole mass spectrometer at a heating rate of 20 K min^{-1} under helium atmosphere (flow rate=100 cm^3 min^{-1}). Sample mass was ca. 3 mg. The mass spectrometer was connected to the thermobalance via a capillary coupling. The ionising voltage of the crossbeam electron impact ionisation source was 70 eV.

3.3.2 Gel Permeation Chromatography (GPC)

Molecular weight was determined by GPC performed at 25 °C using a Knauer 64 GPC system with a refractometric detector and two PL-Gel Mixed-E columns. Tetrahydrofuran (THF) was used as the eluent at a flow rate of 0.8 cm^3 min^{-1}, and sample concentration was 5 mg cm^{-3}. Polystyrene standards (Waters) were used to construct a calibration curve. GPC data were processed using the CHROMA program to calculate average molecular weights, M_n and M_w, as well as polydispersity coefficient, f.

3.3.3 Fourier Transform infrared spectroscopy (FTIR)

FT-IR spectra were recorded on finely ground dispersions of PU samples in spectroscopic grade KBr by using a BIORAD FTS 165 spectrometer, operating in the spectral range of 4000-400 cm^{-1}.

3.4   Results and discussion

Conductive polymers have been the subjects of study for many decades as possible substitute for synthetic metals. Many of these polymers, especially those with a conjugated π-bond system, often yield higher conductivity once having undergone the doping process. However, practical uses of conducting polymers suffer because of their poor mechanical properties (such as strength and processibility) that rarely meet industrial requirements.

By definition, PU elastomers, are polymers containing urethane groups (-NH-CO-O-), created by reacting isocyanates with polyols and chain extenders. By varying the nature of these three components, literally, thousands of different combinations of properties may be created. By increasing the chain extender content (and therefore, the hard segments), the hardness, tensile strength, and tear strength of PU consistently increased. Elongations at break generally decrease with an increase in hard segments. Interestingly, resilience and compression set properties at ambient and elevated temperatures appear largely unaffected by changes in hard segment content. Polyurethane is a unique material with properties not found in other materials. Because of this, it lends itself to designs in which other materials are unsuitable. It also can replace other materials in existing applications at considerable savings because of its longevity.

3.4.1   Thermal study

3.4.1.1   Kinetic equations and models

In general, the thermal decomposition of solids (see models in Table 3.2) is a very complex process even in the simple case of the reaction expressed by the stoichiometric equation

$$A_{solid} \dashrightarrow B_{solid} + C_{gas} \tag{3.1a}$$

The rate of reaction can be described in terms of two functions: the rate constant $k(T)$ and the type of reaction $f(\alpha)$, thus:

$$d\alpha/dt = k(T)f(\alpha) \qquad (3.1b)$$

where α is the degree of conversion, T the temperature in Kelvins.

By substitution of the Arrhenius equation, and rearrangement, the following equation results:

$$d(\alpha)/f(\alpha) = (A/\beta)\exp(-E/RT)dT \qquad (3.2)$$

where E the activation energy, A the pre-exponential factor, and R the gas constant. This equation is given for measurements with a constant heating rate ($T = T_0 + \beta t$).

Table 3.2   The basic kinetic models

Model	Symbol	$f(\alpha)$
Phase boundary-controlled reaction (contracting area)	R2	$(1-\alpha)^{1/2}$
Phase boundary-controlled reaction (contracting volume)	R3	$(1-\alpha)^{2/3}$
Random nucleation. Uni- molecular decay law	F1	$(1-\alpha)$
Reaction n-th order	Fn	$(1-\alpha)^n$
Johnson-Mehl-Avrami	JMA	$n(1-\alpha)[-\ln(1-\alpha)]^{1-1/n}$
Two-dimensional growth of nuclei (Avrami equation)	A2	$2(-\ln(1-\alpha)^{1/2})(1-\alpha)$
Three-dimensional growth of nuclei (Avrami equation)	A3	$3(-\ln(1-\alpha)^{2/3})(1-\alpha)$
One-dimensional diffusion	D1	$1/2\alpha$
Two-dimensional diffusion	D2	$1/(-\ln(1-\alpha))$
Three-dimensional diffusion (Jander equation)	D3	$(3(1-\alpha)^{2/3})/(2(1-(1-\alpha)^{1/3}))$
Three-dimensional diffusion (Ginstling-Brounshtein)	D4	$3/2((1-\alpha)^{-1/3}-1)$

Using an approximation of the exponential integral in a form proposed by Doyle [3.10]

$$\ln p(x) = -5.3305 + 1.052x \tag{3.3}$$

where $x = E/RT$.

It is possible to determine the activation energy of the thermal process by following gravimetrically the decomposition of reactant at several different heating rates [3.11, 3.12] as follows

$$\ln\beta = \ln(AE/R) - \ln G(\alpha) - 5.3305 + 1.052x \tag{3.4}$$

where

$$G(\alpha) = \ln(AE/R) - \ln\beta + \ln p(x).$$

Eq. (3.4) generates a straight line when $\ln(\beta)$ is plotted against $1/T$ for isoconversional fractions, the slope of the line being equal to $-1.052/R$ during a series of measurements with a heating rate of $\beta_1...\beta_j$ at a fixed degree of conversion of $\alpha = \alpha_k$. The temperatures T_{jk} are those at which the conversion α_k is reached at a heating rate of β_j.

Another isoconversional procedure, introduced by Friedman [3.12], uses its basis as the following relationship

$$\ln(d\alpha/dt) = \ln f(\alpha) + \ln A - E/RT \tag{3.5}$$

which makes it possible to find the activation energy value from the slope of the line ($m = -E/R$) when $\ln(d\alpha/dt)$ is plotted against $1/T$ for isoconversional fractions.

In Eqns (3.1b) the term $f(\alpha)$ represents the mathematical expression of the kinetic model. The most frequently cited basic kinetic models are summarized in Table 3.2. Non-isothermal curves of a decomposition reaction must satisfy the kinetic equations developed for the kinetic analysis of "n-th order reactions", even if they follow a quite different mechanism. Results of comparative studies lead to the conclusion that the actual mechanism of a thermal process cannot be discriminated from the kinetic analysis of a single TG or DTG trace [3.13, 3.14]. Besides, both activation energy and pre-exponential factor, given in Eqns (3.2) are mutually corelated. As a consequence of this correlation an apparent kinetic model instead of the appropriate one for a certain value of apparent activation energy can describe any TG curve. Therefore, the kinetic

analysis of TG data cannot be successful unless the true value of the activation energy is known [3.15].

3.4.1.2 Thermal properties of polyurethanes

One of the few drawbacks of polymers with such complex morphology is their low thermal stability and flammability governed primarily by the heat liability of the urethane groups is dependent upon the substituents on these groups [3.16]. The highest degradation temperature (ca. 250 °C) is observed for urethane formed from alkyl isocyanate and alkyl alcohol, followed by an aryl isocyanate–alkyl alcohol combination (degrading at about 200 °C), an alkyl isocyanate and aryl alcohol (stable up to 180 °C), and an aryl–aryl combination whose temperature limit is in the 120 °C range. Low thermal stability and flammability seriously limit the number of new applications, hence, an extensive research has been performed to flame retard these polymers [3.5, 3.17]. One of the approaches is to incorporate an 'additive' or 'reactive' flame retardant into polymer. The 'additive' flame retardant is physically mixed with the parent polymer either prior to, during or right after polymerisation—there is no chemical bonding between the flame retardant and parent polymer. The second group of flame-retardants, the 'reactive' ones, will react with other monomer units by polymerisation, polycondensation or polyaddition reaction. Since they are chemically bonded to the polymer backbone, bleeding and volatilising out of the polymer are prevented, enhancing thus their action in comparison to the 'additive' ones [3.18].

Thermogravimetry (TG) results in dynamic mode showed that PU prepared in one-step procedure described above is thermally stable up to 225 °C ($T_{10\%}$) and the decomposition proceeds in one step. It is noteworthy that the char residue for the samples is low which means that vapour-phase process prevails over condensed-phase reactions. As it will be seen later, vapour-phase reactions are investigated in detail by hyphenated thermal analysis–spectroscopic methods. Results of TG analysis under isothermal conditions, displayed in Figure 3.7, show that there are no unexpected thermal effects that occur when a sample is subjected to elevated temperature for a given time. As such, investigations led to the thermal processes by dynamic methods which evidently showed that introduction of CPD into the polyurethane structure results generally in an increase of the DTG_{max} temperature; based on the PU decomposition process, one can assume that CPD is preferentially located in hard segments— the thermal decomposition

64

starts at hard phase where urethane groups (which are the less stable linkages in polyurethane backbone) are mainly placed [3.19]. Analysis of the data collected indicates that addition of more than 20% of CPD does not increase the DTG_{max} temperature; it is probably connected with the structural features of the multiphase PU morphology. Soft segments form a flexible matrix between the hard domains that in turn provide physical cross-linking, a complex, phase-segregated morphology can be observed that varies with the temperature [3.20].
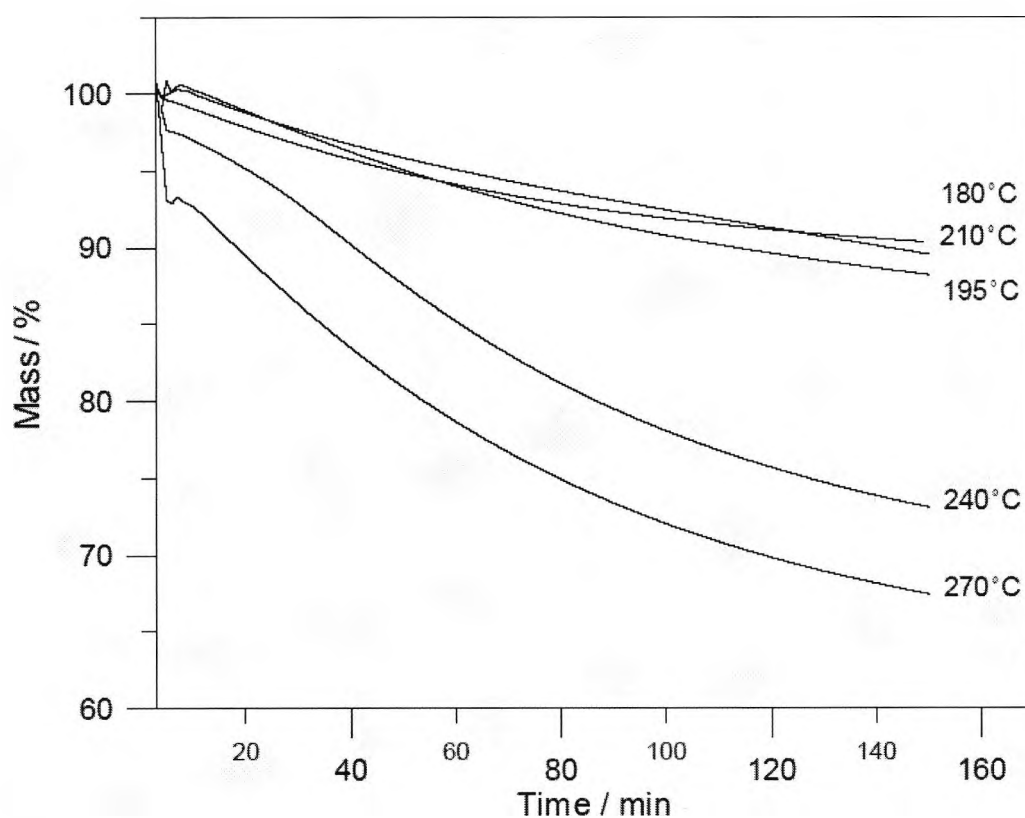
Figure 3.7   Thermogravimetric profiles under isothermal conditions.

Next, in order to gain a deeper look into the mechanism of decomposition, TG analysis coupled with FTIR was used. This technique allows the on-line identification of the volatile products by providing continuous monitoring of the FTIR spectra. Stacked plot of the FTIR spectra of the decomposition products is presented in Figure 3.8. CO_2 evolution that can be regarded as a

measure of the rate of decomposition displays maximal intensity at 237 °C [3.21]. Again, above 300 °C characteristic absorption bands of amines are present, but their intensity was found lower for other samples of modified segmented PU. The obtained results have been confirmed by TG analysis coupled with mass spectroscopy. The main decomposition fragments detected were: CH_2 (m/z=14), CH_3 (m/z=15), O (m/z=16), OH (m/z=17), H_2O (m/z=18), H_3O (m/z=19), C_2H_2 (m/z=26), HCN (m/z=27), C_2H_4 (or CH=NH) (m/z=28), aldehydes (m/z=29, 43, 57), amines (m/z=30, 44, 58), ethers (m/z=31, 45), Cl (m/z=35, 37) and CO_2 (m/z=44), as observed in mass spectrum of selected volatile products at 310 °C.

Evidence for diffusion control was observed and related to the appearance of certain products above 250 °C which are not formed at lower temperatures. This was confirmed by observing the effect of the thickness of the degrading polymer film on the characteristics of the reaction of carbon dioxide formation under identical temperature conditions. The observations are in agreement to Chambers *et al.* [3.22] and Grassie and Zulfigar [3.19]. Chambers *et al.* [3.22] performed investigations of the thermal properties of ^{13}C labelled MDI-based polyurethane and found that HCN and all the other nitriles, generated during high temperature decomposition, originate in the thermal fission of the aromatic ring, the nitrile-carbon being the 2-, 4-, or 6-carbon of MDI. Grassie and Zulfigar [3.19] have suggested that based on the fact that weight loss under nitrogen never catches up with that under vacuum it may be assumed that not only are certain degradation products, which are volatile at degradation temperatures, inhibited by the nitrogen from diffusing out of the polymer but that during their retention in the degrading polymer they may undergo secondary reactions which generate non-volatile products.

3.4.1.3   Thermal properties of polyaniline

Thermal properties of polyaniline have been the subject of some recent studies [3.23, 3.24]. From the TG results it can be found that the degradation process of PANI proceeds in two or three steps being attributed to the evolution of water, loss of dopants and eventually breakdown of the polymer backbone. Some kinetic studies performed so far were, according to the author's knowledge, limited only to methods assuming a given order of reaction (n). This rather simple approach does not allow drawing any conclusions whether the condensed phase decomposition exhibits fractional reaction order or if the (apparent) activation energy (E_{app}) is changing with the

degree of conversion. Such an effect is often observed in reaction systems where factors limiting the global reaction rate are either mixed together (diffusion - reaction) or of different internal nature (e.g. 2D or 3D-diffusion) [3.25]. In this case each reaction pathway is described by another activation threshold leading to changes in the global E value.
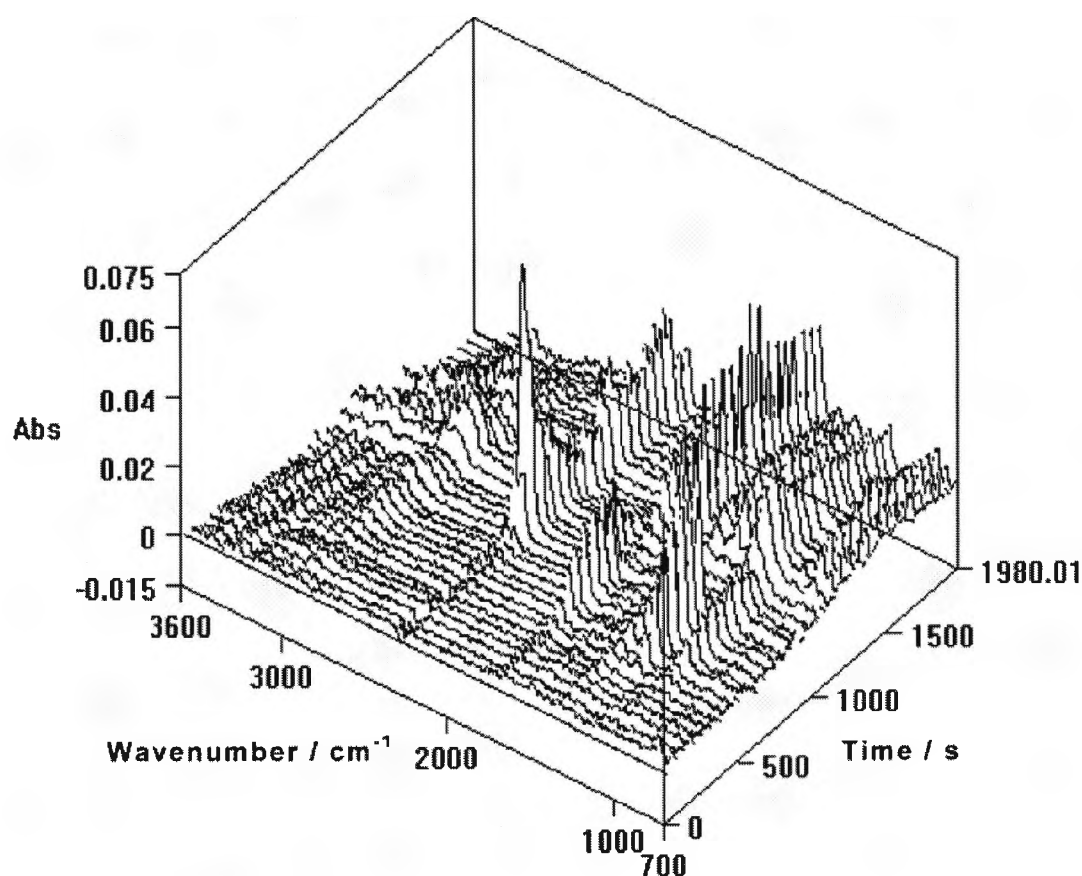
Figure 3.8   Stacked plot of FTIR spectra taken during the decomposition.

Another interesting question concerns applicability of TG studies for providing some information about the structure of PANI subjected to a controlled heating program. Up to now the knowledge about the structure of PANI is rather little. There were some studies on the

crystals of ClO^{4-} and BF^{4-} salts of "tetramers" and "dimers" of PANI [3.26] and on other PANI forms but without a profound explanation [3.27, 3.28]. More detailed investigations by X-ray technique have revealed that two different crystalline forms of the emeraldine base and its hydrogen chloride (HCl) salt occur [3.29]. The latter contains more crystalline phase ($X_c =$ ~50%) with the crystalline domain length, L, equal to 30-70 A and the d spacings in the 2-10 A range. Such dimensions of the crystalline domains exclude some methods whose resolution is not high enough. For example, the measurement by differential scanning calorimetry (DSC) is known to be sensitive to domain structures of the size range between ca. 25-30 nm [3.30, 3.31]. A more sensitive dynamic mechanical measurement allows a characterization of domains down to ca. 15 nm. The CP/MAS ^{13}C NMR measurement of spin-lattice relaxation times permits an analysis of domains with the sizes from a few angstrom to a few tens of nanometers, depending on the use of the relaxation times of either in the rotating frame (i.e., $T_{1\rho}$) or in the laboratory frame (i.e., T_1) [3.32]. In this sense, TG cannot supply direct crystallographic data, but is able, through kinetic parameters, to provide valuable information about processes connected with crystal's decomposition.

For kinetic analysis, an advanced approach containing model-free evaluation of the activation energy and nonlinear regression-based determination of the reaction function has been used. Polyaniline, in form of emeraldine salt (conducting) and emeraldine base (nonconducting) are of general formula - Scheme 3.2. Two forms of thermal behaviour of polyaniline salts are reported in the literature [3.1-3.3]. A two-step weight loss process is one type, in which, initially, water escapes from the polymer chain (although the coevolution of other species such as free acids and oxidant cannot be ruled out), followed by thermal degradation of the polymer salt. In a three-step weight loss process the thermal degradation of PANI commences with an evolution of water, followed by the loss of acid dopant, and finally complete degradation of the skeletal polyaniline chain structure results. A similar type of thermal behaviour was also observed for other polyaniline-based systems, such as poly(aniline-co-o-ethylaniline) [3.33], poly(o-chloroaniline) [3.34], and poly(N-ethylaniline) [3.35]. Since the atmospheric reaction may remarkably influence the degradation course it is logical to divide the discussion according to this parameter.
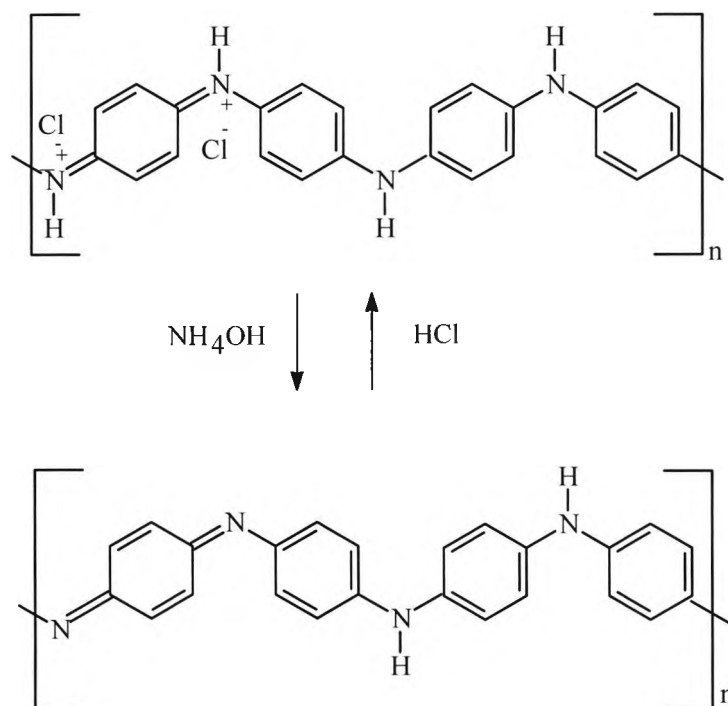
Scheme 3.2 Repeat unit of PANI in the undoped, emeraldine base form (bottom) and the fully acid doped, emeraldine salt form (top).

3.4.1.4 Thermal analysis in argon conditions

Thermogravimetric studies of PANI in its protonated form are carried out. A three-step weight loss process can be observed, with the first step indicating a 3-5% weight loss at temperatures up to 120°C. This step can be attributed to the loss of water molecules. The water evolution was also observed in a different study using TG analysis coupled with FTIR [3.36]. The course of the changes of the calculated value of activation energy by method of Ozawa-Flynn-Wall, plotted as function of degree of conversion (α), was further investigated. Changes of E indicate that the probability of the overall degradation reaction proceeding according to the first order kinetic scheme is rather low and non linear regression for finding the best model fit should be applied.

Test of the distinctiveness between the models (Table 3.2) yields data of several approximations, with the best fit for an nth order kinetic scheme. F_{exp} describes the fit statistically on the basis of F-test procedure. For the second step of acid dopant loss, it should be pointed out

that the shape of the fit curve is strongly influenced by the A parameter in the Arrhenius equation. The physical meaning of pre-exponential factor for the description of the kinetics of thermal decomposition of solids is still a subject of debate [3.25, 3.37]. There is a tendency observed which pays more attention towards E, but this is only justifiable for the preliminary kinetic analysis. The relationship between E and $\ln A$, known as "kinetic compensation effect", add to the confusion if there is no proper choice of the model function describing the reaction mechanism.

Polyaniline in its non-conducting, deprotonated form exhibits different thermal behaviour than the conducting one. There are two distinct degradation steps; the second starts at app. 130 $^\circ$C onward and reaches its maximal rate at 210 $^\circ$C. Friedman analysis yields E data in function of α; two distinct regions (plateau) are observed for $0<\alpha<0.3$ and $0.65<\alpha<0.95$. The area in between is characterized through almost linear increase of E from several to ~70 kJ/mol. Very low values of E for the first degradation step indicate that there are only weak intermolecular forces, such as Van der Waals, between the water molecules and polymer. For this degradation step, the D3 (Jander diffusion) model has been found to be the best theoretical approximation, whereby the second step decomposition kinetics is governed by n-th order reaction model. On the basis of these theoretical models it was possible to predict the thermal behaviour of the polymer for extrapolated time of degradation both with respect to α and to the temperature. One should however note that if a "short time" experiment is used for a "long time" extrapolation a certain approximation in the model parameters might occur, particularly in the "far" temperature regions.

The Jander's model belongs to the general class of shrinking interface models in which the slower of the two principal processes (diffusion or chemical reaction) becomes the rate-controlling process. In case of Jander's model the diffusion process in form of gradual growth of the product layer with instantaneous surface nucleation is rate controlling. The exponent n can be used to predict the type of growth that the nuclei may follow. The term n is equal to the sum of two variables such that $n = b + y$, where b relates to whether initiation occurs homogeneously or heterogeneously, one or zero, respectively, while y relates to the dimensionality of nuclei growth, and is equal to one (one-dimensional or rod-like), two (two-dimensional or disc-like) or three (three-dimensional or spherical). In the physical terms defined by the Jander's equation, n may

be raised due to either a change in initiation due to back reaction (i.e. change in *b*) or due to a change in the dimensionality of nuclei growth because of the possibility of products diffusing away from the region of polymer they were formed, and then re-reacting (change in *y*). It should be pointed out that predictions concerning the physicochemical nature of a degradation process are completely not possible when the simple first order kinetics is applied - there is no knowledge of the model function.

3.4.1.5   Thermal analysis in air conditions

The reaction atmosphere is an important factor considerably affecting the degradation route of a polymer, especially with respect to the practical out-doors applications. For protonated polyaniline, the degradation course followed by TG analysis is characterized by a three step mass loss. Up to temperature of $300^{\circ}C$ there is a relatively small weght loss of app. 13-20%; above this temperature one can observe a rapid degradation, which take place continuously to $500^{\circ}C$. From the Ozawa-Flynn-Wall plot one can see a distinct plateau in the α range of 0.4-0.75, corresponding to the second degradation step as shown on Figure 3.9.
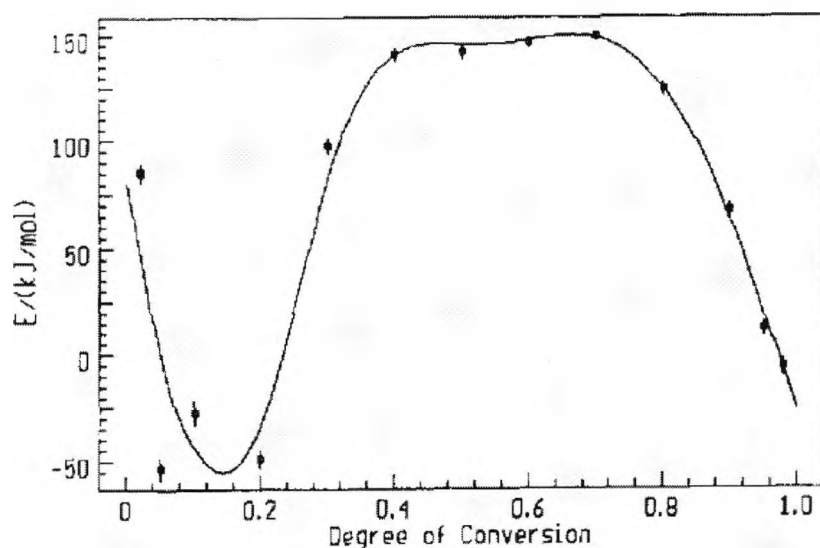
Figure 3.9   Energy of activation (E) as a function of the degree of conversion of degradation process of PANI in its emeraldine salt from under air calculated by Ozawa-Flynn-Wall method.

71

The initial (negative) values of E do not have any physical meaning and they were generated because of the complex reaction mechanism consisting of competitive individual reactions in the presence of oxygen. This can be attributed to the reaction of macroradicals with oxygen to form hydroperoxides which themselves are unstable and will break down rapidly forming more free radicals. According to the general Bolland-Gee mechanism, a macroradical is initially formed which will then react with oxygen to form a peroxy radical [3.37]. The peroxy radicals are reactive and will extract a hydrogen atom either by an intra- or intermolecular process to generate a hydroperoxide group and another macroradical site. The hydroperoxides will then decompose resulting in the formation of alkoxy and hydroxy radicals, which in turn can react with polymer backbone giving water molecules - Scheme 3.3 [3.37]. If the two processes of water evolution, namely water expulsion from the polymer matrix and chemical reaction according to polymer oxidation scheme, would run parallel, it would be extremely complicated to choose between them. This is generally a serious problem of the kinetics of parallel-running reactions.

POLYMER ----------------> P·   (Initiation)

P· + O_2 ----------------> PO_2·

PO_2 + PH ----------------> PO_2H + P·

2 PO_2H ----------------> PO + PO_2 + H_2O (Chain Branching)

PO_2H ----------------> PO + OH·

PH + OH ----------------> P + H_2O

$2PO_2$· ----------------> Inert Products (Termination)

PO_2 + P· ----------------> PO_2P

2P· ----------------> P-P
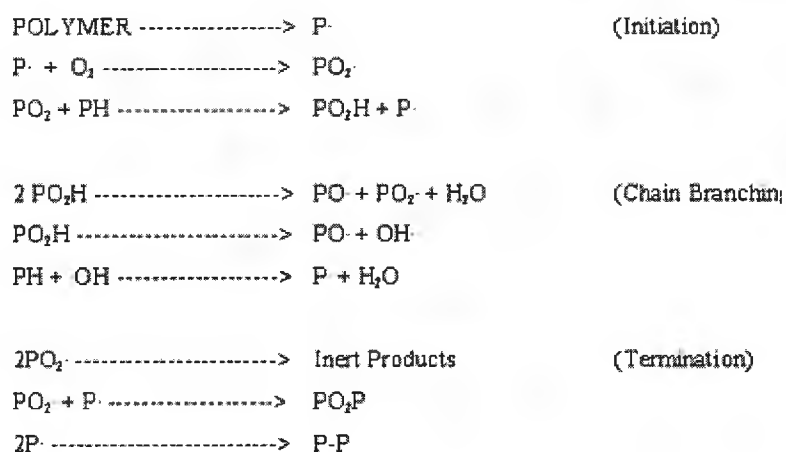
Scheme 3.3 General polymer oxidation scheme [3.37].

For $0.4<\alpha<0.75$ the best fit was found for D3 model (3-Dimensional diffusion of Jander type); extrapolated thermal behaviour in form of α-t and t-T graphs (not shown) was investigated. Comparing to the TG results of deprotonated vs protonated PANI, some differences can be

outlined, especially by the first degradation step up to 130 $^{\circ}$C. For protonated PANI, a confirmation of a single-step reaction can be found on E-α diagram. In the α region of 0.2-0.9 E value is practically the same, app. 116-125 kJ/mol. The best model function was the D3 model, followed closely by other diffusion-controlled processes - Table 3.3. The Jander equation has in the past been applied to the reactions between solids, assuming a spherical shape of reacting/diffusing bodies. Since the polymer examined in this study is a semi-crystalline one, it can be assumed that the physical rather than a chemical process in the crystalline phase is the driving force of the decomposition reaction. After evolution of water, a crystal strain occurs which probably arises from the lattice defect sites, developed during polymerization. As the crystals are heated, domains in pseudoorthorhombic order [3.38] begin moving relative to one another. Further heating causes rapid readjustment, resulting in concurrent decomposition due to dopant loss and shearing of aromatic groups past another. Then, once such strain is relieved, the rates of decomposition begin to slow down. The lower the heating rates are, the longer times have the crystals to anneal. The newly decomposed material, generated from strain induced during the early decomposition stage now suffers from further strain occurring within the already partially decomposed crystal. Therefore the rate of reaction again begins to increase until destruction of the crystalline structure of the polymer accompanied by diffusion of gaseous degradation products completes. Analysing the E value one can observe that E is remarkably higher in an inert atmosphere than in an oxidative one. This is surprising if one would assume degradation processes running only via a radical mechanism. But if there are other mechanisms available, such as molecular or ionic ones, this would support the observation.

Table 3.3   **Results of F-test of the distinctiveness between the models for deprotonated PANI under air**

Model	F_{exp}
D3	1.00
D4	1.39
D2	1,84
F2	2.29
Fn	2.49
F1	2.79

Kinetic equations describing the behaviour of solid-state reactions incorporate variables that provide some information concerning the mechanism of decomposition. From the results presented one can see that the degradation process of PANI is a complicated phenomenon in which chemical reactions or mass transport become rate controlling. In gas phase and in solution kinetic studies where concentrations are physically definable, the experimentally determined parameters such as the pre-exponential factor and the recation order may contribute information regarding the reaction mechanism. In contrast, the term concentration in solid-state decompositions cannot apply (with respect to reactant), hence interpretation of A and n loses its traditional meaning.

3.4.2 Morphology and structural properties

Scanning electron microscopy (SEM) studies revealed a bead-string morphology, formation of which for solution-polymerised systems involve three stages: (1) solvent disorientation, (2) slow stress relaxation, and finally, (3) very slow transition from banding to a polydomain structure—Figure 3.10 and Figure 3.11. Typical dimensions of hard segments are in the range of 2.5 to 15 nm [3.39]. The presence of chemical linkage between the hard and soft segments restricts the phase structure to the microscale. Besides the thermodynamic factor, hard segment mobility, system viscosity and hard segment interactions are the three controlling factors for the phase structure formation [3.5, 3.40].

The domain morphology of the microphase-separated material has been studied with a number of 'model' compounds such as diblock or triblock copolymers. In the case of ABA-type triblock copolymers, both ends of each B block are chemically connected to other A blocks. Its mobility is lower compared with the mobility of corresponding blocks in the AB diblock copolymers. Such comparison helps in better understanding of the complex polyurethane heterogeneous structure of hard and soft domains [3.41]. The hard segments are preferentially oriented in a radial, rather than in a tangential arrangement. The decomposition route is strongly affected by a pseudo-crosslinking effect resulting from the hard-segment aggregation. The hard-segment domain generally exhibits a different degree of order or semicrystalline structure, which was considered to be able to reinforce the hard-segment domain. Hence, the presence of an amorphous region may constitute the weakest part inside the hard-segment domain.
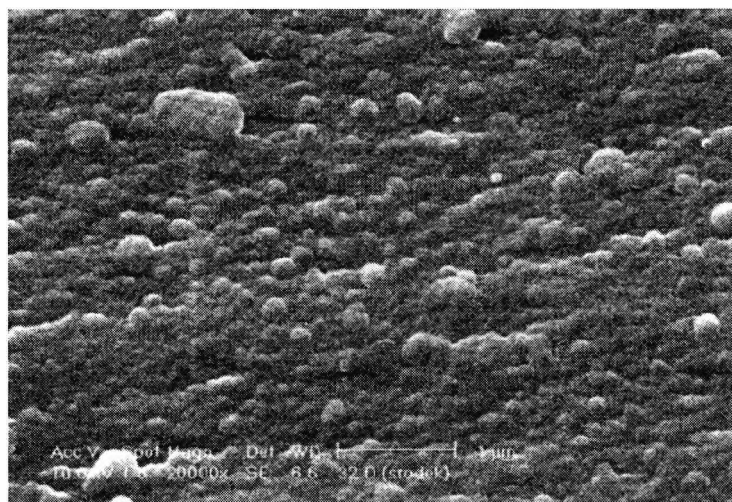
Figure 3.10   Micrograph (SEM) (x20000).
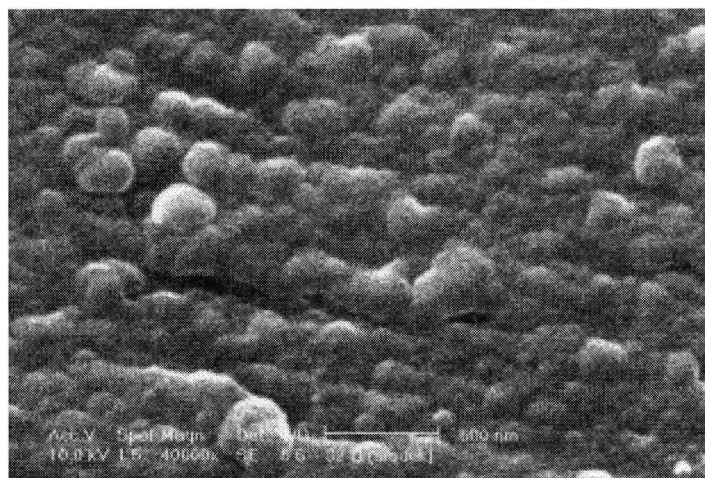
Figure 3.11   Micrograph (SEM) of (x40000)

Evidently, a relatively rough structure of polyurethanes containing CPD plays an important role by inhibiting polymer-specific condensed phase-reactions. Some cooling and fuel-diluting effects of the evaporated CO_2 or crystallized water push the heat- and light-emitting zone of the flame further away from the pyrolysing polymer surface. This increased distance cut down heat transfer. On the other hand, diffusion and that probably control the rate of evolution of volatile products from the degrading polymer while they are retained in the hot zone, the primary

products of degradation may undergo secondary reactions. It can be seen that the increase of CPD in the polymer's structure causes an increase in the Limited Oxygen Index (LOI) value. However, no information on the burning process can be obtained from LOI data only, so the thermovision camera was used. It makes it possible to obtain temperature distribution during the burning of a sample, which has the same dimensions as for the LOI test, thus making it possible to compare data from both measurements. Representative results under (1) LOI conditions, or (2) ambient conditions, are shown in Figure 3.12 and 3.13.
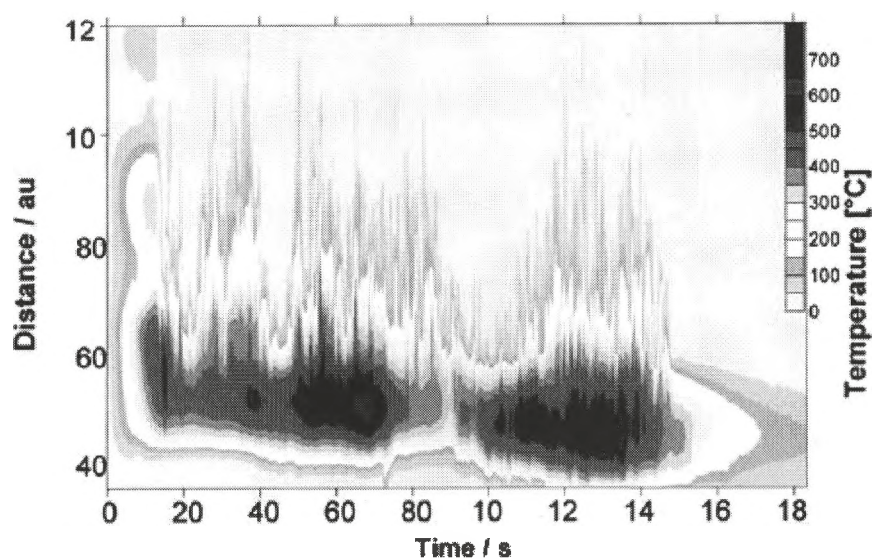
Figure 3.12   Temperature distribution during the burning under LOI conditions.
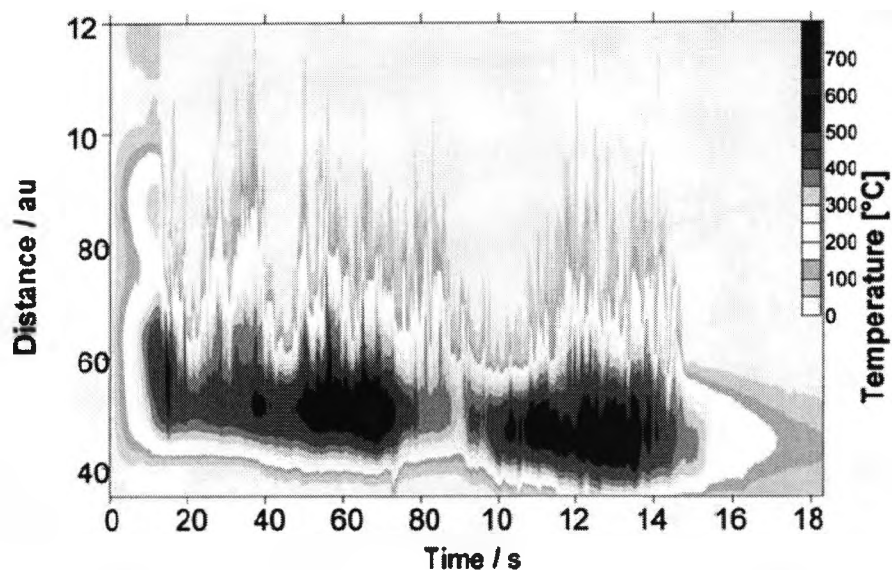
Figure 3.13   Temperature distribution during the burning under ambient conditions.

The values of E, determined by isoconversional methods, were dependent on α. This indicates a complex kinetic scheme that need to be described by all three kinetic parameters (the Avrami exponent, n, activation energy, E, and frequency factor, K). Such studies were performed and it was found that the reaction atmosphere has a deciding effect on the mechanism of decomposition. The 3-dimensional diffusion was found to be the rate-controlling process for all the degradation routes except of protonated PANI under argon, which was governed by the n-th order reaction model. On the basis of obtained information one can confirm the applicability of kinetic analysis (using thermogravimetric data) for studying fundamentals of degradation reactions. Main features of the thermal decomposition of a series of novel polyurethanes containing 3-chloro-1,2-propanediol as a constitutional repeating unit in the main chain which are inherently flame-retarded polymers have been investigated by means of hyphenated methods (TG-FTIR, TG-MS)—it was found out that the main decomposition products are CO_2, amines and HCN.

77

3.5   Conclusions

The recent technological interest concerns the studies on composites containing conductive polymers and an inert polymer matrix. The potential usage of conducting polymer blends includes electro-chromic and electro-optical devices, packaging materials, actuators, batteries, and catalysis. Such elastomers may also have applications as rollers used in electrostatic imaging, cables, EMI-shielding gasket materials, and, potentially, chemical and/or biological sensors. A kinetic study on the thermal degradation of polyaniline in its base and salt forms was carried out. The thermogravimetric profiles were of two or three step weight loss class, indicating a typical degradation scheme with water evolution, dopant loss (in case of protonated PANI) and polymer destruction. Correlation between the amount of chlorine in TPU and the intensity of amines' formation during the main decomposition step around 300 °C has been presented. Based on the results obtained thermal decomposition route was suggested.

A relatively rough structure of polyurethanes containing CPD plays an important role by inhibiting polymer-specific condensed phase-reactions. Some cooling and fuel-diluting effects of the evaporated CO_2 or crystallized water pushed the heat- and light-emitting zone of the flame further away from the pyrolyzing polymer surface. This increased distance assisted in cutting down heat transfer. On the other hand, the rate of evolution of volatile products from the degrading polymer is controlled by diffusion and the primary products of degradation undergo secondary reactions while they are retained in the hot zone.

4 Synthesis and structural properties of polyurethane based conducting thermoplastic elastomer

4.1 Introduction

Not too long ago, carbon based polymers were regarded as insulators and for this reason plastics have been extensively used by the electronics industry. With the advent of intrinsically conductive polymer or electroactive polymers, this perspective has changed in recent years resolving into diversified applications ranging from biomedical, households and semiconductors in electronics, to aerospace, either utilising conductive polymers conductivity or electroactivity. For instance, taking aerospace as a measure of applications standards, conducting polymers have found appliances in smart structures, electrostatic materials, antistatic clothing, conducting adhesives, sensors and actuators, piezo-magnetic constrained layer damping and surface damping layers in aircraft structures just to mention but a few.

Conducting polymers may store charge either via an oxidation process and it could either lose an electron from one of the bands or it could localize the charge over a small section of the chain. Localizing the charge causes a local distortion due a change in geometry, which costs the polymer some energy. However, the generation of this local geometry decreases the ionization energy of the polymer chain and increases its electron affinity making it more able to accommodate the newly formed charges. This method increases the energy of the polymer less than it would have if the charge was delocalized and, hence, it takes place in preference of charge delocalization. This is consistent with an increase in disorder detected after doping by Raman spectroscopy. A similar scenario occurs for a reductive process. As a matter of interest, the extended π-systems of conjugated polymer are highly susceptible to chemical or electrochemical oxidation or reduction. These alter the electrical and optical properties of the polymer, and by controlling this oxidation and reduction, it is possible to precisely control these properties. Since these reactions are often reversible, it is possible to systematically control the electrical and optical properties with a great deal of precision. It is even possible to switch from a conducting state to an insulating state. However, polyaniline (PANI) is the only conducting polymer whose electrical properties can be controlled suitably by charge-transfer doping and/or

protonation. Then again, two major limitations of conducting polyaniline are an inability to process it by conventional methods and its poor mechanical properties. These limitations can be overcome by preparing conducting PANI blends and composites, which possess the mechanical properties of the insulating host matrix and the electrical properties of the conducting PANI guest polymer [4.1, 4.2].

Polyurethane (PU) possess unique physical properties that are derived from their molecular structure as well as the supramolecular structure caused by specific interactions between the polymer chains. The two-phase morphology of PUs as a result of the incompatibility between the soft and hard segments primarily determines polyurethane properties. In addition, the segmental distribution, flexibility and composition ratios of monomers, the chain entanglement and length, the interchain forces and the crosslinking are all important parameters that influence the properties and determine the use of the end-products of PU [4.3]. Segmented PUs are a class of modern materials of commercial importance that are widely used, e.g. as automotive exterior body panels, medical implants or flexible tubing, due to their outstanding mechanical and thermal stability properties. They derive most of their useful properties from the incompatibility of the hard segments (e.g. 4,4'-diphenylmethane diisocyanate (MDI) extended with short-chain diols) and soft segments which are usually composed of long-chain diols. Scheme 4.1 shows the decomposition products (including radicals) of chlorinated PU and Scheme 4.2 shows the decoposition mechanisms of PU [4.4].
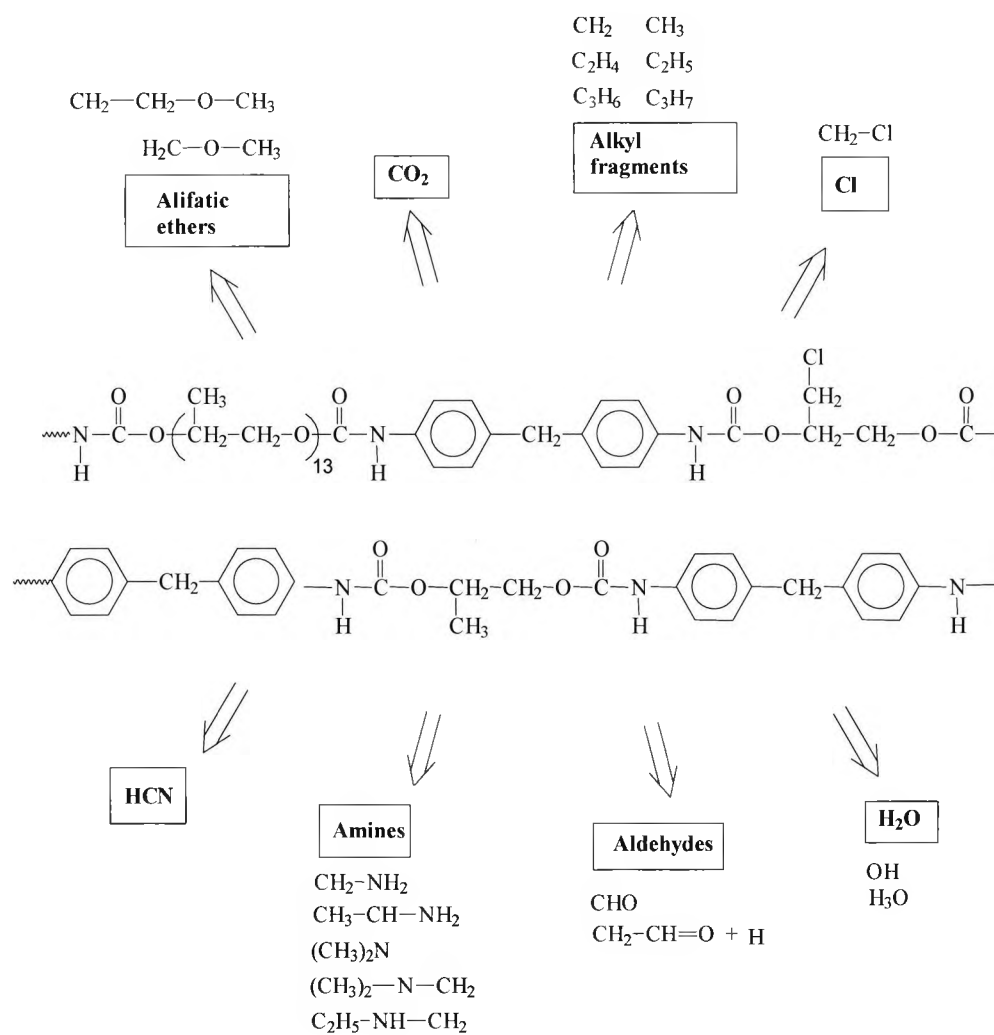
Scheme 4.1   Decomposition products (including radicals) of chlorinated PU

I. Dissociation to isocyanate and alcohol

$$R\,(NH) - \overset{\overset{\displaystyle O}{\|}}{C} - OR' \longrightarrow RNCO + R'OH$$

II. Formation of primary amine and olefin

$$R\,(NH) - \overset{\overset{\displaystyle O}{\|}}{C} - O - \underset{\underset{\displaystyle H}{|}}{CH} - CH_2R' \longrightarrow RNH_2 + CO_2 + R'CH = CH_2$$
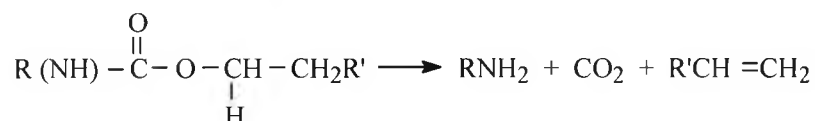
III. Formation of secondary amine

$$R\,(NH) - \overset{\overset{\displaystyle O}{\|}}{C} - O - R' \longrightarrow \underset{\underset{\displaystyle H}{|}}{RNR'} + CO_2$$
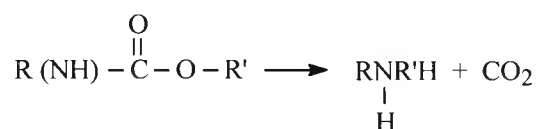
IV. Transesterification type bimolecular displacement

$$R\,(NH) - \overset{\overset{\displaystyle O}{\|}}{C} - OR' + HX \longrightarrow \left[RNH - \overset{\overset{\displaystyle XH}{|}}{\underset{\underset{\displaystyle O}{|}}{C}} - OR' \right]$$

HX=HOR. H₂NR'   RNHCOX + R'OH
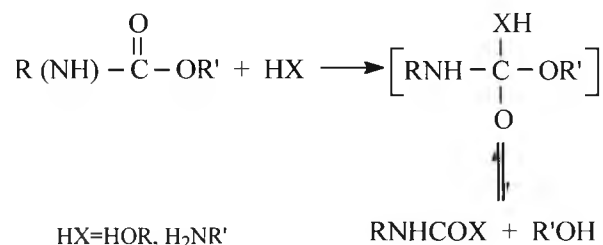
Scheme 4.2   Decomposition mechanisms of PU

Due to the unique achievable properties, PU and PANI have called for a great research interest in both academic and industrial fields [4.5]. In spite of this, basing on a quick literature review, only a handful of works dedicated to PU/PANI elastomers appear to have been reported which mainly deal with elastomeric films. One of the most important advantages offered by the thermoplastics over new toughened thermosets in composites' applications is the potential of

lower cost manufacturing since these polymers are often processed at much lower temperatures than their thermosets counterparts. Still relatively little efforts have been directed to PU/PANI thermoplastics. The poor immiscibility of the two polymers could be a contributing factor for this reason. To mention but a few on PU/PANI thermoplastic elastomers, Yang and Lee [4.6] reported on PANI polyacid complexes blended with water-based PU of different chemical structures and claimed a good compatibility of the resulting blend. A different work by Wang *et al.* [4.7] presented urethane–aniline block copolymers based on PU prepolymer and oligomers of amine-terminated PANI. The amine-terminated functional groups of amine-terminated PANI were introduced into the PU structure as a chain extender to form the hard segment of the copolymer with urea-linkage. The presented results demonstrated good mechanical properties that were attributed to induction of the long rigid rod structure of amine-terminated PANI into the blend.

Taking these facts into account, this work prepared PU/PANI conducting thermoplastic elastomers with good mechanical properties and processability associated with high conductivity or electrochromism. This work therefore aims, at combining the beneficial properties of the two polymers i.e. tensile strength, thermal properties and compatibility.

4.2 Synthesis methodology

One of the methods of preparation of conducting composites is the mechanical mixing where the controlling factors for a good conductive composite are the sizes and uniformity of particles as well as the efficiency of mixing [4.8, 4.9]. Another way to prepare composites is the chemical or electrochemical synthesis in organic solvents [4.10, 4.11]. Since the organic solvents may cause environmental pollution, a trend to replace the organic solvents by supercritical carbon dioxide or iodine is observed [4.12]. These methods are briefly discussed here while further insight can be sought elsewhere in the literature.

4.2.1 Chemical process

PU-based conducting polymers matrices blends and composites can be synthesized via a number of approaches. These synthetic methods for polymerisation can be mainly classified into

chemical and electrochemical synthesis, the chemical approach being the most preferred route mainly due to its simplicity and inexpensiveness in comparison to electrochemical synthesis. Yet, for in situ spectroscopic studies, the electrochemical method is better suited as it holds several advantages in that the synthesis is cleaner, conducting polymer blends and composites are supplied in the form of freestanding films, and also that the electrical properties of the composites can be modified by simply varying the conditions of electrolysis. However, it suffers from the disadvantage that the size of the composite film prepared depends on the size of the electrode. Further, an appropriate matrix polymer–electrolyte system should be available for the penetration of the ionic species (monomer and electrolyte) into the polymer matrix.

The chemical synthesis can be further classified into chemical in situ polymerisation, counterion-induced processibility, melt processing, dry- and solution-blending, and, emulsion– and dispersion polymerisation, while the electrochemical synthesis involves cyclic voltammetry, potentiostatic- and galvanostatic polymerisation [4.13]. The chemical in situ polymerisations involve an intimate mixing of two components and are one of the useful methods for the in situ polymerisation of new materials.

Likewise, counterion-induced approach produces attractive mechanical properties of the polyblend materials as presented by Li et al. [4.13]. The properties of these polymer blend materials may be contrasted with those obtainable using filled polymers, i.e. bulk polymers filled with conducting particles such as carbon black or intractable particles of conducting polymers. For polymer blends made by using the counterion-induced processibility of conducting polymer, the conductivity increases continuously, at remarkably low levels, as a function of the fraction of the conductive polymer complex. This may be compared with the known behaviour of filled polymers, which exhibit a percolation threshold at a volume fraction of about 16%. The smooth onset of conductivity in these polyblend materials indicates an unusual morphology with connected pathways even at remarkably low volume fractions of the conducting complex. Since the mechanical properties remain essentially equivalent to those of the host polymer, the morphology normally consists of an interpenetrating network e.g. a presentation by Banerjee [4.14] from studies on electrically conductive interpenetrating network composites of polyaniline and carboxymethylcellulose. Counterion-induced processibility of conducting polymer has created a class of stable and processible polymer blends in which the electrical conductivity can

routinely be controlled from 10^{-10} S/cm to 100 S/cm in materials, bestowing advantages in processing and with the mechanical properties of the bulk polymers.

Emulsion polymerisation of macromolecular conducting systems is a compartmental polymerisation reaction - taking place in a large number of reactions locally dispersed in a continuous external phase. The reaction is carried out in heterogeneous systems, usually with both aqueous and non-aqueous phases. The monomer as well as the polymer usually belongs to the non-aqueous phase. In inverse systems, water-soluble monomers are dispersed in a non-aqueous medium. A typical emulsion polymerisation consists of 30% monomer, 65% water, with the rest being emulsifier (surfactant), initiator and other additives. Emulsification initially results in micelles swollen with solubilized monomer and surfactant-stabilized monomer droplets. As the initiator decomposes, a new phase appears consisting of the latex particles, which contain macromolecules of a fairly high degree of polymerisation swollen with monomer and stabilized by the surfactant.

The advantage of compartmentalized polymerisation technique over other polymerisation processes is that the molecular weight of the polymer can easily be controlled by the addition of chain transfer agents; thus there can be control over the properties of the final product. Dispersion polymerisation may be defined as the polymerisation of a monomer dissolved in an organic liquid or water to produce an insoluble polymer in the form of a stable colloidal dispersion. The colloidal stability of the resulting particle is provided by the adsorption of an amphilic polymeric stabilizer or a dispersant, which is present in the organic medium on the surface of the polymeric particles. Hence, this process may also be viewed as a kind of precipitation polymerisation in which flocculation is prevented and the particle size is controlled.

Conducting and insulating polymers can also be dissolved in a common solvent and afterwards processed into thin films, a process known as solution blending. In contrast, blending the powders of polyaniline, polypyrrole, polythiophene etc. and the host polymer in a mixer may prepare dry blends. While in melting process, the conducting polymer is dispersed in a thermoplastic polymer matrix by mechanical mixing and then compression moulded in a hot press. A major requirement for this process is that the thermal stability of the conducting polymer should be sufficient to withstand compounding in the melt of the chosen polymer host. For this purpose, the host polymer should possess a low melting temperature.

4.2.2 Electrochemical process

Electrochemical synthesis is cleaner and the polymer composite film can easily be peeled off from the electrode and washed. Simply changing the electrolytic conditions can vary the electrical properties of conducting polymer - insulating polymer films. By electro-oxidative polymerising the conducting polymer on a non-conducting, mechanically superior polymer film-coated electrode, a composite film having a high conductivity and the good mechanical properties of the polymer substrate may be obtained. The advantage of the electrochemical route is that the conducting polymer composite is obtained in the form of a freestanding film, which is often needed for technological applications. In the electrochemical synthesis, the monomer, the solvent and the electrolyte anion diffuse into the insulating polymer coating. As a result, polymerisation starts in the interface between the electrode surface and the polymer film.

The electrochemical synthesis is generally accomplished by potentiostatic or galvanostatic polarization. Alternatively, the synthesis may also be carried out by cyclic voltammetry, driving the electrode potential between the limits of the monomer oxidation and reduction of the synthesized electroactive-conducting polymer. For instance, in Csahok *et al.* [4.15] investigations, PANI was deposited on two adjacent or on all bands by electropolymerisation from 0.2 mol/dm^3 aniline solution in 1 mol/dm^3 HClO$_4$ or H$_2$SO$_4$ solutions, respectively, under continuous potential cycling between -0.2 and +0.75 V (saturated calomel electrode) at a scan rate of 100 mV/s. Here a platinum wire was used as a counter electrode, while the reference electrode was a saturated calomel electrode (SCE). After polymerisation, the polymer-coated electrode was rinsed with the supporting electrolyte solution that was used for the further experiments. Before the in situ conductivity measurements, the films were oxidized and reduced 20–30 times by cycling in order to remove traces of aniline and oligomers. The total amount of the polymer on the surface was determined from the area under the cyclic voltammetric waves in a slow sweep rate experiment.

4.3   Experiment

4.3.1   Materials

For synthesis of segmented polyurethanes partially polymerised 4,4'-diphenylmethane diisocyanate (MDI, 31% of free isocyanate groups in relation to the pure diisocyanate) (Alfapur, Brzeg Dolny, Poland), polyoxypropylenediol (POPD, M=2000, Rokita S.A., Brzeg Dolny, Poland), 1,4-butanediol (1,4 – BD) (Aldrich), and 1-allyl-2-methylimidazole (catalyst) (Zachem) were used. Ethyl acetate (POCh) was used as a solvent during chain extend reaction. Polyaniline was prepared by standard oxidation polymerisation method.

4.3.2   Preparation

Segmented polyurethanes were prepared by a two-step (prepolymer) method, according to the general procedure: in three–necked flask, isocyanate and polyoxypropylene glycol were reacted at 65^0C for 2 hours – Figure 4.1. The obtained prepolymer was mixed with doped polyaniline and subjected to further chain-extend reaction with diol in the presence of catalyst (0.5 wt. %). The reaction time was 15 min.

Isocyanate

Polypropylene glycol

```
┌─────────────────────────┐
│   Prepolymerisation     │
│       65°C, 2h          │
└─────────────────────────┘
```

PANI

```
┌─────────────────────────┐
│     Homogenisation      │
└─────────────────────────┘
```

```
┌─────────────────────────┐
│        Drying           │
│    (under vacuum)       │
└─────────────────────────┘
```

Mixture of diols

Catalyst (0,5% wt.)

```
┌─────────────────────────┐
│      Polyaddition       │
│        30 min           │
└─────────────────────────┘
```
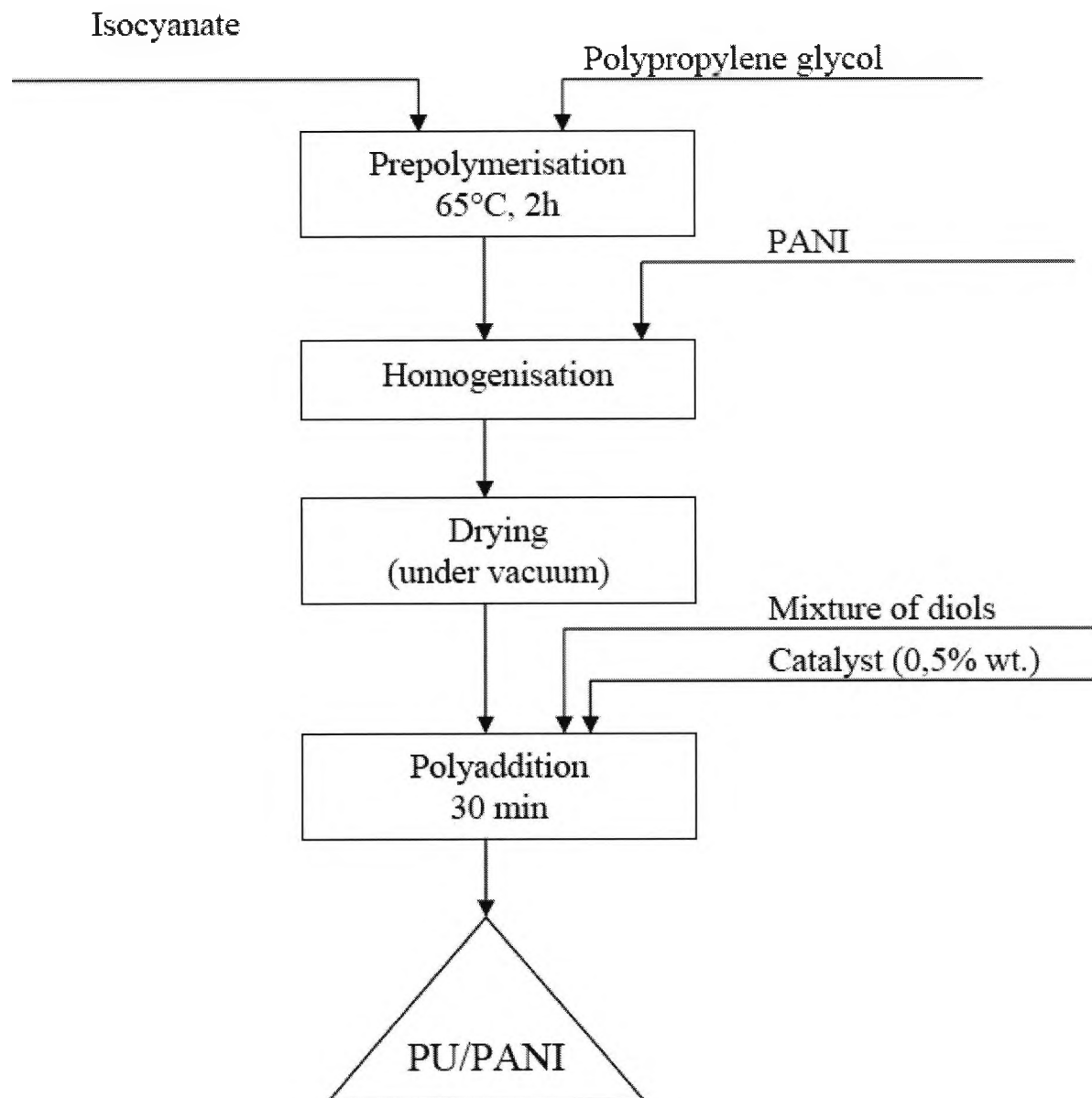
PU/PANI

Figure 4.1   Schematic diagram showing the route for the synthesis of PU/PANI thermoplastic elastomer

4.3.3 Characterisation techniques

4.3.3.1 Thermogravimetry

Thermogravimetric analysis (TGA) was performed on a Netzsch TG 209 thermal analyser, operating in a dynamic mode at a heating rate of 10 Kmin^{-1} or in an isothermal mode for 150 min. The conditions were: sample weight - ~ 5 mg, atmosphere - argon, open α-Al_2O_3 pan.

4.3.3.2 Mechanical measurements

Tensile properties were measured by a Zwick universal testing machine (model 1445) at the crosshead speed of 25 mm/min as per ASTM D638. Mechanical properties were performed at room temperature about 21^{0}C, and for each composition about five specimens were tested, and the average values have been reported.

4.3.3.3 Fourier Transform infra-red spectroscopy (FTIR)

FT-IR spectra were recorded on finely ground dispersions of PU samples in spectroscopic grade KBr by using a BIORAD FTS 165 spectrometer, operating in the spectral range of 4000-400 cm^{-1}.

4.4 Results and discussion

4.4.1 Mechanical properties

Table 4.1 displays the mechanical properties for the thermoplastics investigated. Interestingly, certain percentages of PANI in the elastomer seems to have detrimental effects on the tensile properties and the Young's modulus (3% PANI) while enrichment are seen up to a surface ceiling of 9% PANI content in the elastomer – below this point a decrease in tensile strength is observed. It should be noted that since a lot of benzene rings exist along the segmented PU backbone, the tensile strength of the elastomer is surprisingly higher than that of the neat PU. Especially, the covalent-bonding and inter-molecular H-bonding between the aniline-oligomer blocks and urethane blocks is thought to be one of the major contributions for the tensile strength because those improve the compatibility between the blocks and therefore lead to the higher tensile strength of the resultant elastomer. Thus, the hard-segment acts as not only the physical

cross-links but also a reinforced rigid-rod fibre in the soft-segment matrix to strongly enhance the tensile strength of the elastomer as a molecular composite. The higher the long stiff aniline-oligomer blocks present in the block copolymer, the higher the tensile strength are observed.

Table 4.1 Properties for the thermoplastics investigated.

PU/PANI samples	PANI (wt.%)	E (MPa)	Tensile strength (MPa)	Elongation to break (%)
P1	0	225.82	11.41	34
P2	3	158.25	10.58	48
P3	6	279.26	11.99	33
P4	9	420.26	14.51	33
P5	12	356.8	13.14	25
P6	100	-	-	-

From the published literature, researchers [4.16] have previously investigated the physical and chemical-physical properties of the PU/PANI blends. As evidenced by differential scanning calorimetry (DSC) and dynamic mechanical thermal analysis (DMTA) characterization, the introduction of EB or SPANI in the modified PU matrix enhances the hard-soft phase segregation effect, because of the strong tendency of the conductive polymer chains to aggregate. Moreover, the EB and SPANI chains, grafted to the polyurethane backbone, acting as reinforcing filler, gave rise, compared with the mechanical properties of the insulating matrix, to an increase of the Young modulus and a decrease of the tensile strength.

In this thesis, however, it was additionally observed that the percentage elongation at break was at its best at lower PANI content (3 %) in the elastomer. Above this percentage, the elongation at break seemed to worsen with further increase of the percentage of PANI at the expense of the Young's modulus and the tensile properties. In fact, Jeevananda and Siddaramaiah [4.17] have recently reported that addition of 2.5% PANI to PU/PMMA IPN did not affect its original tensile strength and that the tensile property increased with increase in

PANI content above 2.5% addition, but percent elongation at break of the IPN system decreased with increase in PANI content (except with 2.5% PANI) showing a negative linear correlation. Although not investigated, it was expected that any further addition of PANI above 12% to the PU/PANI elastomer would lead to brittle sheet due to improper crosslinking. Such observations have been noted in other PU conductive elastomers too. For instance, Diaconu *et al.* [4.18] noted that tensile strength characteristics such as tensile stress and elongation at break decreased by incorporation of the polypyrrole who related the effects to enhanced phase mixing by electrostatic interactions of the PU cationomer with oxidizing agents and polypyrrole.

4.4.2   Thermal study

Thermal stabilities of PU and PU/PANI were evaluated by TGA in the temperature range of up to 600^0C under nitrogen conditions, as shown in Figure 4.1 for DTG against temperature and mass loss against temperature depicted on Figure 4.2.
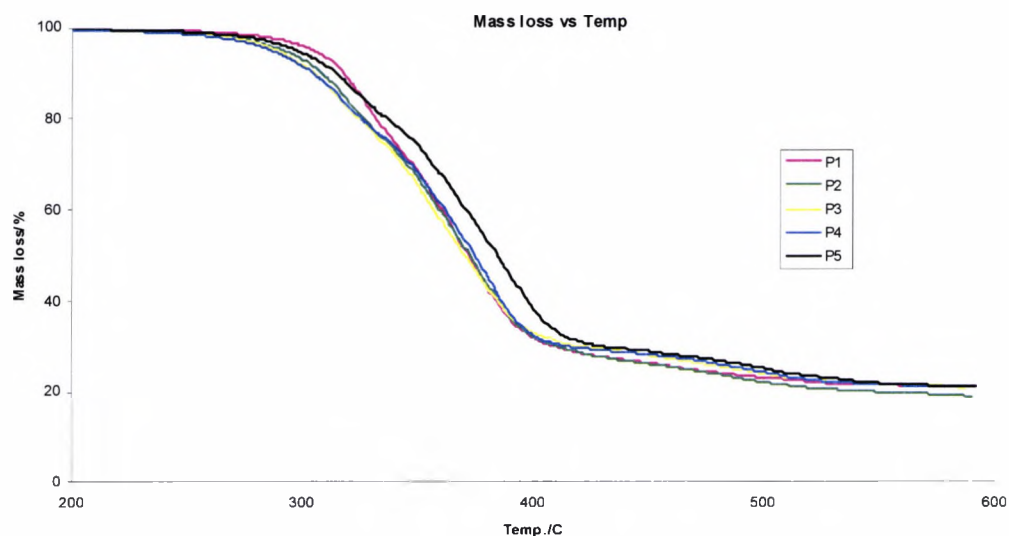
Figure 4.2   The TGA traces under nitrogen conditions of PU and PU/PANI samples displaying the mass loss against temperature
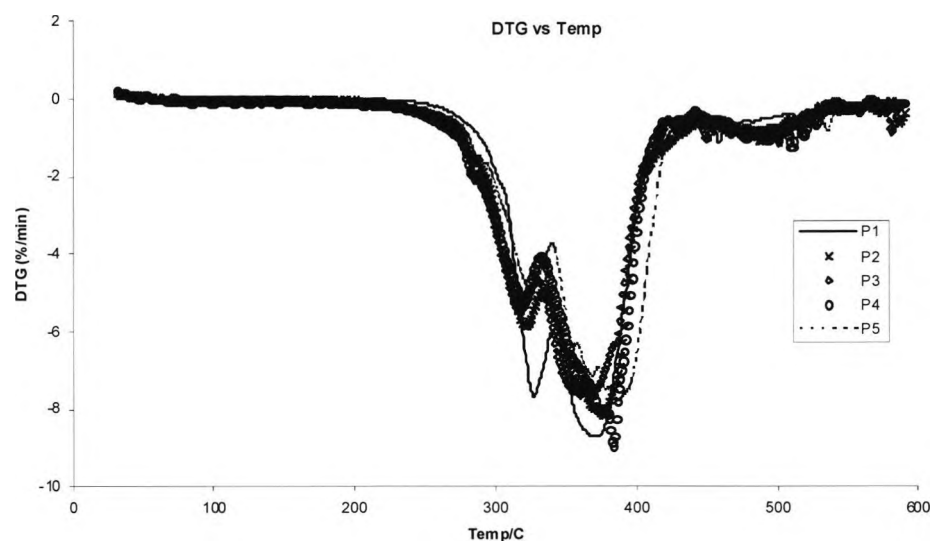
Figure 4.3 **The TG results under nitrogen conditions of PU and PU/PANI showing the DTG against temperature**

As expected, PU started to degrade at low temperatures (around 240^0C) with the formation of a nitrogen-free residue and a nitrogen-containing yellow smoke. With increased temperature, the residue was thought to further decompose to smaller compounds yielding nitrogen-containing products like HCN and acetonitrile. Accordingly, research has already shown that the evolution of nitrogen-containing compounds (acetonitrile, acrylonitrile, propionitrile, pyrrole, pyridine, aniline, benzonitrile, quinoline and phenyl isocyanate) during the thermal decomposition of polyurethanes [4.1, 4.2, 4.19]. (Also, Grassie and co-workers [4.20, 4.21] found that under inert conditions at temperatures above 210^0C the polyurethane linkage disappears without any volatile products being formed, and the initial degradation step is seemingly a simple depolymerisation reaction.) The two monomers are the primary products, and all the other products, which include carbon dioxide, butadiene, tetrahydrofuran, dihydrofuran and water as volatile products and carbodimide and urea amide in the condensed phase, are formed from the monomers in a complex set of secondary reactions while they are diffusing from the hot polymer. The second degradation, which is assigned to the thermal degradation or de-crosslinking of the thermoplastic elastomers, occurred in the range of 330-400^0C. Also, thermal degradation of PU/PANI showed

that the DTG decomposition peak increased with an increase of PU content. PANI, is known to undergo two-step weight loss, the first-step weight loss occurs in the temperature range 80–260^{0}C due to the loss of moisture and unbound dopant present while a major weight loss occurs in the range 275–590^{0}C corresponds mainly to the loss of bound dopant and main chain degradation [4.4, 4.17]. In this case, it is evident from Figure 4.1 (and Figure 4.2), that the sample with high content of PANI (12%) had delayed degradation process as compared to the rest of the samples. This is probably due to strong intermolecular bonds formed in the thermoplastic elastomer. Additional effects may be caused by specific interactions between phases via hydrogen bonding, connected with phase intermixing and dissociation-reorganisation processes. Such a complex microdomain structure strongly influences the degradation route since initial decomposition places are located at different microstructural levels. Additionally, the exothermic heat from the burning process is fed back to the condensed phase, causing further degradation to the polymer. The final weight loss occurs in the third stage in the range 400–592^{0}C, indicating the complete decomposition of PU and the elastomers investigated.

4.4.3   FT-IR spectra

In our experiments, the PU, PANI and PU/PANI elastomers were characterized by FTIR at room temperature in the range 500-3700 cm^{-1} to identify the absorption band in the elastomer. As shown in Figure 4.3, the strong peaks around 3400–37500 cm^{-1} in samples P2-P5 due to the stretching vibration of N---H bond, a strong absorption peaks around 1521~1621 cm^{-1} and 1235 cm^{-1} from the stretching vibration of C=O bond of the urethane, and a---NCO strong peaks occurring at 2270 cm^{-1}. These results are in agreement with Wang *et al.* [4.7] who carried experiments on urethane–aniline block copolymer and similarly observed a strong absorption peaks around 1700~1730 cm^{-1} and also at 2270 cm^{-1}. All of the PU/PANI FTIR spectra (P2-P5 in Figure 4.3) include a moderately strong peak at about 1521~1621 cm^{-1} and 1235 cm^{-1} due to the bond of urea as two peaks disappeared at 2270 cm^{-1} and around 3400~3500 cm^{-1} are due to the urea reactions of the ---NCO group with the ---NH$_2$ group of the OPA resulting in two absorption peaks at 1015 cm^{-1} and 1495 cm^{-1} from symmetric and asymmetric stretching vibration of N–C–N in the resultant copolymers, respectively. It is acknowledgeable that in an ether-based PU thermoplastic, the carbonyl groups exist only in the hard segments. Therefore,

the relative absorbances of the two-carbonyl peaks should serve as an index of the degree to which this group participates in the hydrogen bonding.
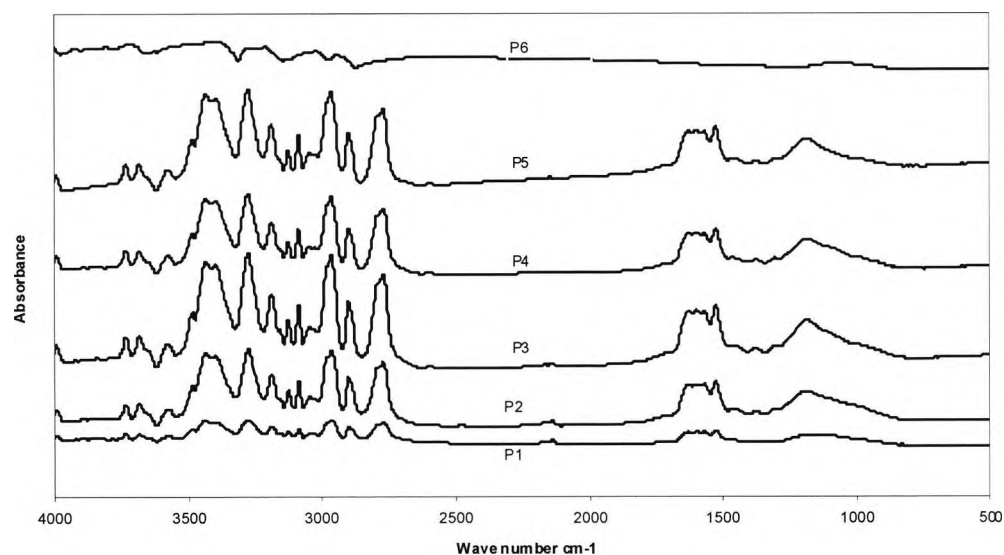
Figure 4.4   FTIR spectra of PU, PU/PANI and PANI samples

In addition, Carone *et al.* [4.16] covalently linked, by an amidation reaction, the terminal NH_2 of emeraldine and sulfonated emeraldine to a free carboxylic group belonging to the repetitive unit of functionalized segmented polyurethane. The reaction was carried out by activating such a carboxylic group with N, N'-dicyclohexylcarbodiimide and N-hydroxysuccinimide. In the ^1H and ^{13}C NMR, UV, and FTIR studies, the reaction course and the chemical properties of the polymers. The average numbers of emeraldine or sulfonated emeraldine aromatic rings per polyether urethane acid repetitive unit, which cannot be assumed to be amidation degree because at this moment the molecular weights of the inserted emeraldine and sulfonated emeraldine chains were unavailable, were six in case of the polymer obtained from the pristine emeraldine and one for that obtained from the sulfonated emeraldine. This result could be because sulfonated emeraldine was used in the acidic form, which depresses the nucleophilicity of the NH_2 group because of the presence of the sulfonic protons. The p-conjugated ring orientation has been studied and compared for PANI against polypyrrole (PPy) by Choi *et al.* [4.22].

Srichatrapimuk and Cooper [4.23] and Goddard and Cooper [4.24] summarised band assignments for the N-H region and the carbonyl region. Yoon and Han [4.2] observed the N-H stretching of ester-based thermoplastic PU from 3150 to 3500 cm^{-1}, and that of carbonyl stretching of ether-based thermoplastic PU from 1650 to 1800 cm^{-1}. The absorption bands at 2857 and 2960 cm^{-1} is associated with symmetric and asymmetric CH_2 stretching vibrations, respectively, of the aliphatic CH_2 groups in ester-based ester-based thermoplastic PU. However, in the case of ether-based thermoplastic PU the absorption bands of CH_2 stretching vibrations appeared at 2857 cm^{-1} (symmetric stretching) and 2940 cm^{-1} (asymmetric stretching).

4.5   Conclusion

The studies performed aim at combining the beneficial properties of the two polymers i.e. tensile strength, thermal properties and compatibility. TGA results depicts that the sample with high content of PANI (12%) had delayed degradation process as compared to the rest of the samples. This is attributed to strong intermolecular bonds formed in the thermoplastic elastomer. It was also observed that the percentage elongation at break was at its best at lower PANI content (3 %) in the elastomer. Above this percentage, the elongation at break seemed to worsen with further increase of the percentage of PANI at the expense of the Young's modulus and the tensile properties. FTIR results showed strong peaks around 3400–37500 cm^{-1} in samples P1-P4 due to the stretching vibration of N---H bond, a strong absorption peaks around 1521~1621 cm^{-1} and 1235 cm^{-1} from the stretching vibration of C=O bond of the urethane, and a---NCO strong peaks occurring at 2270 cm^{-1}.

5 Synthesis of polyurethane/montmorillonite elastomeric nanocomposites

5.1 Introduction

Polymer nanocomposites are currently of great interest because they often exhibit remarkable improvement in materials properties that include high moduli, increased strength and heat resistance, decreased gas permeability and flammability [5.1]. Recently there has been increased interest in theory and simulations addressing the preparation and properties of these materials, which are considered to be unique model systems to study the structure, and dynamics of polymers in confined environments. Nanocomposites have improved physical properties in comparison with conventional composites due to the much stronger interfacial forces between the well-dispersed nanometer-sized domains and the matrices [5.2, 5.3].

Polyurethanes (PU) are versatile polymeric materials, which can be tailored to meet the diversified demands of modern technologies. The physical properties of PUs are derived from their molecular structure as well as the supramolecular arrangement caused by specific interactions between the polymer chains. The two-phase morphology of polyurethane as a result of the incompatibility between the soft and hard segments primarily determines PU properties.

The morphology of segmented PUs depends on the relative amount of the soft and hard phases. PUs with a 70 wt.% of soft segments concentration typically have globular hard domains dispersed in the matrix of soft segments, while co-continuous phases and even lamellar morphology have been postulated in the samples with 50 wt.% soft segments concentration. PUs with 70 wt.% soft segment concentration are soft thermoplastic rubbers whereas the ones with 50 wt.% soft segment concentration are hard rubbers, both being of significant industrial importance. These systems are usually unfilled except for minor additives to hinder aging. In addition, the segmental distribution, flexibility and composition ratios of monomers, the chain entanglement and length, the interchain forces and the crosslinking are all important parameters that influence the properties and determine the use of the end-products of PU [5.4, 5.5]. It is therefore noted that strength, elasticity, toughness, thermal stability, load carrying capacity, transport properties, conductivity and durability of formed composites may all be considerably

improved by the addition of nanoparticles [5.2, 5.3]. For a characteristic filler particle size on the micrometer and larger scale interface can be viewed as a two dimensional boundary between the components. By contrast, when the matrix is filled with nanosized particles, a significant fraction of the material is either at the interface or within its immediate vicinity. These significant changes in both chemistry and morphology in a large volume fraction of the polymer matrix are the basis for potentially tremendous changes in nanocomposite properties [5.6, 5.7].

The most widely researched PU nanocomposites are fabricated from the layered silicate clays mainly due to their high surface area, platy morphology and exceptionally stable oxide network in addition to their inexpensiveness. In certain respects the layered silicate clays share characteristics as the aerogel silicas and precipitated silicas used for the reinforcement of silicones and other polymer systems [5.4]. Montmorillonite (MMT), (Ca, Na, H)(Al, Mg, Fe, Zn)$_2$(Si, Al)$_4$O$_{10}$(OH)$_2$ - xH$_2$O, consisting of layered silicates is the most experimented layered silicate [5.8, 5.9]. MMT belongs to the 2:1 phyllosilicate (Figure 5.1), and the crystal structure of silicate layers is made of two silicates, tetrahedrally fused to an edge-shared octahedral sheet of either aluminium or magnesium hydroxide [5.10, 5.11]. These layered materials are present in the form of the aggregates with a size of about 0.1–10 μm, consisting of several primary particles with a height of about 8–10 nm. The primary particles are composed of a number of layers, and the thickness of the layers is about 0.96–1.0 nm. Each layer consists of a central Al-octahedral sheet fused to two tetrahedral silicate sheets. Isomorphic substitutions of aluminium by magnesium in the octahedral sheet generate negative charges, which are compensated for by alkaline earth or hydrated alkali-metal cations. The electrostatic and van der Waals forces holding the layers together are relatively weak in smectites and the interlayer distance varies depending on the radius of the cation present and its degree of hydration. As a result, the stacks swell in water and the 1 nm thick layers can be easily exfoliated by shearing, giving platelets with high aspect ratio.

○ Al, Fe, Mg, Li
◎ OH
● O
⊕ Li, Na, Rb, Cs

← Tetrahedral
← Octahedral
← Tetrahedral

Exchangeable cations
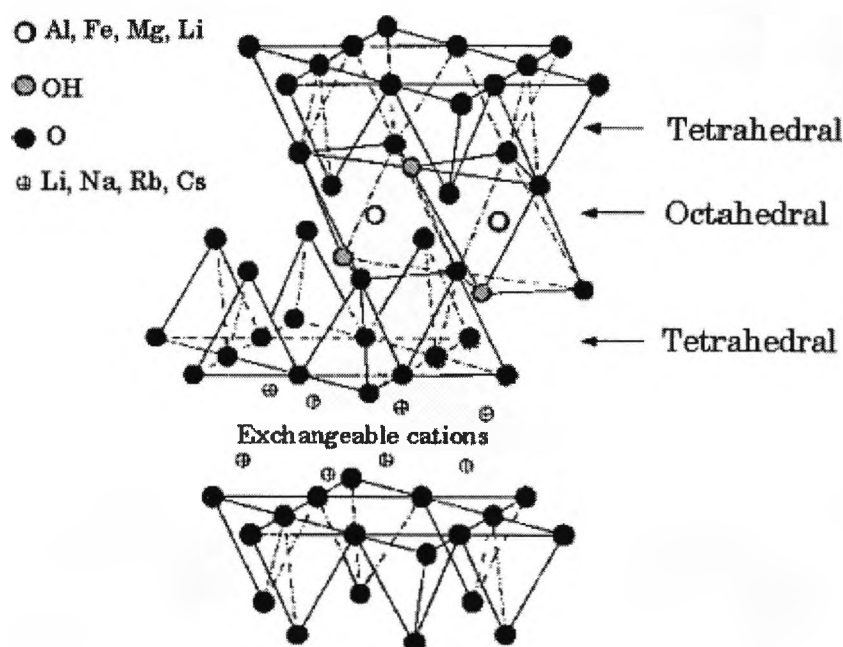
Figure 5.1   Schematic formation of 3-aminopropyltriethoxysilane (APTS)-modified silica (SIAP) by grafting of APTS into the silica nanoparticles surface [4.8].

Although the high aspect ratio of silicate nanolayers is ideal for reinforcement, the nanolayers are not easily dispersed in most polymers due to their preferred face-to-face stacking in agglomerated tactoids. Dispersion of the tactoids into discrete monolayers is further hindered by the intrinsic incompatibility of hydrophilic-layered silicates and hydrophobic engineering plastics [5.1]. However, their inorganic cations can be easily exchanged with organic ions (*e.g.* alkylammonium) to give organically modified montmorillonite that does not suffer from this problem. In this way, long alkyl chains can be ionically bound to the aluminosilicate surface, which increases the basal-plane spacing (*d* spacing) besides decreasing the surface energy. This improves the wetting, swelling and exfoliation of the aluminosilicate in the polymer matrix [5.12]. Figure 5.2 illustrates achievable types of nanocomposites from organically modified layered silicates (OMLS).
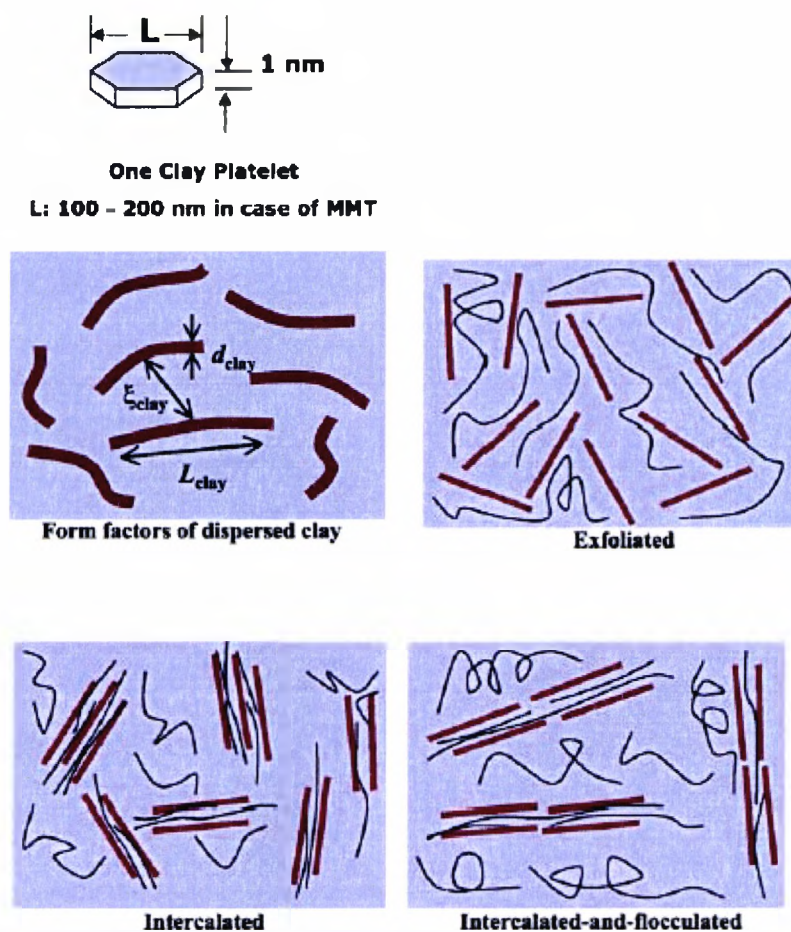
Figure 5.2   Schematic formation of PU/SIAP hybrid nanocomposites [4.8].

Despite the fact that montmorillonite (MMT) is among the most commonly used smectite-type, layered silicates for the preparation of nanocomposites [5.8, 5.9], pure MMT is a hydrophilic phyllosilicate and is only miscible with hydrophilic polymers. It is necessary to exchange alkali counterions with cationic-organic surfactants in order to improve the compatibility of MMT with organic monomers or polymers. Many organic modifiers are used to prepare organic-MMT by a cationic-exchange reaction. These modifiers are able to improve the compatibility between MMT and polymer and thus increase the thermal and mechanical properties of polymer-clay nanocomposites [5.13-5.15]. In this work we applied scanning electron microscopy (SEM) to

characterize the structures of the obtained nanocomposites and thermogravimetry (TG) for evaluation of the thermal stability.

5.2 Experiment

5.2.1 Materials and preparation

Polyurethanes were obtained by a prepolymer method, in which first isocyanate (partially polymerised 4,4'-diphenylmethane diisocyanate) and polyoxypropylene diol (M=2000 g/mol) were reacted (Figure 5.3). In the second step polymer chain was extended with 1,4-butanediole (BD). The nanoadditive was directly added to the prepolymer (MMT) or in form of dispersion in a solvent (in case of O-MMT). The mixture was vigorously mixed. It is worth emphasizing that despite the fact that PU nanocomposites offer potential access to completely new classes of materials with unique properties, one of the most difficult problems with nanocomposites is in developing synthetic and processing approaches that precisely define the volume and shape of the individual phases and their local arrangement. Such efforts are needed to generate nanocomposite materials that permit one to probe how discrete changes in nanostructure affect macroscopic properties.

5.2.2 Characterisation techniques

5.2.2.1 Thermogravimetry

Thermogravimetric analysis (TGA) was performed on a Netzsch TG 209. The conditions were: sample weight - ~ 4 mg, atmosphere - argon, open α-Al_2O_3 pan, heating rate: 10 K/min, argon flow 20 cm^3/min.

5.2.2.2 Scanning electron microscopy

Scanning Electron Microscopy (SEM) was used to evaluate the morphology of PU nanocomposites with particles-matrix adhesion on the fracture surface. The specimens were gold-coated and SEM images were obtained using a Jeol JSM-5310 electron microscope.
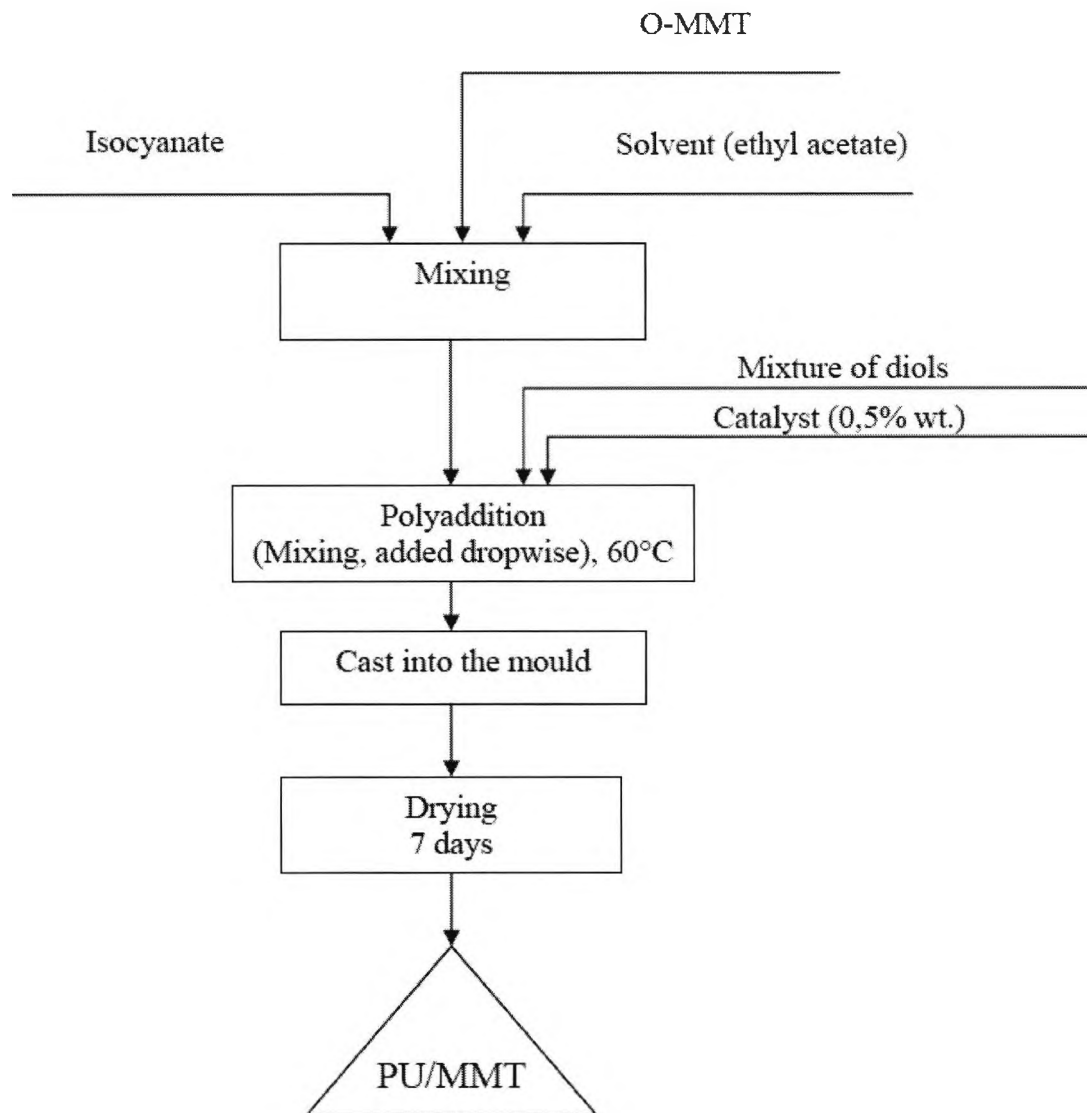
Figure 5.3   Schematic diagram showing the route for the synthesis of PU/O-MMT nanocomposites

5.3   Results and discussion

The high promise for nanocomposites industrial applications has motivated vigorous research, which has revealed concurrent dramatic enhancements of many material properties by the nano

dispersion in polymeric systems. Where the property enhancements originate from the nanocomposite structure, these improvements are generally applicable across a wide range of polymers. The interface bonding influences a larger region surrounding the particle in which the conformational entropy and chain kinetics are significantly altered. These significant changes in both chemistry and morphology in a large volume fraction of the polymer matrix are the basis for potentially tremendous changes in nanocomposite properties. At the same time, there are also discovered property improvements in these nanoscale materials that could not be realized by conventional fillers. However, in some cases there are limitations of the amount of nanoadditive that can be added to the primary polymer system to achieve key enhancements. For this reason among others, a good balance between properties enhancement and synthesis/fabrication parameters need to be struck for a success.

5.3.1 *Thermal study*

TG profiles of PU and PU/O-MMT nanocomposites are presented in Figure 5.4. The results show that the degradation rates of the nanocomposites become slower compared to PU, indicating an improvement of thermal stability of PU due to the role of nanoadditive that prevents the heat transfer and thus limits progress of degradation. Tien and Wei [5.16] reported that the glass transition temperature of the hard-segment phase and the storage modulus of segmented PUs increased substantially in the presence of a small amount of tethered nano-sized layered silicates of montmorillonite (as compared with their pristine state) by approximately three folds. Further, the thermal stability of these MMT/PU nanocomposites was enhanced, as shown by TGA - in particular, a 40^0C increase in the degradation onset temperature and a 14% increase in the activation energy of degradation was found for PU containing 1 wt.% trihydroxyl group swelling agent-modified montmorillonite, compared to that of the pristine PUs.

TGA
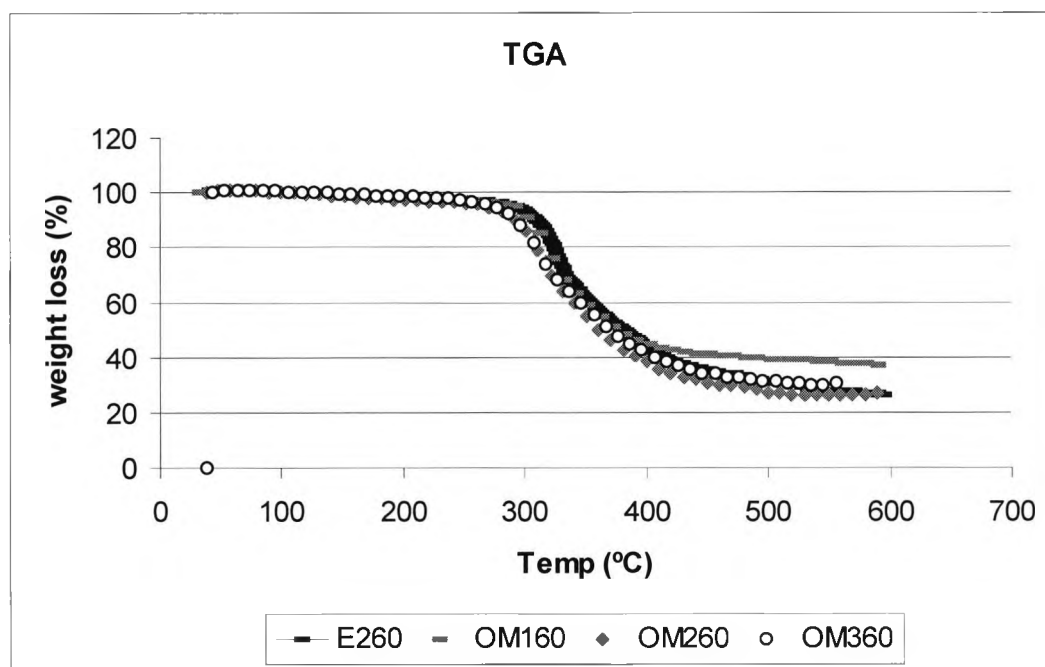
Figure 5.4   **TG profiles for PU and PU nanocomposites containing 1, 3 or 5% of O-MMT.**

Because of the incompatibility between the hard segments and the soft segments, PU undergoes microphase separation resulting in a hard-segment domain, soft-segment matrix, and urethane-bonded interphase. The hard-segment domains act as physical crosslinks in the soft-segment matrix. The primary driving force for phase separation is the strong intermolecular interaction of the urethane units, which are capable of forming intermolecular hydrogen bonds [5.17, 5.18]. Owing to such interactions, interconnected or isolated hard segments remain distributed in the soft segment matrix, though the soft domain may contain some hard segments dissolved in it, which is evident from the hydrogen bonding of the urethane–NH groups with the oxygen of the ether or ester linkages – this complex morphology strongly influences both mechanical and thermal properties of PU. In general, there are three main pathways for the initial degradation of the urethane linkage which are: dissociation to isocyanate and alcohol, dissociation to primary amine, olefin and carbon dioxide as well as the formation of a secondary amine with elimination of carbon dioxide. Polyurethanes degrade at low temperatures (220–

270^0C) with the formation of a nitrogen-free residue and a number of low-molar-mass volatile products. With increased temperature the residue further decomposes to yield nitrogen-containing products like HCN and acetonitrile. Tien and Wei [5.16] reported that the glass transition temperature of the hard-segment phase and the storage modulus of segmented PUs increased substantially in the presence of a small amount of tethered nano-sized layered silicates of montmorillonite (as compared with their pristine state) by approximately three folds. Further, the thermal stability of these MMT/PU nanocomposites was enhanced, as shown by TGA - in particular, a 40^0C increase in the degradation onset temperature and a 14% increase in the activation energy of degradation was found for PU containing 1 wt.% trihydroxyl group swelling agent-modified MMT, compared to that of the pristine PUs.

An important observation concerns formation of larger amounts of char residue during the thermal decomposition of PU nanocomposites in relation to the neat PU. This is a promising result for further flammability studies that are underway. This is in agreement with other findings, e.g. Uhl *et al.* [5.19] showed that presence of modified MMT clay rendered the polymers more susceptible to thermal degradation. In the work of Han *et al.* [5.20] it was described that initial degradation corresponds to the release of little molecules or unstable side chains. The introduction of well-dispersed MMT can prevent the heat transport and then improve the thermal stability of the polymer nanocomposites. Slowing down the volatilization of the degradation products may also occur because of the labyrinth effect of the silicate layers in the polymer matrix [5.21]. However, because the O-MMT itself contains some low-molecular-weight compounds that will release at lower temperature, many of them are to impair the thermal stability of the nanocomposites. At the main degradation stage of PU backbone decomposition, the introduction of MMT limits the motions of PU molecules, causing an enhancement in the thermal stability.

5.3.2 Structure and morphology

In this study, the SEM experimental results showed that the MMT existed in the form of an intercalated layer structure – Figure 5.5. The extent of the reduction of hydrogen bonding in the hard segments depended on the amount of the silicate layers and their dispersion. The combination of the reinforcing effect of the silicate layers and its effect on the morphology of PU

resulted in an optimal enhancement of the maximal strength and the elongation at break, regardless of their hard segments ratios. Published work have indicated that the degree of hydrogen bonding in the hard segments in PU was reportedly reduced due to the presence of the silicate layers, and the resultant morphology of the segmented PU was altered [5.22, 5.23]. Of late, Petrovic and co-workers [5.24] studied the effect of silica nanoparticles on morphology of segmented PUs. It was shown that addition of nanoparticles radically alters the morphology of the hard phase both at 50 and 70 wt.% soft segments concentration by suppressing the formation of fibrils within spherulites and decreasing hard domains size. A single melting peak in wide-angle scattering techniques (WAXS) showed decreasing crystallinity of the hard domains with increasing filler concentration in samples with 70 wt.% soft segments concentration. Also, spherulites of PU with 70 wt.% soft segments concentration were more compact than those of the polymer with 50 wt.% soft segments concentration. Differences were also found in the structure and size of fibrils forming spherulites.

| PU | PU + 3% MMT | PU + 3% O-MMT |
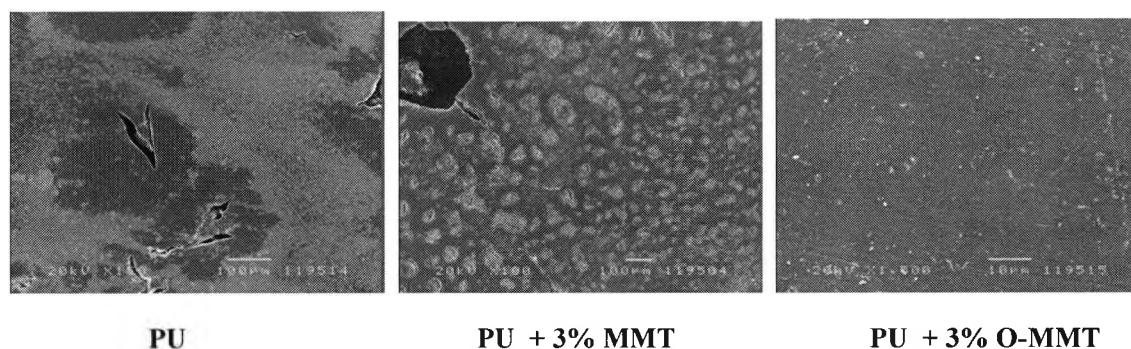
Figure 5.5   SEM micrographs for the PU, and PU/MMT and PU/O-MMT under investigations.

Remarkably, in PU with 70 wt.% soft segments concentration, there was a tendency toward radial growth of fibrils from a nucleating centre. Ultra small-angle scattering techniques (SAXS) provided a link between the presence of the silica and the alteration of the large-scale fibrillar morphology. Even a small amount of silica disrupts the shortscale phase-separated morphology attributed to segment phase separation in unfilled PU. Apparently, the large-scale morphology resulted from the short-scale domain growth in the same way that lamellar crystals result from

short-scale segregation of crystalline and amorphous regions in semicrystalline polymers. When the short-scale domain structure was disrupted, fibrillar growth was impeded. Further, the DSC results of the PU/silica nanocomposites suggested that either the distribution of crystallite sizes was narrower or that a single type of crystalline structure was formed at higher filler loadings, but there was no clear effect of the filler on the glass transition of soft segments.

5.4 Conclusions

Polyurethane nanocomposites with montmorillonite are an interesting group of modern macromolecular materials that have gained a lot of attention recently. The versatile structures of polymer matrices and the subsequent formation of complex nanostructured materials often require an extensive range of physical techniques to characterize the obtained structures over a range of length scales from molecular dimensions to micron size scales. In this work, thermal properties of PU/MMT and PU/O-MMT nanocomposites with intercalated structure, as evidenced by SEM data, prepared by prepolymer method, show a considerably potential for further increase and form a solid basis for further flammability studies. Remarkable differences in the thermal behaviour of neat PU and PU nanocomposites indicate that nanoadditive play an important role by barrier effects that increase during volatilization owing to the reassembly of the reticular of the silicate on the surface. It can be emphasized that the nanoparticles often strongly influence the properties of the composites at very low volume fractions as observed in this study. This is mainly due to their small interparticle distances and the conversion of a large fraction of the polymer matrix near their surfaces into an interphase of different properties as well as to the consequent change in morphology. As a result, the desired properties are usually reached at low filler volume fraction, which allows the nanocomposites to retain the macroscopic homogeneity and low density of the polymer. Besides, the geometrical shape of the particles plays an important role in determining the properties of the composites. This work establishes the foundation for further investigations.

5.5 Polymer Composites: From nano to macrostructures

With continuing quest for lighter and stronger composites, the demand for new types of materials is increasing. No longer can traditional fibrous composites fulfil our stringent requirements, nor can they be engineered at the continuum level, which control properties at the molecular or atomic level. However, it is well known that molecular forces and bonding, the interaction between the interfaces, and the physical phenomena at this level will dictate the aggregate properties of materials. In this nanocrystalline state the solids contain such a high density of defects that the spacing between them approaches interatomic distances and a large fraction of the atoms sits very close to a defect [5.25]. Consequently, nanocrystalline materials are exceptionally strong, hard, and ductile at high temperatures, wear-resistant, corrosion-resistant, and chemically very active.

From the nanofiller reinforcement family of materials, nanoclay are one of the most promising mechanical reinforcing materials for polymeric composites [5.26]. This owes to the fact that extremely high surface area is one of the most attractive characteristic of the nanoparticles because it facilitates creating a large interface in a composite. An interphase of 1 nm thick represents roughly 0.3% of the total volume of polymer in case of microparticle filled composites, whereas it can reach 30% of the total volume in case of nanocomposites. A negligible contribution made by the interphase provides diverse possibilities of performance tailoring and is able to influence the properties of the matrices to a much greater extent under rather low nanofiller loading. Improvement in the tensile performance of polyurethane composites has been reported in the proceeding chapters in terms of stiffening, strengthening and toughening with a low filler content of about 1%.

More recently, nano-sized fillers have been extensively used to the end of improving composite stiffness and strength [5.27, 5.28]. Particularly, nano-sized fillers such as carbon nanotubes [5.29] have been recently employed to improve the dynamic performance of composite materials. These fillers exhibit promising behaviour towards the improvement of the composite's time dependent performance, e.g., vibration damping and/or the damage tolerance characteristics.

Moreover, these improvements are achieved through conventional processing techniques without any detrimental effects on processability, appearance, density and ageing performance of

the matrix. Eventually, these composites are now being considered for a wide range of applications including packaging, coating, electronics, automotive and aerospace industries. While nanoparticles have attractive attributes, their usage in structural composites which are relatively large in dimension is almost non-existent. It is on this foundation that this thesis is built on.

A thorough understanding of processing-structure-property relationships in the nanocomposites is critical and should eventually permit properties prediction toward specific applications. Equally important, is the incorporation of nanosized components that offers the great potential to improve the reproducibility of composite properties, importantly, because complete control of the smallest building segments offers the best potential for controlling macroscopic properties. Moreover, the production of high performance resins will enhance further understanding of hybrid nano-composites.

The geometry of CFRP in the fibre-matrices construction in many ways resembles that one of nanocomposites produced from layered silicate clays. In such nanocomposites, a polymer system is used to fill in the gaps between the layers (see Figure 5.6). Fundamental research in CFRP technology can therefore be adopted to deliver a better understanding of the structural mechanisms of the nanocomposites to allow feasible applications to happen e.g. in noise and vibration damping. Further insight may also be gained from sandwich structures particularly where elastomers are used as the core material. Even further, established knowledge in theoretical formulation of laminated composite structures (for instance using dynamic stiffness matrix methods) may be developed to appropriate theoretical model that can assess possible advantages of layered silicate reinforcements. Notably, the current theoretical models concentrate on macromechanics, or micromechanics. The challenge here is to develop a suitable theoretical model to investigate the three levels (macro, micro and nano) harmonically and to develop appropriate theoretical model hoping to arrive at a point where one may apply the model in real life application, as demonstrated in Figure 5.7.
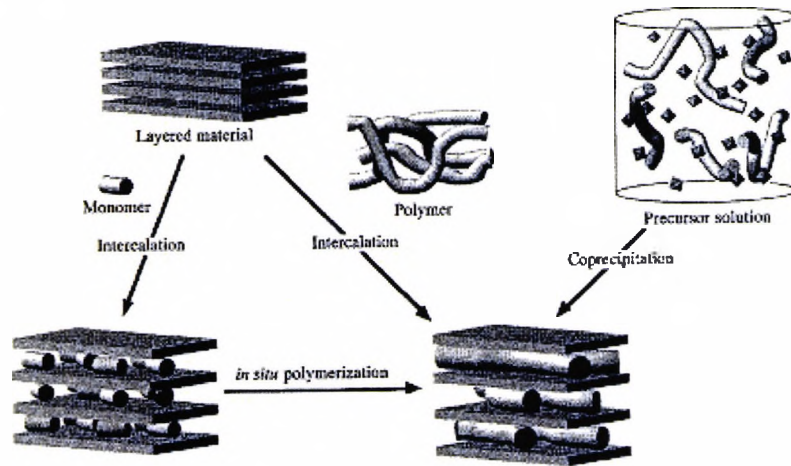
Figure 5.6   Syntheses routes for polymer/montmorillonite

A cost effective aircraft flying with improved lift, manoeuverability and enlarged flutter envelop

Box beam model

Established Concepts

Epoxy-fibre-reinforced-composite beam made of several plies of various orientations +/-(0-90)

Each ply has variable number of laminates ~0.125mm thickness and bonded together by the resins/adhesives

Each laminate has fibres of different orientations bonded by the resins

Polymer

Polymer-layered silicates nanotechnology

Developing

Each laminate has several layers of layered silicates

Lift

airflow

Each layer of the layered silicates behaves like a convectional CFRP laminate when subject to airflow and offer contributions to wash-in and wash-out on the flutter characteristics of composite wing

Blue sky Concepts

Figure 5.7   Futurist application of polymer nanocomposites incorporated into carbon-fibre reinforced composites

109

Future developments may involve the macroproperties i.e. the effect of layered silicates on CFRP and ultimately on structural dynamic problems such as aircraft wing flutter. Since there is no commercially available software to evaluate the effects of nanoadditives in structural dynamics, development of computer modelling capabilities are necessary such that computer models of various orders of complexity may be used to simulate the possible outcomes and the results correlated with experimental and theoretical ones. Adoption of structural dynamics employed in laminated and sandwich structures will facilitate these developments.

6 Investigations into free vibration behaviour of layered sandwich beams using theory and experiment

6.1 Introduction

Sandwich structures are widely used in many weight sensitive and high-energy absorption applications, for example, as components of aircraft, missile and spacecraft structures. They have many advantages over solid isotropic structures. Some benefits of sandwich structures include good specific stiffness, high buckling resistance, formability into complex shapes and easy reparability. A three-layered composite structure in particular, is commonly used in practice, which is generally made of a soft core such as rubber and strong face materials such as steel or aluminium. The present work is concerned with the dynamic analysis of a three-layered sandwich beam using both theory and experiment.

Earlier research on the dynamic behaviour of sandwich beams can be traced back to Di Taranto [6.1], Mead [6.2] and Ahmed [6.3] who used classical differential equation approach and concentrated mostly on theoretical developments. The research on this topic has continued over the years as clearly apparent from the literature. An important feature of the published work is that the value judgements made by various investigators when establishing the model accuracy of a sandwich beam have been interestingly, and often intriguingly, diverse. There is no doubt considerable difficulty in obtaining an accurate analytical (mathematical) model for a sandwich beam because of the very nature of the problem in which materials with markedly different properties are joined together. Only a few relevant earlier investigations are reviewed here. Sisemore and Darvennes [6.4] have considered the effect of compression energy of the core on the damping behaviour of sandwich beams whereas Sainsbury and Zhang [6.5] used Galerkin's method to solve the damped free vibration problem of sandwich beams. On the other hand, Rao [6.6] derived a complete set of equations of motion and boundary conditions governing the vibration of sandwich beams using an energy approach. Banerjee [6.7] used the dynamic stiffness method, which was primarily based on the Bernoulli-Euler theory, when he carried out a free vibration analysis of a three-layer sandwich beam. Later the work was extended by using Rayleigh theory for the face layers and Timoshenko theory for the central layer [6.8]. Banerjee's

work is essentially based on an imposed displacement field. He used Hamiltonian mechanics to derive the governing differential equations whose solution eventually led to the formulation of the dynamic stiffness matrix and free vibration analysis.

The investigation reported in this chapter is carried out in two parts. The first part is theoretical in which the earlier work of Banerjee [6.7, 6.8] is extensively extended. An advanced dynamic stiffness theory for a three-layered sandwich beam is developed in order to investigate its free vibration characteristics. In this new development all three layers of the sandwich beam are assumed to behave according to the Timoshenko beam theory so that the earlier eighth order system of Banerjee [6.7] becomes a tenth order one and a significantly improved model was realised. The second part of this work is experimental. It focused on experimental measurement of the free vibration characteristics, namely the natural frequencies and mode shapes, of sandwich beams by using an impulse hammer kit and associated computer software. In order to achieve this, a number of specimens of three-layered sandwich beams were manufactured using rubber as the core and aluminium as the face materials. Replacing aluminium by steel as face materials a few additional specimens are made.

6.2 Theory

6.2.1 Derivation of the governing differential equations of motion in free vibration

The following general assumptions are made when developing the governing differential equations of motion in free vibration of a three layered sandwich beam of asymmetric cross-section. All displacements and strains are small so that the theory of linear elasticity applies. The faces and core of the sandwich beam are made of homogeneous and isotropic materials and the variation of strain within them is linear. Transverse normal strains in the faces and core are negligible. There is no slippage or delamination between the layers during deformation.

In a rectangular Cartesian coordinate system, Figure 6.1 shows a three-layered sandwich beam of length L. Each layer has its own geometric and material properties with a subscript i denoting the layer number ($i=1$ for the top layer). Thus each layer has thickness h_i, width b_i (so that area $A_i = b_i h_i$), second moment of area I_i, density ρ_i, (so that the mass per unit length $m_i = \rho_i A_i$), Young's modulus E_i, shear modulus G_i, and shear correction or shape factor k_i ($k_i < 1$).

112

The system of displacements used is as follows. All three layers have a common flexure in the y-direction with the flexural displacement denoted by w. The axial displacement (i.e. the displacement in the x-direction) of the mid-plane of each layer is u_i ($i = 1$, 2 and 3) which varies linearly through the thickness. The axial displacement of the interface between layers 1 and 2 is u_{12} whereas for that of the interface between layers 2 and 3 is u_{23} as shown in Figure 6.1. The cross-section of each layer does not rotate so as to be normal to the common flexure, but it necessarily shears leading to the Timoshenko beam formulation.
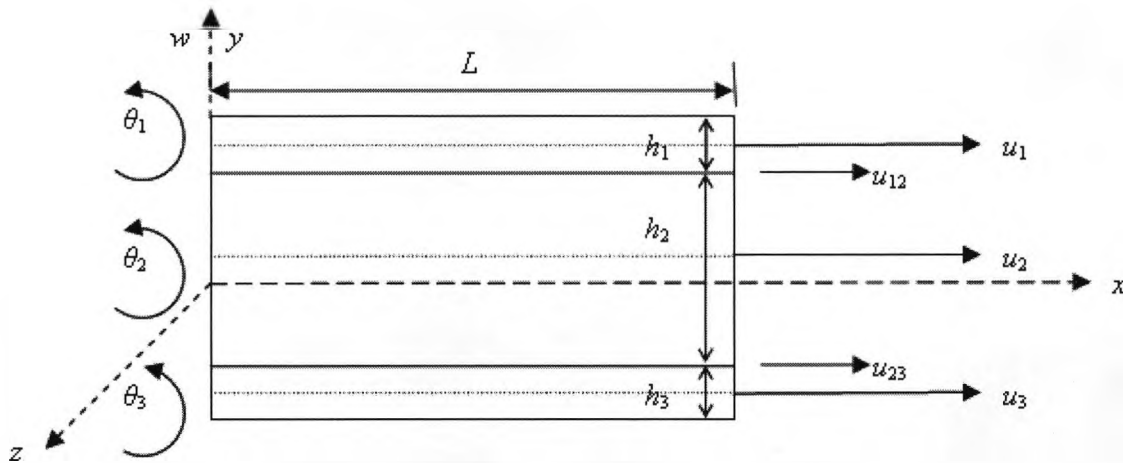
Figure 6.1   The coordinate system and notation for a three-layered sandwich beam

Given the displacement system in layers 1 and 3, the displacement in layer 2 is fully determinate. This carries over into axial stress, which is dependent on derivatives with respect to x of u_i and velocity with time derivatives. Thus a model can be developed in which the behaviour of the central layer is described in terms of the behaviour of the outer layers.

Using the continuity of deformation, the displacement u_{12} and u_{23} at the layer boundaries can be expressed as

$$u_{12} = u_1 + (h_1/2)\theta_1 = u_2 - (h_2/2)\theta_2 \tag{6.1}$$

$$u_{23} = u_3 - (h_3/2)\theta_3 = u_2 + (h_2/2)\theta_2 \tag{6.2}$$

Equations (6.1) and (6.2) give

$$2u_2 = u_1 + u_3 + (h_1\theta_1 - h_3\theta_3)/2 \tag{6.3}$$

$$h_2\theta_2 = u_3 - u_1 - (h_1\theta_1 + h_3\theta_3)/2 \tag{6.4}$$

By allowing each of the three layers to have the same flexural displacement w in direction oy, the local rotations $\theta_1, \theta_2, \theta_3$ which are not identified with w' , where the prime denotes differentiation with respect to x, a Timoshenko beam type model can be constructed. Each layer has linear variation of axial displacement and stress with respect to y in the cross-section, but the shear stress and strain remain constant.

In developing the strain and kinetic energies, repeated use is made of the following well known results.

If $f(x)$ is a linear function of x varying from $f_1 = f(x_1)$ at $x = x_1$ to $f_2 = f(x_2)$ at $x = x_2$ then

$$\int_{x_1}^{x_2} [f(x)]^2 \, dx = (x_2 - x_1)(f_1^2 + f_1 f_2 + f_2^2)/3 \tag{6.5}$$

Strain energy due to axial stress in layer 1 is given by

$$U_{B_1} = \frac{1}{2} \iiint_V E_1 [\varepsilon_x]^2 \, dx \, dy \, dz \tag{6.6}$$

where ε_x varies linearly from $u_1' - \dfrac{h_1}{2}\theta_1'$ to $u_1' + \dfrac{h_1}{2}\theta_1'$ through the thickness

Noting that the width b_1 of layer 1 is constant, the strain energy U_{B_1} becomes

$$U_{B1} = \frac{1}{2} \int_0^L E_1 \frac{b_1 h_1}{3} \left[\left(u_1' - \frac{h_1}{2} \theta_1' \right)^2 + \left(u_1' - \frac{h_1}{2} \theta_1' \right) \left(u_1' + \frac{h_1}{2} \theta_1' \right) + \left(u_1' + \frac{h_1}{2} \theta_1' \right)^2 \right] dx$$

$$= \frac{1}{2} \int_0^L E_1 \frac{b_1 h_1}{3} \left[(u_1')^2 - u_1' h_1 \theta_1' + \frac{h_1^2}{4} (\theta_1')^2 + (u_1')^2 - \left(\frac{h_1}{2} \right)^2 (\theta_1')^2 + (u_1')^2 + u_1' h_1 \theta_1' + \left(\frac{h_1}{2} \right)^2 (\theta_1')^2 \right] dx \qquad (6.7)$$

$$= \frac{1}{2} \int_0^L E_1 b_1 \left[h_1 (u_1')^2 + \frac{h_1^3}{12} (\theta_1')^2 \right] dx$$

$$= \frac{1}{2} \int_0^L \left[E_1 A_1 (u_1')^2 + E_1 I_1 (\theta_1')^2 \right] dx$$

where $I_1 = \frac{b_1 h_1^3}{12}$ is the second moment of area of the cross-section and $E_1 A_1$ and $E_1 I_1$ are

respectively extensional (or axial) and bending (or flexural) rigidities of layer 1

It follows that total strain energy due to axial stresses in all three layers is

$$U_B = \frac{1}{2} \int_0^L \left\{ E_1 A_1 (u_1')^2 + E_2 A_2 (u_2')^2 + E_3 A_3 (u_3')^2 + E_1 I_1 (\theta_1')^2 + E_2 I_2 (\theta_2')^2 + E_3 I_3 (\theta_3')^2 \right\} dx \qquad (6.8)$$

In layer 1, the shear strain is $\gamma_1 = w' - \theta_1$ and this is presumed constant across the cross-section.

The strain energy due to shear force in layer 1 is given by [6.8]

$$U_{S1} = \frac{1}{2} \int_0^L k_1 A_1 G_1 (w' - \theta_1)^2 \, dx \qquad (6.9)$$

where k_1 is the shear coefficient and $k_1 A_1 G_1$ is the shear rigidity of layer 1.

Strain energy due to shear forces in layers 2 and 3 can similarly be obtained and the total strain

energy of the whole beam due to shearing is given by

$$U_S = \frac{1}{2} \int_0^L \left\{ k_1 A_1 G_1 (w' - \theta_1)^2 + k_2 A_2 G_2 (w' - \theta_2)^2 + k_3 A_3 G_3 (w' - \theta_3)^2 \right\} dx \qquad (6.10)$$

Thus the total strain energy U of the sandwich beam due to normal and shear strains can be

written as

$$U = \frac{1}{2} \int_0^L \left[\left\{ E_1 A_1 (u_1')^2 + E_2 A_2 (u_2')^2 + E_3 A_3 (u_3')^2 + E_1 I_1 (\theta_1')^2 + E_2 I_2 (\theta_2')^2 + E_3 I_3 (\theta_3')^2 \right\} \right.$$
$$\left. + \left\{ k_1 A_1 G_1 (w' - \theta_1)^2 + k_2 A_2 G_2 (w' - \theta_2)^2 + k_3 A_3 G_3 (w' - \theta_3)^2 \right\} \right] dx \qquad (6.11)$$

For the kinetic energy, the axial velocity in layer 1 varies linearly from $\dot{u}_1 - \frac{h_1}{2} \dot{\theta}_1$ to $\dot{u}_1 + \frac{h_1}{2} \dot{\theta}_1$, so

that the kinetic energy T_1 for layer 1 is

$$
\begin{aligned}
T_1 &= \frac{1}{2}\int_0^L \rho_1 b_1 \frac{h_1}{3}\left[\left(\dot{u}_1 - \frac{h_1}{2}\dot{\theta}_1\right)^2 + \left(\dot{u}_1 - \frac{h_1}{2}\dot{\theta}_1\right)\left(\dot{u}_1 + \frac{h_1}{2}\dot{\theta}_1\right) + \left(\dot{u}_1 + \frac{h_1}{2}\dot{\theta}_1\right)^2\right]dx \\
&= \frac{1}{2}\int_0^L \rho_1 b_1\left[h_1(\dot{u}_1)^2 + \frac{h_1^3}{12}(\dot{\theta}_1)^2\right]dx \\
&= \frac{1}{2}\int_0^L\left[\rho_1 A_1(\dot{u}_1)^2 + \rho_1 I_1(\dot{\theta}_1)^2\right]dx
\end{aligned}
\tag{6.12}
$$

In this way the total kinetic energy T of the sandwich beam can be expressed as

$$
T = \frac{1}{2}\int_0^L\left\{M\dot{w}^2 + \rho_1 A_1\dot{u}_1^2 + \rho_2 A_2\dot{u}_2^2 + \rho_3 A_3\dot{u}_3^2 + \rho_1 I_1\dot{\theta}_1^2 + \rho_2 I_2\dot{\theta}_2^2 + \rho_3 I_3\dot{\theta}_3^2\right\}dx
\tag{6.13}
$$

where the first term is the transverse velocity contribution to the kinetic energy, and $M = \rho_1 A_1 + \rho_2 A_2 + \rho_3 A_3$ represents the mass per unit length of the whole sandwich beam.

The problem can now be processed using Hamilton's Principle, in which δu_2 and $\delta\theta_2$ are expressible in terms of the allowable variations δu_1, δu_3, $\delta\theta_1$, $\delta\theta_3$. The displacements u_2 and θ_2 will be substituted from Eqs. (6.3) and (6.4) once the variational analysis is complete. Combining T and U from Eqs. (6.13) and (6.11) the Lagrangian $L = T - U$ takes the following form

$$
\begin{aligned}
L = \frac{1}{2}\int_0^L\Big\{ &M\dot{w}^2 + \rho_1 A_1(\dot{u}_1)^2 + \rho_2 A_2(\dot{u}_2)^2 + \rho_3 A_3(\dot{u}_3)^2 + \rho_1 I_1(\dot{\theta}_1)^2 + \rho_2 I_2(\dot{\theta}_2)^2 + \rho_3 I_3(\dot{\theta}_3)^2 \\
&- E_1 A_1(u_1')^2 - E_2 A_2(u_2')^2 - E_3 A_3(u_3')^2 - E_1 I_1(\theta_1')^2 - E_2 I_2(\theta_2')^2 - E_3 I_3(\theta_3')^2 \\
&- k_1 A_1 G_1(w' - \theta_1)^2 - k_2 A_2 G_2(w' - \theta_2)^2 - k_3 A_3 G_3(w' - \theta_3)^2\Big\}dx
\end{aligned}
\tag{6.14}
$$

By applying Hamilton's principle $\delta\int_{t_1}^{t_2} L\,dt = 0$ and using L from Eq. (6.14), the following set of differential equations are obtained

$$
\begin{aligned}
&\left[-\left(\rho_1 A_1 + \frac{1}{3}\rho_2 A_2\right)\frac{\partial^2}{\partial t^2} + \left(E_1 A_1 + \frac{1}{3}E_2 A_2\right)\frac{\partial^2}{\partial x^2} - \left(\frac{k_2 A_2 G_2}{h_2^2}\right)\right]u_1 + \left[\left(-\frac{\rho_2 A_2}{6}\right)\frac{\partial^2}{\partial t^2} + \left(\frac{E_2 A_2}{6}\right)\frac{\partial^2}{\partial x^2}\right. \\
&\left. + \left(\frac{k_2 A_2 G_2}{h_2^2}\right)\right]u_3 + \left[\left(-\frac{\rho_2 A_2}{6}\right)\frac{\partial^2}{\partial t^2} + \left(\frac{E_2 A_2}{6}\right)\frac{\partial^2}{\partial x^2} - \left(\frac{k_2 A_2 G_2}{2h_2^2}\right)\right]h_1\theta_1 + \left[\left(\frac{\rho_2 A_2}{12}\right)\frac{\partial^2}{\partial t^2} - \left(\frac{E_2 A_2}{12}\right)\frac{\partial^2}{\partial x^2}\right. \\
&\left. - \left(\frac{k_2 A_2 G_2}{2h_2^2}\right)\right]h_3\theta_3 - \left(\frac{k_2 A_2 G_2}{h_2}\right)\frac{\partial w}{\partial x} = 0
\end{aligned}
\tag{6.15}
$$

$$
\begin{aligned}
&\left[\left(-\frac{\rho_2 A_2}{6}\right)\frac{\partial^2}{\partial t^2} + \left(\frac{E_2 A_2}{6}\right)\frac{\partial^2}{\partial x^2} + \left(\frac{k_2 A_2 G_2}{h_2^2}\right)\right]u_1 + \left[\left(-\frac{\rho_2 A_2}{3} - \rho_3 A_3\right)\frac{\partial^2}{\partial t^2} + \left(\frac{E_2 A_2}{3} + E_3 A_3\right)\frac{\partial^2}{\partial x^2}\right. \\
&\left. - \left(\frac{k_2 A_2 G_2}{h_2^2}\right)\right]u_3 + \left[\left(-\frac{\rho_2 A_2}{12}\right)\frac{\partial^2}{\partial t^2} + \left(\frac{E_2 A_2}{12}\right)\frac{\partial^2}{\partial x^2} + \left(\frac{k_2 A_2 G_2}{2h_2^2}\right)\right]h_1\theta_1 + \left[\left(\frac{\rho_2 A_2}{6}\right)\frac{\partial^2}{\partial t^2} - \left(\frac{E_2 A_2}{6}\right)\frac{\partial^2}{\partial x^2}\right. \\
&\left. + \left(\frac{k_2 A_2 G_2}{2h_2^2}\right)\right]h_3\theta_3 + \left(\frac{k_2 A_2 G_2}{h_2}\right)\frac{\partial w}{\partial x} = 0
\end{aligned}
\tag{6.16}
$$

116

$$\left[\left(-\frac{\rho_2 A_2}{6}\right)\frac{\partial^2}{\partial t^2}+\left(\frac{E_2 A_2}{6}\right)\frac{\partial^2}{\partial x^2}-\left(\frac{k_2 A_2 G_2}{2h_2^2}\right)\right]h_1 u_1+\left[\left(-\frac{\rho_2 A_2}{12}\right)\frac{\partial^2}{\partial t^2}+\left(\frac{E_2 A_2}{12}\right)\frac{\partial^2}{\partial x^2}+\left(\frac{k_2 A_2 G_2}{2h_2^2}\right)\right]h_1 u_3$$
$$+\left[-\left(\rho_1 I_1+\frac{h_1^2}{12}\rho_2 A_2\right)\frac{\partial^2}{\partial t^2}+\left(E_1 I_1+\frac{h_1^2}{12}E_2 A_2\right)\frac{\partial^2}{\partial x^2}-\left(k_1 A_1 G_1+\left(\frac{h_1^2}{4h_2^2}\right)k_2 A_2 G_2\right)\right]\theta_1$$
$$+\left[\left(\frac{\rho_2 A_2}{24}\right)\frac{\partial^2}{\partial t^2}-\left(\frac{E_2 A_2}{24}\right)\frac{\partial^2}{\partial x^2}-\left(\frac{k_2 A_2 G_2}{4h_2^2}\right)\right]h_1 h_3 \theta_3+\left(k_1 A_1 G_1-\left(\frac{h_1}{2h_2}\right)k_2 A_2 G_2\right)\frac{\partial w}{\partial x}=0 \tag{6.17}$$

$$\left[\left(\frac{\rho_2 A_2}{12}\right)\frac{\partial^2}{\partial t^2}-\left(\frac{E_2 A_2}{12}\right)\frac{\partial^2}{\partial x^2}-\left(\frac{k_2 A_2 G_2}{2h_2^2}\right)\right]h_3 u_1+\left[\left(\frac{\rho_2 A_2}{6}\right)\frac{\partial^2}{\partial t^2}-\left(\frac{E_2 A_2}{6}\right)\frac{\partial^2}{\partial x^2}+\left(\frac{k_2 A_2 G_2}{2h_2^2}\right)\right]h_3 u_3$$
$$+\left[\left(\frac{\rho_2 A_2}{24}\right)\frac{\partial^2}{\partial t^2}-\left(\frac{E_2 A_2}{24}\right)\frac{\partial^2}{\partial x^2}-\left(\frac{k_2 A_2 G_2}{4h_2^2}\right)\right]h_1 h_3 \theta_1+\left[-\left(\frac{h_3^2}{12}\rho_2 A_2+\rho_3 I_3\right)\frac{\partial^2}{\partial t^2}+\left(E_3 I_3+\frac{h_3^2 E_2 A_2}{12}\right)\frac{\partial^2}{\partial x^2}\right.$$
$$\left.-\left(\frac{h_3^2}{4h_2^2}k_2 A_2 G_2+k_3 A_3 G_3\right)\right]\theta_3-\left(\frac{h_3}{2h_2}k_2 A_2 G_2-k_3 A_3 G_3\right)\frac{\partial w}{\partial x}=0 \tag{6.18}$$

$$-\left(\frac{k_2 A_2 G_2}{h_2}\right)\frac{\partial u_1}{\partial x}+\left(\frac{k_2 A_2 G_2}{h_2}\right)\frac{\partial u_3}{\partial x}+\left(k_1 A_1 G_1-\frac{h_1}{2h_2}k_2 A_2 G_2\right)\frac{\partial \theta_1}{\partial x}+\left(-\frac{h_3}{2h_2}k_2 A_2 G_2+k_3 A_3 G_3\right)\frac{\partial \theta_3}{\partial x}$$
$$+\left[-(k_1 A_1 G_1+k_2 A_2 G_2+k_3 A_3 G_3)\frac{\partial^2}{\partial x^2}+M\frac{\partial^2}{\partial t^2}\right]w=0 \tag{6.19}$$

Note the symmetry of the differential operators in Eqs. (6.15) – (6.19).

The associated boundary conditions generated by Hamilton's principle are as follows. The axial forces in layers 1 and 3 (F_1 and F_3) are

$$F_1=-\left(E_1 A_1+\frac{E_2 A_2}{4}+\frac{E_2 I_2}{h_2^2}\right)\frac{\partial u_1}{\partial x}-\left(\frac{E_2 A_2}{4}-\frac{E_2 I_2}{h_2^2}\right)\frac{\partial u_3}{\partial x}-\left(\frac{h_1 E_2 A_2}{8}+\frac{h_1 E_2 I_2}{2h_2^2}\right)\frac{\partial \theta_1}{\partial x}-\left(-\frac{h_3 E_2 A_2}{8}+\frac{h_3 E_2 I_2}{2h_2^2}\right)\frac{\partial \theta_3}{\partial x} \tag{6.20}$$

$$F_3=-\left(\frac{E_2 A_2}{4}-\frac{E_2 I_2}{h_2^2}\right)\frac{\partial u_1}{\partial x}-\left(E_3 A_3+\frac{E_2 A_2}{4}+\frac{E_2 I_2}{h_2^2}\right)\frac{\partial u_3}{\partial x}-\left(\frac{h_1 E_2 A_2}{8}-\frac{h_1 E_2 I_2}{2h_2^2}\right)\frac{\partial \theta_1}{\partial x}-\left(\frac{h_3 E_2 A_2}{8}-\frac{h_3 E_2 I_2}{2h_2^2}\right)\frac{\partial \theta_3}{\partial x} \tag{6.21}$$

Note that each of the above two forces includes a contribution from layer 2.

The bending moments in layers 1 and 3 (M_1 and M_3) are

$$M_1=-\left(\frac{h_1 E_2 A_2}{8}+\frac{h_1 E_2 I_2}{2h_2^2}\right)\frac{\partial u_1}{\partial x}-\left(\frac{h_1 E_2 A_2}{8}-\frac{h_1 E_2 I_2}{2h_2^2}\right)\frac{\partial u_3}{\partial x}-\left(E_1 I_1+\frac{h_1^2 E_2 A_2}{16}+\frac{h_1^2 E_2 I_2}{4h_2^2}\right)\frac{\partial \theta_1}{\partial x}-\left(-\frac{h_1 h_3 E_2 A_2}{16}+\frac{h_1 h_3 E_2 I_2}{4h_2^2}\right)\frac{\partial \theta_3}{\partial x} \tag{6.22}$$

$$M_3=-\left(-\frac{h_3 E_2 A_2}{8}+\frac{h_3 E_2 I_2}{2h_2^2}\right)\frac{\partial u_1}{\partial x}-\left(-\frac{h_3 E_2 A_2}{8}-\frac{h_3 E_2 I_2}{2h_2^2}\right)\frac{\partial u_3}{\partial x}-\left(-\frac{h_1 h_3 E_2 A_2}{16}+\frac{h_1 h_3 E_2 I_2}{4h_2^2}\right)\frac{\partial \theta_1}{\partial x}-\left(E_3 I_3+\frac{h_3^2 E_2 A_2}{16}+\frac{h_3^2 E_2 I_2}{4h_2^2}\right)\frac{\partial \theta_3}{\partial x} \tag{6.23}$$

Note that each of the above two moments includes a contribution from layer 2.

117

The total shear force, S, in the y direction, is given by

$$S = -\left(k_1 A_1 G_1 + k_2 A_2 G_2 + k_3 A_3 G_3\right)\frac{\partial w}{\partial x} - \left(\frac{k_2 A_2 G_2}{h_2}\right)u_1 + \left(\frac{k_2 A_2 G_2}{h_2}\right)u_3$$
$$- \left(-k_1 A_1 G_1 + \frac{h_1 k_2 A_2 G_2}{2h_2}\right)\theta_1 - \left(-k_3 A_3 G_3 + \frac{h_3 k_2 A_2 G_2}{2h_2}\right)\theta_3 \tag{6.24}$$

Now for harmonic oscillation u_1, u_3, θ_1, θ_3 and w may be written in the following form

$$u_1 = U_1 e^{i\omega t}; \quad u_3 = U_3 e^{i\omega t}; \qquad \theta_1 = \Theta_1 e^{i\omega t}; \quad \theta_3 = \Theta_3 e^{i\omega t}; \quad w = We^{i\omega t} \tag{6.25}$$

where U_1, U_3, Θ_1, Θ_3 and W, are the amplitudes of u_1, u_3, θ_1, θ_3 and w, and ω is the angular (or circular) frequency of free vibration, and $i = \sqrt{-1}$

Substituting Eq. (6.25) into Eqs. (6.15)-(6.19) and introducing a non-dimensional length $\xi = x/L$ and writing $D = \frac{d}{d\xi}$ one obtains

$$\left(D^2 + a\right)U_1 + \left(bD^2 + c\right)U_3 + h_1\left(bD^2 + e\right)\Theta_1 - \frac{h_3}{2}\left(bD^2 + c\right)\Theta_3 - \left(fD\right)W = 0 \tag{6.26}$$

$$\left(bD^2 + c\right)U_1 + \left(gD^2 + h\right)U_3 + \frac{h_1}{2}\left(bD^2 + c\right)\Theta_1 - h_3\left(bD^2 + e\right)\Theta_3 + \left(fD\right)W = 0 \tag{6.27}$$

$$\left(bD^2 + e\right)U_1 + \frac{1}{2}\left(bD^2 + c\right)U_3 + h_1\left(zD^2 + m\right)\Theta_1 - \frac{h_3}{4}\left(bD^2 + c\right)\Theta_3 + \left(nD\right)W = 0 \tag{6.28}$$

$$-\frac{1}{2}\left(bD^2 + c\right)U_1 - \left(bD^2 + e\right)U_3 - \frac{h_1}{4}\left(bD^2 + c\right)\Theta_1 + h_3\left(pD^2 + q\right)\Theta_3 - \left(rD\right)W = 0 \tag{6.29}$$

$$-\left(fD\right)U_1 + \left(fD\right)U_3 + h_1\left(nD\right)\Theta_1 - h_3\left(rD\right)\Theta_3 - \left(sD^2 + t\right)W = 0 \tag{6.30}$$

where a, b, c, e etc are non-dimensional quantities dependent on the sandwich beam parameters and are defined in Appendix B.

By extensive algebraic manipulation the differential equations (6.26)-(6.30) can be combined into a single tenth order differential equation satisfied by U_1, U_3, Θ_1, Θ_3 and W as follows.

$$\left(D^{10} + \mu_1 D^8 + \mu_2 D^6 + \mu_3 D^4 + \mu_4 D^2 + \mu_5\right)\Phi = 0 \tag{6.31}$$

where $\Phi = U_1$, or U_3, or Θ_1, or Θ_3, or W.

The coefficients $\mu_j (j = 1, 2, ..., 5)$ are given by

$$\mu_1 = \frac{\eta_2}{\eta_1} ; \qquad \mu_2 = \frac{\eta_3}{\eta_1} ; \qquad \mu_3 = \frac{\eta_4}{\eta_1} ; \qquad \mu_4 = \frac{\eta_5}{\eta_1} ; \qquad \mu_5 = \frac{\eta_6}{\eta_1} \qquad (6.32)$$

with

$$\left. \begin{array}{l} \eta_1 = sA_1 \\[6pt] \eta_2 = b^2 A_2 + b^3 A_3 + 4b^2 sA_4 + b^2 fA_5 + b^2 gA_6 + 4b^2 A_7 + 2bA_8 + A_9 \\[6pt] \eta_3 = 4b^2 sB_1 + 4b^3 tB_2 + b^2 fB_3 + 4aB_4 + 4b^2 B_5 + 4bcB_6 + 4beB_7 + 8bB_8 + 4cB_9 + C_1 \\[6pt] \eta_4 = 4abC_2 + 4aC_3 + 4bcC_4 + C_5 + 4bC_6 + 4c^2 C_7 + 4cC_8 + 16eC_9 + D_1 \end{array} \right\} \qquad (6.33)$$

$$\eta_5 = 4aD_2 + 4bD_3 + 4c^2 D_4 + 4cD_5 + D_6$$

$$\eta_6 = tD_7$$

where A_1-A_9, B_1-B_9 and C_1 –C_9 are defined in Appendix C

The differential equation (6.31) is linear with constant coefficients so that the solution can be assumed in the form

$$X = X_0 e^{r\xi} \qquad (6.34)$$

Substituting Eq. (10.34) into Eq. (10.31) gives the auxiliary equation as follow

$$\lambda^{10} + \mu_1 \lambda^8 + \mu_2 \lambda^6 + \mu_3 \lambda^4 + \mu_4 \lambda^2 + \mu_5 = 0 \qquad (6.35)$$

The above equation is a quintic in $p = \lambda^2$, namely

$$p^5 + \mu_1 p^4 + \mu_2 p^3 + \mu_3 p^2 + \mu_4 p + \mu_5 = 0 \qquad (6.36)$$

which can be solved in a routine way.

Some pair or pairs of complex roots may occur, but as U_1, U_3, Θ_1, Θ_3 and W are all real, the associated coefficients; say X_j in the solution for $X = \sum_{j=1}^{10} X_j e^{r_j \xi}$ will also be complex. As complex roots occur only in conjugate pairs, the associated X_j will also occur in conjugate pairs.

Thus, the solution for U_1, U_3, Θ_1, Θ_3 and W can be written as

$$U_1 = \sum_{j=1}^{10} P_j e^{r_j \xi} ; \quad U_3 = \sum_{j=1}^{10} Q_j e^{r_j \xi} ; \quad \Theta_1 = \sum_{j=1}^{10} R_j e^{r_j \xi} ; \quad \Theta_3 = \sum_{j=1}^{10} S_j e^{r_j \xi} ; \quad W = \sum_{j=1}^{10} T_j e^{r_j \xi} \qquad (6.37)$$

where $r_j (j = 1, 2...10)$ are the 10 roots of the auxiliary equation and P_j, Q_j, R_j, S_j and T_j, $(j = 1,2...10)$ are five sets of ten, possibly complex, constants.

By substituting Eq. (6.37) into Eqs. (6.26)–(6.30) it can be shown that the constants P_j, Q_j, R_j and S_j are related to T_j as follows so that the responses U_1, U_3, Θ_1, Θ_3 and W are linear combination of T_j.

$$P_j = \alpha_j T_j; \qquad Q_j = \beta_j T_j; \qquad R_j = \gamma_j T_j; \qquad S_j = \eta_j T_j \tag{6.38}$$

where $\alpha_j, \beta_j, \gamma_j$ and η_j can be expressed directly from the five differential equations (6.26)-(6.30) and by applying Cramer's rule to the following relationship for the determination of P_j, Q_j, R_j and S_j, see Appendix D.

$$
\begin{bmatrix}
(r_j^2 + a) & (br_j^2 + c) & (br_j^2 + e) & -\frac{1}{2}(br_j^2 + c) \\
(br_j^2 + c) & (gr_j^2 + h) & \frac{1}{2}(br_j^2 + c) & -(br_j^2 + e) \\
(br_j^2 + e) & \frac{1}{2}(br_j^2 + c) & (zr_j^2 + m) & -\frac{1}{4}(br_j^2 + c) \\
-\frac{1}{2}(br_j^2 + c) & -(br_j^2 + e) & -\frac{1}{4}(br_j^2 + c) & (pr_j^2 + q)
\end{bmatrix}
\times
\begin{bmatrix}
P_j \\ Q_j \\ R_j \\ S_j
\end{bmatrix}
=
\begin{bmatrix}
fr_j \\ -fr_j \\ -nr_j \\ rr_j
\end{bmatrix}
T_j
\tag{6.39}
$$

The expressions for the amplitudes of the axial forces in layer 1 and 3 (F_1 and F_3), the shear force across the cross-section (S) and the bending moments in layers 1 and 3 (M_1 and M_3) are given in Eqs. (6.20) – (6.24). With the help of Eqs. (6.37) and (6.38) it can be shown that the loads $F_1(\xi), F_3(\xi), M_1(\xi), M_3(\xi)$ and $S(\xi)$ are also linear combinations of T_j. Noting that these forces and moments vary harmonically during vibratory motion in the same way as the displacements and rotations, so that they are (as functions of the variable $\xi = x/L$) given by

$$
\begin{aligned}
F_1(\xi) = \sum_{j=1}^{10} -&\left\{ \frac{r_j \alpha_j}{L}\left(E_1 A_1 + \frac{1}{4}E_2 A_2 + \frac{1}{h_2^2}E_2 I_2 \right) + \frac{r_j \beta_j}{L}\left(\frac{1}{4}E_2 A_2 - \frac{1}{h_2^2}E_2 I_2 \right) \right. \\
&\left. + \frac{r_j \gamma_j}{L}\left(\frac{1}{8}h_1 E_2 A_2 + \frac{h_1}{2h_2^2}E_2 I_2 \right) + \frac{r_j \eta_j}{L}\left(-\frac{1}{8}h_3 E_2 A_2 + \frac{h_3}{2h_2^2}E_2 I_2 \right) \right\} e^{r_j \xi} T_j
\end{aligned}
\tag{6.40}
$$

$$
\begin{aligned}
F_3(\xi) = \sum_{j=1}^{10} -&\left\{ \frac{r_j \alpha_j}{L}\left(\frac{1}{4}E_2 A_2 - \frac{1}{h_2^2}E_2 I_2 \right) + \frac{r_j \beta_j}{L}\left(E_3 A_3 + \frac{1}{4}E_2 A_2 + \frac{1}{h_2^2}E_2 I_2 \right) \right. \\
&\left. + \frac{r_j \gamma_j}{L}\left(\frac{h_1}{8}E_2 A_2 - \frac{h_1}{2h_2^2}E_2 I_2 \right) + \frac{r_j \eta_j}{L}\left(-\frac{1}{8}h_3 E_2 A_2 - \frac{h_3}{2h_2^2}E_2 I_2 \right) \right\} e^{r_j \xi} T_j
\end{aligned}
\tag{6.41}
$$

$$
\begin{aligned}
M_1(\xi) = \sum_{j=1}^{10} -&\left\{ \frac{r_j \alpha_j}{L}\left(\frac{h_1}{8}E_2 A_2 + \frac{h_1}{2h_2^2}E_2 I_2 \right) + \frac{r_j \beta_j}{L}\left(\frac{h_1}{8}E_2 A_2 - \frac{h_1}{2h_2^2}E_2 I_2 \right) \right. \\
&\left. + \frac{r_j \gamma_j}{L}\left(E_1 I_1 + \frac{h_1^2}{16}E_2 A_2 + \frac{h_1^2}{4h_2^2}E_2 I_2 \right) + \frac{r_j \eta_j}{L}\left(-\frac{h_1 h_3}{16}E_2 A_2 + \frac{h_1 h_3}{4h_2^2}E_2 I_2 \right) \right\} e^{r_j \xi} T_j
\end{aligned}
\tag{6.42}
$$

$$M_3(\xi) = \sum_{j=1}^{10} - \left\{ \frac{r_j \alpha_j}{L}\left(-\frac{h_3}{8}E_2A_2 + \frac{h_3}{2h_2{}^2}E_2I_2 \right) + \frac{r_j\beta_j}{L}\left(-\frac{h_3}{8}E_2A_2 - \frac{h_3}{2h_2{}^2}E_2I_2 \right) \right.$$
$$\left. + \frac{r_j\gamma_j}{L}\left(-\frac{h_1h_3}{16}E_2A_2 + \frac{h_1h_3}{4h_2{}^2}E_2I_2 \right) + \frac{r_j\eta_j}{L}\left(E_3I_3 + \frac{h_3{}^2}{16}E_2A_2 + \frac{h_3{}^2}{4h_2{}^2}E_2I_2 \right) \right\} e^{r_j\xi} T_j \qquad (6.43)$$

$$S(\xi) = \sum_{j=1}^{10} - \left\{ \frac{r_j}{L}(k_1A_1G_1 + k_2A_2G_2 + k_3A_3G_3) + \alpha_j\left(\frac{k_2A_2G_2}{h_2} \right) - \beta_j\left(\frac{k_2A_2G_2}{h_2} \right) \right.$$
$$\left. + \gamma_j\left(-k_1A_1G_1 + \frac{h_1k_2A_2G_2}{2h_2} \right) + \eta_j\left(-k_3A_3G_3 + \frac{h_3k_2A_2G_2}{2h_2} \right) \right\} e^{r_j\xi} T_j \qquad (6.44)$$

6.2.2   Formulation of the dynamic stiffness matrix

The amplitudes of the responses and loads of the freely vibrating sandwich beam are given by Eqs. (6.37) and (6.40)-(6.44), respectively which can now be related by the dynamic stiffness matrix on eliminating the arbitrary constants T_j ($j = 1, 2, 3,\ldots.10$). Referring to Figure 10.2 the boundary conditions for responses and loads of the sandwich beam are as follows.

At the left hand end, $\xi = 0$ ($x = 0$), the responses are $U_1(0)$, $U_3(0)$, $\Theta_1(0)$, $\Theta_3(0)$ and $W(0)$. The corresponding responses at the right hand end, $\xi = 1$ ($x = L$), are $U_1(1)$, $U_3(1)$, $\Theta_1(1)$, $\Theta_3(1)$ and $W(1)$, see Figure 6.2. By substituting $\xi = 0$ and $\xi = 1$ in Eq (10.37), these boundary conditions give

$$U_1(0) = \sum_{j=1}^{10} P_j \; ; \; U_3(0) = \sum_{j=1}^{10} Q_j \; ; \; \Theta_1(0) = \frac{1}{L}\sum_{j=1}^{10} R_j \; ; \; \Theta_3(0) = \frac{1}{L}\sum_{j=1}^{10} S_j \; ; \; W(0) = \sum_{j=1}^{10} T_j \qquad (6.45)$$

$$U_1(1) = \sum_{j=1}^{10} P_j e^{r_j} \; ; U_3(1) = \sum_{j=1}^{10} Q_j e^{r_j\xi} \; ; \Theta_1(1) = \frac{1}{L}\sum_{j=1}^{10} R_j e^{r_j} \; ; \Theta_3(1) = \frac{1}{L}\sum_{j=1}^{10} S_j e^{r_j} \; ; \; W(1) = \sum_{j=1}^{10} T_j e^{r_j} \qquad (6.46)$$
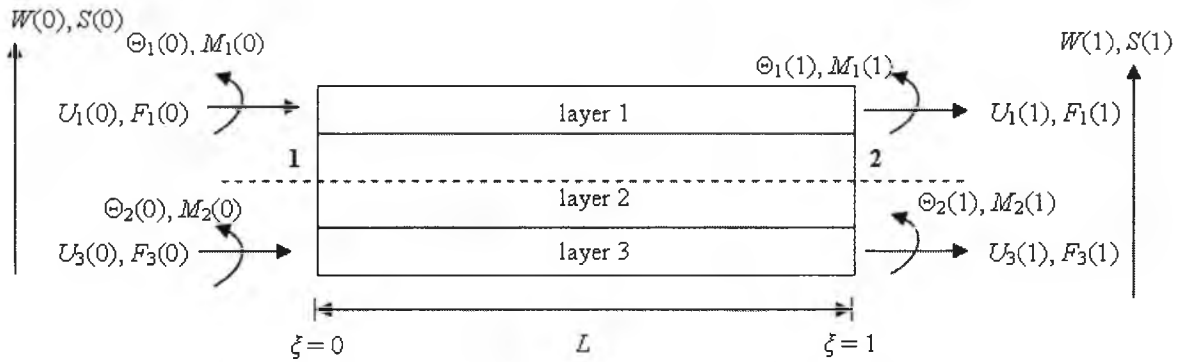
Figure 6.2   End conditions for responses and loads for the three-layered sandwich beam

Equations (6.45) and (6.46) can be written in the following matrix form and by using Eq. (6.38) and simply referring the state vector of response $U_1(0)$, $U_3(0)$, $\Theta_1(0)$, $\Theta_3(0)$, $W(0)$, $U_1(1)$, $U_3(1)$, $\Theta_1(1)$, $\Theta_3(1)$ and $W(1)$, to only one set of arbitrary constants T_j as follows.

$$
\begin{bmatrix}
U_1(0) \\
U_3(0) \\
\Theta_1(0) \\
\Theta_3(0) \\
W(0) \\
U_1(1) \\
U_3(1) \\
\Theta_1(1) \\
\Theta_3(1) \\
W(1)
\end{bmatrix}
=
\begin{bmatrix}
\alpha_1 & \alpha_2 & \alpha_3 & \alpha_4 & \alpha_5 & \alpha_6 & \alpha_7 & \alpha_8 & \alpha_9 & \alpha_{10} \\
\beta_1 & \beta_2 & \beta_3 & \beta_4 & \beta_5 & \beta_6 & \beta_7 & \beta_8 & \beta_9 & \beta_{10} \\
\gamma_1 & \gamma_2 & \gamma_3 & \gamma_4 & \gamma_5 & \gamma_6 & \gamma_7 & \gamma_8 & \gamma_9 & \gamma_{10} \\
\eta_1 & \eta_2 & \eta_3 & \eta_4 & \eta_5 & \eta_6 & \eta_7 & \eta_8 & \eta_9 & \eta_{10} \\
1 & 1 & 1 & 1 & 1 & 1 & 1 & 1 & 1 & 1 \\
\alpha_1 e^{r1} & \alpha_2 e^{r2} & \alpha_3 e^{r3} & \alpha_4 e^{r4} & \alpha_5 e^{r5} & \alpha_6 e^{r6} & \alpha_7 e^{r7} & \alpha_8 e^{r8} & \alpha_9 e^{r9} & \alpha_{10} e^{r10} \\
\beta_1 e^{r1} & \beta_2 e^{r2} & \beta_3 e^{r3} & \beta_4 e^{r4} & \beta_5 e^{r5} & \beta_6 e^{r6} & \beta_7 e^{r7} & \beta_8 e^{r8} & \beta_9 e^{r9} & \beta_{10} e^{r10} \\
\gamma_1 e^{r1} & \gamma_2 e^{r2} & \gamma_3 e^{r3} & \gamma_4 e^{r4} & \gamma_5 e^{r5} & \gamma_6 e^{r6} & \gamma_7 e^{r7} & \gamma_8 e^{r8} & \gamma_9 e^{r9} & \gamma_{10} e^{r10} \\
\eta_1 e^{r1} & \eta_2 e^{r2} & \eta_3 e^{r3} & \eta_4 e^{r4} & \eta_5 e^{r5} & \eta_6 e^{r6} & \eta_7 e^{r7} & \eta_8 e^{r8} & \eta_9 e^{r9} & \eta_{10} e^{r10} \\
e^{r1} & e^{r2} & e^{r3} & e^{r4} & e^{r5} & e^{r6} & e^{r7} & e^{r8} & e^{r9} & e^{r10}
\end{bmatrix}
\times
\begin{bmatrix}
T_1 \\
T_2 \\
T_3 \\
T_4 \\
T_5 \\
T_6 \\
T_7 \\
T_8 \\
T_9 \\
T_{10}
\end{bmatrix}
\tag{6.47}
$$

or

$$\delta = QT \tag{6.48}$$

where δ and $\mathbf{T}$ are displacement and constant vectors respectively and $\mathbf{Q}$ is the 10×10 square matrix given above.

Similarly at the left hand end, $\xi = 0\,(x = 0)$, the loads are $F_1\,(0)$, $F_3\,(0)$, $M_1\,(0)$, $M_3\,(0)$ and $S\,(0)$, and the corresponding loads at the right hand end at $\xi = 1\,(x = L)$, are $F_1\,(1)$, $F_3\,(1)$, $M_1\,(1)$, M_3 (1) and $S\,(1)$, see Figure 6.2. By substituting $\xi = 0$ and 1 in Eqs. (6.40)-(6.44), and noting that the signs for the forces must be reversed at the right hand end as a consequence of the convention, these boundary conditions give the following matrix relationship.

$$
\begin{bmatrix} F_{11} \\ F_{31} \\ M_{11} \\ M_{31} \\ S_1 \\ F_{12} \\ F_{32} \\ M_{12} \\ M_{32} \\ S_2 \end{bmatrix} =
\begin{bmatrix}
a_{11} & a_{12} & a_{13} & a_{14} & a_{15} & a_{16} & a_{17} & a_{18} & a_{19} & a_{110} \\
a_{21} & a_{22} & a_{23} & a_{24} & a_{25} & a_{26} & a_{27} & a_{28} & a_{29} & a_{210} \\
a_{31} & a_{32} & a_{33} & a_{34} & a_{35} & a_{36} & a_{37} & a_{38} & a_{39} & a_{310} \\
a_{41} & a_{42} & a_{43} & a_{44} & a_{45} & a_{46} & a_{47} & a_{48} & a_{49} & a_{410} \\
a_{51} & a_{52} & a_{53} & a_{54} & a_{55} & a_{56} & a_{57} & a_{58} & a_{59} & a_{510} \\
a_{61} & a_{62} & a_{63} & a_{64} & a_{65} & a_{66} & a_{67} & a_{68} & a_{69} & a_{610} \\
a_{71} & a_{72} & a_{73} & a_{74} & a_{75} & a_{76} & a_{77} & a_{78} & a_{79} & a_{710} \\
a_{81} & a_{82} & a_{83} & a_{84} & a_{85} & a_{86} & a_{87} & a_{88} & a_{89} & a_{810} \\
a_{91} & a_{92} & a_{93} & a_{94} & a_{95} & a_{96} & a_{97} & a_{98} & a_{99} & a_{910} \\
a_{101} & a_{102} & a_{103} & a_{104} & a_{105} & a_{106} & a_{107} & a_{108} & a_{109} & a_{1010}
\end{bmatrix} \times
\begin{bmatrix} T_1 \\ T_2 \\ T_3 \\ T_4 \\ T_5 \\ T_6 \\ T_7 \\ T_8 \\ T_9 \\ T_{10} \end{bmatrix}
\tag{6.49}
$$

or

$$\mathbf{F = RT} \tag{6.50}$$

where $\mathbf{F}$ is the state vector of loads, $\mathbf{T}$ is the vector of constants and the elements of the 10×10 square matrix $\mathbf{R}$ are as follows.

$$
\left.
\begin{aligned}
a_{1j} = & -\frac{r_j \alpha_j}{L}\left(E_1 A_1 + \frac{1}{4}E_2 A_2 + \frac{1}{h_2{}^2}E_2 I_2 \right) - \frac{r_j \beta_j}{L}\left(\frac{1}{4}E_2 A_2 - \frac{1}{h_2{}^2}E_2 I_2 \right) \\
& -\frac{r_j \gamma_j}{L}\left(\frac{1}{8}h_1 E_2 A_2 + \frac{h_1}{2h_2{}^2}E_2 I_2 \right) - \frac{r_j \eta_j}{L}\left(-\frac{1}{8}h_3 E_2 A_2 + \frac{h_3}{2h_2{}^2}E_2 I_2 \right)
\end{aligned}
\right\}
\tag{6.51}
$$

$$
\left.
\begin{aligned}
a_{2j} = & -\frac{r_j \alpha_j}{L}\left(\frac{1}{4}E_2 A_2 - \frac{1}{h_2{}^2}E_2 I_2 \right) - \frac{r_j \beta_j}{L}\left(E_3 A_3 + \frac{1}{4}E_2 A_2 + \frac{1}{h_2{}^2}E_2 I_2 \right) \\
& -\frac{r_j \gamma_j}{L}\left(\frac{h_1}{8}E_2 A_2 - \frac{h_1}{2h_2{}^2}E_2 I_2 \right) - \frac{r_j \eta_j}{L}\left(-\frac{1}{8}h_3 E_2 A_2 - \frac{h_3}{2h_2{}^2}E_2 I_2 \right)
\end{aligned}
\right\}
\tag{6.52}
$$

$$
\left.
\begin{aligned}
a_{3j} = & -\frac{r_j \alpha_j}{L}\left(\frac{h_1}{8}E_2 A_2 + \frac{h_1}{2h_2{}^2}E_2 I_2 \right) - \frac{r_j \beta_j}{L}\left(\frac{h_1}{4}E_2 A_2 - \frac{h_1}{2h_2{}^2}E_2 I_2 \right) \\
& -\frac{r_j \gamma_j}{L}\left(E_1 I_1 + \frac{h_1{}^2}{16}E_2 A_2 + \frac{h_1{}^2}{4h_2{}^2}E_2 I_2 \right) - \frac{r_j \eta_j}{L}\left(-\frac{h_1 h_3}{16}E_2 A_2 + \frac{h_1 h_3}{4h_2{}^2}E_2 I_2 \right)
\end{aligned}
\right\}
\tag{6.53}
$$

$$a_{4j} = -\frac{r_j \alpha_j}{L}\left(-\frac{h_3}{8}E_2A_2 + \frac{h_3}{2h_2^2}E_2I_2\right) - \frac{r_j \beta_j}{L}\left(-\frac{h_3}{8}E_2A_2 - \frac{h_3}{2h_2^2}E_2I_2\right)$$
$$\left.- \frac{r_j \gamma_j}{L}\left(-\frac{h_1 h_3}{16}E_2A_2 + \frac{h_1 h_3}{4h_2^2}E_2I_2\right) - \frac{r_j \eta_j}{L}\left(E_3I_3 + \frac{h_3^2}{16}E_2A_2 + \frac{h_3^2}{4h_2^2}E_2I_2\right)\right\}$$

(6.54)

$$a_{5j} = -\frac{r_j}{L}\left(k_1A_1G_1 + k_2A_2G_2 + k_3A_3G_3\right) - \alpha_j\left(\frac{k_2A_2G_2}{h_2}\right) + \beta_j\left(\frac{k_2A_2G_2}{h_2}\right)$$
$$\left.- \gamma_j\left(-k_1A_1G_1 + \frac{h_1k_2A_2G_2}{2h_2}\right) - \eta_j\left(-k_3A_3G_3 + \frac{h_3k_2A_2G_2}{2h_2}\right)\right\}$$

(6.55)

$$a_{6j} = -a_{1j}e^{r_j} \;;\quad a_{7j} = -a_{2j}e^{r_j} \;;\quad a_{8j} = -a_{3j}e^{r_j} \;;\quad a_{9j} = -a_{4j}e^{r_j} \;;\quad a_{10j} = -a_{5j}e^{r_j}$$

(6.56)-(6.60)

where $j = 1, 2, 3, \ldots\ldots\ldots 10$.

The dynamic stiffness matrix can now be formulated by eliminating $\mathbf{T}$ from the Eqs. (6.48) and (6.50) to give

$$F = R\,Q^{-1}\delta = K\,\delta$$

(6.61)

where

$$K = R\,Q^{-1}$$

(6.62)

is the required dynamic stiffness matrix.

6.3 Application of the dynamic stiffness matrix and numerical results

The above dynamic stiffness matrix can now be used to compute the natural frequencies and mode shapes of either a single three-layered sandwich beam or an assembly of such beams, for example a continuous sandwich beam on multiple supports. An accurate and reliable method of calculating the natural frequencies and mode shapes is to apply the algorithm of Wittrick and Williams [6.9, 6.10] to the dynamic stiffness matrix. The algorithm is simple to use and relies principally on the Sturm sequence property of the dynamic stiffness to converge on any natural frequency with certainty. It has featured in literally hundreds of papers the details of which are

not repeated here, but for further insight interested readers are referred to the original work of Wittrick and Williams [6.9, 6.10].

First of all, for illustrative purposes two examples of a three-layered sandwich beam are provided to compare results obtained from the present theory to the ones computed using earlier (and simpler) theories. The first example is a three-layered sandwich beam of length 0.5m with rectangular cross-section. The top and bottom layers are made of steel with thicknesses 15 mm and 10mm respectively, whereas the middle layer is of rubber material with thickness 20 mm. The width is 40 mm for all layers. The properties used for steel and rubber are as follows with the suffix s denoting the properties for steel and the suffix r denoting the properties for rubber: $E_s = 210GPa$, $G_s = 800GPa$, $\rho_s = 7850 kg/m^3$, $E_r = 1.5MPa$, $G_r = 0.5MPa$ and $\rho_r = 950 kg/m^3$. The shear correction or shape factor used in the analysis for each layer is set to 2/3 which is generally used for a rectangular cross-section. The second example is similar to the first one except that only the central layer (i.e. the core) which was rubber in the first example, is now replaced by lead with material properties (using suffix l): $E_l = 16GPa$, $G_l = 5.5GPa$ and $\rho_l = 11100 kg/m^3$.

The complete set of data used in the analysis for the two illustrative examples is shown in Table 6.1 for interested readers who wish to develop the present theory further or wish to check their own theories. The first four natural frequencies of the two examples, with cantilever end conditions, are shown in Table 6.2 together with the results obtained by using the earlier theory of Banerjee and Sobey [6.8]. The differences in the natural frequencies are quite small. This is to be expected because of the relatively important role played by the core which is modelled as a Timoshenko beam both in the present theory as well as in the earlier theory of Banerjee and Sobey [6.8]. The main difference between the present theory and the earlier theory is essentially in the modelling of the top and bottom layers for which the effects of both shear deformation and rotatory inertia are included in the present theory, whereas only the effects of rotatory inertia are included in the earlier theory. For the results of the two examples shown in Table 6.2, shear deformation of the face layers is not expected to have any major effect.

Table 6.1   Data used for computation of natural frequencies and mode shapes of examples 1 and 2

Properties	Layer 1 (Steel)	Layer 2 (Rubber) Example 1	Layer 2 (Lead) Example 2	Layer 3 (Steel)
b (m)	0.04	0.04	0.04	0.04
h (m)	0.015	0.02	0.02	0.01
A (m^2)	0.0006	0.0008	0.0008	0.0004
I (m^4)	1.125×10^{-08}	2.67×10^{-08}	2.67×10^{-08}	3.33×10^{-09}
G (GPa)	80	0.0005	5.5	80
E (GPa)	210	0.0015	16	210
ρ (kg/m^3)	7850	950	11100	7850
k	2/3	2/3	2/3	2/3
EA (N)	1.26×10^8	1.20×10^3	1.28×10^7	8.40×10^7
EI (Nm^2)	2.36×10^3	4.00×10^{-2}	4.27×10^2	7.00×10^2
kAG (N)	3.20×10^7	2.67×10^3	2.93×10^6	2.13×10^7
ρA (kg/m)	4.71	0.76	8.88	3.14
ρI (kgm)	8.83125×10^{-5}	2.53×10^{-5}	0.000296	2.62×10^{-5}

Table 6.2   Natural frequencies of a three-layered sandwich beam with cantilever end conditions.

Frequency No.	Natural frequencies (rad/s)			
	Example 1		Example 2	
	Using the theory of Banerjee and Sobey [6.8]	Present Theory	Using the theory of Banerjee and Sobey [6.8]	Present Theory
1	291.687	291.50	776.09	776.4
2	1691.39	1684.48	3880.57	3841.1
3	4669.07	4623.98	8899.37	8753.1
4	9104.77	8945.18	11461.7	11459.2

Figures 6.3 and 6.4 illustrate the first four natural frequencies and mode shapes of the two cantilever sandwich beams. The results reveal some interesting features. For the first example the modes are all dominated by flexure (W displacement). This occurs because of the soft core and strong face materials. The fundamental mode exhibits flexural displacement associated with small axial displacements (U_1 and U_3) of the face layers that are moving in opposite directions. The second and third modes have similar trends, but the fourth mode is a pure flexural one. In the second example, where the central core is replaced by lead, the first three modes are similar to the ones shown for the first example so that the free vibratory motion is predominantly flexural. However, the fourth mode is purely axial with U_1 and U_3 displacements in the same direction, but no flexural motion. (Note that the two graphs shown in Figure 6.4 and Figure 6.5 for U_1 and U_3 in the fourth mode are coincident.) This is in sharp contrast to the fourth mode of the first example. The high density and low Young's modulus of lead used for the core in the second example is the main reason for this type of mode. This is in accord with the earlier investigation carried out by Banerjee and Sobey [6.8].
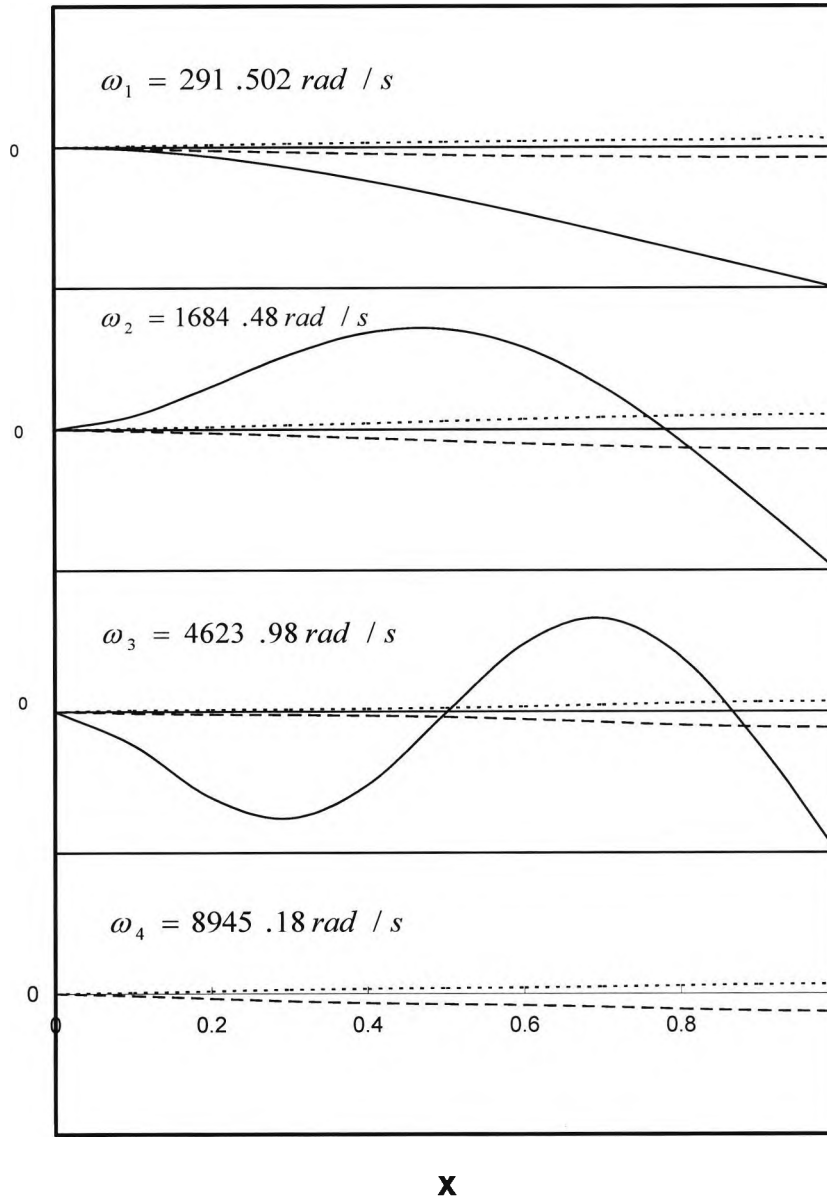
Figure 6.3 Natural frequencies and mode shapes of the three-layered sandwich beam of Example 1 (....) U_1; (---) U_3; (-) W
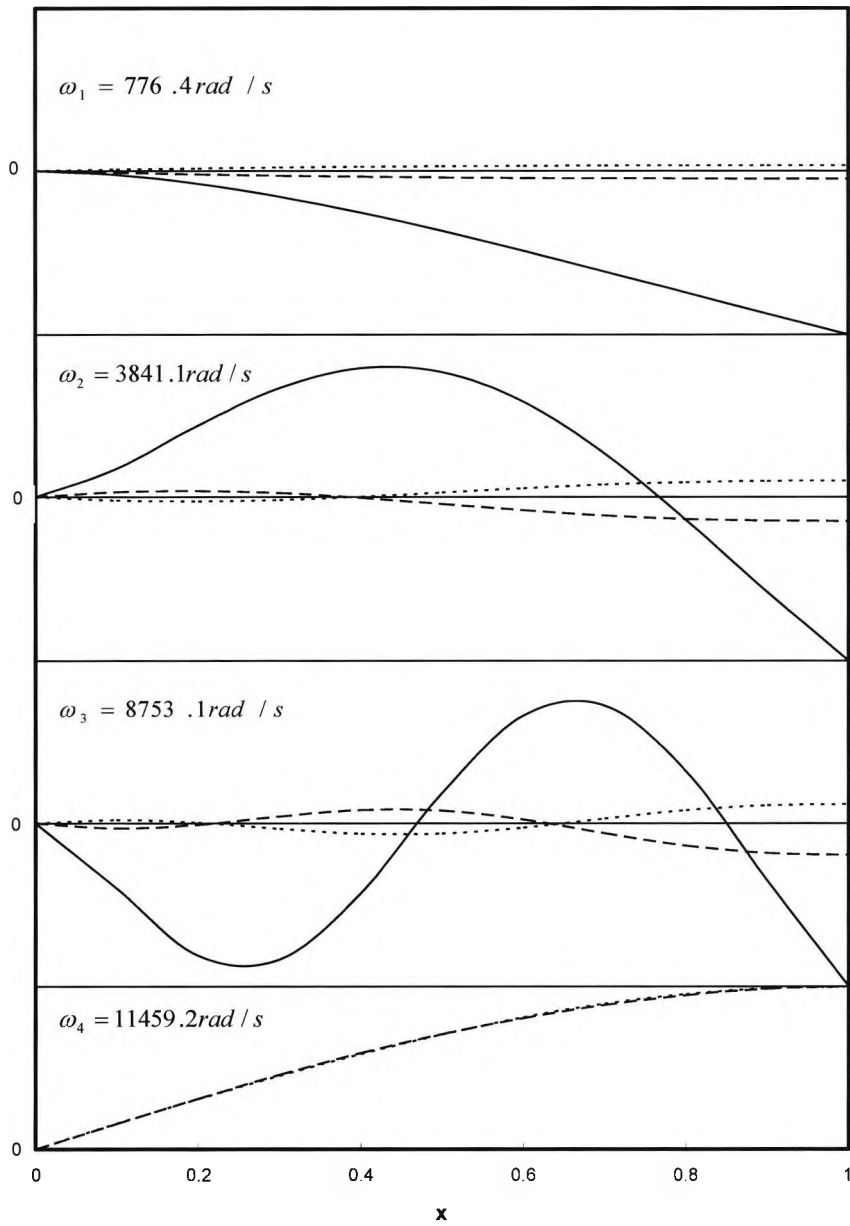
Figure 6.4   Natural frequencies and mode shapes of the three-layered sandwich beam of Example 2 (....)

U_1; (---)U_3; (-) W

129
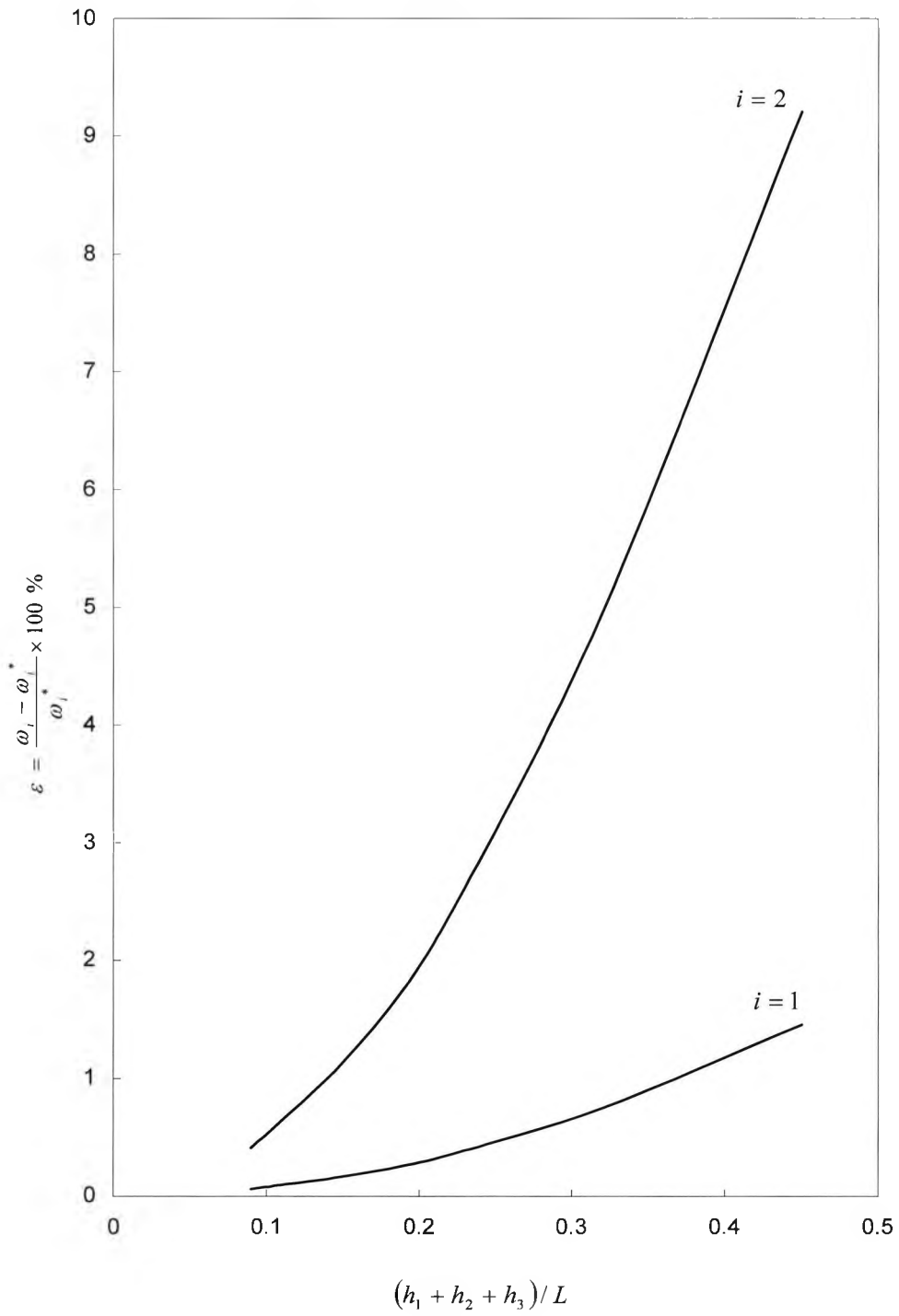
Figure 6.5   The plot of error against h/L **of Example 1**
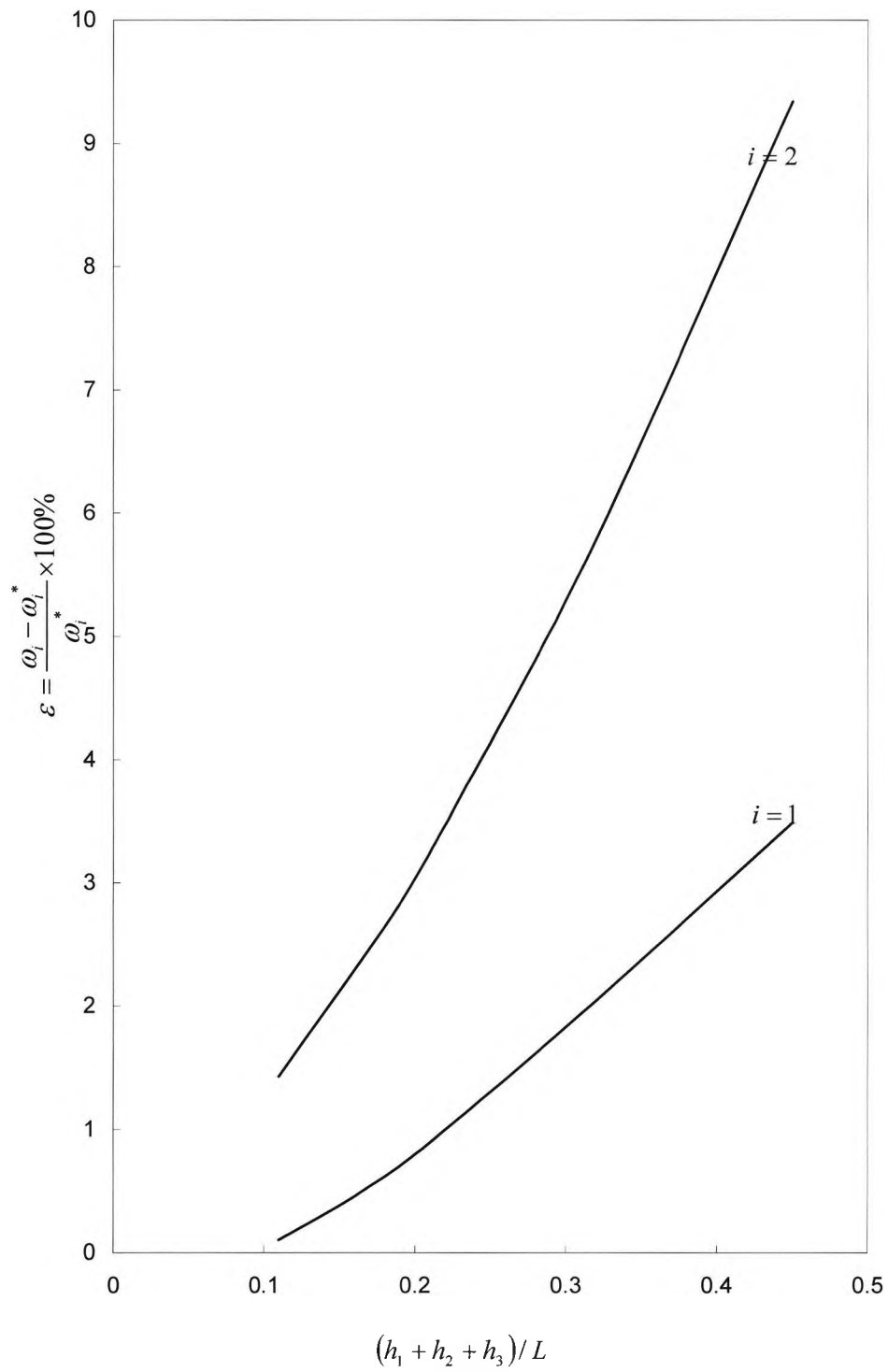
Figure 6.6   The plot of error against h/L of Example 2

6.4   Modal testing of sandwich beam samples and the ANSYS finite element analysis

Experimental measurements of natural frequencies of three sandwich beam samples have been carried out using an impulse hammer kit with its associated software for data capturing and analysis. The beam samples are fabricated from aluminium, steel and rubber sheets that are pre-treated and polished first. Later they are degreased using acetone for 2 minutes before applying the adhesive (Araldite 2011). The surfaces are then dried and the adhesive applied evenly using a glue gun on the rubber surface, and the metal skin is laid on top for each side at a time. This is repeated for the other side of the rubber after allowing for 24 hours of curing time. Once the adhesive is applied the sandwich samples are cured for a further period of 24 hours in a press. Basically, the samples are laid on the base of the press between two thick metal plates to ensure pressure is distributed evenly all through the structure. The finished products are (with thicknesses shown in parentheses): (i) aluminium (2 mm)–rubber (18 mm)–aluminium (2 mm), (ii) steel (1.5 mm)–rubber (18 mm)–steel (2.4 mm), and (iii) steel (1.5 mm)–rubber (18 mm)–aluminium (2 mm), sandwich beams of length 500 mm and width 50 mm for each.

The experimental modal testing set up using the impact hammer kit consisting of a PC driven ACE dynamic signal analyser and an accelerometer is shown in Figure 6.7. All test specimens were cantilevered with one end fully built-in in order to prevent all displacements. The accelerometer is set at a fixed position on the test specimen, which is considered to be the reference point while the impact hammer is used at a number of points to generate the excitation forces on the test specimen, corresponding to the degrees of freedom allowed in the model. The location of the driving and measurement points is carefully chosen to identify all important modes of vibration of the structure within the desired frequency range. The transfer function between the driving force and the resulting response is computed using the data obtained during the measurement. Sandwich test specimens are excited at specified grid points that define the number of degrees of freedom of the structure. The Dynamic Signal Analyser system is used to extract force and signal response from the structure under test. The response signals recorded by the accelerometer attached to the test specimen and the force signals recorded by the force transducer fitted inside the hammerhead are averaged from three repeated excitations and measurements at each location. The signal analyser further processes these signals and the frequency response functions (FRFs) are plotted against frequency from which the natural frequencies are identified (Figure 6.8 and Figure 6.9). The first three

measured natural frequencies of the above three specimens (except for the third natural frequency of sample 3 which apparently did not show any peak) are shown in Table 6.3 alongside those calculated using the present theory as well as using the commercially available software ANSYS22. Eight-node tetrahedral structural solid element SOLID 45 was used for the finite element analyses. The element has three degrees of freedom at each node: translations in the nodal x, y, and z directions. Mesh refinement was performed until the changes in the results were sufficiently small. A representative meshed sandwich beam having 2,042 elements and 642 nodes is shown in Figure 6.10. Reduced method was used for mode extraction.
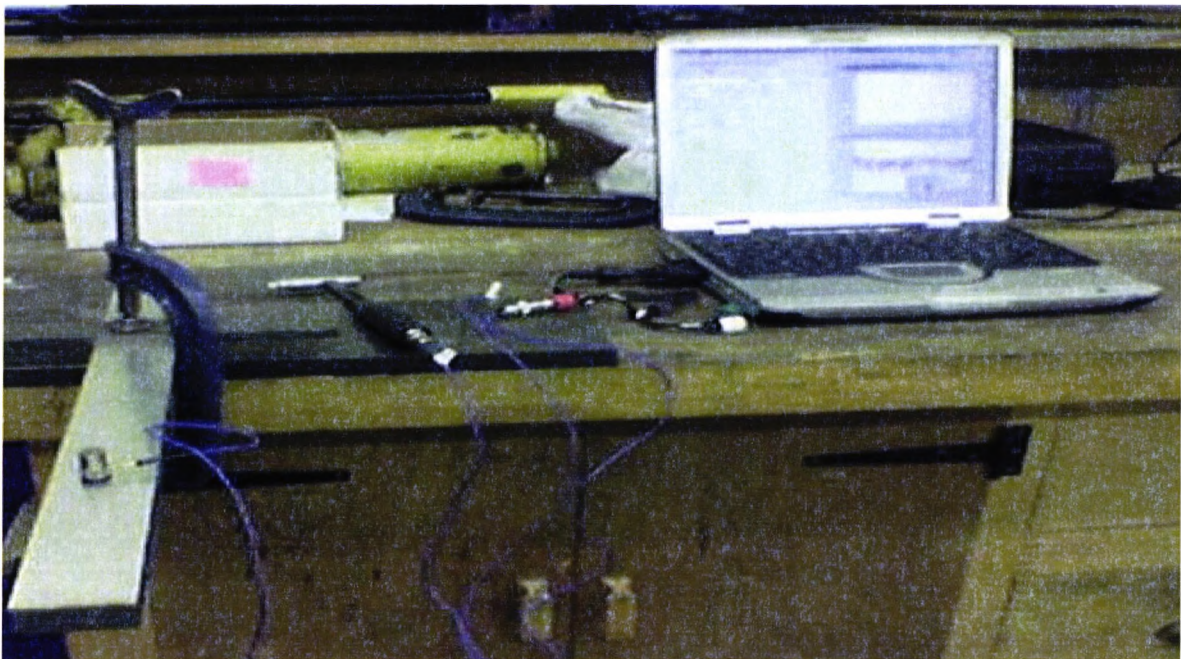
Figure 6.7   Experimental set up for modal testing of a cantilever sandwich beam
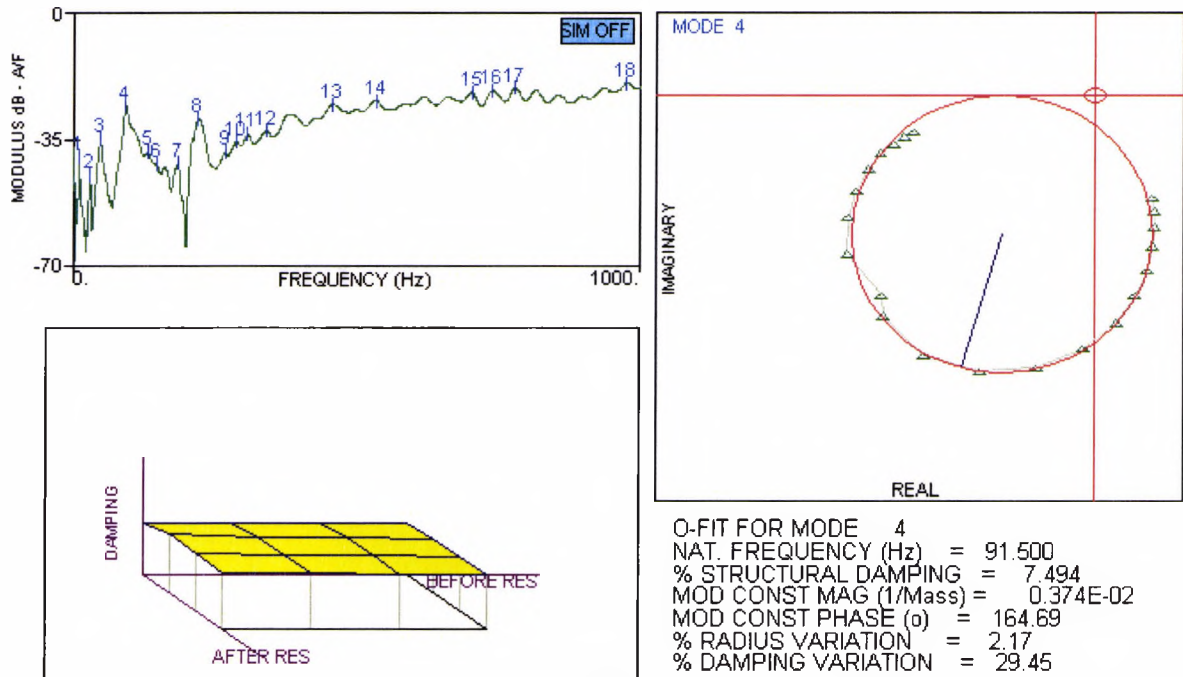
Figure 6.8 **Circle-fit for the 4th mode of the steel-rubber-steel sandwich beam and its damping properties**
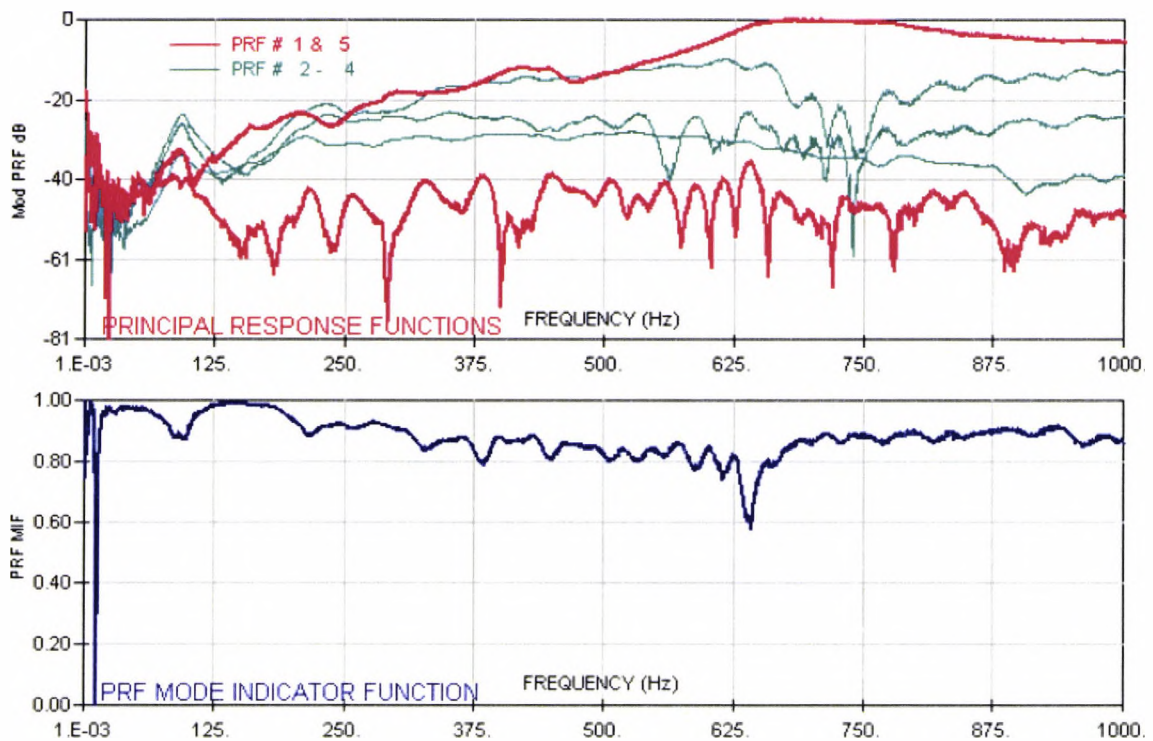
Figure 6.9 **Principal response frequencies (PRF) analysis 0-1000 Hz for aluminium-natural rubber-aluminium sandwich composite beam**
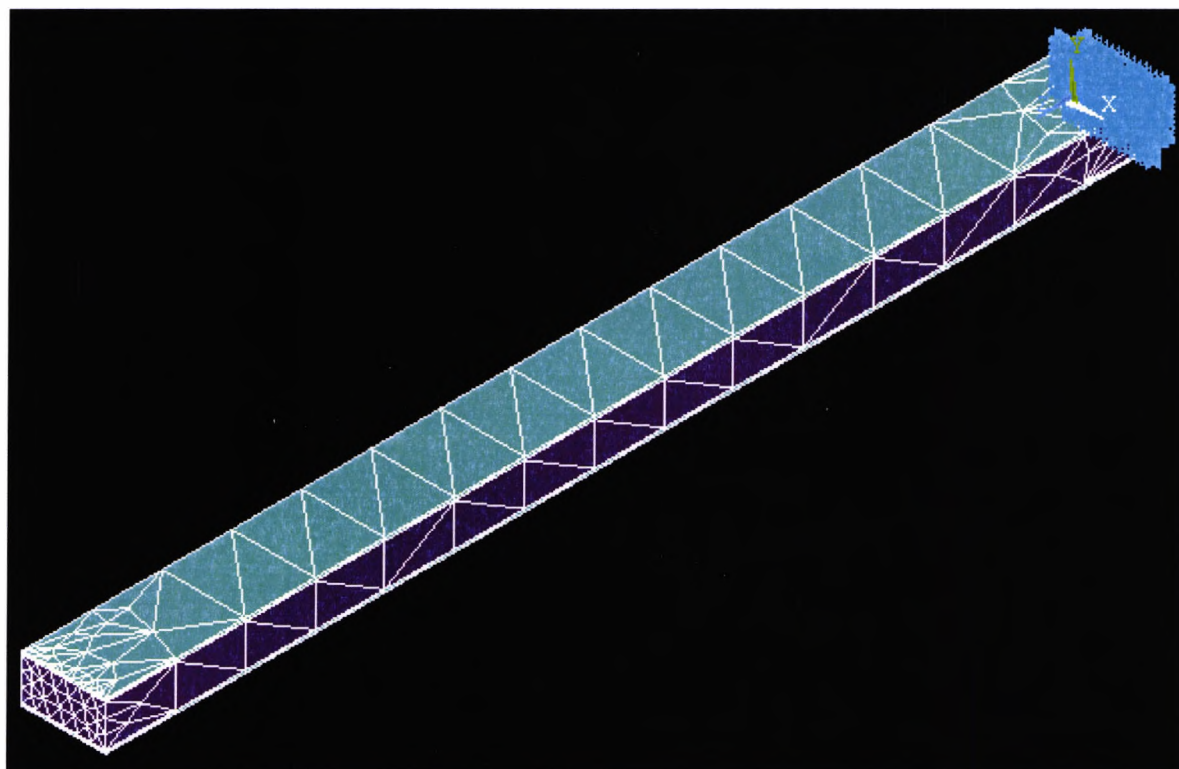
Figure 6.10   A representative meshed sandwich beam using ANSYS 10 (SOLID 45 elements)

Although there are some variations in the three sets of results, taken overall, the theoretical and experimental natural frequencies match reasonably well. The natural frequencies using the present theory agrees very well with ANSYS results which are based on the plate theory, with the exception of the first natural frequency of the second sample. The author has been unable to pin-point the exact reason for this. However, for the discrepancies with experimental results, part of the problem lies in the difficulties encountered when carrying out the experiment, particularly when applying the built-in boundary condition at one end of the cantilever sandwich beam. The properties used for rubber in the theoretical analysis have been averaged from the data given by different manufactures and some variations in the properties are possible that may alter the results slightly. The proposed method, nevertheless, offers optimism for future studies because the differences noticed are generally within engineering accuracy.

Table 6.3   Experimental and theoretical natural frequencies of a three-layered sandwich beam.

Sandwich Beam Specimens	Frequency No (i)	Natural frequencies (Hz)			% difference with Experiment (and ANSYS)
		Experiment	ANSYS	Present Theory	
(i)Aluminium-Rubber-Aluminium	1	11.25	11.47	10.46	7.02 (8.81)
	2	33.75	34.92	36.31	7.59 (3.98)
	3	93.75	73.91	75.94	19.0 (2.75)
(ii) Steel-Rubber-Steel	1	10.62	10.89	9.04	14.9 (16.8)
	2	29.38	33.10	33.88	15.3 (2.36)
	3	53.75	63.49	63.73	18.6 (0.38)
(iii)Steel-Rubber-Aluminium	1	10.63	10.55	9.45	11.1 (9.95)
	2	29.38	32.10	33.30	13.3 (3.74)
	3	-	68.30	70.74	(3.57)

6.5   Conclusions

An accurate dynamic stiffness matrix for a three-layered sandwich beam of asymmetric cross-section has been developed using Timoshenko beam theory, Hamiltonian mechanics and symbolic computation. The resulting dynamic stiffness matrix is applied using Wittrick-Williams algorithm to compute the natural frequencies and mode shapes of some illustrative examples. An impulse hammer test has been carried out on three different sandwich beam samples and the experimental results match reasonably well with theoretical predictions using the present theory and ANSYS. The investigation provides optimism for future studies on the dynamic analysis of complex sandwich structural systems.

7   Rigidity properties of composite beams

7.1   Introduction

The material bending-torsion coupling is one of the most important characteristics of laminated fibrous composite structures, which can be used in design process to prevent aeroelastic phenomenon such as divergence or flutter of aircraft wings [7.1]. This is possible because the material coupling effect is mainly dependent on the fibre orientation in the laminated composites and so can be manipulated by the designer to achieve desirable aeroelastic effects. The material coupling property of composite structures has been taken advantage of in many other ways, especially in aeroelastic tailoring work [7.2, 7.3] and its full potential has yet to be realised. Bending-torsion coupled composite beams or columns have been characterised in the literature [7.4, 7.5] by three important parameters, related to the flexural rigidity (EI), the torsional rigidity (GJ) and the material bending-torsion coupling rigidity (K). Several theoretical and experimental estimates of these rigidities have been reported in the literature for various thin-walled (rectangular or cylindrical tubes) laminated fibrous composite beams/columns [7.6, 7.7].

The macromechanical properties of the composites form the background of the aeroelasticity of composite wings. The rigidities (static) and other properties need to be known in advance as they are used in the design data. As a consequence, the search for a refined theory for evaluation of properties that can be safely applied to the special case of composite wing has been going on for some time. The challenge has been on how to determine the theoretical and experimental values of the rigidities. The development has lead to the establishment of the cross-coupling parameter, ψ, which is a measure of bending–torsion coupling present in a structure, thus establishing trends, generalising the results and also underpinning the aeroelasticity of composite wings. The laminate analysis is based on assumptions that the laminate is thin and that the bond between the plies in a laminate is perfect. Other assumptions include the small deformation theory, macroscopic homogeneity, plane stress and the theory of linear elasticity.

7.2 Theory

7.2.1 Composite beam of solid cross-section

At any cross-section of the beam, (see Figure 7.1), the relation between the internal bending moment resultant, M, torque, T, and the beam curvature $\dfrac{\partial^2 h}{\partial^2 y}$ and the twist rate, $\dfrac{\partial \psi}{\partial y}$, may be expressed as,

$$\begin{Bmatrix} M \\ T \end{Bmatrix} = \begin{bmatrix} EI & -K \\ -K & GJ \end{bmatrix} \begin{Bmatrix} h'' \\ \psi' \end{Bmatrix} \tag{7.1}$$

where primes denotes differentiation with respect to y, the axial coordinate.
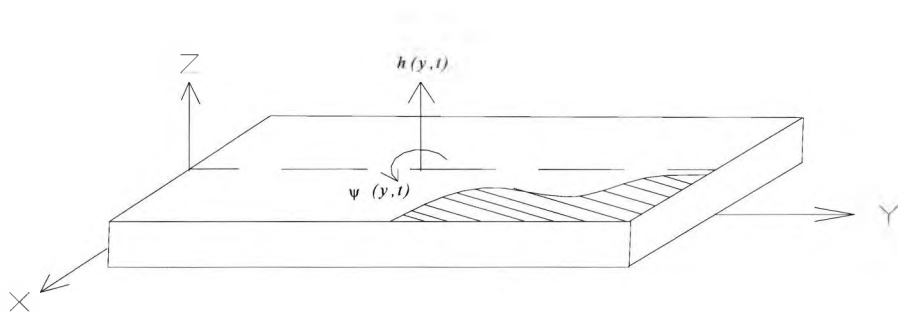
Figure 7.1   Coordinate system and sign convention for positive ply angle of a laminated composite beam

The moment-curvature and in-plane stress- strain relations for the general case of a laminate can be established as follows,

$$\begin{Bmatrix} N \\ M \end{Bmatrix} = \begin{bmatrix} A & B \\ B & D \end{bmatrix} \begin{Bmatrix} \varepsilon \\ k \end{Bmatrix} \tag{7.2}$$

where

$$N = \begin{Bmatrix} N_x \\ N_y \\ N_{xy} \end{Bmatrix} \text{ are in-plane forces,}$$

$$M = \begin{Bmatrix} M_x \\ M_y \\ M_{xy} \end{Bmatrix}$$ are the out of plane bending and twisting moments,

$$k = \begin{Bmatrix} k_x \\ k_y \\ k_{xy} \end{Bmatrix}$$ are the bending and twisting curvatures,

and A_{ij}, B_{ij} and D_{ij} are the in-plane, coupling, and flexural moduli respectively.

For generally orthotropic ply, the laminates are usually constructed in such a way that the principal material axes do not coincide with the material reference axes - to get the required stiffness and strength of an element in desired directions. This means the material properties are a function of orientation at a point in the ply. For isotropic case, the properties are the same in every direction at a point in the ply and hence not a function of orientation at a point in the ply. Anisotropic ply has no planes of material property symmetry through a point in the ply – the properties are therefore a function of orientation at a point in the ply. The stiffness matrix defining a composite structure is dependent on A, B and D matrices that comprise elements A_{ij}, B_{ij} and D_{ij} respectively. The A_{ij} terms describe the extensional stiffness which relate the membrane (in-plane) forces to the laminate mid-plane membrane strains. The B_{ij} terms are the coupling stiffness that relates the membrane forces to the out-of plane curvature deformations. It can therefore, be said that, an extensional force on a laminate with non-zero B_{ij} term possess extensional deformations and also twisting and/or bending deformations of the laminate. Clearly, any applied moment in a laminate with coupling stiffness terms present, will cause an extension of the middle surface.

The D_{ij} terms relate the moments to the bending curvatures. It is evident that the coupling and bending stiffness terms B_{ij} and D_{ij} respectively are dependent on the ply position relative to the laminate mid-plane unlike the A_{ij} terms, which are also dependent on the ply thickness. Depending on the way the fibre angle in the ply and the sequence in which the plies are stacked, some of the terms may turn out to be zero. Other terms may be eliminated or minimised. A symmetric laminate of multiple generally orthotropic plies exhibits no coupling between bending and extension, i.e. B_{ij} terms are zero, and the B matrix will decouple to give load-deformation relationship for the force intensities. In such a case, the A_{ij}, and D_{ij}, particularly A_{13}, A_{23}, D_{13} and D_{23} terms are required to produce coupling between normal

forces and shearing strain, shearing force and normal strains, normal moments and twist, and twisting moment and normal curvatures.

The symmetry of a laminate about the middle surface is sometimes desirable to increase aeroelastic stability by selection of laminate thickness and fibre orientation. However, in many industrial applications, laminated composites require non-symmetric lay-up to achieve design objectives. A good example is on the coupling between extension and twist, which is a necessary feature to design jet turbine fan blades with pre-twist. The antisymmetric lay-up displays extension-torsion coupling and bending-shear coupling, instead of the bending-torsion coupling and extension-shear coupling expected in the symmetrical case. As such, the coupling between normal forces and shearing strain, shearing force and normal strains, normal moments and twist, and twisting moment and normal curvatures are non-existent in the antisymmetric laminates.

In the case of mid-surface symmetrical laminate, the elements of matrix B of Eqs. (7.2) will be zero and thus the relationship between bending moments, twisting moments and curvatures may be expressed in Cartesian axis system as follows

$$
\begin{Bmatrix} M_x \\ M_y \\ M_{xy} \end{Bmatrix} = \begin{bmatrix} D_{11} & D_{12} & D_{13} \\ D_{12} & D_{22} & D_{23} \\ D_{13} & D_{23} & D_{33} \end{bmatrix} \begin{Bmatrix} k_x \\ k_y \\ k_{xy} \end{Bmatrix}
\tag{7.3}
$$

The element D_{ij} are anisotropic flexural moduli of a laminated composite plate and are functions of laminate ply geometry, material properties and stacking sequence, while k_x, k_y and k_{xy} are the plate curvatures.

Now, if the coordinate system shown in Figure 7.1 is adopted with the y-axis aligned in the spanwise direction and the fibre angle measured from y- to x-axis, then, Eqs. (7.3) must be modified as

$$
\begin{Bmatrix} M_x \\ M_y \\ M_{xy} \end{Bmatrix} = \begin{bmatrix} D_{22} & D_{12} & D_{23} \\ D_{12} & D_{11} & D_{13} \\ D_{23} & D_{13} & D_{33} \end{bmatrix} \begin{Bmatrix} k_x \\ k_y \\ k_{xy} \end{Bmatrix}
\tag{7.4}
$$

Using the coordinate system given in Figure 7.1, with no chordwise moment M_x, but with spanwise moment M_y and an end torque M_{xy}, Eqs. (7.4) is modified as follows,

$$\begin{Bmatrix} 0 \\ M_y \\ M_{xy} \end{Bmatrix} = \begin{bmatrix} D_{22} & D_{12} & D_{23} \\ D_{12} & D_{11} & D_{13} \\ D_{23} & D_{13} & D_{33} \end{bmatrix} \begin{Bmatrix} k_x \\ k_y \\ k_{xy} \end{Bmatrix} \quad (7.5)$$

By eliminating k_x we can deduce that,

$$\begin{bmatrix} M_y \\ M_{xy} \end{bmatrix} = \begin{bmatrix} D_{22} - D_{12}^2/D_{11} & D_{23} - D_{12}D_{13}/D_{11} \\ D_{23} - D_{12}D_{13}/D_{11} & D_{33} - D_{13}^2/D_{11} \end{bmatrix} \begin{bmatrix} k_y \\ k_{xy} \end{bmatrix} \quad (7.6)$$

An element by element comparison between Eqs. (7.1) and Eqs. (7.6) shows that,

$$EI = c\left(D_{22} - D_{12}^2/D_{11}\right) \quad (7.7)$$

$$GJ = 4c\left(D_{33} - D_{13}^2/D_{11}\right) \quad (7.8)$$

$$K = 2c\left(D_{23} - D_{12}D_{13}/D_{11}\right) \quad (7.9)$$

where c is the plate chord.

7.2.2 Flat Beam: A High-Aspect-Ratio Plate (HARP) model

In the case of mid-surface symmetric laminated plate, the relationship between plate bending moments, twisting moment and curvatures may be expressed as

$$k_x = \frac{\partial^2 w}{\partial x^2} \; ; k_y = \frac{\partial^2 w}{\partial y^2} \; ; k_{xy} = -2\frac{\partial^2 w}{\partial x \partial y} \quad (7.10)$$

If the same coordinate system and sign convection is used as in Figure 7.1, the plate deflection $w(x, y)$, the beam deflection $h(y)$ and rotation $\psi(y)$ are defined as,

$$h(y) = w(0, y) \quad (7.11)$$

and

$$\left.\frac{\partial w}{\partial x}\right|_{x=o} = -\psi(y) \quad (7.12)$$

The plate curvature in this case can be approximated as follows:

$$k_y = -\theta' \quad (7.13)$$

and

$$k_{xy} = 2\frac{\partial^2 w}{\partial x \partial y}\bigg|_{x=o} = -2\psi' \quad (7.14)$$

The relationships between moment resultants on the beam cross-section and those on the plate cross-section are defined as [7.8]

$$M = -M_y c \quad (7.15)$$

$$T = 2cM_{xy} \tag{7.16}$$

where c is the plate chord. Again, by elimination and substitution procedure Eqs. (7.5) reduces to the following form, as Eqs. (7.1),

$$\begin{Bmatrix} M \\ T \end{Bmatrix} = c \begin{bmatrix} D_{22} - D_{12}^2/D_{11} & 2(D_{23} - D_{12}D_{13}/D_{11}) \\ (D_{23} - D_{12}D_{13}/D_{11}) & 4(D_{33} - D_{13}^2/D_{11}) \end{bmatrix} \begin{Bmatrix} \theta \\ \psi' \end{Bmatrix} \tag{7.20}$$

An element by element comparison between Eqs. (7.1) and Eqs. (7.20) show that,

$$EI = c(D_{22} - D_{12}^2/D_{11}) \tag{7.21}$$

$$GJ = 4c(D_{33} - D_{13}^2/D_{11}) \tag{7.22}$$

$$K = 2c(D_{23} - D_{12}D_{13}/D_{11}) \tag{7.23}$$

A stiffness cross-coupling parameter, ψ, is identified as a measure of bending-torsion coupling present in a structure [7.9]. This non-dimensional parameter is defines as,

$$\psi = \frac{K}{\sqrt{EIGJ}} \tag{7.24}$$

$$\psi = \frac{D_{13}D_{22} - D_{12}D_{23}}{\sqrt{(D_{11}D_{22} - D_{12}^2)(D_{33}D_{22} - D_{23}^2)}} \tag{7.24}$$

with limits

$$-1 < \psi > 1 \tag{7.25}$$

The above limits of the bending-torsion coupling parameter enables one to categorise a beam-like structure as highly coupled, with values of ψ near unity.

Eqs. (7.12) and Eqs. (7.13) have been used as approximations to the plate curvatures in order that the dimensional plate model to be reduced to a one dimensional beam model. It is also worth noting that in the above plate model the chordwise curvature k_x or "camber" bending has not been restrained.

7.2.3 Flat beam: A Chordwise-Rigid Laminated Plate (CRLP) model

In realistic wings high torsional rigidity is usually provided by closely spaced ribs. When this is the case, chordwise rigidity can be assumed in terms of bending displacement and torsional rotation, and a modified flat beam (plate) model can be used to calculate the stiffness of a wing (beam). The approach used originally to symmetrical balanced laminates [7.10] and later to symmetrical, unbalanced laminates [7.9] is hereby used to develop the model.

The assumed displacement

$$w(x, y) = \theta(y) - x\psi(y) \tag{7.26}$$

is used for plate deflection. The assumption of chordwise rigidity results in the following expressions for plate curvatures:

$$k_x = 0 \, ; k_y = -\theta^{'} \, ; k_{xy} = -2\theta^{'} \tag{7.27}$$

Therefore, Eqs. (3.3) reduce to

$$\begin{Bmatrix} M_x \\ M_y \\ M_{xy} \end{Bmatrix} = \begin{bmatrix} D_{22} & D_{12} & D_{23} \\ D_{12} & D_{11} & D_{13} \\ D_{23} & D_{13} & D_{33} \end{bmatrix} \begin{Bmatrix} 0 \\ -\theta^{'} \\ -2\psi^{'} \end{Bmatrix} \tag{7.28}$$

In this case the chordwise moment, M_x is not zero, but is given by

$$M_x = -D_{12}\theta^{'} - 2D_{23}\psi^{'} \tag{7.29}$$

Using the same relationships between moment resultants on the beam cross-section and those on the plate cross-section as in Eqs. (7.15) and Eqs.(7.16), the bending, torsional, and coupling stiffness for the chordwise rigidity laminated plate can then be obtained from Eqs. (7.28) as follows,

$$EI = cD_{11} \tag{7.30}$$

$$GJ = 4cD_{33} \tag{7.31}$$

$$K = 2cD_{13} \tag{7.32}$$

which means,

$$\psi = \frac{D_{13}}{\sqrt{(D_{11}D_{33})}} \tag{7.33}$$

A term by term comparison between Eqs. (7.30) to (7.32) and Eqs. (7.21) to (7.23) shows that HARP and CRLP models are identical only when the term D_{22} tends to infinity (i.e chordwise rigidity assumption).

7.2.4 *Stiffness modelling of thin-walled single-cell composite beams*

For a typical thin-walled beam the stiffnesses may be denoted as C_{ij}, where i, j can be numbers from 1-6. Such a model is Bernoulli-Euler beam in bending and St. Venant in twisting. It is a simplification of that of Refs. [7.11] in that section warping and transverse shear deformations are neglected.

Twisting deformation corresponds to Eqns. (7.37) and spanwise bending to (7.38). The appropriate stiffnesses are [7.11]

$$C_{44} = \frac{4A_e^2}{c^2} \oint K_{22} ds \tag{7.34}$$

$$C_{45} = \frac{2A_e}{c} \oint K_{12} ds \tag{7.35}$$

$$C_{55} = \oint K_{11} z^2 ds \tag{7.36}$$

where y, z and s are the special coordinates, A_e is the enclosed area of the cell and c is the circumference of the cell.

The wall plane stress stiffensses are

$$K_{11} = A_{11} - (A_{12})^2 / A_{22} \quad \text{(extensional)} \tag{7.37}$$

$$K_{12} = A_{16} - A_{12} A_{26} / A_{22} \quad \text{(coupling)} \tag{7.38}$$

$$K_{22} = A_{66} - (A_{26})^2 / A_{22} \quad \text{(shear)} \tag{7.39}$$

The in-plane stiffnesses associated with A -matrix come from the membrane version of classical lamination theory.

$$A_{ij} = \sum_{k=1}^{N} \overline{Q}_{ij}^{(k)} h_k \quad (k = 1,2,6) \tag{7.40}$$

The stiffnesses $\overline{Q}_{ij}^{(k)}$ are the plane stress stiffnesses for the k -th ply. The ply thicknesses are h_k , and N is the total number of plies.

Both the high-aspect-ratio plate (HARP) and chordwise-rigid laminated plate (CRLP) models do not account the transverse shear effects that occur on thin-walled (single and multi-celled) torque boxes used in the aircraft wing design. From the literature review, two methods, the circumfrential uniform stiffness (CUS) and circumferentially asymmetrical stiffness (CAS) have been considered for thin-walled beams. The CUS configuration produces extension-torsion and bending shear couplings [7.1]. The axial, coupling and shear stiffness A, B and C given in Eqs. (7.41) to Eqs. (7.43) are constant through out the cross-section, and the ply lay-ups on opposite flanges are of reversed orientation. The CAS configuration produces bending-torsion and extension shear couplings [7.1]. The stiffness A

in Eqs. (7.41), is constant throughout the cross-section while the coupling stiffness, B (Eqs.7.42) in opposite members is of opposite sign. The stiffness C Eqs. (7.43) in opposite member is equal. The ply lay-ups along the horizontal members are symmetrical. The stiffness A, B and C are related to the usual laminate in-plane stiffness matrix A of classical lamination theory as follows,

$$A = A_{11} - A_{12}^2 / A_{11} \tag{7.41}$$

$$B = \left(A_{13} - \frac{A_{12} A_{23}}{A_{22}} \right) \tag{7.42}$$

$$C = 4 \left(A_{33} - A_{12}^2 / A_{22} \right) \tag{7.43}$$

7.3 Parametric studies on various flat and box composite beam models

The cross-sectional (static) rigidity and other properties of the wing are used as data, are known in advance, and are used to get the insight in to the characteristics and the resulting into coupling behaviour of composite beams (wings). A composite wing is characterised by its three main rigidities i.e. EI, GJ, and K. The role of material coupling rigidity, K, which is dependent on ply orientation and stacking sequence, is of great significance for composite wings because it can be exploited to an advantage for the purpose of aeroelastic tailoring. In preliminary design stage, the rigidity and deflection characteristics of flat beam or thin-walled beam are used to understand and study the bending-torsion features of actual lifting surfaces with moderate-to-high aspect ratio. Both the flat beams and box-beams have ply symmetry with respect to the middle surface. Since the stiffness are symmetrical about $\theta = 90^0$, the fibre angle is allowed to vary between 0^0 and 90^0.

The illustrations that follow show the EI, GJ and K as a function of ply angle, for the flat beam. The bending stiffness data has been non-dimensionalised with respect to the EI_{REF} and GJ_{REF}, the bending stiffness and torsional rigidity respectively, of the beam model when the fibre angle of all sides is set to $\theta = 0^0$. To start with, an investigation is carried out on an unswept wing with a length (L) = 0.6 m, width (c) = 0.0762 m, thickness (t) = 1.876 mm, mass per unit length (m) = 0.2172 kg/m and mass moment inertia per unit length, I_α = 0.1052x10^{-3} kgm. The beam is made of 14 – ply graphite/epoxy laminate. Figure 7.2 displays

the stiffness properties of the flat beam. The aim is to determine where the bending - torsional coupling parameter, ψ, is at a maximum, which influences the maximum achievable flutter speed. The bending, torsional and bending-torsion coupling rigidities are calculated and subsequently used in free vibration and flutter analysis of the composite wing in the next chapter.
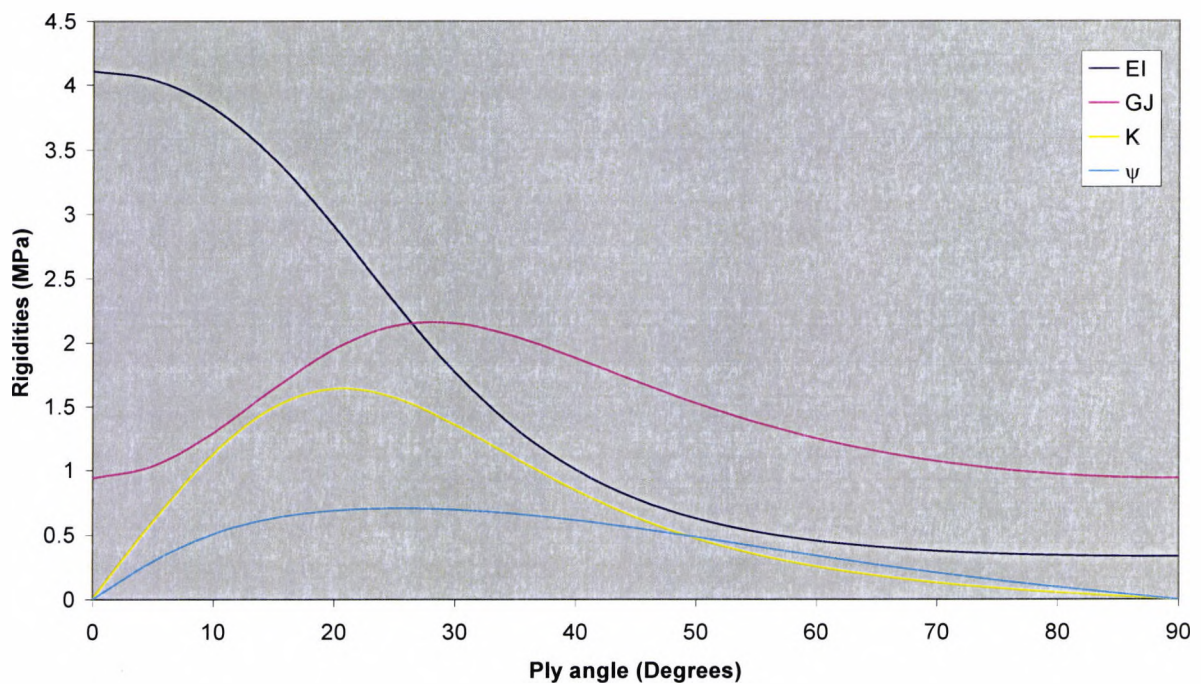
Figure 7.2 **The bending rigidity (*EI*), torsional rigidity (*GJ*), bending-torsion coupling rigidity and bending-torsion parameter ψ of the θ_{14} flat beam. Note: ($-1 \leq \psi \leq 1$ and has no units)**

The second type of composite beam considered has featured in the literature [7.12] from a programme of research at the Massachusetts Institute of Technology, USA. This beam is hereafter referred to as MIT-beam. The MIT-beam is flat and of solid rectangular cross-section with stacking sequence $[\theta_2/0]_s$. Table 7.1 displays the material properties of the two beams.

Table 7.1   Material properties for the $|\theta_2/0|_2$ MIT glass epoxy beam model and the glass epoxy box - beam GIT model.

Property	Flat beam	Box beam
E_{11}	98 GN/m^2	206.9 GN/m^2
E_{12}	7.9 GN/m^2	5.17 GN/m^2
υ_{12}	0.28	0.25
G_{12}	5.6 GN/m^2	3.1 GN/m^2
G_{21}	0.2356 GN/m^2	3.1 GN/m^2
ρ	1520 GN/m^2	1529 kg/m^3

Figure 7.3 (below) illustrates the stiffness properties of MIT beam using this study. The laminated composite beam $(\pm\theta_2/0)_s$, has the following characteristics; length $(L) = 0.3048$ m, width $(c) = 0.0762$ m, thickness $(t) = 0.804$mm, mass per unit length $(m) = 93.1225 \times 10^{-3}$ kg/m and mass moment inertia per unit length, $I_{\alpha} = 45.0641985 \times 10^{-6}$ kgm. As can be seen from the graph, Figure 7.3 the stiffness are symmetrical about $\theta = 0^0$ and the ply angle is allowed to vary between $\theta = 0^0$ and 90^0. The maximum bending resistance is obtained when the fibres are aligned in the direction of the applied membrane i.e. when $\theta = 0^0$ and the load falling off rapidly with a small change in the ply orientation. Similarly, the least bending resistance is obtained in the transverse direction when $\theta = 90^0$. The maximum shear modulus GJ is obtained when $\theta = 25^0$. The bending - torsional coupling stiffness is greatest in the region of $\theta \approx 15 - 25^0$ (slightly off the intersection point of EI and GJ) and leading to infinity at $\beta = 0^0$ and 90^0. The bending - torsional coupling parameter, ψ, maximum value are at about $\theta = 20^0$, and falls gently to infinity at both when $\theta = 0^0$ and 90^0. Significance of these results is reflected on the predicted results of the free vibration and flutter analysis discussed later in the following Chapters (9 and 10).
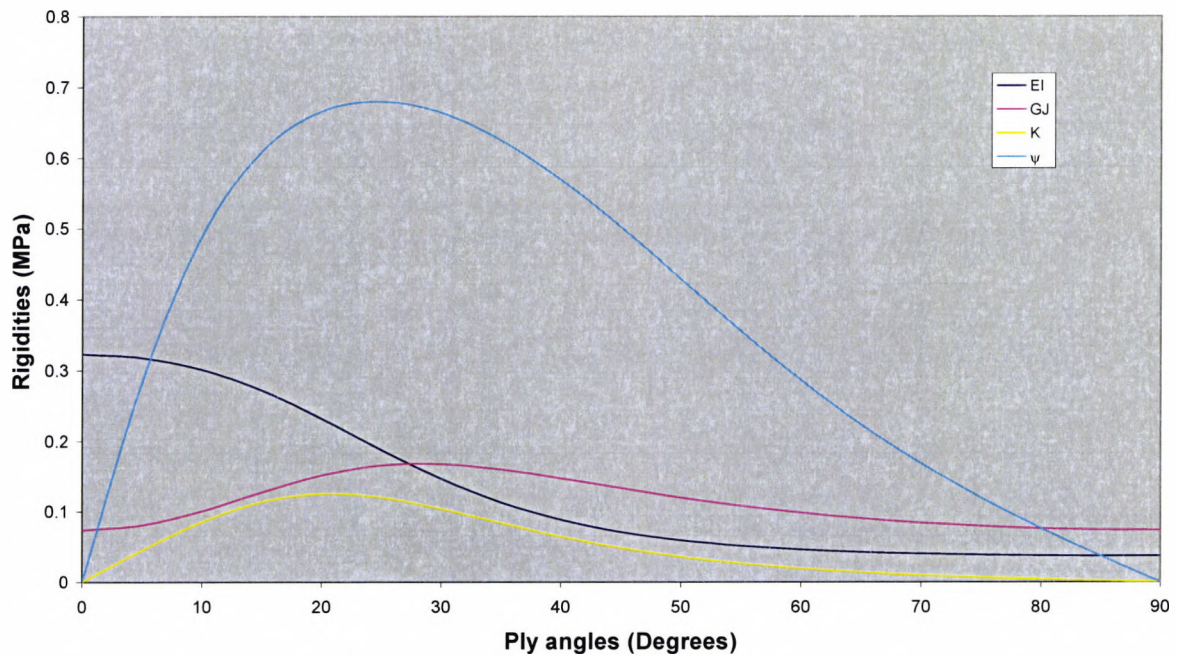
Figure 7.3 **The bending rigidity (*EI*), torsional rigidity (*GJ*), bending-torsion coupling rigidity and**
bending-torsion parameter ψ of the MIT beam Note: ($-1 \leq \psi \leq 1$ and has no units)

In the third example, a single lamina made of glass epoxy of length (L) = 0.1905m, width
(c) = 0.0127m, thickness (t) = 0.00318m, E_1=9.71 GN/m^2, E_2=3.25 GN/m^2, G_{12}=0.9025
GN/m^2, G_{23}=0.2356 GN/m^2, G_{13}=0.9025 GN/m^2, ρ = 1347 kg/m^3 and v_{13} = 0.29 was
investigated. As can be seen in Figure 7.4, the highest value of *EI* is at $\theta = 0^0$ while for the *GJ*
is at $\theta = 25^0$ similar to other cases examined on this study. The beam is highly coupled
between the region of $\theta \approx 20 - 25^0$, where the maximum values ψ are obtained.
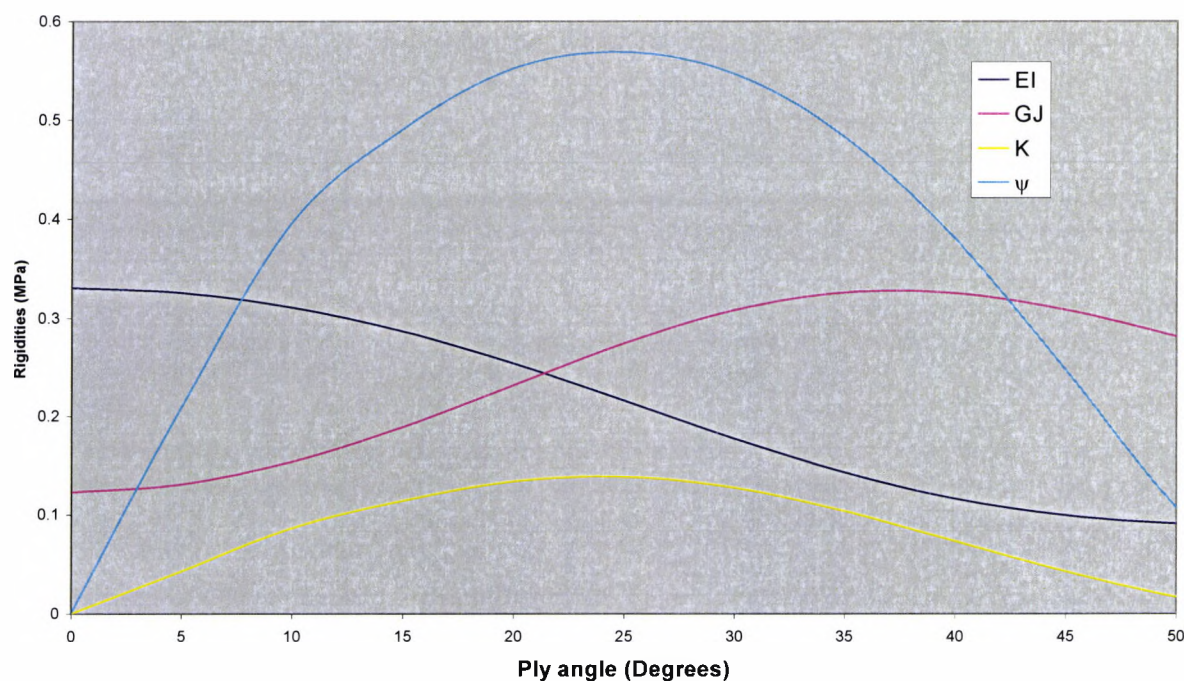
Figure 7.4 **The bending rigidity (*EI*), torsional rigidity (*GJ*), bending-torsion coupling rigidity and bending-torsion parameter ψ of fibre-glass reinforced flat beam model. Note: ($-1 \leq \psi \leq 1$ and has no units)**

Further, an investigation is carried out on an aircraft wing modelled into a thin-walled single cell cross-sectional shape, box beam, made of graphite/epoxy. The type of composite beam considered has featured in the literature [7.13] and is referred to as GIT-beam [7.13] because it stems from research at the Georgia Institute of Technology, USA. The GIT-beam is of box cross-section with lay-ups for the top, bottom, front and rear sides being $[+\theta/+\theta]$, $[-\theta/-\theta]$, $[+\theta/-\theta]$ and $[-\theta/+\theta]$, respectively. Table 7.1 displays the material properties of the two beams. The configuration of the GIT beam, which has a length of 2.032 m, is shown in Figure 7.5. The ply angle is varied from 0^0 to 90^0, depending on the configuration of the cross section. The box-beam is of length (L) = 2.032m, depth, (h) = 0.0508 m, width (c) = 0.254mm, thickness (t) = 0.254mm, mass per unit length (m) = 5.82216 kg/m and mass moment inertia per unit length, $I\alpha$ = 3.3162 x10^{-2} kgm. Comparison of the results obtained from various theories: Rehfield Simplified Formula (RSF) [7.14], Armanios General Formula (AGF) [7.15] and Armanios simplified Formula (ASF) [7.16], are all used to determine the exact results and thereby reflecting the significance of the study. It should be recognised that

the box-beam can be idealised as two flat beams (one at the top and one at the bottom) although this is not covered in this study.
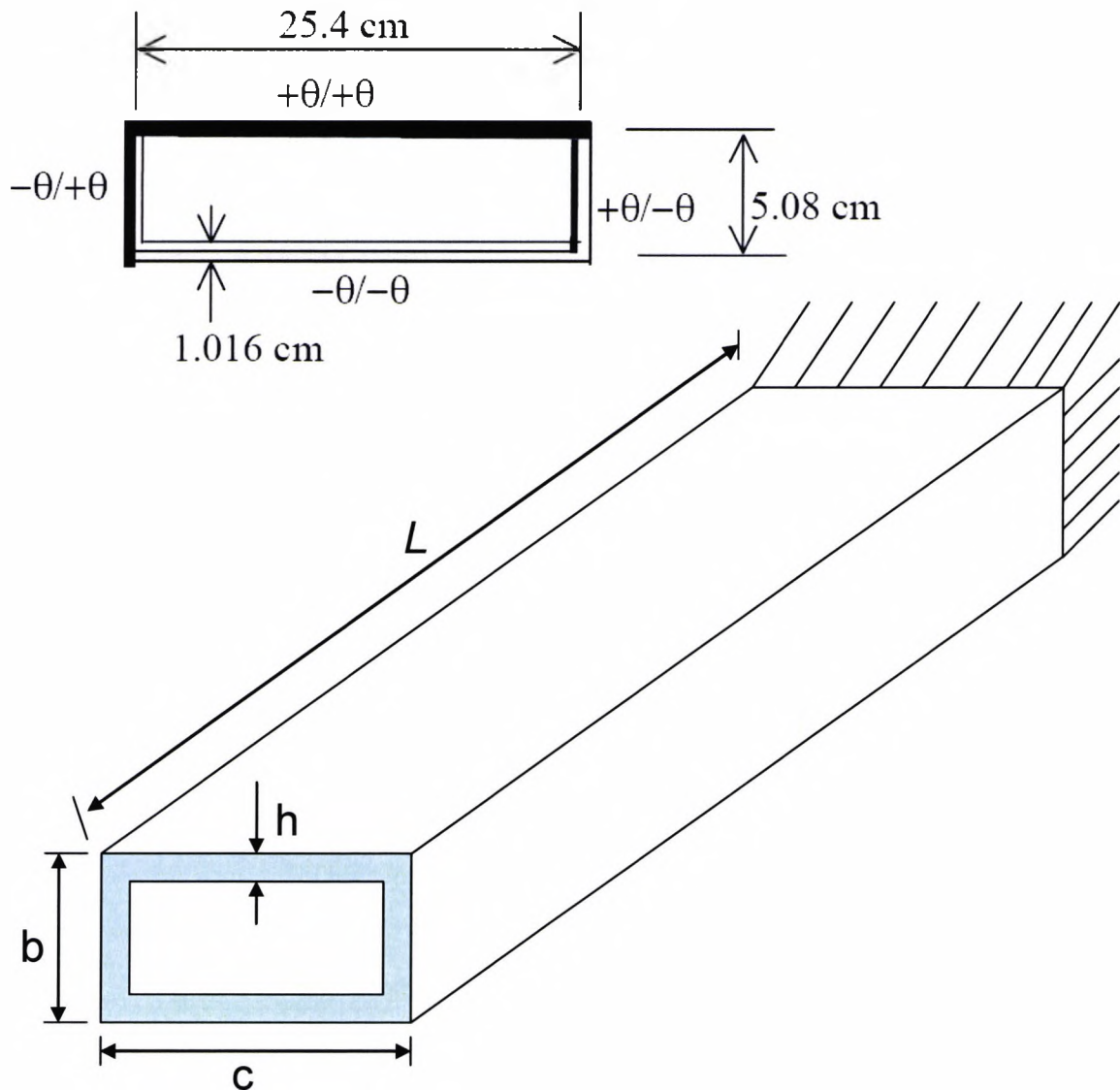
Figure 7.5   Configuration of the GIT box beam - *c* and *b* are centreline dimensions

Comparison of the results obtained from RSF, AGF and ASF in Figure 7.6 shows that the three formulae estimate the values *EI* to almost the same value though varies a little bit for AGF case in all the angles expect between $\theta \approx 20 - 30^0$. The *GJ* graphs (Figure 7.7) are same at $\theta = 0 - 10^0$ and $\theta = 90^0$, with the greatest values obtained from ASF. The approximations

obtained for K (Figure 7.8) from RSF and AGF shows only a small variation although those of ASF remain significantly very small. On ASF, as can be seen on Figure 7.6-7.9, both ψ and K are very small as compared to EI and GJ. The highest value of EI is obtained at $\theta = 0$ while for GJ it is between $\theta = 40^0$ and $\theta = 50^0$ unlike in any other case studied on. Both EI and GJ intersect at about $\theta = 22^0$ and both fall to infinity at $\theta = 90^0$. It can be said that the shear resistance is significantly high though this might not be necessarily true as can be demonstrated by the results obtained from Rehfield Simplified Formula and Armanios General Formula of the same beam under the same conditions. The results obtained through the Rehfield Simplified Formula displays bending rigidity (EI), torsional rigidity (GJ), bending-torsion coupling rigidity (K) and bending-torsion parameter ψ of the box-beam with significantly values much higher in comparison to the flat beams studied earlier on. Again the results are symmetrical at $\theta = 0^0$. The ply has a high bending rigidity as compared to the torsion rigidity. However, bending-torsion parameter ψ value is very small compared to the ply rigidities. The results obtained through AGF are very much similar to those of RSF. The maximum values of EI are at $\theta = 0^0$ while for GJ it is $\theta \approx 20 - 30^0$ with both rigidities having an even value at approximately $\theta = 27^0$. Like in the previous case, bending-torsion parameter ψ value is very small compared to the ply rigidities.
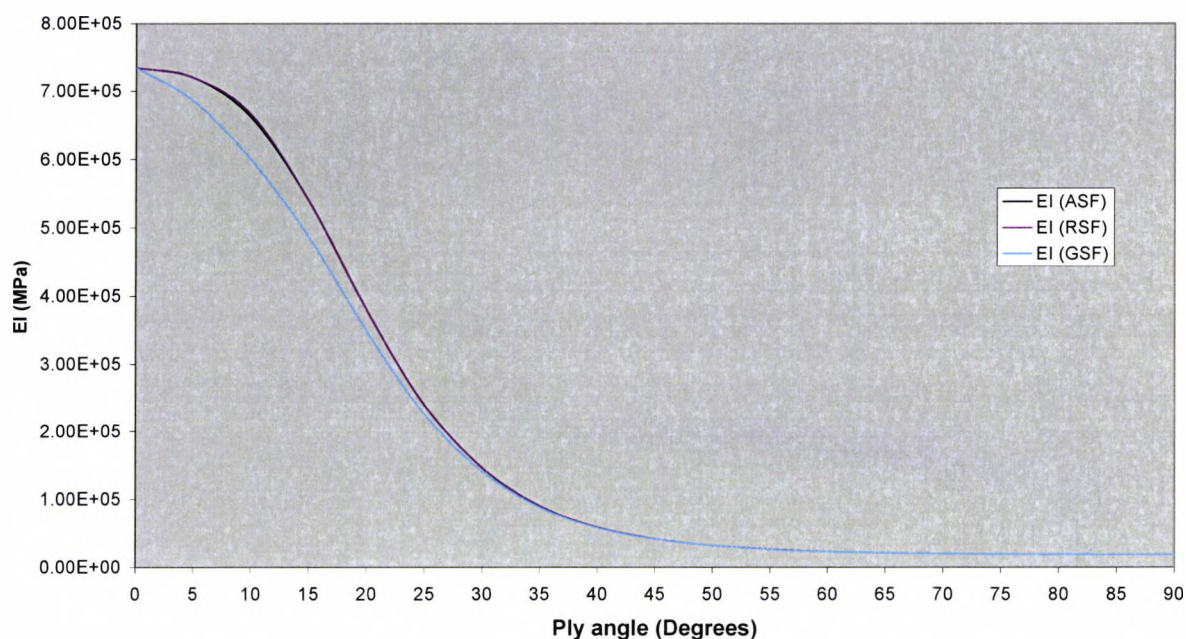
Figure 7.6 **The comparison of the bending rigidity (EI) for the box-beam obtained through Armanios Simplified Formula (ASF), Armanios General Formula (AGF) and Rehfeild Simplified Formula (RSF).**
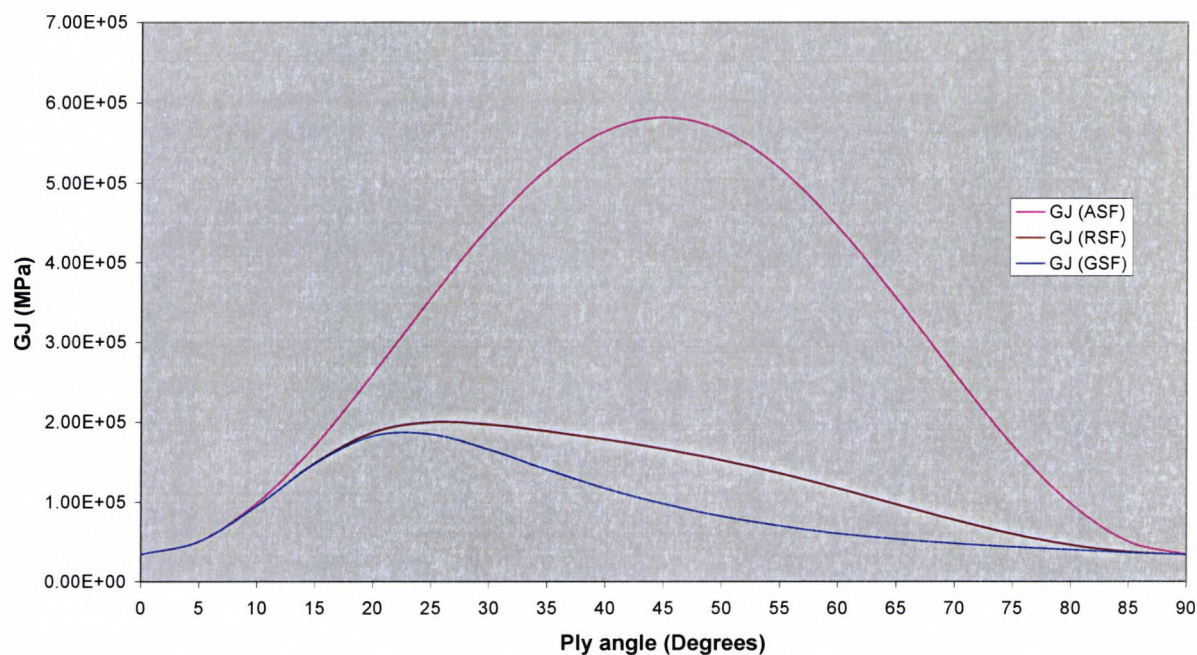
Figure 7.7 The comparison of the torsional rigidity (*GJ*) for the box-beam obtained through Armanios Simplified Formula (ASF), Armanios General Formula (AGF) and Rehfeild Simplified Formula (RSF).
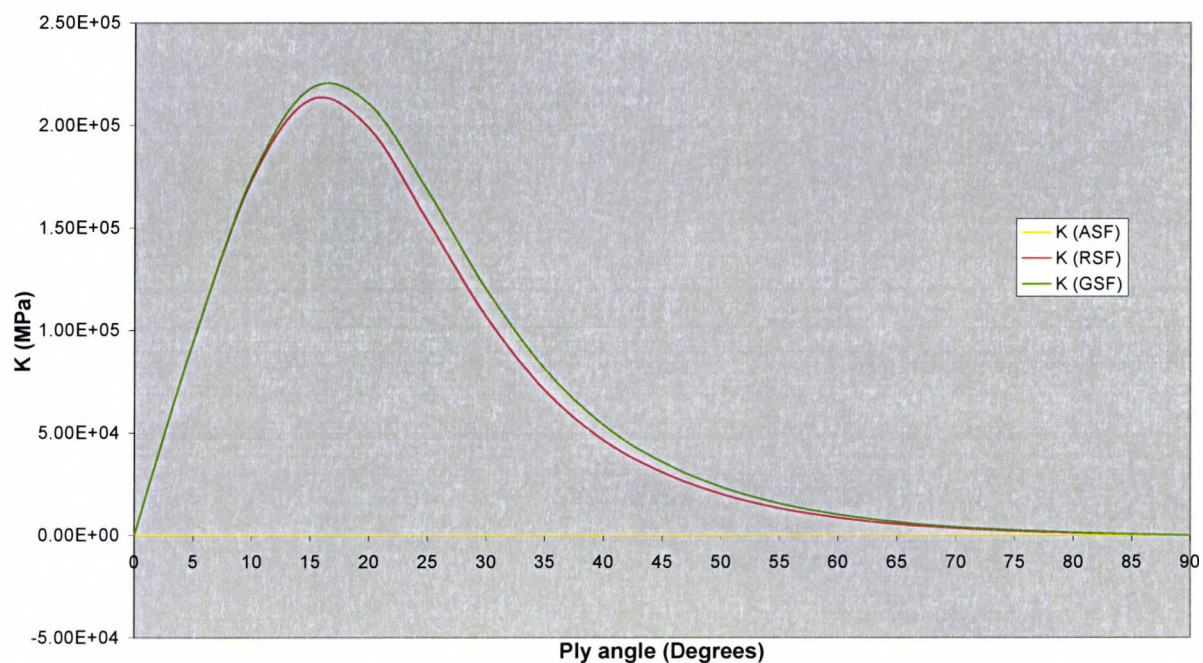
Figure 7.8 The comparison of the bending-torsion coupling rigidity (K) for the box-beam obtained through Armanios Simplified Formula (ASF), Armanios General Formula (AGF) and Rehfeild Simplified Formula (RSF)

Figure 7.9 illustrates the bending-torsion parameter, ψ, from the three theories on box beam, RSF, AGF and ASF. Still ASF results are too small to be displayed. Both AGF and RSF have the same approximations at $\theta = 0 - 10^0$ and at $\theta = 85 - 90^0$ and varies significantly in every other ply angle. The comparison successfully shows that various results can be obtained in various cases on variation to the ply angle. Thus, it will then be upon the wing designer to choose the right ply orientation to achieve the desired results. It is also evident that changes in chord length affect the rigidities as this affects the aspect ratio of the beam (wing). The stiffness are symmetrical about $\theta = 90^0$ in all case when the fibre angle is allowed to vary between 0^0 and 90^0.
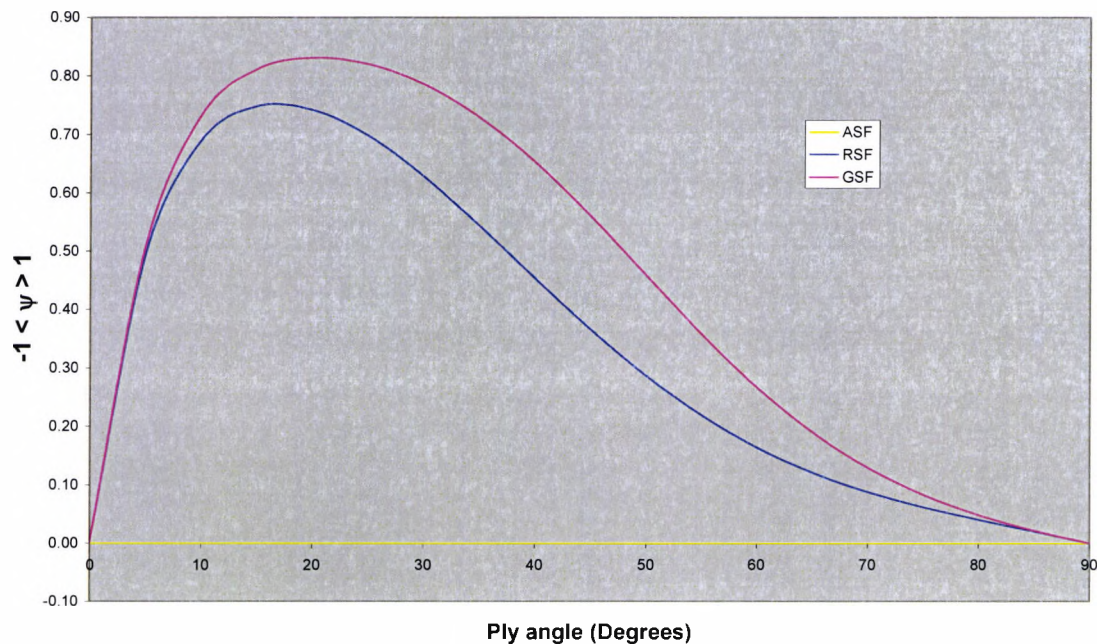
Figure 7.9   **The comparison of the bending-torsion coupling parameter, ψ, of the box-beam obtained through Armanios Simplified Formula (ASF), Armanios General Formula (AGF) and Rehfeild Simplified Formula (RSF)**

7.4   Conclusions

The study shows that it is possible to design laminates to exhibit a desired set of stiffnesses. The antisymmetric lay-up beam displays extension-torsion coupling and bending-shear

coupling, instead of the bending-torsion coupling and extension-shear coupling expected in the symmetrical case. As such, the coupling between normal forces and shearing strain, shearing force and normal strains, normal moments and twist, and twisting moment and normal curvatures are non-existent in the antisymmetric laminates. The A_{ij} terms describe the extensional and stiffness which relate the membrane (in-plane) forces to the laminate mid-plane membrane strains. The B_{ij} terms are the coupling stiffness that relates the membrane forces to the out-of plane curvature deformations. It can therefore, be said that, an extensional force on a laminate with non-zero B_{ij} term posses extensional deformations and also twisting and/or bending of the laminate. Furthermore, any applied moment in a laminate with coupling stiffness terms present, will cause an extension of the middle surface. The D_{ij} terms relate the moments to the bending curvatures. It is evident that the coupling and bending stiffness terms B_{ij} and D_{ij} respectfully are dependent on the ply position relative to the laminate mid-plane unlike the A_{ij} terms, which are dependent on the ply thickness. The magnitude and sense (sign) of D_{13} and D_{23} terms are crucial in determining the direction and the extent of bending-torsion coupling present in a structure – *wash-in* and *wash out* deformations. The signs of D_{13} and D_{23} terms depend on the coordinate system adopted and also on the definition of positive fibre. Here a positive fibre angle results in positive reduced stiffness terms $\overline{Q}_{ij}$ and as a consequence in positive bending-torsion coupling stiffness, K. This in turn gives a positive bending-torsion coupling parameter ψ – which is a measure of bending-torsion coupling present in a structure.

8 Coupled flexure-torsion buckling analysis of composite and metallic columns

8.1 Introduction

Elastic stability (or buckling) of beams, plates, and shells is one of the most important criteria in the design of any structure. Often, it is the critical design issue (even more than strength) in sizing certain structural elements. Because of this crucial role of elastic stability, it is extremely useful to have results of buckling analysis expressed in closed form, even if they are approximate, whenever possible for design analysis [8.1-8.4]. Although such approximate analyses cannot replace an over-all elastic stability analysis of the entire structure, the ease of implementation and the physical insight that such forms give allows valuable design tradeoffs to be made in the preliminary design phase; which may lead to significant improvements in cost and performance of the structural design. On this line of interest, active buckling controls of laminated composite plates [8.5, 8.6], beams [8.7-8.10] and beam columns [8.11] with surface bonded or embedded piezoelectric sensors that are either continuous or segmented have been presented. The problem of bending-torsion coupled elastic buckling analysis of metallic columns has been extensively researched for the past six decades and is well documented [8.12-8.14]. However, a striking feature of most of this research is that they focus on the flexural-torsional behaviour of an individual column [8.15]. In contrast, less work has been carried out on the stiffness matrix based solution, which covers frameworks as well as individual members.

Only a very few investigators have apparently used the stiffness matrix method to solve problems using coupled flexural-torsional column theory. They are Barsoum and Gallagher [8.16], who formulated the finite element stiffness matrix of a bending-torsion coupled column using an approximate displacement field, and Renton [8.17, 8.18] who used a method, which derived the exact stiffness matrix from the classical differential equations of a coupled metallic column. Renton's work is significant because it used exact classical theory as opposed to the more usual approximate theory of finite element method. However, it appears that his work was not followed up and has often been overlooked by later investigators. It should be recognised that Renton developed his exact stiffness matrix before a well-known algorithm [8.19, 8.20], which uses exact member theory to solve buckling and/or vibration eigenvalue problems, was available. Wittrick and Williams developed this algorithm [8.19,

8.20] to ensure the prediction of any eigen-value with certainty, when using exact theory. This algorithm has since featured in literally hundreds of research papers, using exact member theory [8.21] when dealing with buckling and/or vibration problems for structures or structural elements.

Investigation into the buckling behaviour of thin-walled composite structures is a relatively recent phenomenon [8.22-8.24] and is mostly confined to laminated plates or structures assembled from them. Kapania and Raciti [8.25] give an extensive bibliography on the subject. A review of the existing literature about refined theory for the thin-walled composite structures [8.26-8.30] reveals that thin-walled metallic beams exhibit geometric coupling between bending and torsion, which generally occurs when the centroid (mass centre) and shear, centre of the beam cross section are non-coincident. Thin-walled composite beams can show additional coupling effect such as the flexural-torsional coupling due to anisotropic (or directional) nature of laminated fibrous composites.

Following a rigorous formulation, the exact stiffness matrix is derived from the basic bending-torsion coupled differential equations, which govern the elastic buckling behaviour of composite columns. Thus, the stiffness expressions for the elements of the stiffness matrix are based upon the closed form analytical solution of the governing differential equations. These equations are simplified with the help of a symbolic computation package called REDUCE. Simultaneous flexure and twist in a composite column, caused by both geometric and material coupling terms, which are usually present in thin-walled cross-section are included in the theory. Results for composite column with both geometric and material bending-torsion coupling are given, discussed and commented on. Applications of the derived stiffness matrices are discussed with particular reference to the Wittrick-Williams algorithm that is generally used in transcendental eigen-value as in the present case.

8.2 Theory

8.2.1 Theory for composite columns

A straight uniform composite column of length L is shown in Figure 8.1, with x_α being the separation between the centroidal axis and the elastic axis, i.e. between the loci of respectively the centroid and the shear centre of the cross-section. In the right handed coordinate system of Figure 8.1, the Y axis coincides with the elastic axis, which is permitted flexural translation $u(y)$ and torsional rotation $\psi(y)$ as indicated, where y is measured from the origin. The

constant compressive axial load *(P)* is assumed to act through the centroid of the cross section. *P* can be negative, so that tension is included. Characterisation of bending-torsion coupled composite columns by the use of three important parameters, namely the flexural rigidity *(El)*, the torsional rigidity *(GJ)* and the bending-torsion material coupling rigidity *(K)*, is essential in the derivations, which follows,
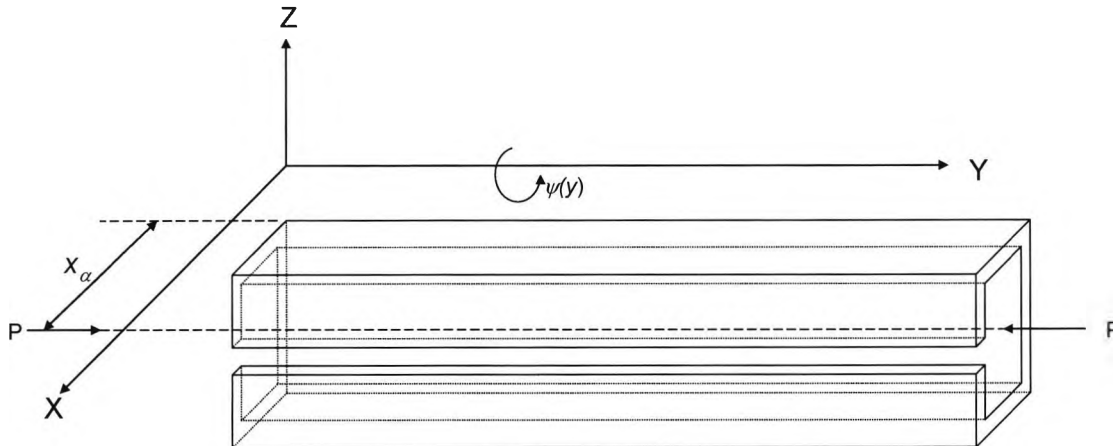
Figure 8.1   The co-ordinate system and notation for a bending-torsion buckling of composite or metallic beam

Using coupled flexural torsional beam theory for thin-walled composites with shear deformation and warping stiffness neglected, the governing differential equations for static behaviour are given by Mansfield and Sobey [8.31]

$$EIu'''' + K\psi''' + P(u'' - x_\alpha\psi'') = 0 \tag{8.1}$$

$$GJ\psi''' + Ku''' + P(r_0^2\psi'' - x_\alpha u'') = 0 \tag{8.2}$$

where primes denotes differentiation with respect to *y; El, GJ* and *K* have already been defined above; and r_0 is the radius of gyration of the beam cross section about the Y axis, i.e. the elastic axis, so that the polar second moment of area of the cross section is Ar_0^2, *A* being the cross sectional area.

Substituting

$$\xi = y/L \text{ and } D = d/d\xi \tag{8.3}$$

into Eqns (8.1)-(8.2) gives

$$D^4 u (KL/EI) D^3 \psi + \left(PL^2/EI \right) \left\{ D^2 u - x_\alpha D^2 \psi \right\} = 0 \tag{8.4}$$

$$L D^2 \psi (KL/GJ) D^3 u - \left(PL^2/GJ \right) \left\{ r_0^2 D^2 \psi - x_\alpha D^2 u \right\} = 0 \tag{8.5}$$

Equations (8.4) and (8.5) can be combined into one equation by eliminating either u or ψ give

$$D^2 \left(D^2 + \overline{\alpha}^{-2} \right) W = 0 \tag{8.6}$$

where

$$W = h \text{ or } \psi \text{ and } \overline{\alpha}^{-2} = b(1+c)/(1-a) \ \overline{a}^2 = b(1+c)/(1-a) \tag{8.7}$$

with

$$a = K^2/EI(GJ - Pr_0^2)$$
$$b = PL^2/EI \tag{8.8}$$
$$c = Px_\alpha^2/EI(GJ - Pr_0^2)$$

The solution of the differential equation (8.6) is

$$W(\xi) = \overline{C}_1 + \overline{C}_2 \xi + \overline{C}_3 S(\alpha,\xi) + \overline{C}_4 C(\alpha,\xi) \tag{8.9}$$

where $\overline{C}_1 - \overline{C}_4$ are constants, and

$$\alpha = \sqrt{j\overline{a}^2} \tag{8.10}$$

$j = 1$ when $\overline{a}^2$ is positive, $j = -1$ when $\overline{a}^2$ is negative and

$$j = 1; \ S(\alpha,\xi) = \sin\alpha\xi; \ C(\alpha,\xi) = \cos\alpha\xi \ \text{ for } \overline{a}^2 > 0 \tag{8.11a}$$

$$j = -1; \ S(\alpha,\xi) = \sinh\alpha\xi; \ C(\alpha,\xi) = \cosh\alpha\xi \text{ for } \overline{a}^2 < 0 \tag{8.11b}$$

$W(\xi)$ in Eqn (8.9) represents the solution for both the flexural displacement u and the torsional rotation ψ, but with different constants. Thus

$$u(\xi) = C_1 + C_2 \xi + C_3 S(\alpha,\xi) + C_4 C(\alpha,\xi) \tag{8.12}$$

$$\psi(\xi) = C_5 + C_6 \xi + C_7 S(\alpha,\xi) + C_8 C(\alpha,\xi) \tag{8.13}$$

It can be readily verified by substituting equations (8.12) and (8.13) into equation (8.4), that the constants C_7 and C_8 are related to the constants C_3 and C_4 by

$$C_7 = (v/L)C_3 + (j\mu\alpha/L)C_4 \tag{8.14a}$$

$$C_8 = (\mu\alpha/L)C_3 - (v/L)C_4 \tag{8.14b}$$

where

$$\mu = K/(GJ - \mathrm{Pr}_0^2); \quad v = PLx_\alpha/(GJ - \mathrm{Pr}_0^2) \tag{8.15}$$
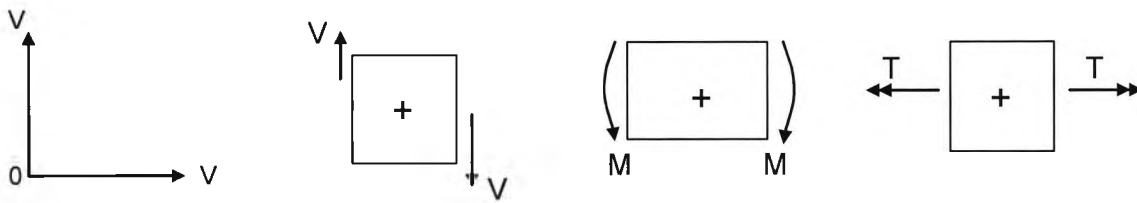
Figure 8.2   Sign conversion for positive shear force (V) bending moment (M) and torque (T) at the elastic axis.

Using the sign convention of Figure 8.2, the anticlockwise rotation $\theta(\xi)$, the bending moment $M(\xi)$, the shear force $V(\xi)$ and the torque $T(\xi)$ can be obtained by substituting equations (8.12) and (8.13) into the following equations

$$\theta(\xi) = (1/L)\, du/d\xi \tag{8.16}$$

$$M(\xi) = (EI/L^2)\, d^2u/d\xi^2 - (K/L)\, d\psi/d\xi \tag{8.17}$$

$$V(\xi) = (EI/L^3)\, d^3u/d\xi^3 + (K/L^2)\, d^2\psi/d\xi^2 + (P/L)(du/d\xi - x_\alpha\, d\psi/d\xi) \tag{8.18}$$

$$T(\xi) = (GJ/L)\, d\psi/d\xi + (K/L^2)\, d^2u/d\xi^2 - (\mathrm{Pr}_0^2/L)\, du/d\xi + (Px_\alpha/L)\, du/d\xi \tag{8.19}$$

The end conditions for displacements and forces, see Figure 8.3, are respectively,

at end 1 $(\xi = 0)$; $u = u_1$; $\theta = \theta_1$ and $\psi = \psi_1$ \hfill (8.20a)

at end 2 $(\xi = 1)$; $u = u_2$; $\theta = \theta_2$ and $\psi = \psi_2$ \hfill (8.20b)

and

at end 1 $(\xi = 0)$; $V = V_1$; $M = M_1$ and $T = T_1$ \hfill (8.21a)

at end 2 $\left(\xi =1\right)$; $V = V_2$; $M = -M_2$ and $T = T_2$ (8.21b)
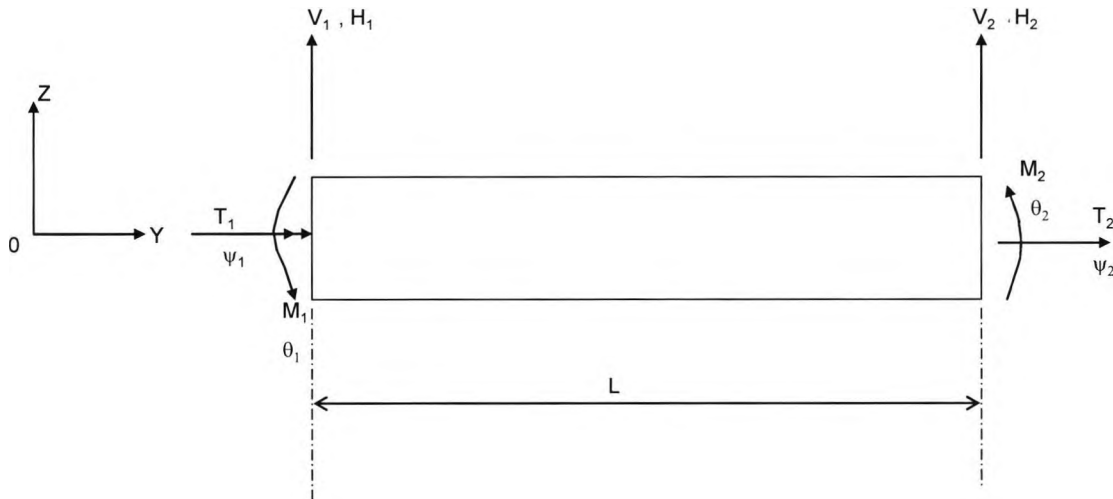
Figure 8.3   End conditions for forces and displacements at the elastic axis

Substituting equations (8.20) into equations (8.12), (8.13) and (8.16) and making use of equations (8.14), the end displacements of the column can be related to the constants $C_1 - C_4$ by

$$
\begin{bmatrix} u_1 \\ \theta_1 \\ \psi_1 \\ u_2 \\ \theta_2 \\ \psi_2 \end{bmatrix} = \begin{bmatrix} 1 & 0 & 0 & 1 & 0 & 0 \\ 0 & 1/L & \alpha/L & 0 & 0 & 0 \\ 0 & 0 & -\alpha\mu/L & -v/L & 1 & 0 \\ 1 & 1 & S_\alpha & C_\alpha & 0 & 0 \\ 0 & 1/L & \alpha C_\alpha/L & -j\alpha S_\alpha/L & 0 & 0 \\ 0 & 0 & h_\alpha/L & k_\alpha/L & 1 & 1 \end{bmatrix} \begin{bmatrix} C_1 \\ C_2 \\ C_3 \\ C_4 \\ C_5 \\ C_6 \end{bmatrix}
$$
(8.22)

or

$$U = AC$$ (8.23)

where

$$S_\alpha = \sin\alpha; \ C_\alpha = \cos\alpha \ \text{for} \ \overline{a}^2 > 0$$ (8.24a)

$$S_\alpha = \sinh\alpha; \ C_\alpha = \cosh\alpha \ \text{for} \ \overline{a}^2 < 0$$ (8.24b)

and

$$h_\alpha = -vS_\alpha - \alpha\mu C_\alpha; \quad k_\alpha = -j\alpha\mu S_\alpha - vC_\alpha \tag{8.25}$$

Substituting the end conditions for forces given by equations (8.21) into Eqns (8.17) - (8.19) and making use of Eqns (8.12)-(8.15), the end forces can be related to the unknown constants by

$$
\begin{bmatrix} V_1 \\ M_1 \\ T_1 \\ V_2 \\ M_2 \\ T_2 \end{bmatrix} =
\begin{bmatrix}
0 & P/L & 0 & 0 & 0 & -Px_\alpha/L \\
0 & 0 & \alpha vK/L^2 & j\alpha^2(EI-\mu K)/L^2 & 0 & -K/L \\
0 & -Px_\alpha/L & 0 & 0 & 0 & -(GJ-Pr_0^2)/L \\
0 & -P/L & 0 & 0 & 0 & -Px_\alpha/L \\
0 & 0 & -f_\alpha/L^2 & -g_\alpha/L & 0 & K/L \\
0 & Px_\alpha/L & 0 & 0 & 0 & (GJ-Pr_0^2)/L
\end{bmatrix}
\begin{bmatrix} C_1 \\ C_2 \\ C_3 \\ C_4 \\ C_5 \\ C_6 \end{bmatrix} \tag{8.26}
$$

or

$$\mathbf{F} = \mathbf{BC} \tag{8.27}$$

where

$$f_\alpha = \alpha vKC_\alpha + j\alpha^2(EI-\mu K)S_\alpha \tag{8.28a}$$

$$g_\alpha = j\alpha^2(EI-\mu K)C_\alpha - j\alpha vKS_\alpha \tag{8.28b}$$

Eliminating C from equation (8.27) with the help of equation (8.23) gives

$$\mathbf{F} = \mathbf{KU} \tag{8.29}$$

or

$$
\begin{bmatrix} V_1 \\ M_1 \\ T_1 \\ V_2 \\ M_2 \\ T_2 \end{bmatrix} =
\begin{bmatrix}
K_{1,1} & K_{1,2} & K_{1,3} & K_{1,4} & K_{1,5} & K_{1,6} \\
 & K_{2,2} & K_{2,3} & K_{2,4} & K_{2,5} & K_{2,6} \\
 & & K_{3,3} & K_{3,4} & K_{3,5} & K_{3,6} \\
 & & & K_{4,4} & K_{4,5} & K_{4,6} \\
 & Sym. & & & K_{5,5} & K_{5,6} \\
 & & & & & K_{6,6}
\end{bmatrix}
\begin{bmatrix} u_1 \\ \theta_1 \\ \psi_1 \\ u_2 \\ \theta_2 \\ \psi_2 \end{bmatrix} \tag{8.30}
$$

where

$$\mathbf{K=BA^{-1}} \tag{8.31}$$

is the required stiffness matrix.

The stiffness matrix of equation (8.31) is obtained by inverting the A matrix of equations (8.22) and (8.23) and premultiplying by the matrix B of equations (8.26) and (8.27). This can

be done numerically or algebraically. However, if explicit analytical expressions for each of the stiffness elements of Eqn (8.30) are generated by performing the matrix inversion and matrix multiplication steps of Eqn (8.31) algebraically (or symbolically), a significant saving in computational time can be achieved, as demonstrated by Banerjee and Williams [8.32] in their investigations on related problems. Explicit expressions are particularly useful when some, but not all, of the stiffness terms are needed. So the tedious task of inverting the A matrix algebraically and premultiplying the resulting matrix by the B matrix was undertaken, using the symbolic computing package REDUCE [8.33, 8.34]. The derived expressions are presented in concise form in Eqn (8.32), as follows

$$
\left.
\begin{aligned}
K_{1,1} &= K_{4,4} = K_{1,1} = \left(EI/L^3 \right) \Phi_1/\Delta \\
K_{1,2} &= K_{2,4} = \left(EI/L^2 \right) \Phi_2/\Delta \\
K_{1,3} &= K_{4,6} = -K_{1,6} = -K_{3,4} = \left(EI/L^2 \right) \Phi_3/\Delta \\
K_{1,5} &= K_{4,5} = \left(EI/L^2 \right) \Phi_4/\Delta \\
K_{2,2} &= \left(EI/L \right) \Phi_5/\Delta \\
K_{2,3} &= K_{5,6} = -K_{2,6} = -K_{3,5} = \left(EI/L \right) \Phi_6/\Delta \\
K_{2,5} &= \left(EI/L \right) \Phi_7/\Delta \\
K_{3,3} &= K_{6,6} = -K_{3,6} = \left(GJ/L \right) \Phi_8/\Delta \\
K_{5,5} &= \left(EI/L \right) \Phi_9/\Delta
\end{aligned}
\right\}
\tag{8.32}
$$

where

$$
\eta = K/EI \,; \zeta = 1 - \mathrm{Pr}_0^2/GJ \,; \varepsilon = x_\alpha/L
\tag{8.33}
$$

$$
\delta = 1 + \varepsilon v \,; \gamma = \mu + v \,; \lambda = 1 - \eta \mu
\tag{8.34}
$$

$$
\Delta = \alpha S_\alpha - 2j \left(1 - C_\alpha \right)
\tag{8.35}
$$

and

$$\left.\begin{aligned}
\Phi_1 &= -b\left(\alpha S_\alpha + 2j\varepsilon v\left(1-C_\alpha\right)\right)\\
\Phi_2 &= b\left(\mu\Delta - \alpha S_\alpha + j\delta\left(1-C_\alpha\right)\right)\\
\Phi_3 &= b\varepsilon\Delta\\
\Phi_4 &= b\Delta + \Phi_1 - \Phi_2\\
\Phi_5 &= \mu\gamma\Delta + \alpha\lambda\left(\alpha C_\alpha - S_\alpha\right)\\
\Phi_6 &= \eta\Delta\\
\Phi_7 &= -\eta\mu\Delta - \alpha\lambda\left(\alpha - S_\alpha\right)\\
\Phi_8 &= \zeta\Delta\\
\Phi_9 &= \Phi_5 - 2\eta v\Delta
\end{aligned}\right\} \qquad (8.36)$$

The geometric coupling term x_a, and/or the material coupling term K, can optionally be substituted to zero in the above stiffness expressions without causing any overflow or underflow (i.e. division by zero), but the axial load P must not be substituted to zero. When the shear centre and centroid of the cross-section coincide, x_a is put to zero in Eqns (8.32) to (8.36) and the remaining matrix represents the exact stiffness matrix of a composite column with no geometric coupling, as it can occur for many common and practical closed sections. Then, the stiffness elements $K_{1,3}$, $K_{4,6}$, $K_{1,6}$ and $K_{3,4}$ of Eqns (8.30)-(8.31) are zero, because $\Phi_3 = 0$ when $x_\alpha = 0$. Similarly, when K is put to zero in equations (8.32) to (7.36) the resulting matrix represents the exact stiffness matrix of a metallic column with only geometric coupling, which is expectedly the same as what was obtained by Renton [8.17, 8.18]. Furthermore, for a metallic column, the coupling between flexure and torsion occurs only in the presence of an axial load P. Hence, when $P = 0$, the stiffness matrix becomes the standard one of the usual uncoupled Bernoulli-Euler beam [8.35]. Nevertheless, a separate set of stiffness expressions are needed when $P = 0$. The elements of the stiffness matrix for any value of x_α, but with $P = 0$ can be expressed in the following simple form

$$\left.\begin{aligned}
K_{1,1} &= K_{4,4} = K_{1,4} = \left(12EI/L^3\right)\left(1 - K^2/EIGJ\right)\\
K_{1,2} &= K_{1,5} = -K_{2,4} = -K_{4,5} = \left(6EI/L^2\right)\left(1 - K^2/EIGJ\right)\\
K_{1,3} &= K_{4,6} = K_{1,6} = K_{3,4} = 0\\
K_{2,2} &= K_{5,5} = \left(4EI/L\right)\left(1 - 3K^2/4EIGJ\right)\\
K_{2,3} &= K_{5,6} = -K_{2,6} = -K_{3,5} = K/L\\
K_{2,5} &= \left(2EI/L\right)\left(1 - 3K^2/2EIGJ\right)\\
K_{3,3} &= K_{6,6} = -K_{3,6} = GJ/L
\end{aligned}\right\} \qquad (8.37)$$

When the flexure torsion material coupling term K is set to zero, Equation (8.37) gives the stiffness matrix of the usual uncoupled Bernoulli-Euler beam [8.35]. The determination of the elastic critical buckling load of a single composite column, or of a structure assembled from such columns, follows from the application of the Wittrick-Williams algorithm [8.19, 8.20], either to the single exact stiffness matrix of the column or to the overall stiffness matrix assembled from such columns, respectively. The same principle applies when calculating the elastic critical buckling load of metallic columns.

8.2.2 Theory for metallic column

The governing differential equation for flexural-torsional buckling of metallic columns can be derived in the same way as for the composite column, but $K = 0$ with in Eqns (8.1) and (8.2), so that the equivalent of Eqn (8.6) is

$$D^2\left(D^2 + \alpha_m^{-2}\right)W = 0 \tag{8.38}$$

where

$$\alpha_m^{-2} = b\left(1 - \frac{c}{(1-a)}\right) \tag{8.39}$$

with

$$\left.\begin{array}{l} a = GJ/\mathrm{P}r_0^2 \\ b = PL^2/EI \\ c = x_a^2/r_0^2 \end{array}\right\} \tag{8.40}$$

$$\left.\begin{array}{l} K_{1,1} = K_{4,4} = -K_{1,4} = \left(EI/L^3\right)\left(\Phi_1/\Delta\right) \\ K_{1,2} = K_{1,5} = -K_{4,5} = -K_{2,4} = \left(EI/L^2\right)\left(\Phi_2/\Delta\right) \\ K_{1,3} = K_{4,6} = -K_{1,6} = -K_{3,4} = \left(EI/L^2\right)\left(\Phi_3/\Delta\right) \\ K_{2,2} = K_{5,5} = \left(EI/L\right)\left(\Phi_4/\Delta\right) \\ K_{2,3} = K_{5,6} = K_{2,6} = K_{3,5} = 0 \\ K_{2,5} = \left(EI/L\right)\left(\Phi_5/\Delta\right) \\ K_{3,3} = K_{6,6} = -K_{3,6} = \left(GJ/L\right)\left(\Phi_6/\Delta\right) \end{array}\right\} \tag{8.41}$$

$$\Phi_1 = -b\left(\alpha S_\alpha - 2jc(1-C_\alpha)/(1-a)\right)$$
$$\Phi_2 = -\alpha^2(1-C_\alpha)$$

where
$$\Phi_3 = b\varepsilon\Delta$$
$$\Phi_4 = \alpha(\alpha C_\alpha - S_\alpha)$$
$$\Phi_5 = \alpha(\alpha C_\alpha - \alpha)$$
$$\Phi_6 = \zeta\Delta$$

$$(8.42)$$

with (using $j = \pm 1$ to make α real

$$\alpha = \sqrt{j}\,\alpha_m^{-2}; \quad \varepsilon = x_\alpha/L; \quad \zeta = 1 - \mathrm{Pr}_0^2/GJ \qquad (8.43)$$

$$\Delta = -\alpha S_\alpha - 2j(1-C_\alpha) \qquad (8.44)$$

and

$$j = 1; \quad S_\alpha = \sin\alpha; \quad C_\alpha = \cos\alpha \quad \text{for } \alpha_m^{-2} > 0$$
$$j = -1; \quad S_\alpha = \sinh\alpha; \quad C_\alpha = \cosh\alpha \quad \text{for } \alpha_m^{-2} < 0$$

$$(8.45)$$

For a metallic column, the coupling between flexure and torsion is caused by the geometric coupling term x_α as can be seen above, the coupling occurs only in the presence of an axial load P. Hence when $P = 0$, the stiffness matrix becomes the standard one of the usual uncoupled Bernouli-Euler beam [8.35] i.e Eqn. (8.37) with $K = 0$. The stiffness given by Eqns (8.41)-(8.45) are essentially the same as obtained by Renton [8.18]. The stiffness expressions from the composite column given by Eqn. (8.32) with the material coupling term $K = 0$, give the same stiffnesses as the expression for the metallic column given above, as expected.

8.2.3 Application of the exact stiffness matrix

The determination of the elastic critical buckling load of a single composite (or metallic) column, or of a structure assembled from such columns, follows from the application of the Wittrick-Williams algorithm [8.19, 8.20] to, respectively, either the single exact stiffness matrix assembled from such columns. For clarity and completeness, the procedure is now briefly summarised.

If the load factor F, which scales either the datum load P in the single columns forming a structure, is increased from zero to F^*, the number of critical buckling load passed i.e. exceeded, is given by

$$J = J_0 + s\{K_f(F^*)\} \qquad (8.46)$$

where $K_f(F^*)$ is the overall stiffness matrix revaluated at $F = F^*$, $s\{K_f(F^*)\}$ is the number of negative elements on the leading diagonal of the triangulated matrix obtained by applying Gauss elimination in its usual form to $K_f(F^*)$ and J_0 is the number of critical buckling loads of the structure still exceeded by $F = F^*$ when the displacement components to which $K_f(F^*)$ corresponds are all constrained to be zero. J_0 can still be non-zero even when these constraints clamp both ends of every member of the structure (as is always the case if substructuring has not been used) because exact member equations allow each member to have infinite number of buckling modes when its ends are clamped. Thus

$$J_0 = \sum J_m \qquad (8.47)$$

where J_m is the number of critical buckling loads between $F = 0$ and $F = F^*$ for component column with its ends clamped, while the summation is over all the columns of the structure. (Clearly, for an unloaded member or member with tensile load, J_m will be always zero.) Hence Eqns (8.46) and (8.47) used with Eqns (8.32) or (8.41), enable the critical buckling load of the structure to be found with ease and certainty, e.g. by bi-section, since J can be computed for each successive trial value F^* of the load factor.

As mentioned in the above paragraph, the identification of the clamped-clamped critical buckling load (i.e. buckling load with clamped-clamped end conditions) of each individual column in a structure is an essential requirement for the application of the Witrrick-Williams algorithm so as to ensure that no critical buckling load of the structure is missed. Thus, an explicit expression from which the clamped-clamped critical buckling loads can be found, facilitates an easy and straightforward application of the algorithm. Δ in Eqn, (8.35) is such an expression for a metallic column and Δ in Eqn. (8.44) is the corresponding expression for metallic column, because the clamped-clamped buckling loads are given by $\Delta = 0$.

8.3 Results and discussion

In the following, the stiffness matrix for the degenerated case of the metallic column, for which geometric coupling exists but there is no material coupling, is obtained from the general case. Using the exact stiffness matrices developed and applying the Wittrick-Williams

algorithm [8.19] in the usual way, critical buckling loads are calculated for representative examples of metallic (flat) and composite (flat, and box) columns. Only the first critical buckling load, which is of practical importance, is calculated in each case. It should be noted that although for simplicity, attention is confined to singly or doubly symmetric cross-sections (most commonly used shapes), the theory developed here can be readily extended to other cross-sections.

The first example is the MIT beam [8.36] previously investigated in Chapter 7 for rigidity properties. The laminated composite beam $(\pm\theta_2/0)_s$, has the following characteristics; length $(L) = 0.3048$ m, width $(c) = 0.0762$ m, thickness $(t) = 0.804$mm, mass per unit length $(m) = 93.1225 \times 10^{-3}$ kg/m and mass moment inertia per unit length, $I_\alpha = 45.0641985 \times 10^{-6}$ kgm, $X_\alpha = 0.001$ and $r^0 = 0.002320948$. Figure 8.4 shows the variation of the buckling load of the column against ply angle for cantilever configuration - clamped-free (C-F) end conditions. The buckling load decreases when the ply angle increases as expected.
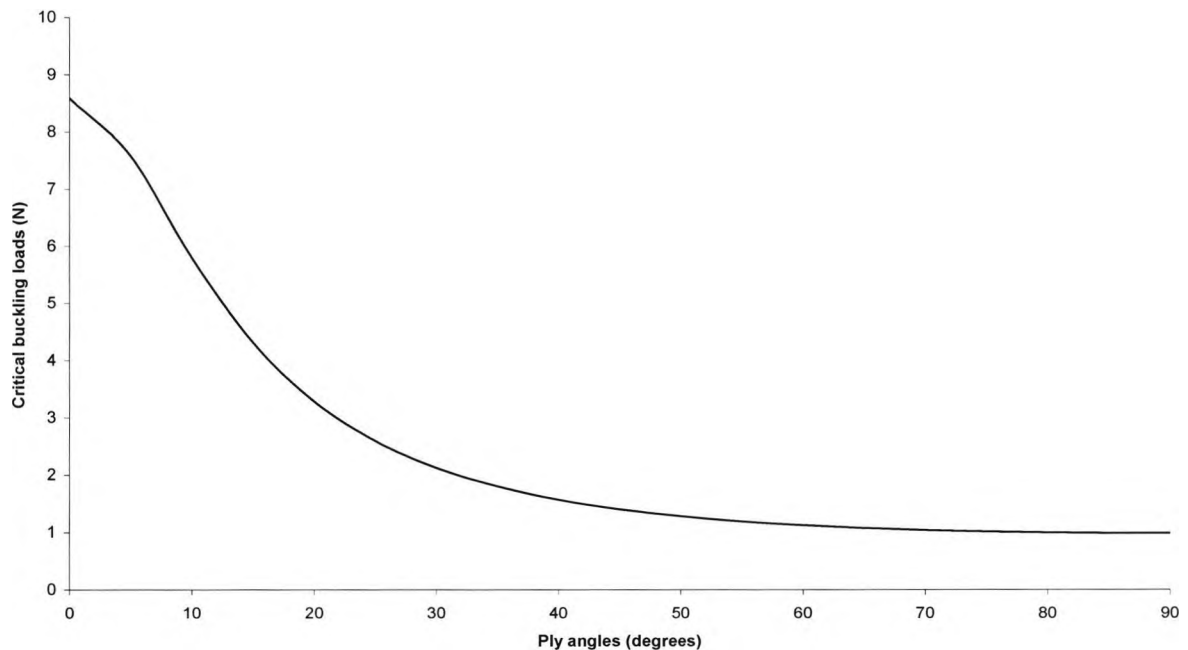
Figure 8.4   The influence of ply angle orientation into critical buckling load for the MIT beam

The second example is a rectangular box column (GIT box-beam) made of carbon fibre-reinforced composite (CFRP) whose rigidity properties are given in Chapter 7. The box-beam is of length (L) = 2.032 m, depth, (h) = 0.0508 m, width (c) = 0.254 mm, thickness (t) = 0.254mm, mass per unit length (m) = 5.82216 kg/m and mass moment inertia per unit length, I_α = 3.3162 x10^{-2} kgm, $X_\alpha = 0.001$ and $r^0 = 0.019612$. In Chapter 7, the stiffness are symmetrical about $\beta = 0^0$ and the fibre angle is allowed to vary between $\beta = 0^0$ and 90^0. Figure 8.5 shows the variation of the buckling load of the column against ply angle for cantilever configuration (C-F), as expected, the buckling load decreases when the ply angles increase.
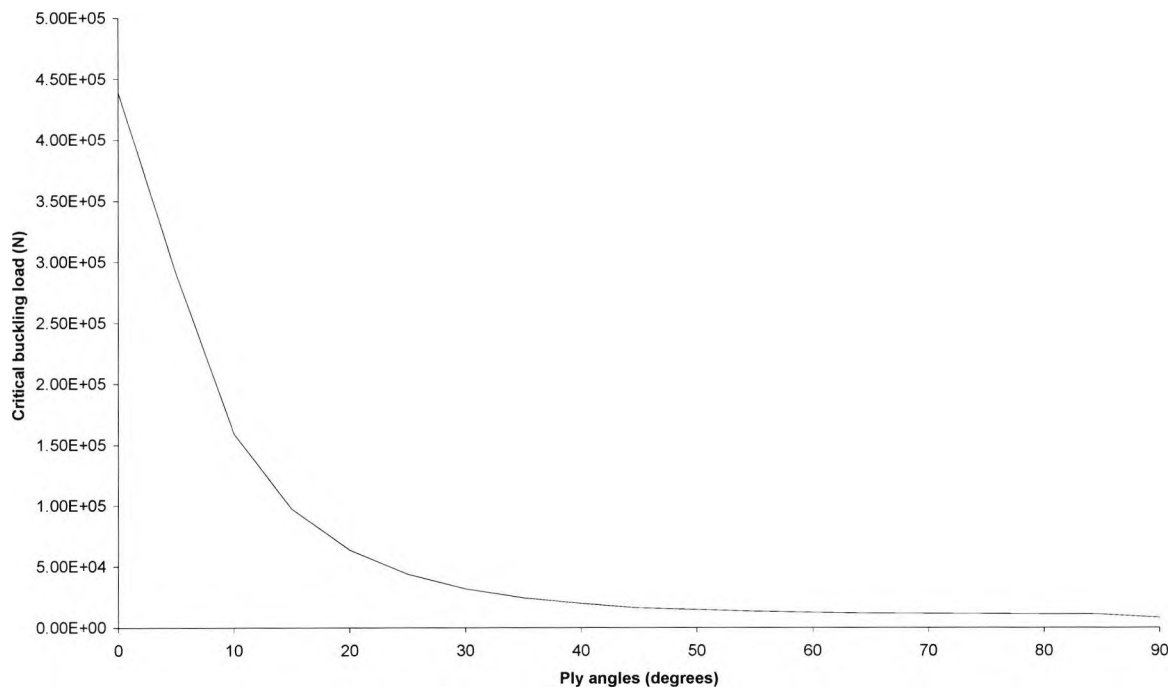
Figure 8.5   The critical buckling load for GIT beam

The third example is a metallic column with the following properties; EI=70 GPa, GJ=27 GPa length = 0.2459 m, width = 0.0295 m and 0.0012m thickness. An experimental buckling investigation was carried out using Instron Testing Machine to completement the dynamic stiffness method. The critical elastic buckling loads were calculated for C-C end conditions for the column and are presented in Table 8.1. The results show very good agreement with the

experimental ones. These results were then compared with those given by Akesson [8.37]. He proposed the following equation which represents the non-dimensionalised exact expression of the critical elastic buckling load of an individual column with classical end conditions, when coupling exists between bending and torsional deformations [8.37]

$$P_{y\theta} = \frac{P_y - P_\theta}{2\left(1 - x_\alpha^2/r_0^2\right)} \left\{ 1 - \frac{4 P_y P_\theta}{\left(P_y - P_\theta\right)^2}\left(1 - x_\alpha^2/r_0^2\right)^{0.5} \right\}$$

(8.48)

where

$$P_y = \frac{\pi^2 EI}{\lambda^2 L^2} \text{ and } P_\theta = \frac{GJ}{r_0^2}$$

(8.49)

with λ = 2, 1, 0.6992 and 0.5 for clamped-free (C-F), (S-S), (C-S) and (C-C) end conditions, respectively. The results for the beam columns agreed with the results obtained using Akesson's theory [8.37].

Table 8.1   The comparison of the theoretical and experimental critical buckling results

Length, L (m)	Theoretical results, P_{Cr} (N)	Experimental results, P_{Cr} (N)
0.25	48.5	46
0.2	73.4	71
0.2	60.6	56

8.4   Conclusions

Analogously, a composite structure can also be tailored to achieve desirable buckling strength and this work forms a basic step towards this important goal. Several numerical examples have been given for illustrative purposes. Simultaneous flexure and twist in a composite column, caused by both geometric and material coupling terms, which are usually

present in thin-walled cross-section are included in the theory. Applications of the derived stiffness matrices are discussed with particular reference to the Wittrick-Williams algorithm that is generally used in transcendental eigen-value as in the present case. The results are fully discussed and commented on. In short, the results obtained from the present method are in agreement with other theories on flexural-torsional buckling behaviour and the small discrepancies among the results can be due to the assumptions between different theories. The present theory provides a conservative estimate of the elastic buckling load. The primary contribution of this work is to include the material coupling effect for a composite column when establishing its stiffness matrix for exact bending-torsion buckling analysis. Although for simplicity, attention is confined to singly or doubly symmetric cross-sections (most commonly used shapes), the theory developed here can be readily extended to other cross-sections.

9 Free vibration of composite beams with application to aircraft wings

9.1 Introduction

The free vibration analysis of laminated composite beams has attracted considerable attention in recent years [9.1-9.6]. An important finding of this research has shown that the material coupling in composite beams which arises as a result of stacking sequence and ply orientation can have profound effect on the free vibration characteristics. This can be significant from the point of view of vibration [9.7] and aeroelastic tailoring [9.8, 9.9]. The vibration problems of composite beams are generally solved using numerical methods because of the inherent difficulties involved in obtaining closed form analytical solutions. However, the recent advancement in symbolic computation [9.10] has made it possible to solve engineering problems algebraically rather than numerically. It has thus been possible to derive explicit expressions for the frequency equations and mode shapes of cantilever composite beams [9.11]. The present investigation is focused on obtaining results for two different types of carbon-epoxy composite beams by using the theory developed in Ref. [9.11]. The first type of composite beam considered has featured in the literature [9.12] from a programme of research at the Massachusetts Institute of Technology, USA. This beam is referred to as MIT-beam. The latter type is referred to as GIT-beam [9.13] because it stems from research at the Georgia Institute of Technology, USA. The MIT-beam is flat and of solid rectangular cross-section with stacking sequence $[\theta_2/0]_s$. In contrast the GIT-beam is of box cross-section with lay-ups for the top, bottom, front and rear sides being $[+\theta/+\theta]$, $[-\theta/-\theta]$, $[+\theta/-\theta]$ and $[-\theta/+\theta]$, respectively. (See Table 7.1, for the material properties of the two beams, Chapter 7). Both of these types of composite beams exhibit coupling between bending and torsional modes of deformation which is important from an aeroelastic point of view. First the stiffness properties of these beams are obtained using classical lamination theory. Next, these beams with cantilever end conditions are examined in detail for their free vibration characteristics. This is relevant in the context of composite aircraft wings. In particular the effect of the ply angle (θ) on the first five natural frequencies and mode shapes of the above two types of composite beams are studied. One of the intriguing features of the investigation is that the ply orientation in the laminate can cause modal interchanges (or

swap-over), and as a consequence, the character of a mode can change fundamentally. For instance, a bending dominated mode can change to a torsion dominated one and vice versa due to ply orientation in the laminate. The results presented in this chapter highlight some of these interesting features

9.2   Theory

Stiffness or rigidity modelling of bending-torsion materially coupled composite beams of both solid and thin-walled cross sections has been reported in the literature by a number of investigators [9.13-9.17]. It is generally acknowledged that in essence there are three main structural parameters that characterise a bending-torsion coupled composite beam. These are the bending rigidity, EI, the torsional rigidity, GJ, and bending-torsion material coupling rigidity, K. However, for composite beams or wings the bending-torsion material coupling rigidity K is of great significance because it is dependent on the ply orientation and stacking sequence which can be altered favourably, particularly for the purposes of aeroelastic tailoring [9.8, 9.9]. There have been several attempts [9.13-9.17] to obtain the theoretical and experimental values for the rigidities EI, GJ, and K that are essential to the derivation of frequency equation and mode shapes of composite beams [9.11](see Chapter 7).

Figure 7.1 in Chapter 7 shows a straight composite beam of length L with a solid rectangular cross section and with a symmetric but unbalanced lay-up. It is well known that bending-torsion coupling occurs for such configurations [9.6, 9.7, 9.14-9.16, 9.18]. The rectangular cross-section is considered here only for convenience, but the theory developed can be applied to composite beams of any general cross-section so long as the rigidities EI, GJ and K are known (either by theory or by experiment). In the right-handed axis system shown, the Y-axis which coincides with the (central) geometric axis, is permitted to have bending displacement $h(y, t)$ and torsional rotation $\psi(y, t)$ where y is measured from the origin shown and t is time. Using the coupled bending-torsional beam theory for thin-walled composites with shear deformation, rotatory inertia and warping effects neglected, the governing differential equations of motion of the beam in free vibration are given by [9.6, 9.11]

$$EIh'''' + K\psi''' + m\ddot{h} = 0 \qquad\qquad (9.1)$$

$$GJ\psi'' + Kh''' - I_a\ddot{\psi} = 0 \tag{9.2}$$

where m is the mass per unit length along the Y-axis, I_a is the polar mass moment of inertia per unit length about the Y axis, and primes and dots denote differentiation with respect to position y and t, respectively.

If a harmonic (periodic) variation of h and ψ, with circular frequency ω, is assumed, then

$$h(y, t) = H(y)\, e^{i\omega t},$$

$$\psi(y, t) = \Psi(y)\, e^{i\omega t} \tag{9.3}$$

where $H(y)$ and $\Psi(y)$ are the amplitudes of the sinusoidally varying bending displacement and torsional rotation, respectively.

Substituting eqns (9.3) into eqns (9.1) and (9.2) gives

$$EIH'''' + K\Psi''' - m\omega^2 H = 0 \tag{9.4}$$

$$GJ\Psi'' + KH''' + I_\alpha\omega^2\Psi = 0 \tag{9.5}$$

Introducing the non-dimensional length ξ and the differential operator D as follow

$$\xi = y/L$$

$$D = d/d\xi \tag{9.6}$$

equations (9.4) and (9.5) can be combined into one equation by eliminating either H or Ψ to give

$$(D^6 + aD^4 - bD^2 - abc)W = 0 \tag{9.7}$$

where

$$W = H \text{ or } \Psi \tag{9.8}$$

$$a = \bar{a}/c$$

$$b = \bar{b}/c$$

$$c = 1 - K^2/(EIGJ) \tag{9.9}$$

with

$$\bar{a} = I_\alpha\omega^2 L^2/GJ$$

$$\bar{b} = m\omega^2 L^4/EI \tag{9.10}$$

In eqn (9.7) a, b and c are non-dimensional coefficients of the differential equation and are all positive because it is known that [9.7]

$0 < c < 1$ (9.11)

The solution of the differential equation (7.7) shows that both $H(\xi)$ and $\Psi(\xi)$ have the form [9.6, 9.11]

$W(\xi) = C_1 \cosh\alpha\xi + C_2 \sinh\alpha\xi + C_3 \cos\beta\xi + C_4 \sin\beta\xi + C_5 \cos\gamma\xi + C_6 \sin\gamma\xi$ (9.12)

where C_1-C_6 are constants, and

$\alpha = \pm[2(q/3)^{1/2} \cos(\phi/3) - a/3]^{1/2}$

$\beta = \pm[2(q/3)^{1/2} \cos\{(\pi - \phi)/3\} + a/3]^{1/2}$

$\gamma = \pm[2(q/3)^{1/2} \cos\{(\pi + \phi)/3\} + a/3]^{1/2}$ (9.13)

with

$q = b + a^2/3$

$\phi = \cos^{-1}[(27abc - 9ab - 2a^3)/\{2(a^2 + 3b)^{3/2}\}]$ (9.14)

Hence,

$H(\xi) = A_1 \cosh\alpha\xi + A_2 \sinh\alpha\xi + A_3 \cos\beta\xi + A_4 \sin\beta\xi + A_5 \cos\gamma\xi + A_6 \sin\gamma\xi$ (9.15)

$\Psi(\xi) = B_1 \cosh\alpha\xi + B_2 \sinh\alpha\xi + B_3 \cos\beta\xi + B_4 \sin\beta\xi + B_5 \cos\gamma\xi + B_6 \sin\gamma\xi$ (9.16)

where $A_1 - A_6$ and $B_1 - B_6$ are two different sets of constants.

Substituting Eqns (9.15) and (9.16) into Eqn (9.4) shows that the constants $A_1 - A_6$ are related to the constants $B_1 - B_6$ by the following relationships:

$B_1 = (k_\alpha/L)A_2, \quad B_2 = (k_\alpha/L)A_1, \quad B_3 = (k_\beta/L)A_4, \quad B_4 = -(k_\beta/L)A_3, \quad B_5 = (k_\gamma/L)A_6,$

$B_6 = -(k_\gamma/L)A_5$

(9.17)

where

$k_\alpha = (\bar{b} - \alpha^4)/(\bar{k}\alpha^3),$

$k_\beta = (\bar{b} - \beta^4)/(\bar{k}\beta^3),$

$k_\gamma = (\bar{b} - \gamma^4)/(\bar{k}\gamma^3)$ (9.18)

with

$\bar{k} = K/EI$ (9.19)

The expressions for bending rotation $\Theta(\xi)$, the bending moment $M(\xi)$, the shear force $S(\xi)$, and the torque $T(\xi)$, can be obtained from eqns (9.15) and (9.16) as follows with prime now denoting differentiation with respect to ξ instead of y [9.6, 9.11]

$$\Theta(\xi)=H'(\xi)/L=(1/L)\{A_1\alpha\sinh\alpha\xi+A_2\alpha\cosh\alpha\xi -A_3\beta\sin\beta\xi+A_4\beta\cos\beta\xi -A_5\gamma\sin\gamma\xi +A_6\gamma\cos\gamma\xi\}$$

$$(9.20)$$

$$M(\xi)= - (EI/L^2)H''(\xi)-(K/L)\Psi'(\xi)$$

$$= - (EI/L^2)\{H''(\xi)+ \bar{k}L\,\Psi'(\xi)\}$$

$$=-(EI/L^2)\{A_1\,\bar{\alpha}\cosh\alpha\xi+A_2\,\bar{\alpha}\sinh\alpha\xi- A_3\,\bar{\beta}\cos\beta\xi-A_4\,\bar{\beta}\sin\beta\xi -A_5\,\bar{\gamma}\cos\gamma\xi - A_6\,\bar{\gamma}\sin\gamma\xi\}$$

$$(9.21)$$

$$S(\xi) = (EI/L^3)H'''(\xi) + (K/L^2)\Psi''(\xi)$$

$$= (EI/L^3)\{H'''(\xi)+ \bar{k}L\,\Psi''(\xi)\}$$

$$= (EI/L^3)\{A_1\alpha\,\bar{\alpha}\sinh\alpha\xi+A_2\alpha\,\bar{\alpha}\cosh\alpha\xi +A_3\beta\,\bar{\beta}\sin\beta\xi - A_4\beta\,\bar{\beta}\cos\beta\xi+A_5\gamma\,\bar{\gamma}\sin\gamma\xi$$

$$- A_6\gamma\,\bar{\gamma}\cos\gamma\xi\}$$

$$(9.22)$$

$$T(\xi) = (GJ/L)\Psi'(\xi) + (K/L^2)H''(\xi)$$

$$= (GJ/L)\{\Psi'(\xi) + (K/GJL)H''(\xi)\}$$

$$= (GJ/L^2)(A_1g_\alpha\cosh\alpha\xi+A_2g_\alpha\sinh\alpha\xi -A_3g_\beta\cos\beta\xi-A_4\,g_\beta\sin\beta\xi-A_5g_\gamma\cos\gamma\xi-A_6g_\gamma\sin\gamma\xi)$$

$$(9.23)$$

where

$$\bar{\alpha}= \bar{b}/\alpha^2, \quad \bar{\beta}= \bar{b}/\beta^2, \quad \bar{\gamma}= \bar{b}/\gamma^2$$

$$(9.24)$$

$$g_\alpha =(\bar{b}-c\alpha^4)/(\bar{k}\alpha^2),$$

$$g_\beta =(\bar{b}-c\beta^4)/(\bar{k}\beta^2),$$

$$g_\gamma =(\bar{b}-c\gamma^4)/(\bar{k}\gamma^2)$$

$$(9.25)$$

The above expressions can be used to formulate the frequency equation and mode shapes of a composite beam for any classical boundary conditions including the demanding case of a cantilever [9.6, 9.11] as applicable to an aircraft wing or a helicopter blade.

9.2.1 Frequency Equation

The stiffness or rigidity modelling of bending-torsion materially coupled composite beams of both solid and thin-walled cross sections has been presented in the previous Chapter

(Chapter 7). The theory is now used to formulate the frequency equation and mode shapes of a composite beam for any classical boundary conditions. The demanding case of a cantilever as applicable to an aircraft wing or a helicopter blade is taken up in detail the following.

The frequency equation for a composite beam (see Figure 7.1, Chapter 7) with cantilever boundary conditions is now derived by applying the boundary conditions, and eliminating the arbitrary constants A_1–A_6. At the built-in end ($\xi = 0$), all displacements are zero, i.e. $H(\xi) = 0$, $\Theta(\xi) = 0$ and $\Psi(\xi) = 0$ whereas at the free end ($\xi = 1$), all forces are zeroes, i.e. $S(\xi) = 0$, $M(\xi) = 0$ and $T(\xi) = 0$. When these conditions are substituted into equations (9.15)-(9.16) and (9.20)-(9.23) and the constants A_1–A_6 are eliminated, the frequency equation is first obtained in a 6×6 determinantal form which is generally solved by numerical means to yield natural frequencies of the composite beam. Here the determinant is expanded algebraically, and then simplified very considerably. This formidable task was carried out with the help of the symbolic computation package *REDUCE* [9.17].

The expression for the frequency equation is given below in a surprisingly concise form

$$f(\omega)=\lambda_1 C_\beta\ C_\gamma\ C_{h\alpha}\ +\lambda_2 C_\beta\ S_\gamma\ S_{h\alpha}\ +\lambda_3 C_\gamma\ S_\beta\ S_{h\alpha}\ +\ \lambda_4\ S_\beta\ S_\gamma\ C_{h\alpha}\ +\xi_1 C_\beta\ +\xi_2 C_\gamma\ +\xi_3 C_{h\alpha}=0$$

$$(9.26)$$

where

$$C_{h\alpha}=\cosh\alpha\ ,C_\beta=\cos\beta,\ C_\gamma=\cos\gamma$$
$$S_{h\alpha}=\sinh\alpha, S_\beta=\sin\beta, S_\gamma=\sin\gamma \qquad (9.27)$$

and

$$\lambda_1=-2\alpha\ \bar{\alpha}\mu_2 v_2-\alpha\ \bar{\gamma}\mu_2 v_1-\ \bar{\alpha}\gamma\mu_1 v_2-2\gamma\ \bar{\gamma}\mu_1 v_1,$$
$$\lambda_2 =-\alpha\ \bar{\alpha}\mu_1 v_2 +\gamma\ \bar{\gamma}\mu_2 v_1,$$
$$\lambda_3 = -\alpha\ \bar{\alpha}\mu_3 v_2 -\ \bar{\alpha}\beta\mu_2 v_2 -\beta\ \bar{\gamma}\mu_2 v_1,$$
$$\lambda_4 = -\ \bar{\alpha}\beta\mu_1 v_2 -\beta\ \bar{\gamma}\mu_1 v_1 +\gamma\ \bar{\gamma}\mu_3 v_1 \qquad (9.28)$$

$$\xi_1=\alpha\ \bar{\alpha}\mu_2 v_1+\gamma\ \bar{\gamma}\mu_1 v_2,$$
$$\xi_2 =\alpha\ \bar{\alpha}\mu_2 v_3 -\alpha\ \bar{\beta}\mu_2 v_2 -\ \bar{\beta}\gamma\mu_1 v_2,$$
$$\xi_3 =\alpha\ \bar{\beta}\mu_2 v_1 +\ \bar{\beta}\gamma\mu_1 v_1 -\gamma\ \bar{\gamma}\mu_1 v_3 \qquad (9.29)$$

with

$$\mu_1 =\alpha\ k_\beta -\beta\ k_\alpha,\ \mu_2=\beta\ k_\gamma -\gamma\ k_\beta,\ \mu_3=\gamma\ k_\alpha -\alpha\ k_\gamma \qquad (9.30)$$

and

$$v_1 = \bar{\alpha}\, g_\beta - \bar{\beta}\, g_\alpha \,,$$

$$v_2 = \bar{\beta}\, g_\gamma - \bar{\gamma}\, g_\beta \,,$$

$$v_3 = \bar{\gamma}\, g_\alpha - \bar{\alpha}\, g_\gamma \tag{9.31}$$

with α, β, γ and k_α, k_β, k_γ, and g_a, g_β, g_γ and $C_{h\alpha}$, C_β, C_γ, $S_{h\alpha}$, S_β, S_γ already defined in eqns (9.13), (9.18), (9.25) and (9.27) respectively.

Thus the natural frequencies of the composite beam can now be determined from equation (9.1) by computing the values of $f(\omega)$ for a range of frequencies ω, and successively tracking the changes of its sign.

9.2.2 Mode shapes

Once the natural frequency ω_n is determined from Eqn (9.26), the corresponding mode shape is obtained in the usual way by fixing one of the six coefficients A_1–A_6 arbitrarily, and solving for the remaining five in terms of the arbitrarily chosen one. (For the present problem A_2–A_6 are expressed in terms of A_1.) The symbolic computing package REDUCE [9.17] was used again to derive the mode shapes coefficients in explicit form as follows:

$$A_2 = (\Phi_1/\chi)A_1; \quad A_3 = (\Phi_2/\chi)A_1, \quad A_4 = (\Phi_3/\chi)A_1;$$

$$A_5 = (\Phi_4/\chi)A_1, \quad A_6 = (\Phi_5/\chi)A_1 \tag{9.32}$$

where

$$\Phi_1 = -\beta\, \bar{\beta}\mu_2\zeta_3 S_\beta + \gamma\, \bar{\gamma}\mu_2\zeta_1 S_\gamma - \alpha\, \bar{\alpha}\mu_2\zeta_2 S_{h\alpha} \tag{9.33}$$

$$\Phi_2 = \bar{\alpha}\, \bar{\beta}\delta_3 C_{h\alpha}C_\beta + \bar{\alpha}\, \gamma\tau_2 C_{h\alpha}C_\gamma - \bar{\beta}\mu_3\varepsilon_3 S_\beta + \alpha\, \gamma\tau_1 S_{h\alpha}S_\gamma + \bar{\beta}\, \gamma\delta_3 C_\beta\, C_\gamma + \tau_3 \tag{9.34}$$

$$\Phi_3 = \bar{\alpha}\, \bar{\beta}\delta_3 C_{h\alpha}S_\beta + \gamma\, \bar{\gamma}\mu_3\zeta_1 S_\gamma - \alpha\, \bar{\alpha}\mu_3\zeta_2 S_{h\alpha} + \bar{\beta}\, \gamma\delta_3 S_\beta\, C_\gamma \tag{9.35}$$

$$\Phi_4 = -\bar{\alpha}\, \bar{\beta}(\delta_3 + \alpha\mu_2)\, C_{h\alpha}C_\beta + \gamma\, \bar{\gamma}\mu_1\zeta_1 C_\gamma - \alpha\, \bar{\beta}\delta_1 S_{h\alpha}\, S_\beta - \bar{\gamma}\mu_1\, \varepsilon_1 S_\gamma - \alpha\, (\bar{\alpha})^2\mu_2 - (\bar{\beta}\,)^2\delta_3 \tag{9.36}$$

$$\Phi_5 = -\beta\, \bar{\beta}\mu_1\zeta_3 S_\beta + \gamma\, \bar{\gamma}\mu_1\zeta_1 S_\gamma - \alpha\, \bar{\alpha}\mu_1\zeta_2 S_{h\alpha} \tag{9.37}$$

with

$$\zeta_1 = \bar{\alpha}C_{h\alpha} + \bar{\beta}C_\beta \,,$$

$$\zeta_2 = \overline{\beta} C_\beta - \overline{\gamma} C_\gamma ,$$

$$\zeta_3 = \overline{\gamma} C_\gamma + \overline{\alpha} C_{h\alpha} \tag{9.38}$$

$$\varepsilon_1 = \alpha \, \overline{\alpha} S_{h\alpha} - \beta \, \overline{\beta} S_\beta ,$$

$$\varepsilon_2 = \beta \, \overline{\beta} S_\beta - \gamma \, \overline{\gamma} S_\gamma ,$$

$$\varepsilon_3 = \gamma \, \overline{\gamma} S_\gamma - \alpha \, \overline{\alpha} S_{h\alpha} \tag{9.39}$$

$$\delta_1 = \alpha\mu_3 + \beta\mu_2 ,$$

$$\delta_2 = \beta\mu_1 - \gamma\mu_3 ,$$

$$\delta_3 = \gamma\mu_1 + \alpha\mu_2 \tag{9.40}$$

$$\tau_1 = \alpha\mu_1 + \gamma\mu_2 ,$$

$$\tau_2 = \alpha\mu_2 - \gamma\mu_1 ,$$

$$\tau_3 = \alpha \, \overline{(\alpha)}^2 \mu_2 - \gamma \, \overline{(\gamma)}^2 \mu_1 \tag{9.41}$$

$$\chi = \alpha\overline{\alpha}\mu_2\zeta_2 C_{h\alpha} + \overline{\alpha}\mu_2\varepsilon_2 S_{h\alpha} - \overline{\beta\gamma}(\delta_3 + \lambda\mu_1) C_\beta C_\gamma - \overline{\beta\gamma}\delta_2 S_\beta S_\gamma + \overline{(\beta)}^2 \delta_3 + \gamma\overline{(\gamma)}^2 \mu_1 \tag{9.42}$$

and μ_1, μ_2 and μ_3 have already been defined in Eqn (9.30).

Note that α, β, γ, and k_α, k_β, k_γ and $\overline{\alpha}$, $\overline{\beta}$, $\overline{\gamma}$, and $C_{h\alpha}$, $S_{h\alpha}$, C_β, S_β, C_γ, and S_γ appearing in Eqns (9.33) to (9.42) are given by Eqns (9.13), (9.18), (9.24) and (9.27), but must be calculated for the particular natural frequency ω_n at which the mode shape is required.

Thus the mode shape of the bending-torsion coupled composite beam is given in explicit form by rewriting Eqns (9.15) and (9.16) with the help of Eqns (9.17) and (9.32) in the form

$$H(\xi) = A_1(\cosh\alpha\xi + R_1\sinh\alpha\xi + R_2\cos\beta\xi + R_3\sin\beta\xi + R_4\cos\gamma\xi + R_5\sin\gamma\xi) \tag{9.43}$$

$$\Psi(\xi) = A_1(k_\alpha \sinh\alpha\xi + R_1 k_\alpha \cosh\alpha\xi - R_2 k_\beta \sin\beta\xi + R_3 k_\beta \cos\beta\xi - R_4 k_\gamma \sin\gamma\xi + R_5 k_\gamma \cos\gamma\xi)/L \tag{9.44}$$

where the ratios R_1, R_2, R_3, R_4 and R_5 are respectively A_2/A_1, A_3/A_1, A_4/A_1, A_5/A_1 and A_6/A_1, and follow from eqns (9.32).

9.3 Experimental modal testing and ANSYS modelling

The modal testing is carried out using an impact hammer kit consisting of a PC driven ACE dynamic signal analyser, ICATS modal analysis software [9.19], and an accelerometer, in a similar procedure to the one described in section 6.4 of Chapter 6. Eight-node tetrahedral structural solid element SHELL 99 (ANSYS) was used for the finite element analysis. The element is designed to model thin to moderately thick plate and shell structures with a side-to-thickness ratio of roughly 10 or greater. The element has six degrees of freedom at each node: translations in the nodal x, y, and z directions and rotations about the nodal x, y, and z-axes. No slippage is assumed between the element layers of composite beam. Shear deflections are included in the element. However, normals to the centre plane before deformation are assumed to remain straight after deformation. The stress varies linearly through the thickness of each layer. Interlaminar transverse shear stresses are based on the assumption that no shear is carried at the top and bottom surfaces of an element. A representative meshed laminated beam having 256 elements and 642 nodes is shown in Figure 9.1. Reduced method was used for mode extraction.
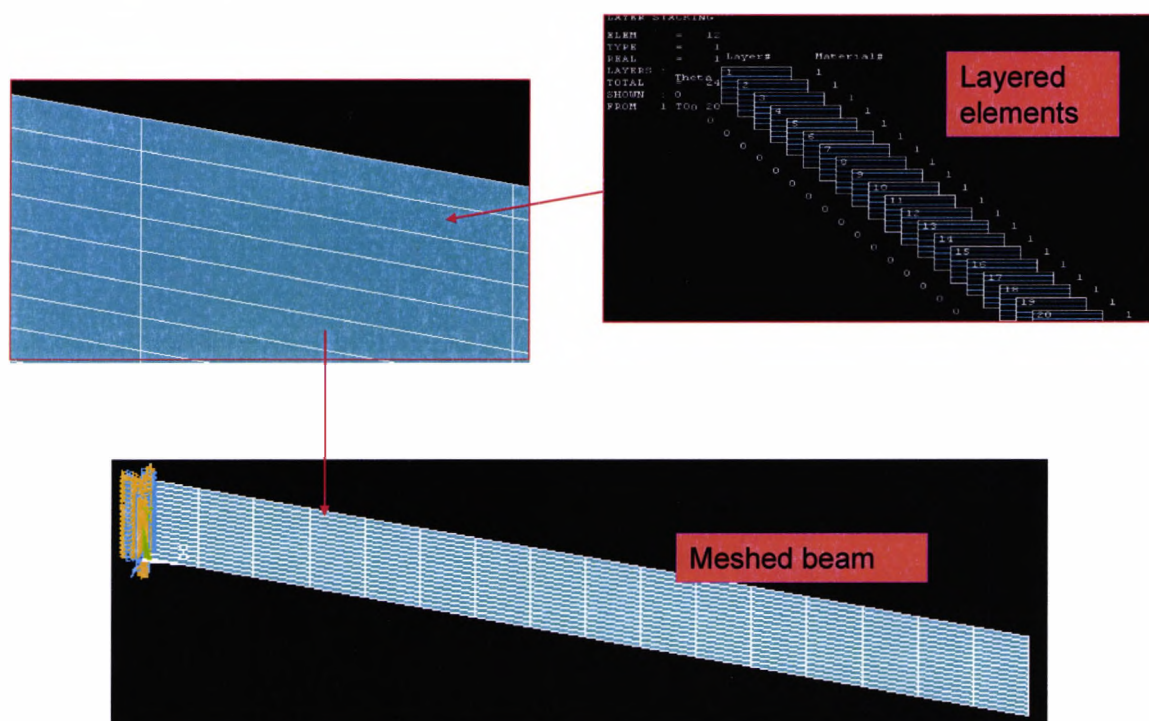
Figure 9.1   A representative meshed laminated composite beam

9.4 Results and discussion

9.4.1 Numerical studies

The expressions for the frequency equation and mode shapes given by Eqns (9.1), (9.2) and (9.44) can now be used to compute the natural frequencies and mode shapes of cantilever composite beams. Two illustrative examples of laminated composite beams are chosen from the literature of which one is a flat beam called the MIT beam [9.12] and the other is a thin-walled box beam called the GIT beam [9.13]. Both of these beams are made of carbon/epoxy material. The MIT beam has a length = 304.8mm, width = 76.2 mm and thickness = 0.804 mm with stacking sequence $[\theta_2/0]_s$. The configuration of the GIT beam, which has a length of 2.032 m, is shown in Figure 7.5 (Chapter 7).

The rigidity properties of the MIT and GIT beams are established using the theories of Weisshaar and Foist [9.7] and Armanios and Badir [9.1], respectively.. Based on these rigidity properties a free vibration analysis has been carried out by applying the above theory. Using the frequency Eqn (9.1) and computing the roots of $f(\omega)=0$, the first five natural frequencies of the MIT and GIT beams with cantilever end condition were determined for ply angles within the range $0^0 \leq \theta \leq 90^0$ and at 5^0 interval. Representative results for the first three natural frequencies of the MIT beam using the present theory are shown in Table 9.1 alongside the results of Ref. [9.12]. For different lay-ups, there is a varying degree of agreement between the finite element and experimental results and the ones obtained using the present theory, the maximum discrepancy being around 20%. In view of the complexity of the problem and different theoretical models and material properties used in the analysis, the discrepancy is understandable. Similar results for the GIT beam [9.13] were obtained, but these are not shown for brevity and also because no comparative results were available for its natural frequencies. Note that the authors of Ref. [9.13] report result for divergence and flutter speeds, but do not quote the natural frequencies of the box beam.

Table 9.1   Natural frequencies of the MIT beam.

Ply angle (θ)	First three natural frequencies (rad/s)		
	Finite Element Method	Experimental Results [9.12]	Present Method
15^0	55.9	59.1	50.13
	269.5	287.8	258.0
	394.0	416.0	331.1
30^0	39.6	41.5	35.4
	234.4	251.3	213.0
	357.5	371.3	323.0
45^0	30.8	30.2	28.6
	189.1	187.2	177.0
	310.4	322.3	282.6
60^0	26.4	27.0	25.6
	164.0	170.3	159.7
	262.0	299.7	241.4

Next the effects of ply orientation on the first five natural frequencies of the two beams are studied. These are illustrated in Figures 9.2 and 9.3, respectively. The letters B and T have been used to denote bending or torsion dominated modes. Clearly for both beams, the first natural frequency corresponds to a bending mode for all ply angles. However, for higher natural frequencies the natures of the mode changes with ply angles. For the MIT beam the mode corresponding to the second natural frequency starts off as a torsion-dominated mode and remains so until the ply angle reaches 30^0 when it becomes a bending mode and remains so for higher ply angles, see Figure 9.2. In contrast the third mode starts as a bending mode when the ply angle is 0^0, but then with increasing ply angle beyond 15^0 it becomes a torsional mode. Interestingly the fourth mode starts as a torsional mode and continues to be so until the ply angle reaches around 20^0 when it becomes a bending mode for the remaining range of the ply angle. It is clear from Figure 9.2 that the fifth mode of the MIT beam is always a torsional mode.
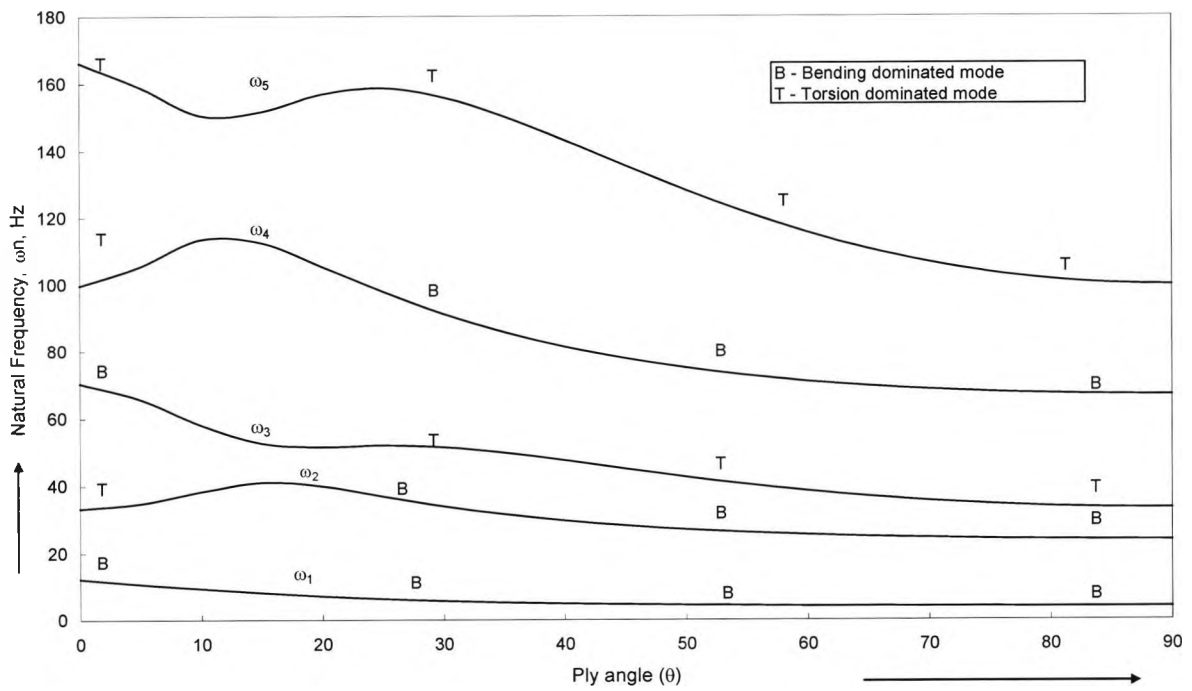
Figure 9.2   Natural frequencies for the MIT beam. . ω_1-ω_5 represents the first to the fifth natural frequency while the letters B and T have been used to denote bending or torsion dominated modes.
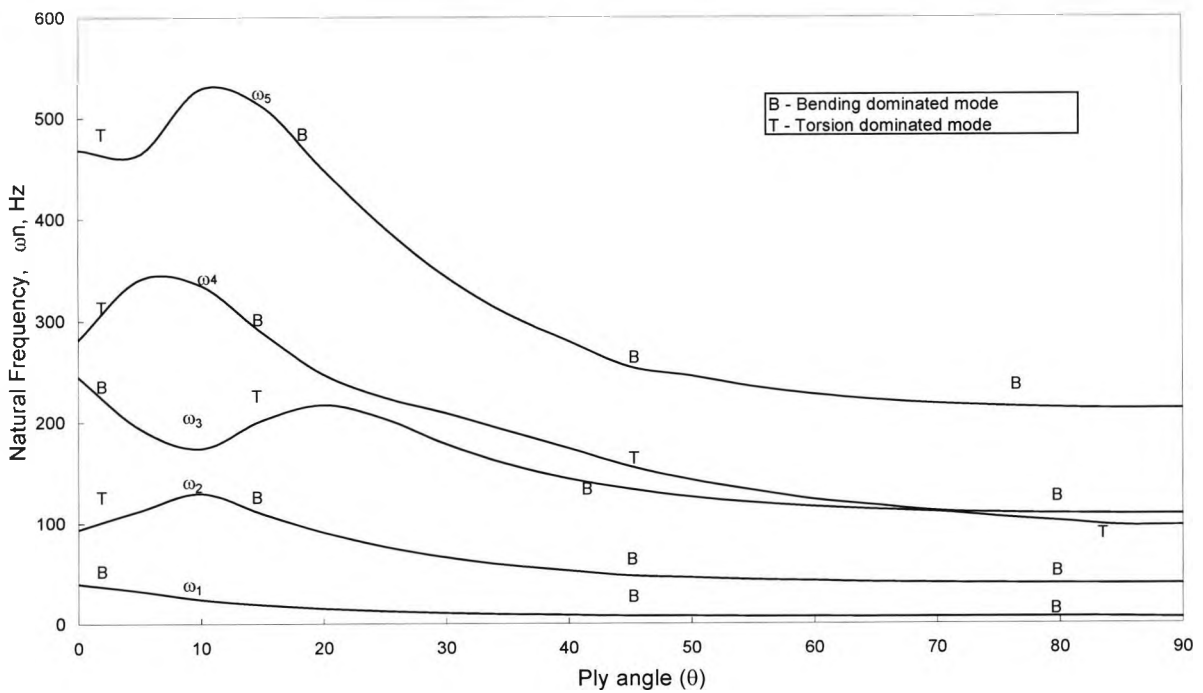
Figure 9.3   Natural frequency for the GIT beam. ω_1-ω_5 represents the first to the fifth natural frequency while the letters B and T have been used to denote bending or torsion dominated modes.

The results of the GIT beam shown in Figure 9.3 reveal a different picture. The first mode is predominantly a bending mode for all ply angles, as was the case with the MIT beam. However, the characteristics of the rest of the modes change beyond the ply angle of 25^0. For instance the second mode starts as a torsional mode and then changes to a bending mode around the ply angle of 25^0 and onwards. The third mode behaves in a similar manner except that it starts as bending mode and changes to a torsional mode around 25^0 ply angle and then becomes a bending mode again around the ply angle 35^0 and onwards. The fourth mode starts as torsional mode and then around ply angle 25^0 it becomes a bending mode before becoming a torsional mode around 35^0 and onwards. Finally the pattern for fifth mode shows that it starts as a torsional mode and then becomes a bending mode beyond the ply angle of 25^0.

It is evident that directional stiffness properties of fibre-reinforced composites can produce significant differences in free vibration behaviour of such structures. Most of all, these can be taken advantage of from an aeroelastician point of view. As a result the mode shape forms a vital study as reflected in the following discussion. With dropping EI and rising GJ and K on the MIT flat beam study, the bending displacements remain stable with only torsional displacements dominating as shown on Figure 9.2.

At ply angle of 0^0, the bending and torsional amplitudes are at unity on the third and the fourth modes while the first two mode shapes (third and the fourth mode shapes) have prominent torsinal deformations. The torsional effects are converging as the ply angle increases to 5^0 with more bending and torsional coupled mode shapes appearing at higher frequencies on fifth and sixth mode shapes. As both *GJ* and *K* on Figure 7.8 and 7.9 (Chapter 7 Rehfeild Simplified Formula (RSF) results) increase to the peak values, the corresponding modal amplitudes at high frequencies (Figure 9.3) simulate a sinusoidal torsional deformation wave, with most prominent ones at $\theta = 15^0$ though this features can also be picked from the ply angles of 10^0. The characteristics are illustrated on Figure 9.4 (a). The modal amplitudes at 15^0 can also be related to the modal natural frequencies obtained at this ply angle as shown in Figure 9.3. At $\theta = 20^0$, the torsional modal amplitudes changes sign with the fourth modal amplitude changing sign again as the ply angles increases to 30^0 which can be related to K getting on its peak and then starting to descend. Conversely, the modal frequencies on Figure 9.3 shows a descend other than the third and fifth modes which show a small rise before falling steadily. Nevertheless, some prominent modal amplitude can be noted at $\theta = 35^0$ at high natural frequencies through 60^0 and unsteady third and fifth mode shapes at ply $\theta = 70^0$

on the MIT flat beam (graph not presented). At ply angle of 90^0, the bending and torsional amplitudes are pretty much even. It is evident that bending modal amplitudes obtained on the entire MIT flat beam study remains steady and hardly change except on the sixth modal amplitude at $\theta = 5^0$, which may be attributed to low stiffness as compared with the GIT box beam that is highly rigid.

The first few modal amplitude of the GIT box beam, at ply angle of 0^0 to 5^0 are pretty much bending and torsionally coupled with the only effect being on torsional amplitudes at high natural frequencies from the third mode onwards. There is hardly any effect on bending amplitudes and as a result the amplitudes appear as a straight line. This can be attributed to the high bending rigidity at these ply angles. At $\theta = 10^0$, it is totally different, the torsional amplitudes significantly dominating the box beam. There are also bending effects on the first to the third mode shapes though not as well pronounced like the torsional deformations. These effects are probably due to the falling *EI*, as *GJ* rise consistently while *K* heads to maximum at around 15^0 (Figure 7.6-7.8, Chapter 7 Rehfeild Simplified Formula (RSF) results). The features can also be reflected by the natural frequencies (Figure 9.3) which take a rise to the peak on the second, fourth and fifth modes and directly opposite on the first and second unlike at any other ply angle investigated. It is evident that at as the modal frequencies rises; the torsional amplitudes become more pronounced.

Again, the results obtained from ply angles ranging from 55^0 through 90^0 are very much the same except of bending effects dominance at ply angles of 50^0 through 75^0 while the torsional amplitudes appear to be settled probably as a result of relatively higher *GJ* values Figure 7.7, (Chapter 7 Rehfeild Simplified Formula (RSF) results) combined with the closing in modal frequencies on the third and the fourth modes with the latter falling gently. As well, the torsional amplitudes seems to be prominent at higher natural frequencies at these ply angles. It can therefore be deduced that the torsional amplitudes are more prominent at lower ply angles while the bending amplitudes remain stable in most cases within the ply angles studied on the GIT box beam study. Interesting features appear at the lower ply angles of 0^0 through 30^0 as evident with both the stiffness rigidities (Figure 7.7, Chapter 7 Rehfeild Simplified Formula (RSF) results) and modal frequencies (Figure 9.3) results obtained. Figure 9.4 (a) - (c) and Figure 9.5 displays the obtained mode shapes for MIT and GIT beam respectively.
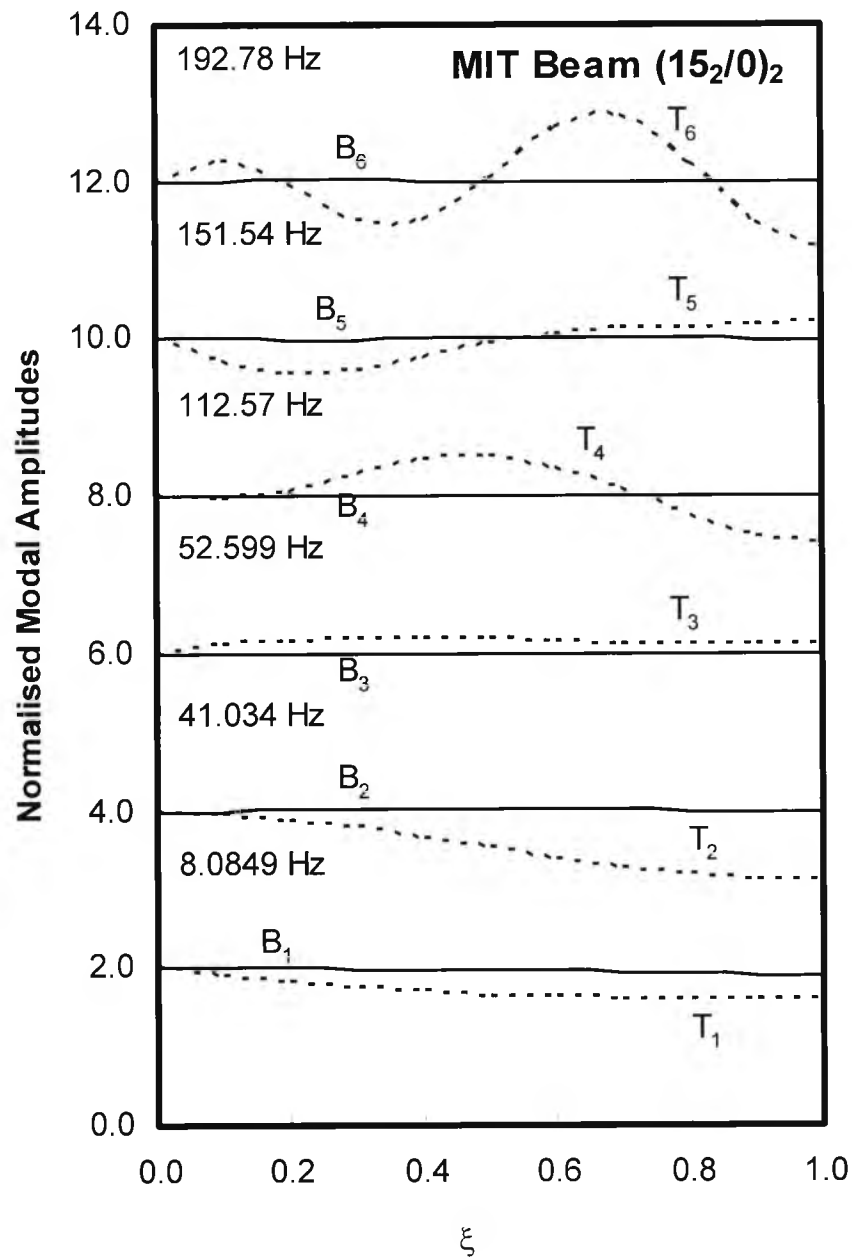
Figure 9.4 (a) The modal amplitudes for the MIT flat beam, $[\theta_2/0]_2$, with ply angles of : (a) $\theta = 15^0$. The letters B and T have been used to denote bending or torsion dominated modes and the numbers 1-6 represent mode numbers.
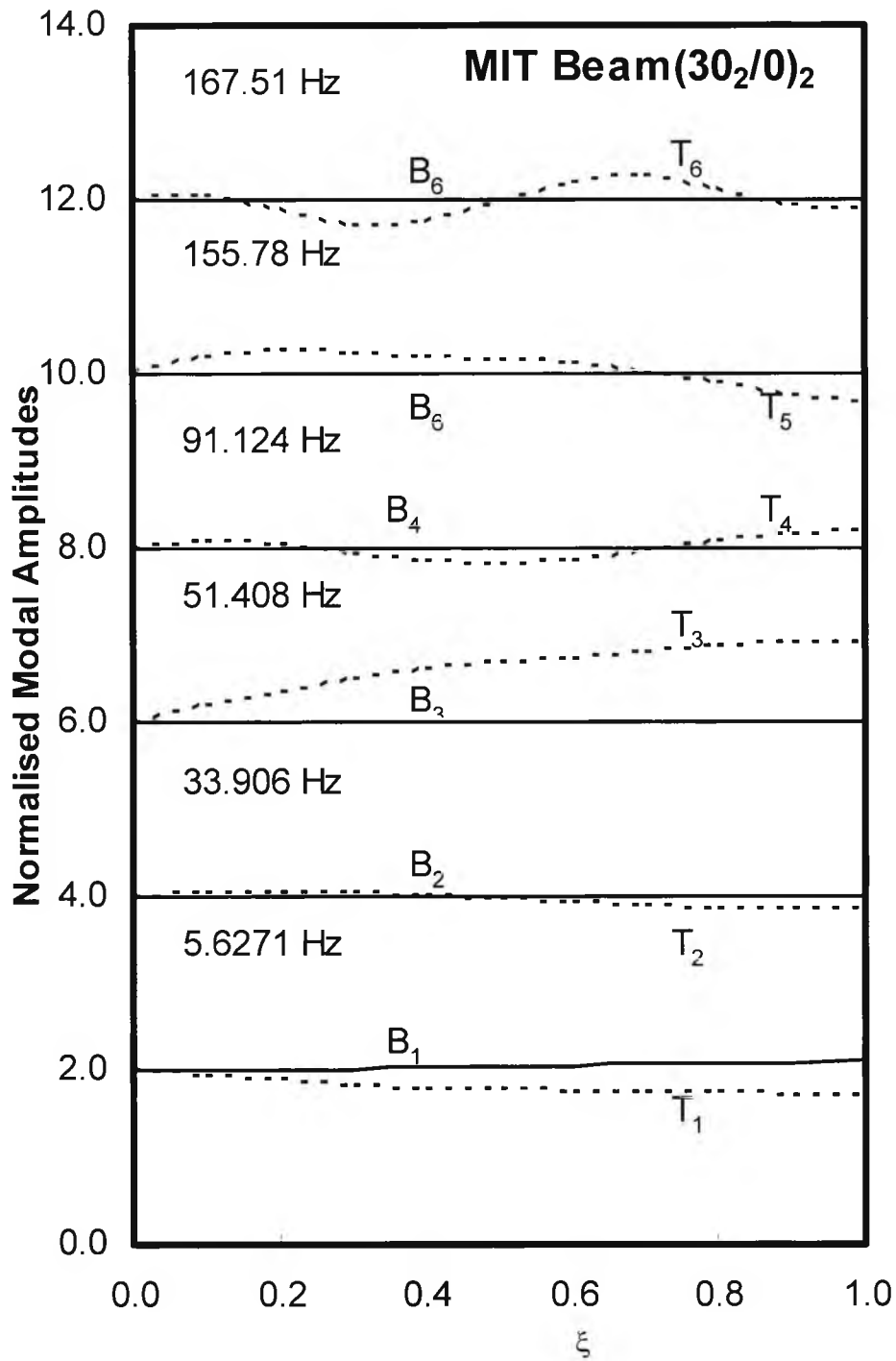
Figure 9.4(b) $\theta = 30$. The letters B and T have been used to denote bending or torsion dominated modes and the numbers 1-6 represent mode numbers.
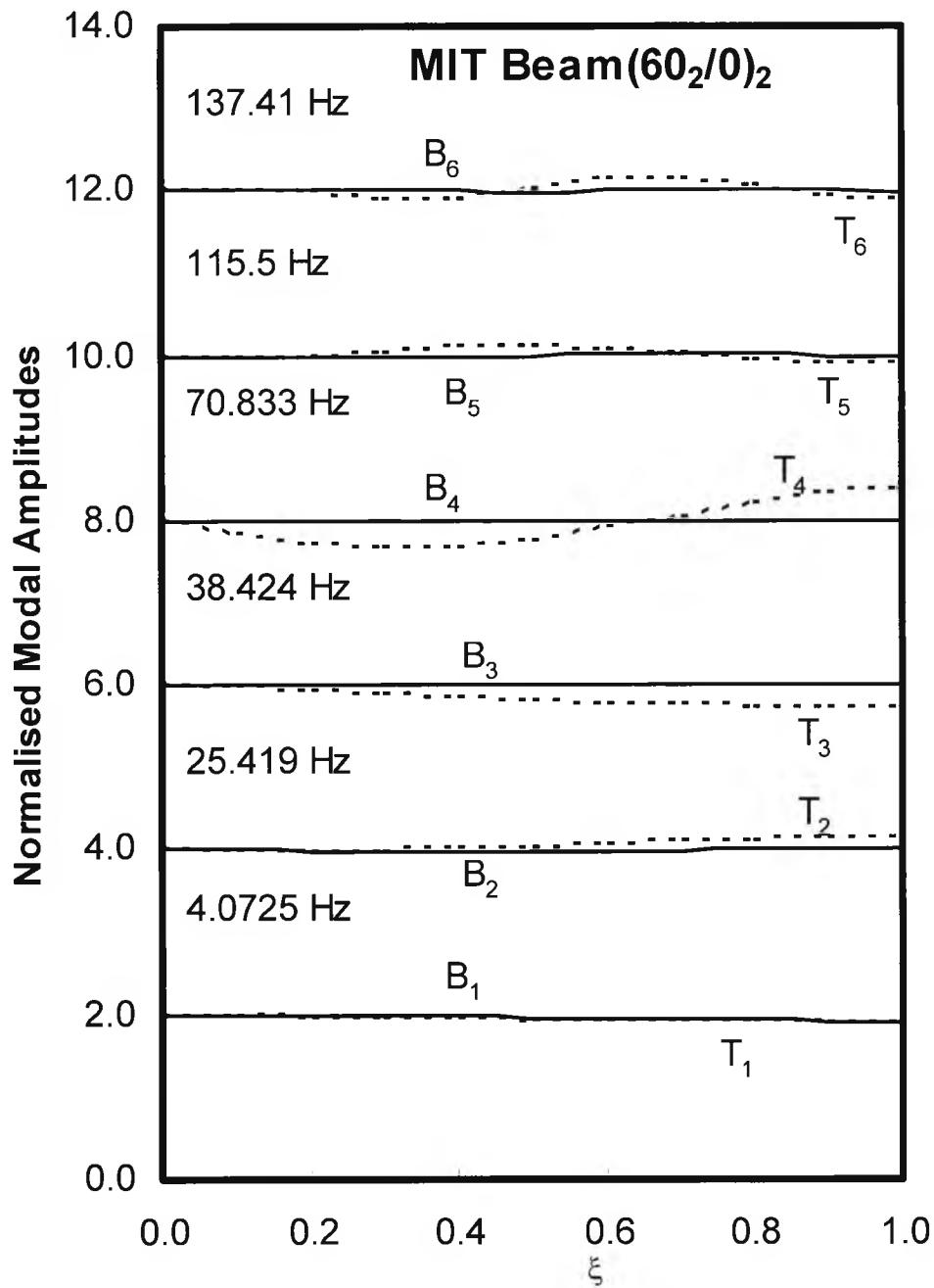
Figure 9.4(c) $\theta = 60$. The letters B and T have been used to denote bending or torsion dominated modes and the numbers 1-6 represent mode numbers.
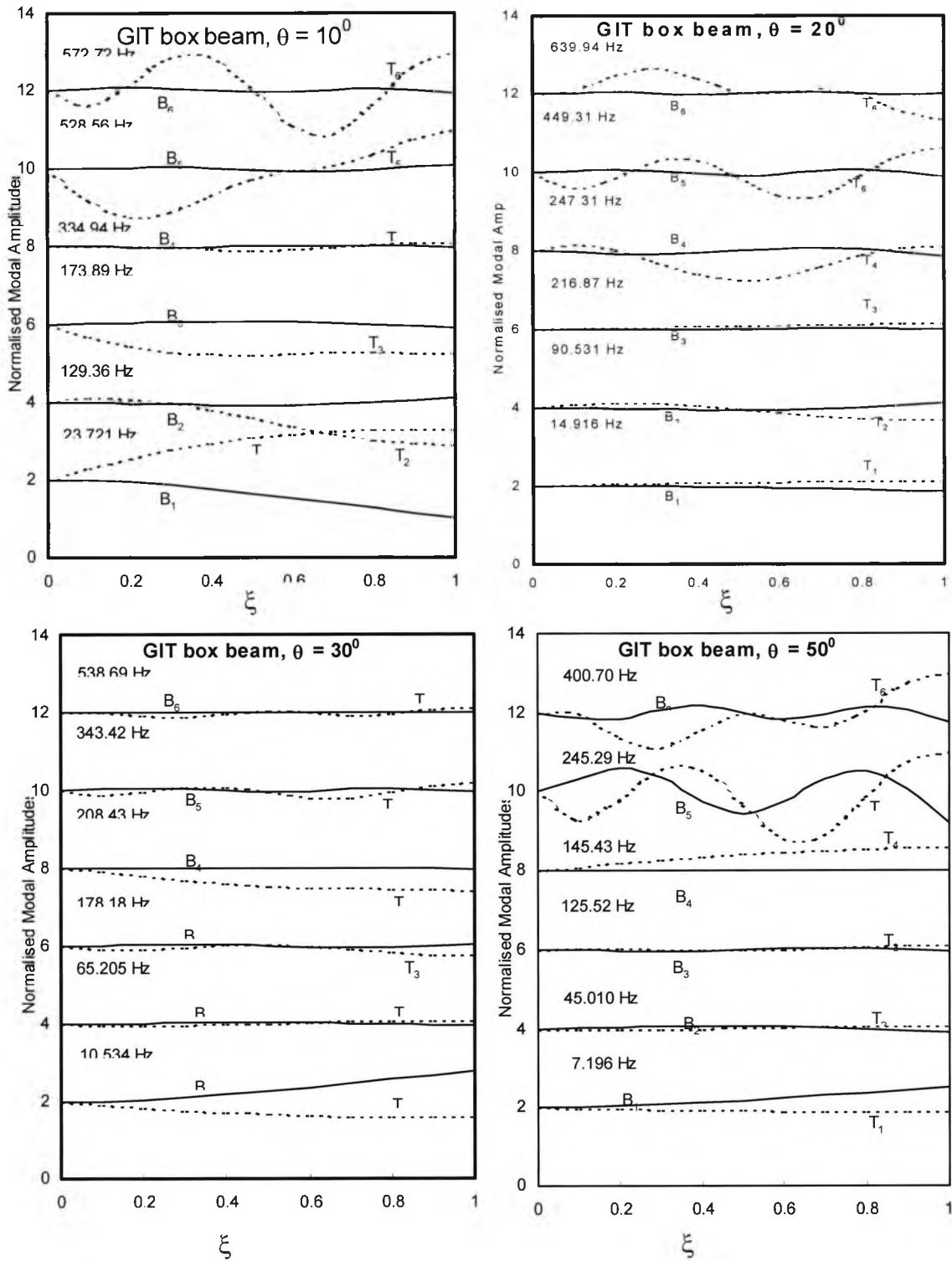
Figure 9.5 The modal amplitudes for the GIT box-beam, with ply angles of (a) $\theta = 10$ (b) $\theta = 20$, (c) $\theta = 30$ and (d) $\theta = 50$. The letters B and T have been used to denote bending or torsion dominated modes and the numbers 1-6 represent mode numbers.

9.4.2   *The influence of geometrical and material coupling into free vibration behaviour*

In order to access the individual and combined effect of the material and geometric coupling, it is first decided (by the author of this thesis) that the geometric coupling is non–existent. Note that the third of Eqn. (9.9) has both geometric and material coupling terms x_α and K respectively. It was thus necessary to assume the mass axis corresponds to the elastic axis in the preliminary analysis. Table 9.2 shows the comparison of the first five natural frequencies (Hz) for the geometrically and materially coupled MIT composite beam to the materially coupled MIT composite beam. For both flat and box beam results in Table 9.2 and 9.3, it is clear that as ξ decreases, there is considerable reduction of the natural frequencies values in descending manner in the first mode. However as the ξ tends to zero in all the other modes, the natural frequency values are ascending dramatically with the higher the mode the higher the natural frequencies discrepancy from the material coupled case. This is mainly attributed to the geometrical effects to the associated deformations. It is therefore conclusive that the natural frequency varies considerably when the materially coupled beam has the added geometrical effect. The associated mode shapes agree to this conclusion too, Figure 9.6 illustrate this aspect.

Table 9.2   Comparison of the first three natural frequencies (Hz) for the materially (ξ=0) and geometrically (ξ =1) coupled MIT composite beam

Ply Angle, θ	Mode No.					
	ξ	1	2	3	4	5
0^0	0	10.67	53.324	120.24	191.3	263.36
	0.25	10.791	51.242	81.152	123.42	199
	0.5	10.922	44.833	67.377	123.37	179.9
	0.75	11.066	38.154	66.813	115.97	158.52
	1	11.225	33.219	70.346	99.658	166.1
30^0	0	5.158	31.104	81.813	147.58	222.37
	0.25	5.216	31.5187	82.782	106.89	151.07
	0.5	5.287	32.142	73.267	86.502	154.52
	0.75	5.383	32.81	51.971	87.93	158.61
	1	5.627	33.906	51.408	91.126	155.78
45^0	0	4.3122	26.257	70.259	129.55	199.64
	0.25	4.3443	26.583	71.082	93.203	133.05
	0.5	4.3826	26.956	64.111	74.117	136.22
	0.75	4.4329	27.406	52.382	75.147	140.13
	1	4.5548	28.17	44.984	77.663	135.49

Table 9.3   The first three natural frequencies (Hz) for the geometrically and materially coupled composite box-beam to the materially coupled composite box-beam with both variations of the non-dimensional parameter, ξ and ply angle, θ.

$\square$	Mode No.					
	ξ	1	2	3	4	5
0	0	36.242	168.13	366.17	567.21	769.79
	0.5	37.465	129.74	216.76	370.66	538.7
	1	39.076	93.698	244.88	281.1	468.49
15	0	16.583	100.16	262.62	470.97	704.99
	0.5	17.087	103.19	265.33	299.25	486
	1	18.476	109.41	201.69	288.72	512.02
30	0	9.96	61.706	169.11	321.08	510.2
	0.5	10.121	62.744	171.99	299.27	328.21
	1	10.533	65.203	178.17	208.74	343.41
45	0	7.2836	45.29	125.12	240.43	387.75
	0.5	7.3517	45.824	126.93	218.34	245.58
	1	7.5183	46.944	130.46	152.86	254.31
60	0	6.5281	40.595	112.27	216.13	349.45
	0.5	6.5568	40.92	113.67	177.58	177.58
	1	6.6218	41.471	115.92	124.99	227.02
75	0	6.2219	38.625	106.55	204.45	329.28
	0.5	6.2349	38.882	107.89	150.34	209.78
	1	6.2594	39.224	105.95	109.84	215.16
90	0	5.3198	33.045	91.246	175.31	282.79
	0.5	5.3237	33.21	92.243	132.6	179.56
	1	5.3272	33.385	93.479	93.712	183.18

(a) $\xi = 0$ (b) $\xi = 0.5$ (c) $\xi = 1$
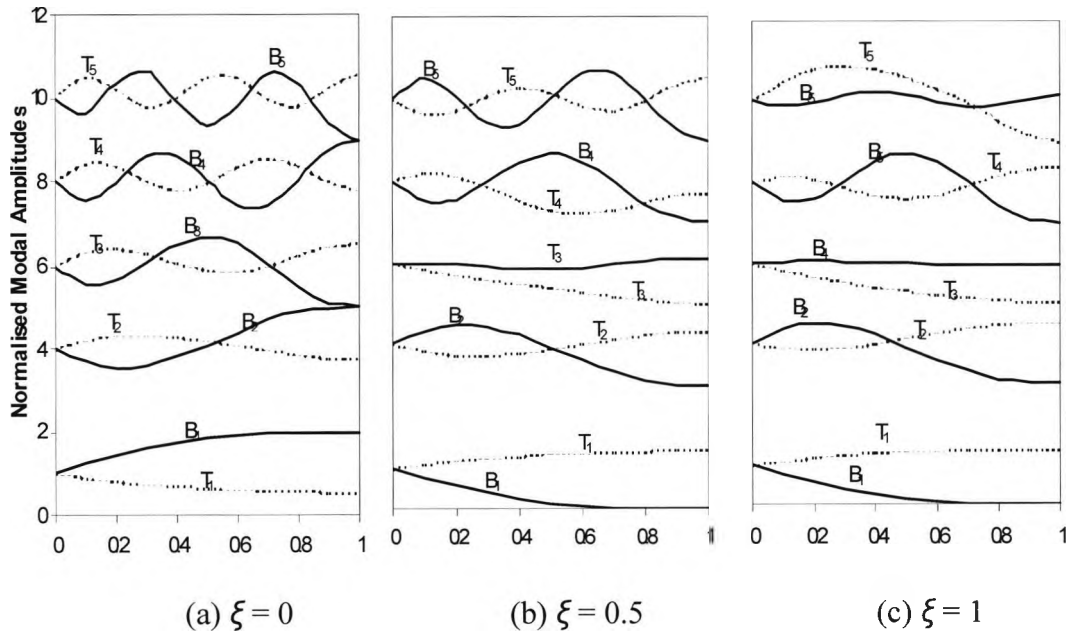
Figure 9.6   **Normalised modal amplitudes for a materially and geometrically coupled MIT composite beam when θ=45⁰. B and T are the recorded bending and torsion couplings respectively while 1 corresponds to the lowest mode shape and 5 to the highest ones.**

9.4.3 Experimental studies

ICATS modal analysis software [9.19] has several curve fitting algorithms that can be used for many degrees of freedom (MDOF) analysis – see sub-Chapter 6.4 (Chapter 6). Figure 9.7 illustrates the experiment set up. For this investigation Global-M has been preferred since it is specially optimised for analyses cases with close or split modes and relatively low damping. The combined FRF plot is inspected for measurement errors and significant order-of magnitude differences between the co-ordinate directions. As a further check of the data acquired, some FRF are regenerated using the processed modes only, and therefore compensating for residuals, and the Nyquist plot is inspected. Upon quality check, the obtained results are then checked against those obtained by SDOF Circle- and Line-Fit analyses, for instance see Figure 9.8 and Figure 9.9, respectively. It is therefore acceptable that the results obtained from the analyses are satisfactory for correlation with those obtained from the numerical analyses.

Figure 9.7   The experiment set up for the modal testing.

O-FIT FOR MODE   2
NAT. FREQUENCY (Hz)   = 147.438
% STRUCTURAL DAMPING =   6.298
MOD CONST MAG (1/Mass) =   0.288E-02
MOD CONST PHASE (o)   = -172.59
% RADIUS VARIATION   =   2.22
% DAMPING VARIATION   = 22.55
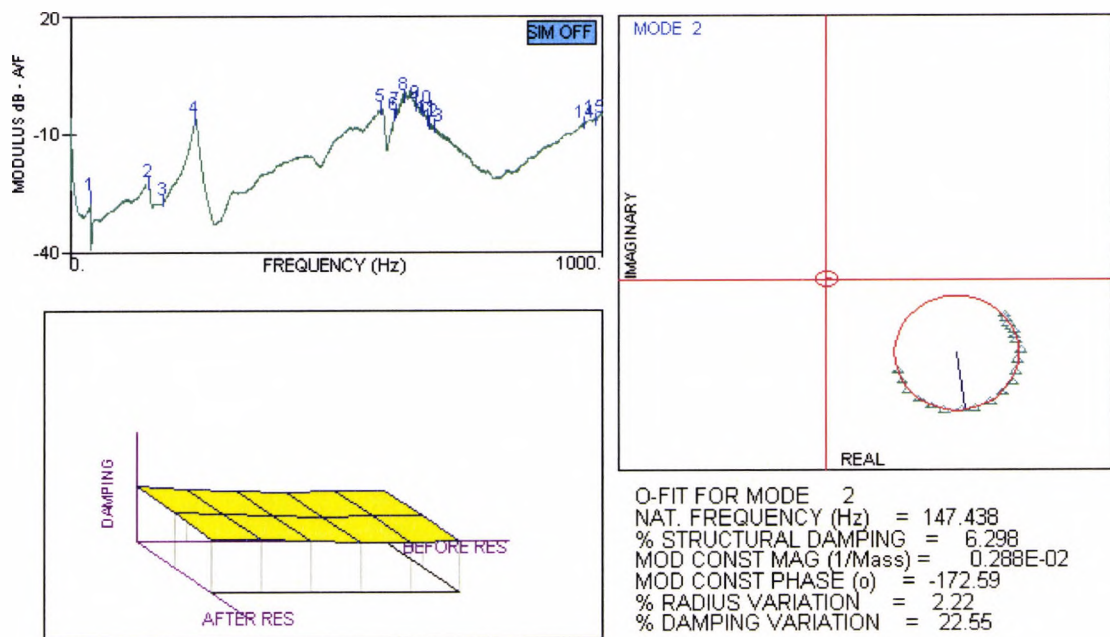
Figure 9.8   Circle-fit for second mode for the 25^0 ply orientation CFRP composite beam
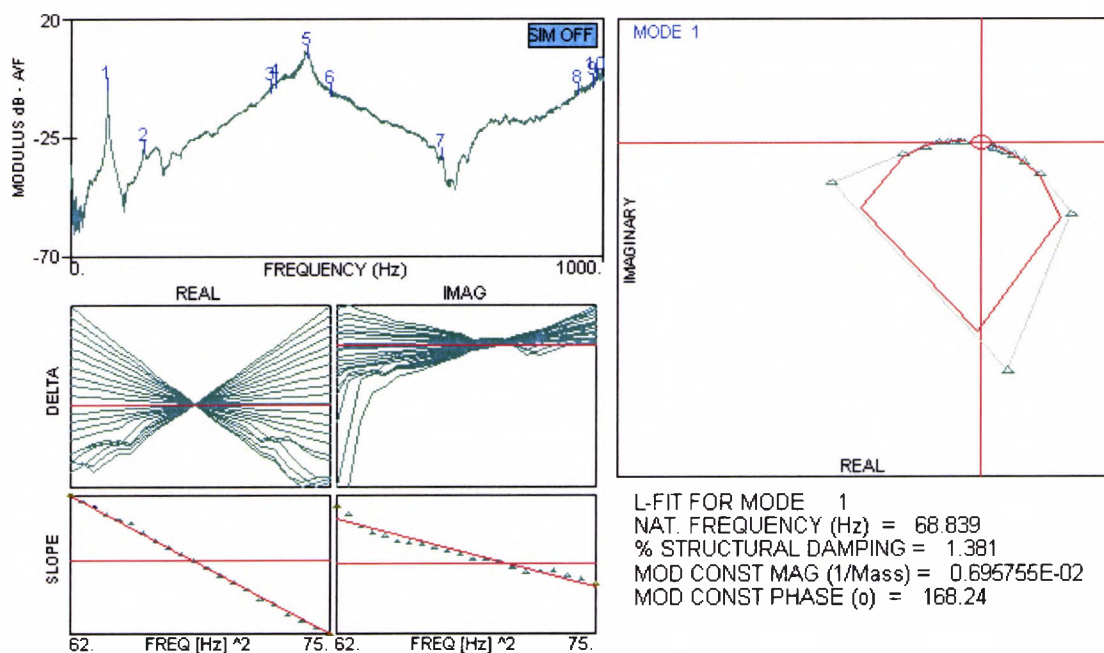
Figure 9.9   Line-fit for first mode for the 0^0 ply orientation CFRP composite beam

In the first example, four flat solid rectangular cross-section carbon-epoxy composite beams, θ_{16}, (ply orientation 0^0, 20^0, 30^0 and 40^0) are tested and experimented on. They are all tested and analysed individually. Each of the four composite beams has eight layers made of carbon/epoxy materials and they all share the same geometrical properties: 0.21m in length, 0.035m in width and 0.002m thicknesses. To start with the beams stiffness rigidities are calculated using dynamic stiffness approach and are hereby presented on Table 9.4. This is followed by calculation of the natural frequencies using the dynamic stiffness approach. The experimental test results are first obtained and then analysed using ICATS. A comparison of the obtained theoretical (dynamic stiffness method) to experimental results is presented in Table 9.5. The discrepancy can be attributed to the circle-fit analysis that gives rough estimates of the damping data. Thus, damping and modal constants for these modes had to be obtained via MDOF analyses algorithm (GLOBAL-M, a function within ICATS software) that averages the damping of all the FRFs included in the test.

Table 9.4   The stiffness properties of the beams under study

Ply Orientation	EI (Nm^2)	GJ (Nm^2)	K (Nm^2)
0^0	2.287	0.5227	0
20^0	1.614	1.087	0.913
30^0	0.9843	1.1197	0.7562
40^0	0.5604	1.047	4.714

Table 9.5   The comparison of the first three natural frequencies of the composite beams tested

Ply Orientation (Degrees)	Mode No.	Theoretical Results (Hz)	Experiment Results (Hz)
0	1	58.83	54.83
	2	260.7	263.26
	3	368.68	343.46
20	1	35.67	27.02
	2	217.3	160.33
	3	382.56	402.07
30	1	27.63	21.24
	2	170.72	127.08
	3	396.1	347.2
40	1	22.93	18.82
	2	142.67	141.56
	3	267.83	271.41

A careful inspection on natural frequencies of the 0^0 composite beam results (Table 9.5), the first and third modes are bending dominated while the third and fourth modes are torsion dominated as expected for composite beams. Previous research work [9.20] on effect of ply orientation free vibration of laminated composite beams explored this characteristic. It is also evident that the first three modes are below 10% error while the last mode exceeds this margin. Although this aspect is not clearly evident from the results obtained, the torsional frequencies from experimental results are expected to vary considerably since the static deflection due to weight of the beam, has not been accounted for in the theoretical analysis. The static deflection would also be expected to have more significant effects on the 20^0, 30^0 and 40^0 generally orthotropic composite beams which happen to have higher torsion stiffness and apparently lower bending stiffness as compared to the 0^0 specially orthotropic composite beam [9.4].

The high percentage error of the bending modes can be related to the applied excitation force. Analytical model force vector is a sinusoidal excitation force or a point of load with a fixed magnitude. As the natural frequencies are directly proportional to the applied force, an applied load over a range of frequencies may give the same value for the resonance frequency. Also, the experiment was conducted using impulse force as the beam got excitation on various points. This aspect can be demonstrated by animating some of the modes e.g. animation of the second mode obtained from experimental analyses for the 40^0 composite beam reveals is not a real mode since its animated shape consist of vibration from a couple of nodes only. Table 9.6 presents obtained damping results from further experimental analyses for the 30^0 and 40^0 composite laminate beam.

Table 9.6   Analysis results for composite beams with 30^0 and 40^0 ply orientations

Ply orientation →		30^0 composite beam			40^0 composite beam		
Mode No. ↓	Properties	SDOF circle-fit	SDOF line-fit	MDOF GlobalM	SDOF circle-fit	SDOF line-fit	MDOF GlobalM
1	$\varpi_r(H_Z)$	21.312	20.95	21.02	19.31	18.77	18.73
	$\%D_{Structural}$	11.85	1.944	1.26	10.772	1.223	3.59
	$A_{modal\ constant}$	0.194	0.07	0.02	0.15	0.08	0.04
2	$\varpi_r(H_Z)$	127.62	126.64	127.02	115.69	115.07	114.67
	$\%D_{Structural}$	4.705	4.029	5.51	3.815	3.851	3.84
	$A_{modal\ constant}$	2.83	2.366	3	2.59	2.42	2.405
3	$\varpi_r(H_Z)$	347.75	346.86	347.23	269.25	269.82	271
	$\%D_{Structural}$	2.59	2.47	2.22	5.80	5.151	6.41
	$A_{modal\ constant}$	5.22	5.04	4.64	7.63	6.70	9.84
4	$\varpi_r(H_Z)$	578.5	581	576.15	339.5	339.15	340.98
	$\%D_{Structural}$	2.15	2.26	3.12	1.934	1.423	2.15
	$A_{modal\ constant}$	10.4	12.55	15.05	4.45	3.58	4.48

The second example is a set of laminated composite beams (shown in Figure 9.10) with ply orientations of 0^0, 5^0, 10^0, 15^0, 20^0, 25^0 and 30^0 and   each made of 24 layers, which were fabricated in the University of Hertfordshire (UK). All of the beams have the same geometrical features measuring 0.3 m x 0.03 m x 0.003 m. Again, the 0^0- 30^0 ply orientation range is investigated as the most interesting features happen in this range. However, the stiffnesses are observed to be much higher (not shown) than previous investigations due to the higher number of layers in the composite beam. Nevertheless, the stiffness characteristics are very much familiar. The frequencies are observed to decrease with increase in ply orientations. The investigation also confirms the profound effect of ply orientation on composite beams as reported by various authors [9.2, 9.6, 9.13-9.15]. Basing on the obtained results, it can be affirmed that the natural frequencies are consistently reducing with increase in ply orientation mainly attributed to the flexural bending, which has direct effects on natural frequencies. Again this is as expected and in line with previous investigations. Table 9.7 shows the theoretical, experimental and finite element method (FEM) results obtained which

compare satisfactory. As can be seen, considerable disagreement range can be picked up in some modes. This may be associated to the extra stiffness on the beam as a result of the epoxy resin used to fabricate the laminates.

Figure 9.10   Tested composite beams

Table 9.7   Theoretical, experimental and FEM results for composite beams of ply orientations ranging from 0^0-30^0.

Ply angles (degrees)	Theoretical Results (Hz)	Experiment Results (Hz)	FEM analysis Results
0	41.96	38.75	40.44
	263	137.50	262.22
	308.96	275.62	368.21
5	39.74	38.12	39.25
	247.37	134.938	251.57
	325.93	381.88	371.01
10	34.832	34.38	36.28
	215.8	222.5	230
	365.25	347.5	327.72
15	29.741	23.12	32.54
	184.34	155.62	207.04
	409.78	302.5	281.68
20	20.10	20	28.85
	124.87	144.38	185.51
	239.12	266.25	242.7
25	17.52	37.50	25.58
	109.07	48.12	166.22
	301.55	219.38	212.17
30	15.556	38.75	22.8
	97.02	240	149.34
	269.34	250.62	188.74

In the third example, an aluminium I-beam is also tested and analysed for comparative purposes. The aluminium I-beam material properties (Young's Modulus = 70 GN/m^2, density = 2700 kg/m^3 and Shear Modulus = 27 GN/m^2) and the geometrical properties were readily available. Table 9.8 shows the comparison of the theoretical results against experimental results while Table 9.9 shows the comparison of the various analysis techniques (single

degree of freedom (SDOF) circle-fit and line fit, multi-degrees of freedom (MDOF); denoted GlobalM) available in ICATS for the determination of the modal frequencies.

Table 9.8   The obtained experimental and theoretical modal results for aluminium I-beam

	Theoretical Results (Hz)	Experiment Results (Hz)
Aluminium I-beam	63.53	60.06
	398.13	271.56
	730.49	480.07
	1114.8	806.15

Table 9.9   Aluminium beam analysis results

Mode No.	Properties	SDOF circle-fit	SDOF line-fit	MDOF GlobalM
1	$\varpi_r(H_Z)$	60.25	60.07	60.24
	$\%D_{Structural}$	8.72	7.11	7.03
	$A_{modal\ constant}$	0.45	0.37	0.37
2	$\varpi_r(H_Z)$	272.43	271.33	271.92
	$\%D_{Structural}$	3.29	3.48	3.85
	$A_{modal\ constant}$	5.62	5.86	6.43
3	$\varpi_r(H_Z)$	474.5	472.84	474.73
	$\%D_{Structural}$	2.91	3.12	4.09
	$A_{modal\ constant}$	5.13	5.96	8.4
4	$\varpi_r(H_Z)$	809.5	809.88	808.23
	$\%D_{Structural}$	1.88	2.01	2.17
	$A_{modal\ constant}$	2.73	2.88	3.39

9.5 Conclusions

The free vibration behaviour of laminated composite beams exhibiting coupled bending-torsional vibration has been investigated using an exact analytical method. Results are obtained for two different types of carbon-epoxy composite beams of which one is flat with solid rectangular cross-section whereas the other is a thin-walled box beam. The ply angles in the stacking sequence of these beams are varied and their subsequent effects on the free vibration characteristics are studied. The investigation has shown that ply orientations can have significant effects on the natural frequencies and mode shapes of a composite beam. It is evident from the results that modal interchanges between bending and torsional modes and vice versa can occur as a result of ply orientation in the laminate which can be significant from an aeroelastic stand point.

It has been shown that the geometric-material couplings can have significant effects on the natural frequencies and mode shapes of metallic and composite beams. In comparison, modal interchange occurring as a result of geometric coupling in metallic beams is relatively less significant. The results confirm the potential advantage of fibre orientation in composite beams that can be used to produce desirable aeroelastic effects in aeronautical design. However, further in-depth investigations are necessary to pinpoint the effect on a loaded wing. It should be noted that damping properties have not been thoroughly discussed since the damping data for the numerical model was not available.

10 Flutter analysis of laminated composite wings

10.1 Introduction

Flutter denotes a characteristic form of self-excited oscillations that can arise through the interaction of an aerodynamic flow with the elastic modes of a mechanical structure, e.g. the bending and torsion modes of an aircraft wing. Emergence of flutter compromises not only the long term durability of the wing structure, but also the operational safety, flight performance and energy efficiency of the aircraft. Effective means of flutter prevention are, therefore, mandatory in the certification of new flight vehicles, and considerable effort, theoretically as well as experimentally, is devoted to the study of methods for active flutter control and of the interaction between structural dynamics and unsteady airflows. If left unchecked, flutter vibrations can completely destroy the structure leading to catastrophe [10.1]. Furthermore, knowledge gained from the study of flexible structures and unsteady airflows in aircraft can be transitioned back to more traditional flutter studies. It is also well acknowledged that carefully designed and embedded sensors and actuators can lead to actively/passively controlled structures with some beneficial contributions as per minimisation of flutter occurrences.

Classically, the flutter properties of a system are the lowest critical speed (U_F) and the associated reduced frequency (ω_F) for which a structure at a given density and temperature will sustain simple harmonic motion. Flight at U_F represents a neutral stability boundary, as all small structural oscillations must be stable below U_F. Above U_F, however, the small oscillations are not damped out and the structure is unstable for a range of speed (or at all speeds) above U_F. The calculation can be broken down into the following steps [10.2]:

Determine the vibration modes of the structure with no aerodynamic forces present.

a) Calculate the aerodynamic forces on the structure due to simple harmonic oscillations of the in vacuo normal modes as functions of speed and reduced frequency.

b) Search for combinations of these parameters for which simple harmonic motion yields equilibrium between the structural inertial forces and the unsteady aerodynamic forces. These combinations are the flutter boundary.

In practice the calculation of (a) assumes that the vibration modes are a superposition of a finite number of preassigned mode shapes, i.e., all the vibrations are linear. Torsion and bending can be coupled but all modes are linear. The aerodynamic force calculations in (b) generally assume some sort of linearized aerodynamic theory and hence do not capture the effect of flow separation, even though generally vortex flows can precipitate flutter. The methods for flutter analysis are classified according to the characteristics of unsteady aerodynamics, and the governing equations used to calculate the unsteady aerodynamic forces. For subsonic and supersonic flows, where the unsteady aerodynamic forces show strong linearity, DPM (doublet point method) [10.3], HGM (harmonic gradient method) [10.4], a KFM (Kernel function method) [10.5] and frequency-domain flutter analysis method [10.6] have been used, since these linear methods are effective with small computing time. In the same sense, the lifting surface methods are widely used in the field of aeroelasticity.

With the advent of active/passive control technology for flutter suppression, and gust load alleviation, and with the increasing need of evaluating the time-dependent subcritical aeroelastic response of lifting surfaces, the time domain representation of unsteady aerodynamic loads becomes a necessary prerequisite toward achieving these goals. It is also of paramount importance to the understanding of fluid–structure interaction for successful flutter analysis. In other words, the design of aircraft wings requires knowledge of how a highly flexible aerofoil will deform under aerodynamic loading and the effect of that deformation on airfoil efficiency.

This work intends to address the flutter phenomenon highlighting the associated issues in flutter analyses. Further insights have explored on the flutter speeds characteristics of composite wings. A beam-box model (GIT box beam [10.7]) discussed earlier (Chapters 7 - 9) is intrinsically investigated to understand further the flutter behaviour of composite wings. The ply angles are varied against sweep angles to intrinsically study the effects of ply orientation on flutter speeds as applicable in convectional unswept and sweptback aircraft wings (Figure 10.1). But first, the importance of aeroelastic coupling is emphasised in brief.
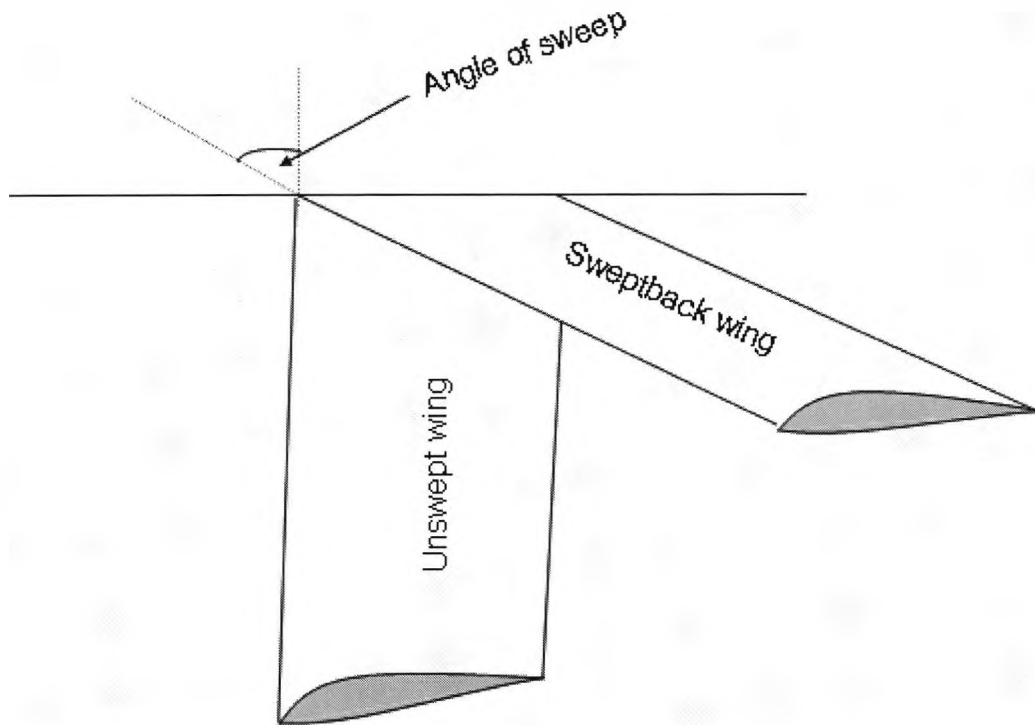
Figure 10.1   An illustration of a convectional unswept and sweptback aircraft wing

10.2   Aeroelastic coupling and its importance

Understanding the fluid–structure interaction is more fundamental than simply plugging a hole in the existing analysis. Numerical and experimental work so far has centred on rigid wings because the aeroelastic interaction between the wing and surrounding fluid could then be neglected and the overall complexity of the problem is greatly reduced [10.8]. Given the complex unsteady fluid mechanics problem at hand, it is reasonable to simplify the problem in order to start the analysis. Computational methods and the fluid mechanical analyses have advanced to the point, where the aeroelastic interaction can probably be included. The design of aircraft wings requires knowledge of how a highly flexible airfoil will deform under aerodynamic loading and the effect of that deformation on airfoil efficiency. The wing shape itself depends upon many physical parameters such as camber, chord and span length, and, most importantly, the mass and stiffness distribution. But dynamic quantities such as the time dependent pressure loading, wing speed, freestream velocity, and local acceleration of the wing surface also directly drive the instantaneous wing deformation. Therefore, it is the

dynamic coupling between the wing and surrounding air that decides the final lift and thrust force. With this in mind, it poses the interesting question: Can manipulation of the wing's aeroelastic properties lead to improved performance? Clearly, changes in the wing deformation will affect the aerodynamics and so it seems quite possible that changes in the physical properties of the wing could yield better performance. In many respects, this is an inverse problem, where the desired result is known, but not the wing shape needed to achieve it. How this could be accomplished both with passive and active control methods remains an open research question, but one worth future exploration.

10.3 Theory

10.3.1 Modal analysis using the dynamic stiffness methods

The primary structure of the wing is idealized as a thin walled laminated composite cantilever beam. The governing differential equations given by Lottati [10.9], among others are used as follows to represent the free vibration motion of the cantilever composite wing, Figure 7.1 (Chapter 7), but with the effect of shear deformation, rotatory inertia and warping ignored:

$$EI\frac{\partial^4 h}{\partial y^4} + K\frac{\partial^3 \Psi}{\partial y^3} + m\frac{\partial^2 h}{\partial t^2} + mX_\alpha \frac{\partial^2 \Psi}{\partial t^2} = -L \tag{10.1}$$

$$-GJ\frac{\partial^2 \Psi}{\partial y^2} - K\frac{\partial^3 h}{\partial y^3} + mX_\alpha \frac{\partial^2 h}{\partial t^2} + I_\alpha \frac{\partial^2 \Psi}{\partial t^2} = M \tag{10.2}$$

where h and Ψ are the transverse displacement and rotation of the wing respectively; m, I_α and X_α are the mass, polar mass moment of inertia per unit length and distance between mass and geometric elastic axes of the wing cross-section respectively.

The differential equations for each of the beam elements representing the wing are then rewritten in matrix form by implementing the dynamic stiffness matrix method [10.10]. The Wittrick-Williams algorithm [10.11, 10.12] is subsequently used to calculate the natural frequencies and mode shapes of the composite cantilever wing structure represented by the assembly of the beam elements along the wingspan.

10.3.2 Flutter analysis using the determinant and V-g methods

In structural idealisation of the wing, beam and lumped mass elements are used in an aeroelastic package called CALFUN (CALculation of Flutter speed Using Normal modes) [10.13] to obtain the mass matrix $[M]$ and the stiffness matrix $[K]$ of the wing. (CALFUN is a computer program that uses the normal mode method and generalised coordinates to compute the flutter speed of a high aspect ratio aircraft wing from its nbasis structural and aerodynamic data). The natural frequencies ω_i and the normal mode shapes ϕ_i (where is the order of the natural frequency/normal mode are then calculated following the usual eigensolution procedure [10.14-10.16].Appendix A gives the evaluation of generalised aerodynamic matrix.

Using the normal modes (obtained from the dynamic stiffness), the flutter equation for an oscillating wing in the range of incompressible airflow and subsonic speed can be written in generalized coordinates as

$$\left\{ [K_D(\omega)] - \frac{\rho V^2}{2}[QA]_R + i\omega[D] + i\frac{\rho V^2}{2}[QA]_I \right\}\{q\} = 0 \tag{10.3}$$

where $[K_D(\omega)]$ is a frequency-dependent dynamic stiffness matrix and $[D]$ is the damping matrix of the structure; $\{q\}$ is the vector of n generalised coordinates q_i $(i = 1, 2, ... n)$ $[QA]_R$ and $[QA]_I$ are the real and imaginary parts respectively of the generalized aerodynamic matrix as a function of the reduced frequency parameter $k = \omega b / V$.

For computational efficiency, the V-g method is used; for accuracy, the determinant method is also used as an alternative way to calculate the flutter speed and frequency. In order to implement the V-g method, the above flutter equation needs to be rewritten in a suitable form so as to present a standard complex eigenvalue problem. This procedure requires the unknown frequency to be expressed explicitly in the dynamic stiffness matrix. It was thus necessary to express the dynamic stiffness matrix $[K_D(\omega)]$ in the Taylor's series expansion form with the stiffness and mass matrices being separated as follows:

$$[K_D(\omega)] = [K]_0 - \omega^2[M]_0 - \omega^4[M]_1 - .... \tag{10.4}$$

It is clear from Eqns.(10.4) that, when high order terms above ω^2 are ignored, $[K]_0$ and $[M]_0$ reduce to finite element stiffness and mass matrices respectively as a degenerate

(approximate) case of the dynamic stiffness matrix $[K_D(\omega)]$. Having performed the exact modal analysis based on $[K_D(\omega)]$, the approximation $[K_D(\omega)] = [K]_0 - \omega_i^2[M]_0$ is now introduced into the flutter equation to give

$$\left\{ [K]_0 - \frac{\rho V^2}{2}([QA]_R + i[QA]_1) + i\omega[D] - \omega^2[M]_0 \right\}\{q\} = 0 \tag{10.5}$$

10.4 Results and discussion

Studies of flutter analysis of composite wings shows that worthwhile improvements in the flutter speed can be achieved by suitable combination of fibre and sweep angles. Based on the rigidity variations caused by ply orientations of a laminate, the flutter speed of the composite wing was computed for the MIT beam. The variation of rigidity properties against ply orientations are shown on Figure 7.3 (Chapter 7). The first five modes were used to compute the flutter speed and were subsequently found to be adequate. Results are expressed in terms of the nondimensionalized flutter speed ratio V_F/V_{F0}, where V_F is the flutter speed of the laminated wing for a given stacking order, and V_{F0} is the corresponding flutter speed when the ply orientation in each of the beam representing the wing is set to zero. The investigation is carried out for swept-back wing. (Note that the wing is rotated about the axis at the root, perpendicular to the wing planform, to provide the required sweep angle). The variation of V_F/V_{F0} with ply angle for the wing is shown in Figure 10.2. The wing flutter results shows that for all sweep angles the maximum flutter speed occurs when the ply angle is around 15°. At this ply angle it is observed that K and bending-torsion cross-coupling parameter ψ (defined as $\psi = K/\sqrt{EIGJ}$) reaches its maximum value whereas GJ is still significant.
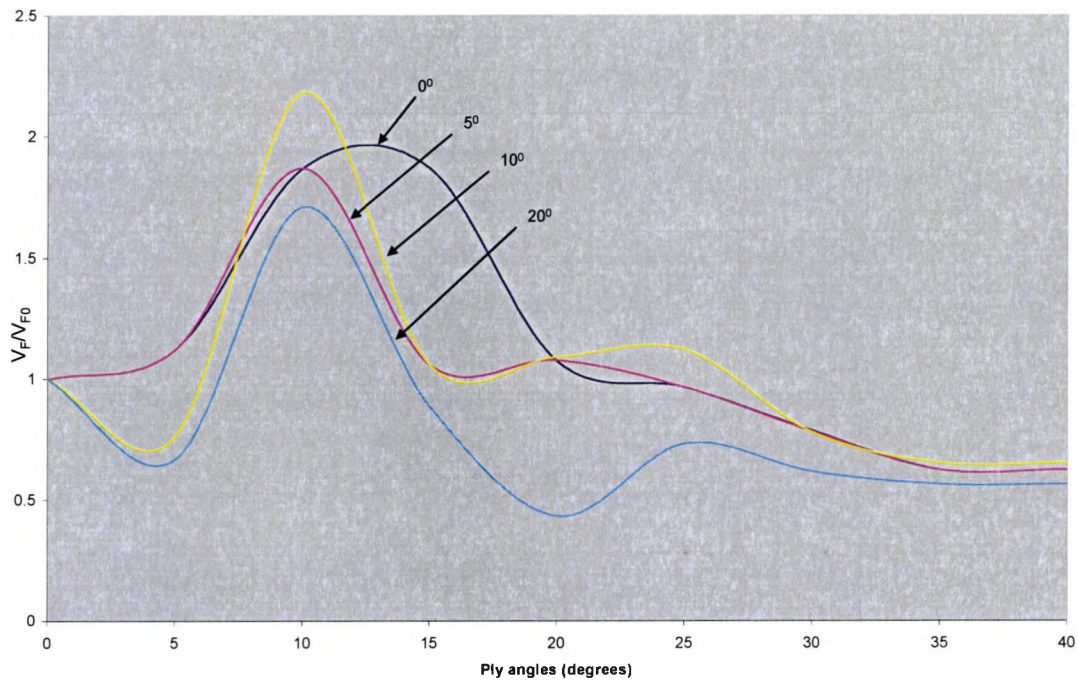
Figure 10.2   The effect of ply orientation on unswept (0^0) and swept-back wings (5^0- 20^0)

The results shown in Figure 10.2 clearly indicate that the maximum flutter speed for the unswept composite wing can be obtained when the plies are alternatively ± 15°, which gives the maximum possible GJ.   Interestingly, the maximum achievable flutter speed for the unswept wing shown in Figure 10.2 occurs at much higher ply angles than the swept wings. The effect of sweep-back angle is quite pronounced for all the wings shown. However, the flutter speed increases with the angle of sweep for wings in which the coupling parameter K and φ have significant values. The effect of sweep angle is most pronounced in the region of maximum values of GJ (i.e. when the plies are alternatively at angles ± 15°) which was the case for the unswept wing.

It is worth noting that the maximum flutter for a swept wing does not occur at the maximum torsional rigidity which was the case for unswept wing. In additional, as the wing's angle of sweep increases, the maximum flutter speed occurs at a reduced ply orientation. The reduction from the original ply orientation for the unswept case becomes pronounced when the angle of sweep increases to its maximum value. It can be generally observed that a combination of high GJ and high negative coupling parameter with high seep

angle maximises the flutter speed. However it should be noted that GJ and ψ are inversely proportional to each other and also the rigidities EI, GJ, and K are not all independent. Therefore a delicate balance is needed to achieve a maximum flutter speed.

The obtained results are in good agreement with published studies which have evidently shown that most interesting features appear at fibre/ply angles between 0°-25° orientations. For instance, Georghiades and Banerjee [10.17-10.19] examined the significance which *wash-out* can have on the flutter characteristics relating to swept and unswept wings composite wings. Sarigul-Klijn and Oguz [10.20] reported on the effect of aspect ratio and ply orientation on aeroelastic response of composite plates and explored the importance of divergence and flutter behaviour in flight vehicles. Another work reported on the nonlinear effects of fibre orientations on the transonic and supersonic flutter characteristics of a composite missile wing model [10.21]. Free vibration of composite wings has been extensively investigated too [10.22, 10.23]. Khot [10.24, 10.25] reported on a composite wing structure with enhanced roll manoeuvre capability at high dynamic pressures using a control system to retwist and recamber the wing.

GIT box-beam is hereby further investigated as our second example. For continuity purposes, the rigidity properties (Figure 10.3 and 10.4) are reproduced to assist in the assessment of their contributions to the flutter of composite wings. The coupling parameter K is shown on Figure 10.4 whereas the effect of ply orientation on the ψ is displayed on Figure 10.4. In Figure 10.6-10.8, the ply angles are varied against sweep angles to intrinsically study the effects of ply orientation on flutter speeds as applicable in convectional swept back aircraft wings. The obtained results confirmed that the most dramatic effects occurs in the range of $\theta = 0°$-45° degrees with little or no contributions observed at higher ply orientation angles no matter the increase in sweep angles. The most interesting characteristics are shown on Figure 10.10 observed from 0° and 15° degrees ply orientations. At 15°, the highest flutter speeds (1600 m/s) were recorded. The maximum coupling (K) (Figure 10.4) was observed at this point too. However, this drops down significantly as the sweep angles increased. For $\beta = 0°$ flutter speeds significantly increases as at 15° sweep angle and stabilising at 1400 m/s. This is followed by a fall from around sweep angle, $\Lambda = 35°$. Interestingly a nearly perfect mirror image from the $\beta = 0°$ and 15° (Figure 10. 5) case can be derived by driving a cutting line at around 1000 m/s flutter speed. In Figure 10.6 -10.8,

different sweep angles seem to be adopting a similar behaviour resulting to either contribution in low, middle or higher values of Λ .
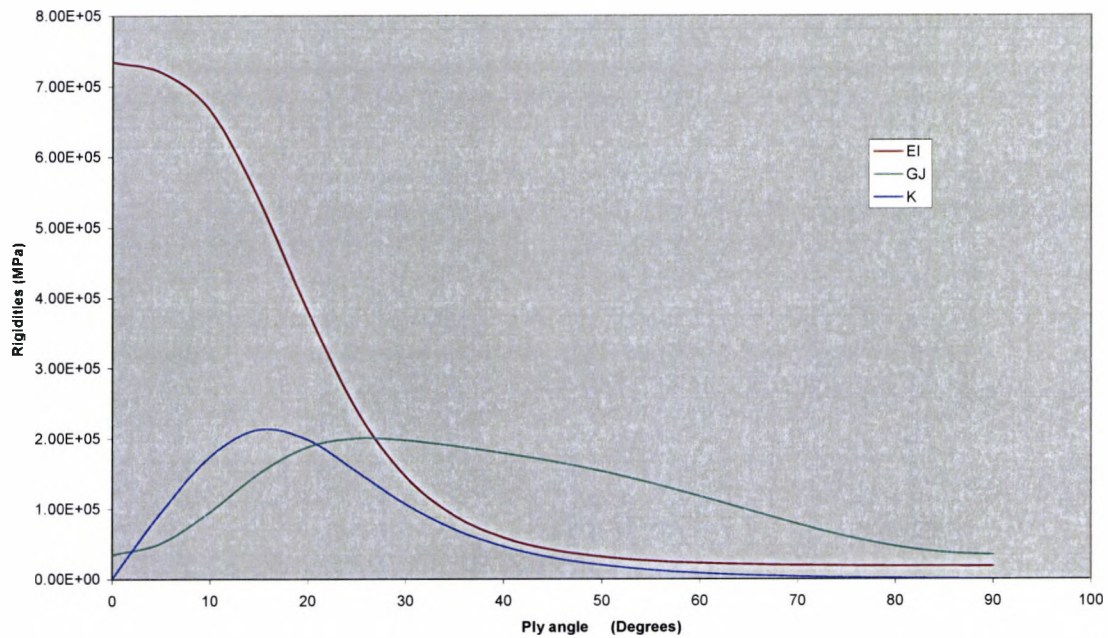
Figure 10.3   The effect of ply orientation on rigidity properties for GIT beam
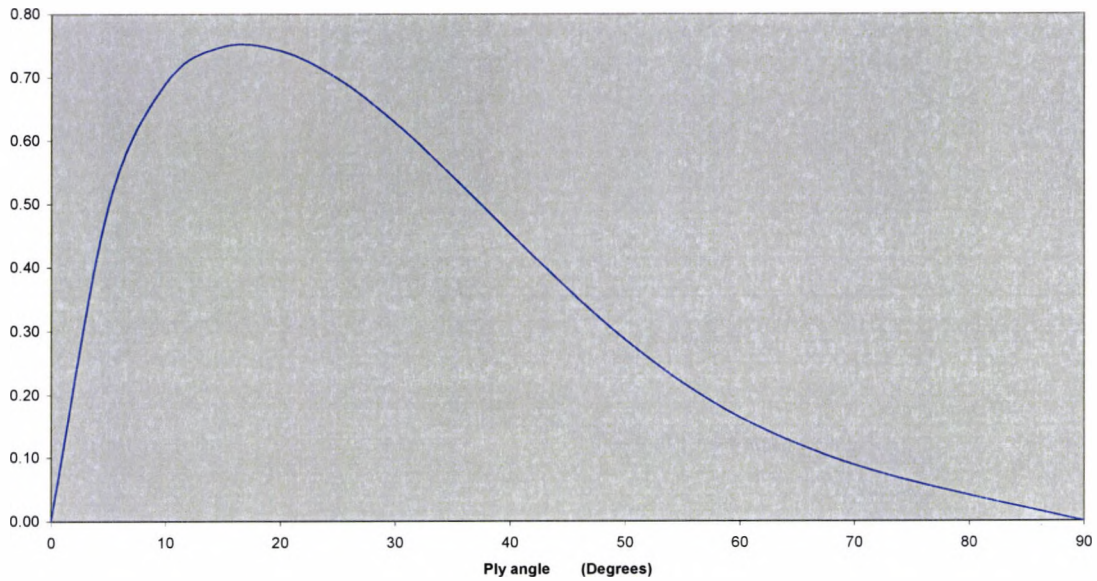
Figure 10.4   The effect of ply orientation on the coupling parameter ψ for GIT beam
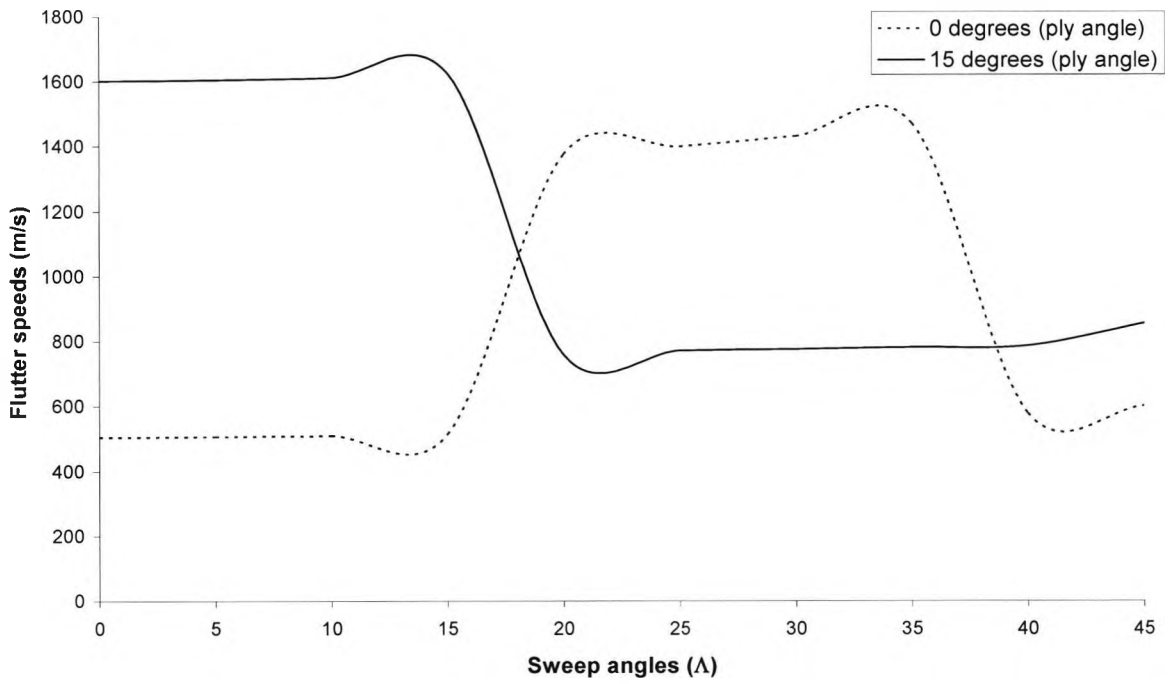
Figure 10.5   Flutter speeds against sweep angles at $\beta = 0°$ and $\beta = 15°$.
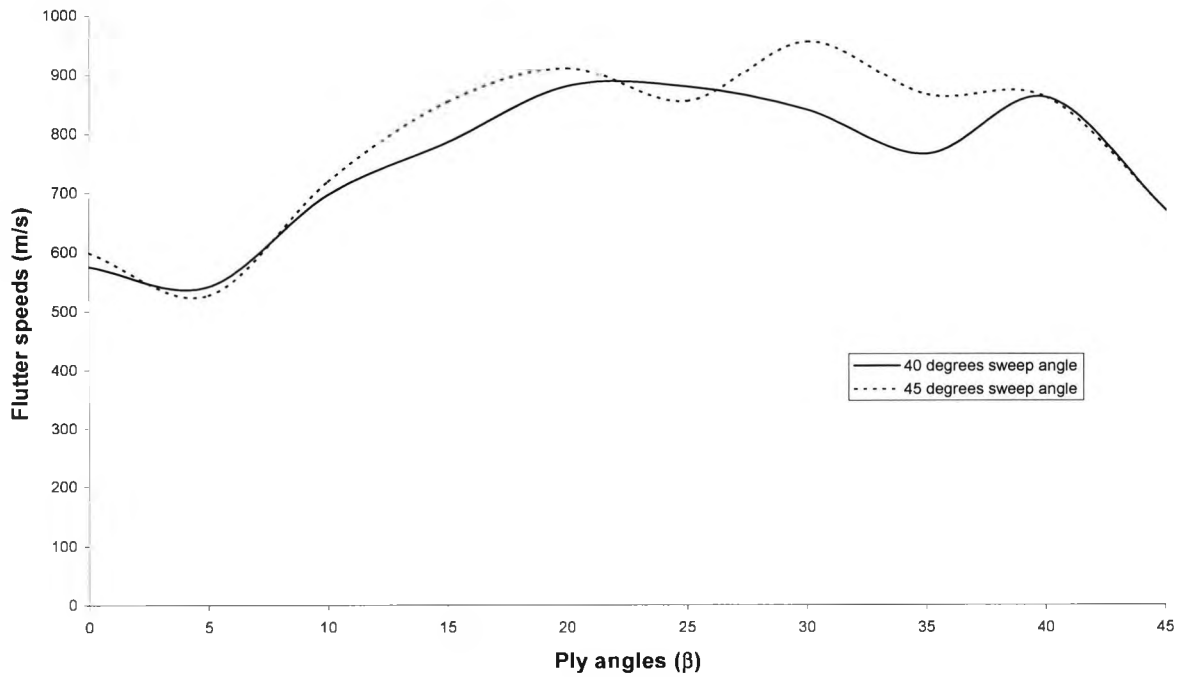
Figure 10.6   The variation of flutter speeds against ply angles at $\Lambda = 40°$ and $45°$.
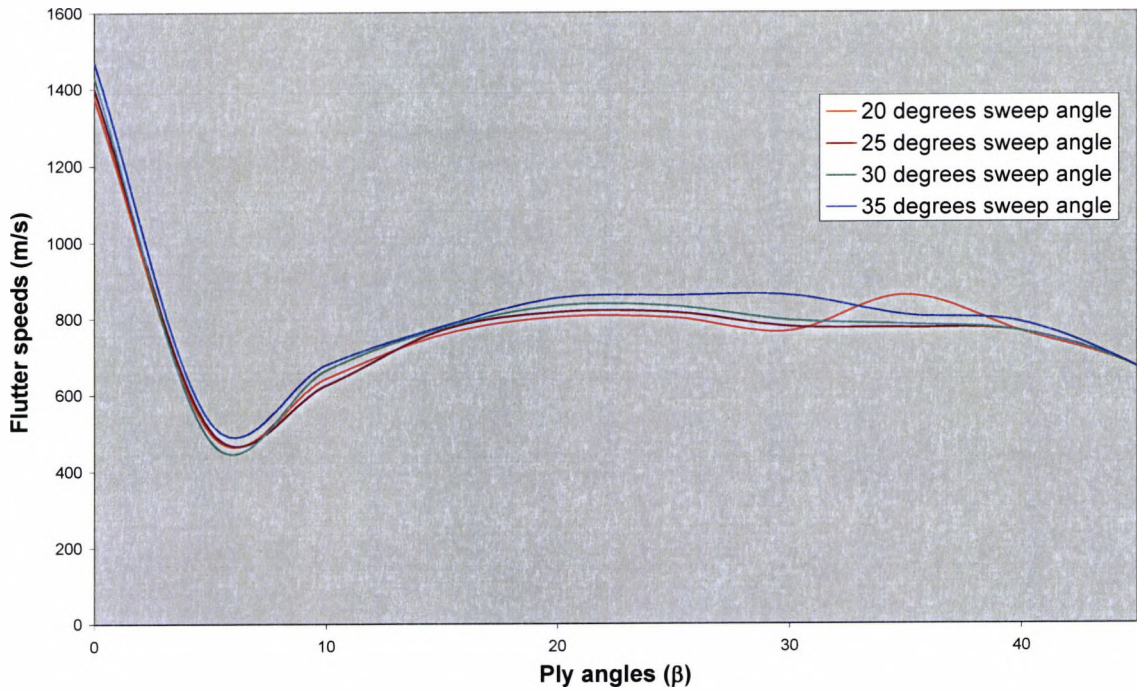
Figure 10.7   The variation of flutter speeds against ply angles at Λ = 20°-35°.
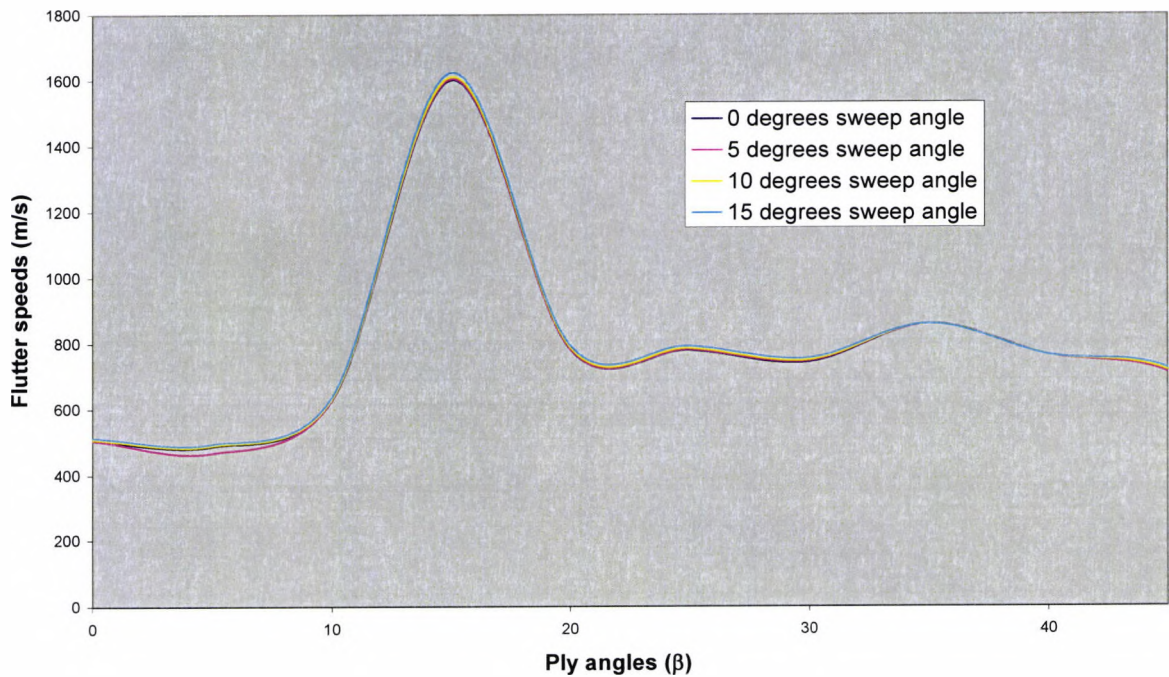
Figure 10.8   The variation of flutter speeds against ply angles at Λ = 0°-15°.

In addition, Figures 10.6-10.8 provides evidence that the main ply orientation effects are found in the range of $\beta = 0°\text{-}45°$, thus supporting previous observations deduced from Figures 10.2. This is also in accordance with previous published reports found in the literature [10.17-10.19, 10.22, 10.23, 10.26, 10.27]. For instance, Guo *et al.* [10.27] analytical study on optimisation of a thin walled wing box model made of laminated composite material showed that up to 18% increase in flutter speed and 13 wt.% reductions can be achieved without compromising the strength. The work also reported that in comparison with the bending rigidity, both the torsional and the coupling rigidities have much more significant effects on the flutter speed of a composite wing. The torsional rigidity also played a relatively more dominant role in aeroelastic tailoring although the work failed to determine a clear trend of the coupling rigidity effect on the flutter speed.

The ply orientation effects on flutter speeds of conventional aircraft wing can classified into three categories as shown in Figures 10.6-10.8 with very minor discrepancies with each category. According to these results, it seems that various ply orientations have similar effects on flutter i.e. when $\beta = 0°\text{-}15°$; $\beta = 20°\text{-}35°$; and $\beta = 40°$ and $45°$. This is a fundamental observation from an engineering design point of view since a designer will only need to select from only three categories as required to achieve the desired results. It is expected that these observations for $\beta = 0°\text{-}90°$ would be a mirror image to negative values of β ranging from $0°$ to $-90°$ though this assumption is beyond the scope of this work. Again, as observed in Figure 10.8, the highest contributions are observed in cases when $\beta = 0°$ and/or when $\beta = 15°$, Figure 10.6 and Figure 10.8 . It is also at these rigidity values of EI and K are highest.

10.5 Conclusions

Studies of flutter analysis of composite wings show that worthwhile improvements in the flutter speed can be achieved by suitable combination of fibre/ply angles and sweep angles. This work intends to address the flutter phenomenon experienced in composite wings. Flutter characteristics of composite wings sought. The flat-beam and box-beam model discussed earlier on is investigated to further understand the flutter behaviour of composite wings. The

plies angles are varied against sweep angles to study the effects of ply orientation on flutter and divergence speeds as applicable in convectional sweptback aircraft wings. The obtained results confirmed that the most dramatic effects occur in the range of 0-30 degrees ply orientations with little or no contributions observed at higher ply orientation angles no matter the increase in sweep angles. It has also been demonstrated that two very important parameters which affect the flutter speed of unswept composite wing are ratio of the uncoupled fundamental bending and torsional natural frequencies and the bending-torsional cross coupling parameter. The results show that when the uncoupled bending and torsional natural frequencies is less than about 0.1, the maximum flutter speed for unswept composite wing can be achieved from the maximum value of the torsional rigidity whereas when the ratio is above this value, the maximum flutter speed can be achieved from the maximum value of the negative cross-coupling parameter. Therefore the maximum flutter speed can be achieved by maximising either the torsional rigidity or the negative cross-coupling parameter.

11   Principal conclusions and suggestions for future work

Experimental investigations have been carried out on polyurethanes (PU) and polyanilines (PANI), PU/PANI blended composites, PU/montmorillonite (PU/MMT) nanocomposites to examine the morphology, compatibility, mechanical and thermal properties. In particular, thermogravimetry analysis (TGA) results depict that the sample with high content of PANI (12%) had delayed degradation process as compared to the rest of the samples. This is attributed to strong intermolecular bonds formed in the thermoplastic elastomer. It is also observed that the percentage elongation-at-break was at its best at lower PANI content (3%) in the PU/PANI elastomer and above this percentage, the elongation-at-break seemed to worsen with further increase of the percentage of PANI at the expense of the Young's modulus and other tensile properties. In addition, thermal properties of PU/MMT nanocomposites with intercalated structure, as evidenced by scanning electron microscopy (SEM) data, prepared by prepolymer method, showed a considerably huge potential for increase thermal degradation properties and form fundamental research for further flammability studies. Significant differences in the thermal behaviour of neat PU and PU nanocomposites indicate that nanoadditives play an important role due to barrier effects that increase during volatilization owing to the reassembly of the reticular of the silicate on the surface. It has been established that PU thermoplastics elastomers make a perfect multipurpose core for sandwich composites destined for structural applications. It is also shown that the nanoparticles strongly influence the properties of the composites at very low volume fractions. This is mainly due to their small interparticle distances and the conversion of a large fraction of the polymer matrix near their surfaces into an interphase of different properties as well as to the consequent change in morphology. As a result, the desired properties are reached at low filler volume fraction, which allows the nanocomposites to retain the macroscopic homogeneity and low density of the polymer. Besides, the geometrical shape of the particles plays an important role in determining the properties of the composites.

The research further focuses on the theoretical and experimental modal analysis of sandwich composite structures with polymeric cores. A dynamic stiffness theory for a three-layered sandwich beam is developed in order to investigate its free vibration characteristics. In this new development all three layers of the sandwich beam are modelled as Timoshenko beam. The modal analysis results for both the theoretical and experimental investigations show good agreement and provide confidence in the analysis.

Following the investigations of sandwich beam, free vibration behaviour of composite beams with both solid and thin-walled rectangular cross-sections has been carried out. The investigations show that ply orientations and stacking sequences can have significant effects on the natural frequencies and mode shapes of a composite beam. It is evident from the results that modal interchanges between bending and torsional modes can occur as a result of ply orientation in the laminate which can be significant from an aeroelastic stand point. The selection of fibres and resins, and more importantly the manner in which they are arranged i.e. the ply orientation and stacking sequence must be carefully controlled to achieve desirable stiffness properties. Buckling behaviour of composite thin-walled composite and metallic columns has also been investigated. In particular, the variations of stiffness properties and buckling loads have been studied in details. The results, which are in good agreement with published buckling theories, show that composite structures can also be tailored to achieve desirable buckling strength. This work includes the bending-torsion material coupling effects in a composite beam when establishing its stiffness matrix and buckling strength.

The investigation on free vibration analysis has led to subsequent aeroelastic analysis. In this respect, flutter characteristics of composite wings have been established using composite beam idealisation and two dimensional Theodorsen aerodynamics. Studies on flutter analysis of composite wings show that substantial improvements in the flutter speed can be achieved by suitable combination of fibre/ply and sweep angles. The ply and/or fibre orientation have proved to be an efficient way of controlling flutter. The flat-beam and box-beam models have been used as examples to understand the flutter behaviour of composite wings. The investigation has shown that ply angles as well as sweep angles have significant effects on flutter speeds.

11.1 Suggestions for future works

A research direction into structural analysis through the production of engineering models of structural behaviour in order to understand the effect of the inclusion of fillers at the nanoscale level in a polymeric matrix for aerospace CFRP structures is crucial. In this case, more efforts may also be dedicated to modification and adoption of the traditional available processing technologies for CFRP in order to accommodate nanocomposites materials. The complete production of CFRP nanocomposites prototype starting from the single components may be considered.

Montmorillonites are constructed of repeating triple-layer sheets composed of two tetrahedral silica sheets fused to an edge-shared octahedral sheet of either aluminium or magnesium hydroxide with a thickness of < 1 nm and a length of ~100 to several hundred nanometres. A future research objective would be aimed to exploit the layered silicates (intercalated, exfoliated, and, intercalated-and-exfoliated) in the high performance nanoresins applicable to manufacturing of laminated carbon fibre-reinforced composites for aeroelastic benefits - (nano-laminates within micro/macro-laminates).

The nano-films stands as potential adhesive fillers on normal sandwich composites for both sandwich and laminated composites - to explore applicability in mechanical and thermal properties enhancements. However, the nano-films must be engaged as adhesives right from the initial fabrication of composite plies. Experimental, computational and theoretical work is necessary to understand associated properties.

Conducting polymers may be used to transmit power within the structure while still offering other functionality. For instance, a loaded sandwich beam with a conducting polymer core may be used to reduce excessive wiring in the automotives. Further investigations are necessary to ascertain such ambitious concepts.

Vibration damping using sandwich structures (passive damping through elastomeric cores) is another new research direction. The damped energy may be converted to useful energy e.g. converted to electric power for use in electrical appliances.

The research results confirm the potential advantage of ply orientation and stacking sequences in composite beams that can be used to produce desirable aeroelastic effects in aeronautical design. However, further in-depth investigations are necessary for loaded wings. Additionally, more research into structural optimisation is required.

The research reported here is fundamental to sandwich composites research. In addition, much deeper investigation will be required when the face layers of the sandwich beam is replaced by composite laminates made of fibre reinforced composites.

Material requirements for highest tensile and shear strengths of laminates are often incompatible with requirements for highest toughness. Compared with fracture in metals, research into the fracture behaviour of composites is in its infancy. Much of the necessary theoretical framework is not yet fully developed and there is no simple recipe for predicting the toughness of all composites. Engineers are not able yet to design with certainty the structure of any composite so as to produce the optimum combination of strength and toughness. This remains a central research direction.

12   References

Chapter 1

[1.1] Lincoln, DM, Vaia, RA, Beown, JM., Tolle, THB. Revolutionary nanocomposite materials to enable space systems in the 21st-century, Proceedings of IEEE Aerospace Conference. 2000. p.183-192.

[1.2] Njuguna J, Pielichowski K. Polymer nanocomposites for aerospace applications: properties. Advanced Engineering Materials. 2003;5(11)769-778.

[1.3] Njuguna J, Pielichowski K. Recent developments in polyurethane-based conducting composites. Journal of Material Science. 2004;39(13)4081-4094.

[1.4] Harris, C.E., Shuart, M.J., Gray,H.R.,. A survey of emerging materials for revolutionary aerospace vehicle structures and propulsion systems. NASA/TM-2002-211664. May 2002;p. 45.

[1.5] See . http://www.hexcelfibers.com/Markets/Products/Continuous/_Productlist.htm.

[1.6] Subramoney S,. Novel nanocarbons - structure, properties, and potential applications. Advanced Materials. 1998;10(15)1157-1171.

[1.7] Lu JP,. Elastic properties of carbon nanotubes and nanoropes. Physical Review Letters 1997;79(7)1297-1300.

[1.8] Reinhart TJ . Technical Chairman, Composites Engineering Handbook, Vol. I: Published by ASM International, Metals Park, Ohio 44073, 1987.

[1.9] Sinnott SB., Shenderova OA., White CT., Brenner DW. Mechanical properties of nanotubule fibres and composites determined from theoretical calculations and simulations. Carbon. 1998;36(1-2)1-9.

[1.10] Star A, Stoddart JF, Steuerman D, Diehl M, Boukai A, Wong EW, Yang X, Chung S, Choi H,Heath JR. Preparation and properties of polymer-wrapped single-walled carbon nanotubes. Angew Chemistry International Edition 2001;40(9)1721-1725.

[1.11] Szodruch J, Hilbig R. Building the future aircraft design for the next century. AIAA Paper 98-0135, 1998.

[1.12] Globus A. Molecular Nanotechnology in Aerospace - 1999. Proceedings of Space 2000. 2000. p.502-529.

[1.13] Banerjee JR, Sobey, AJ. Dynamic stiffness formulation and free vibration analysis of a three-layered sandwich beam. International Journal of Solids and Structures. 2005;42(8)2181-2197.

[1.14] Banerjee JR. Free vibration of sandwich beams using dynamic stiffness method. Computers and Structures. 2003;81(18-19)1915-1922.

Chapter 2

[2.1]   M. Shioya, E. Hayakawa,A.Takaku,. Non-hookean stress-strain response and changes in crystallite orientation of carbon fibres J. Mater. Sci. 1996;31(17)4521-4532.

[2.2]   R. Perret, W. Ruland,. The microstructure of PAN-base carbon fibres. Journal of Applied Crystallography. 1970;3525.

[2.3]   L. Fischer W. Ruland. Influence of graphitization on the mechanical properties of carbon fibers. Colloid Polymer Science. 1980;(258)917.

[2.4]   M. G. Northolt, L. H. Veldhuizen,H.Jansen,. Tensile deformation of carbon fibers and the relationship with the modulus for shear between the basal planes Carbon. 1991;29(8)1267-1279.

[2.5]   H. L. Cox . The elasticity and strength of paper and other fibrous materials. British Journal Applied Physics. 1952;3;72-79.

[2.6]   W. Kelly R. Tyson. Tensile Propertles of Flbre-Reinforced MetalsCopper/Tungsten and Copper Molybdenum. Journal of Mechanics of Physical Solids. 1965;13;329-350.

[2.7]   L. Nielsen . Mechanical properties of copolymer and composites. Journal of Applied Polymer Sciences. 1973;173819.

[2.8]   K. E. Dujardin, T. W. Ebbesen, P. N. Yianilos,M.M.J.Treacy,. Young's modulus of single-walled nanotubes. Physical Reviews B. 1998;58(20)14013-14019.

[2.9]   B. Pipes, S. J. Frankland, P. Hubert,E.Saether, Self-consistent physical properties of carbon nanotubes in composite materials. ICASE Report 2002-46, 2002, 20.

[2.10] H. D. Wagner, O. Lourie, Y. Feldman,R.Tenne,. Stress-induced fragmentation of multiwall carbon nanotubes in a polymer matrix. Appl. Phy. Lett. 1998;72 (12)188-190.

[2.11] E. Hernandez, C. Goze, P. Bernier,A.Rubio,. Elastic properties of single-wall nanotubes. Applied Physics A. 1999;68(3)287-292.

[2.12] C.F. Cornwell, L. T. Wille. Elastic properties of single-walled carbon. nanotubes in compression. Solid State Commun. 1997;101;555.

[2.13] J. P. Perdew AZ. Self-interaction correction to density-functional approximations for many-electron systems. Phys. Rev. B. 1981;23(10-15)5048-5079.

[2.14] D. M. Ceperley, B. J. Alder. The low density phases of the electron gas. Physical Review Letters. 1980;45(C-7)566.

[2.15] O. Atsushi, S. Okada,S.Saito,. Scope of the Tsukuba Symposium on Carbon Nanotube in Commemoration of its 10th Anniversary, Physica B. 2002;323;21.

[2.16] N. Troullier J. L. Martins. Efficient pseudopotentials for plane-wave calculations. Physical Review B. 1991;43(3)1993-2006.

[2.17] P. Glatkowski, P. Mack, J. L. Conroy, J. W. Piche,P.Winsor. Polymenr nanocomposites and methods of preparations. US Patent Application Pub. No. US2002/0143094 A1.

[2.18] J. Sandler, P. Werner, M. S. P. Shaffer, V. Demchuk, V. Altstädt,A.H.Windle. Carbon-nanofibre-reinforced poly(ether ether ketone) composites. Composites Part A. 2002;33(8)1033-1039.

[2.19] R. F. Egerton. Electron energy loss spectroscopy in the electron microscope, Plenum Publishing, NewYork, 1996.

[2.20] R. W. Siegel, S. K. Chang, B. J. Ash, J. Stone, P. M. Ajayan, R. W. Doremus, L.S.Schadler. Mechanical behavior of polymer and ceramic matrix nanocomposites. Scripta Materials. 2001;44(8-9)2061-2069.

[2.21] Lau KT, Shi SQ. Failure mechanisms of carbon. nanotube/epoxy composites pretreated in different. temperature environments. Carbon. 2002;40(1)2961-2968.

[2.22] A. Thess, R. Lee, P. Nikolaev, H. Dai, P. Petit, J.Robert. Crystalline ropes of metallic carbon nanotubes. Science. 1996;273(5274)483-487.

[2.23] Loidl, D., Peterlik,H. Müller, M. Riekel, C. Paris,O. Elastic moduli of nanocrystallites in carbon fibers measured by in-situ X-ray microbeam diffraction. Carbon. 2003;41(3)563-570.

[2.24] M. P. S. Shafier,A.H.Windle. Fabrication and characterization of carbon nanotube/poly(vinyl alcohol) composites. Advanced Materials. 1999;11(11)937-941.

[2.25] Poulin P, Vigolo B, Launois P. Films and fibres of oriented single wall nanotubes. Carbon. 2002;40(10)1741-9.

[2.26] G. G. Tibbetts J. J. McHugh. Mechanical properties of vapor-grown carbon fiber composites with thermoplastic matrices. Journal of Materials Research. 1999;14(7)2871-2880.

[2.27] H. Yamanashi, H. Ushijima, M. Katsumata,M.Endo. Properties of epoxy composite using vapor grown carbon fibers (VGCF's) as an advanced adhesive in The 21st Biennial Conference on Carbon, Buffalo, June 1993, p.88.

[2.28] M. Okamoto, P. H. Nam, K. T. Maiti, N. Hasegawa,A.Usuki. A house of cards structure in polypropylene/clay nanocomposites under elongational flow. Nano Lett. 2001;1 (6)1295-1298.

[2.29] F. J. Medellin-Rodriguez, C. Burger, B. Hsiao, B. Chu, R. A. Vaia,S.Phillips. Time-resolved shear behavior of end-tethered Nylon 6-clay nanocomposites followed by non-isothermal crystallization. Polymer. 2001;42(21)9015-9023.

[2.30] B. Ng, R. W. Siegel, B. Ash,L.S.Schadler. A study of the mechanical and permeability properties of nano-and micron-TiO_2, filled epoxy composites. Advanced Composites Letters. 2001;10(3)101-111.

[2.31] R. A. Vaia, G. Price, P. N. Ruth, H. T. Nguyen,J.Lichtenhan. Polymer/layered silicate nanocomposites as high performance ablative materials. Applied Clay Sciences. 1999;15(1)67-92.

[2.32] C. Chenggang C. David. Preparation, characterization and nanostructural evaluation of epoxy nanocomposites, 46th Inter/l SAMPE Symposium and Exhibition, 2001, 1, 362.

[2.33] C. M. Lukehart, W. D. King, S. B. Milne, F. E. Jones III, J. D. Corn, D. L Boxall, K.C.Kwiatkowski. Polymetallic precursors and compositions and methods for making supported polymetallic nanocomposites for fuel cell use. US Patent No. 6232264. 2001

[2.34] X. Gong, J. Liu, S. Baskaran, R. D. Voise, J.S.Young. Surfactant-Assisted Processing of Carbon Nanotube/Polymer Composites. Chemistry of Materials. 2000;12(4)1049-10-52.

[2.35] V. Lordi N. Yao. Molecular mechanics of binding in carbon-nanotube-polymer composites. Journal of Material Reseaarch. 2000;15(12)2770-2749.

[2.36] Cooper CA, Young RJ, Halsall M. Investigation into the deformation of carbon nanotubes and their composites through the use of Raman spectroscopy. Composites - Part A: Applied Science and Manufacturing. 2001;32(3-4)401-411.

[2.37] P. M. Ajayan, L. S. Schadler, C. Giannaris, A.Rubio. Single-walled carbon nanotube-polymer composites. Strength and weakness. Adv. Mater. 2000;12(10)750-753.

[2.38] C. Chenggang DC,. Nanophase and Nanocomposite Materials IV. Symposium Mater. Res. Society Symposium Proceedings, 2002, 703, 3.

[2.39] See . http://nano-lab.com/productdatasheets.html.

[2.40] R. J. Kuriger, M. K. Alam, D. P. Anderson, R.L.Jacobsen. Processing and characterization of aligned vapor grown carbon fiber reinforced polypropylene. Composites Part A. 2002;33(1)53-82.

[2.41] C. J. Dasch, W. J. Baxter, G.G.Tibbetts. Thermoplastic composites using nanometer-size. vapor-grown carbon fibers. The 21st Biennial Conference on Carbon, Buffallo, June 1993, p. 82.

[2.42] R. D. Patton, C. U. Pittman Jr., L. Wang,J.R.Hill,. Vapor. grown carbon fiber composites with epoxy and. poly(phenylene sulfide) matrixes Composites Part A. 1999;30;1081.

[2.43] A. Singh RH,. Oligomer-modified layered inorganic compounds and their use in nanocomposites. United States Patent No. 6057035.

[2.44] A. Blumstein. Multivariate analysis of golden marmot maximum running speed: a new method. A. Bulletin of Chemical Society. 1961;899.

[2.45] S. D. Burnside, E.P. Giannelis. Synthesis and properties of new poly (dimethylsiloxane) nanocomposites. Chemistry of Materials. 1995;71597.

[2.46] E. Giannelis . Adv. Mater. Polymer layered silicate nanocomposites. 1996;829.

[2.47] J. W. Gilman, C. L. Jackson, A. B. Morgan, R. Jr. Harris, E. Manias, E. P. Giannelis, M. Wuthenow, D. Hilton, S.H.Phillips. Flammability properties of polymer-layered-silicate nanocomposites. polypropylene and polystyrene nanocomposites. Chemistry of Materials. 2000;12(7)1866-1873.

[2.48] C. S. Triantafillidis, P. C. LeBaron, T.J.Pinnavaia. Thermoset epoxy-clay nanocomposites: the dual role of alpha, omega-diamines as clay surface modifiers and polymer curing agents. Journal of Solid State Chemistry. 2002;167(2)354-362.

[2.49] G. Beyer. Flame retardant properties of EVA-nanocomposites and improvements by combination of nanofillers with aluminium trihydrate. Fire Materials. 2002;262(5)91-95.

[2.50] Lincoln, D.M.., Vaia, R.A., Beown, J.M., Tolle,T.H.B.,. Revolutionary nanocomposite materials to enable space systems in the 21st-century, Proceedings of IEEE Aerospace Conference. 2000. p.183-192.

[2.51] M. L. Lake . Fabrication of vapour grown carbon fibre/thermoplastic composites by injection and compression moulding in Proceedings of the NATO Advanced Study Institut. 2001, p. 331.

[2.52] Di Taranto RA. Theory of vibratory bending of elastic and viscoelastic layered finite-length beams. Journal of Applied Mechanics. 1965;ASME 32881-886.

[2.53] Mead DJ, Sivakumaran S. The Stodola method applied to sandwich beam vibration. In: Anonymous of the symposium on numerical methods for vibration problems. University of Southampton, UK, 1966.

[2.54] Mead DJ, Markus S,. The Forced Vibration of a Three-layer, Damped Sandwich Beam with Arbitrary Boundary Conditions. Journal of Sound and Vibration. 1969;10;163-175.

[2.55] Ahmed KH,. Dynamic analysis of sandwich beams. Journal of Sound and Vibration. 1972;21263-276.

[2.56] Baber TT, Maddox RA, Orozco CE. A finite element model for harmonically excited viscoelastic sandwich beams. Computers & Structures. 1998/1;66(1)105-113.

[2.57] Sainsbury MG, Zhang QJ. The Galerkin element method applied to the vibration of damped sandwich beams. Computers & Structures. 1999/5;71(3)239-256.

[2.58] Fasana A, Marchsiello S. Rayleigh-Ritz analysis of sandwich beams. Journal of Sound and Vibration. 2001/4/5;241(4)643-652.

[2.59] Mead DJ. A comparison of some equations for the flexural vibration of damped sandwich beams. Journal of Sound and Vibration. 1982;83(3)363-377.

[2.60] Rao DK. Frequency and loss factors of sandwich beams with various boundary conditions. Journal of Mechanical Engineering Science. 1978;20(5)271-282.

[2.61] Bhimaraddi A. . Sandwich beam theory and the analysis of constrained layer damping. Journal of Sound and Vibration. 1995;179(4)591-602.

[2.62] Frostig Y, Baruch M. Free vibration of sandwich beams with a transversely flexible core: a high order approach. Journal of Sound and Vibration. 1994;176(2)195-208.

[2.63] Sakiyama T. , Matsuda H. , Morita C. Free vibration analysis of sandwich beam with elastic or viscoelastic core by applying the discrete green function. Journal of Sound and Vibration. 1996/3/28;191(2)189-206.

[2.64] Sainsbury MG, Ewins DJ. Vibration analysis of a damped machinery foundation structure using the dynamic stiffness coupling technique. Journal of Engineering Industrial Transactions ASME. 1974;96 Series B(3)1000-1005.

[2.65] Banerjee JR. Free vibration of sandwich beams using dynamic stiffness method. Computers and Structures. 2003;81(18-19)1915-1922.

[2.66] Banerjee JRS,A.J. Dynamic stiffness formulation and free vibration analysis of a three-layered sandwich beam. International Journal of Solids and Structures. 2005;42(8)2181-2197.

[2.67] Howson WP, Zare A. Exact dynamic stiffness matrix for flexural vibration of three-layered sandwich beams. J Sound Vibrat. 2005;282(3-5)753-67.

[2.68] Volovoi VV, Hodges DH, Cesnik CES, Popescu B. Assessment of beam modeling methods for rotor blade applications. Mathematical and Computer Modeling. 2001;33;1099-1112.

[2.69] W. Yu, V. Volovoi CESC,. On Timoshenko-like modeling of initially curved and twisted composite beams. International Journal of Solids and Structures. 2002;39;5101-5121.

[2.70] Berdichevsky VL. Variational-asymptotic method of constructing a theory of shells. PMM. 1979;43664-687.

[2.71] Popescu B, Hodges DH. On asymptotically correct Timoshenko-like anisotropic beam theory. International Journal of Solids and Structures. 1999;37;535-558.

[2.72] Jung SN, Nagaraj VT, Chopra I. Assessment of composite rotor blade modeling techniques. Journal of the American Helicopter Society. 1999;44;188-205.

[2.73] Rosen A,. Structural and dynamic behavior of pretwisted rods and beam. Applied Mechanics Reviews. 1991;44(12)483-515.

[2.74] Hodges DH,. A review of composite rotor blade modeling. AIAA Journal. 1990;28561-565.

[2.75] Pandey, M., Kabir, M., Sherbourne,A. Flexural-torsional stability of thin-walled composite I-section beams. Composites Engineering. 1995;5;321-342.

[2.76] Bauld Jr. NR, Tzeng LS. Vlasov theory for fiber-reinforced beams with thin-walled open cross sections. International Journal of Solids and Structures. 1984;20;277-297.

[2.77] Volovoi VV, Hodges DH, Berdichevsky VL, Sutyrin V. Asymptotic theory for static behavior of elastic anisotropic I-beams. International Journal of Solids and Structures. 1998;36,1017-1043.

[2.78] Hodges DH, Peters DA,. Lateral-torsional buckling of cantilevered elastically coupled composite strip- and I-beams. International Journal of Solids and Structures. 2001;38(9)1585-1603.

[2.79] Georghiades GA, Banerjee JR. Role of modal interchange on the flutter of laminated composite wings. Journal of Aircraft. 1998;35(1)157-161.

[2.80] Georghiades GA, Banerjee JR. Significance of Wash-Out on the Flutter Characteristics of Composite Wings. Journal of Aircraft. 1998;35(5)823-825.

[2.81] Georghiades GA, Guo SJ, Banerjee JR. Flutter characteristics of laminated composite wings. Journal of Aircraft. 1996;33(6)1204-1206.

[2.82] Sarigul-Klijn NO,S. Effect of aspect ratio and ply orientation on aeroelastic response of composite plates. Journal of Aircraft. 1998;35(4)657-659.

[2.83] Kim, D. H. Lee,I. Nonlinear flutter characteristics of composite missile wing in transonic/low-supersonic flows. Journal of Aircraft. 2002;39(5)889-892.

[2.84] Njuguna J,. Dynamics of composite wings. 2001;MSc. Thesis.

[2.85] Njuguna, J., Su, H., Cheung,C.W.Banerjee J.R.,. The influence of ply orientation on the free vibration of composite beams. In UNSW 2002 Conference Proceedings, Sydney, Australia, Eds. Bandyopadhyay, N. Gowripalan, S. Rizkalla, ACUN-4. 2002;p.307-314.

[2.86] Khot NS. Design of composite smart wing to enhance roll maneuver. Proceedings of - The Iinternational Society for the Optical Engineers (SPIE). 1996;3321;436-446.

[2.87] Guo SJ, Bannerjee, J. R. Cheung,C.W.. The effect of laminate lay-up on the flutter speed of composite wings. Proceedings of the Institute of Mechanical Engineers Vol. 217 Part G: J. Aerospace Engineering. 2003;pp.115-122.

[2.88] Chandrashekhara K, Bhatia K,. Active buckling control of smart composite plates-finite-element analysis. Smart Materials and Structure. 1993;2(1)31-39.

[2.89] Chase JG, Bhashyam S,. Optimal stabilization of plate buckling. Smart Materials and Structure. 1999;8(2)204-211.

[2.90] Meressi T, Paden B. Buckling control of a flexible beam using piezoelectric actuators. Journal of Guidance Control and Dynamics. 1993;16(5)977-980.

[2.91] Thompson SP, Loughlan J. The active buckling control of some composite column structure strips using piezoceramic actuators. Composite Structures. 1995;32(1-4)59-67.

[2.92] Yang Y, Ju, Soh CK. Analytical and semi-analytical solutions for vibration control of a cantilevered column using a piezoelectric actuator. Journal of Smart Materials and Structures. 2003;12(2)193-203.

[2.93] Wang Q. On buckling of column structures with a pair of piezoelectric layers. Engineering Structures. 2002;24(2)199-205.

[2.94] Sedaghat A, Cooper JE, Leung AYT, Wright JR. Estimation of the hopf bifurcation point for aeroelastic systems. Journal of Sound and Vibration. 2001;248(1)31-42.

[2.95] Munk MM,. Propeller containing diagonally disposed fibrous material, U.S Patent 2,484,308, 1111, Oct.1949.

[2.96] Jensen DW, Crawley, Dugundji J. Vibration of cantilevered graphite/epoxy plate with bending-torsion coupling. Journal of Reinforced Plastics and Composites. 1982;1;254-270.

[2.97] Hodges, D. H., Atilgan, A. R., Fulton, M. V., Refield, L.W.,. Free vibration analysis of composite beams. Journal of American Helicopter Society. 1991;36;36-47.

[2.98] Shi G, Lam KY,. Finite element vibration analysis of composite beams based on higher-order beam theory. Journal of Sound and Vibration. 1999;219;707-721.

[2.99] Mahapatra, D. R.,Gopalakrishnan S.T., Sankar S. . Spectral-element-based solutions for wave analysis of multiply connected unsymmetric laminated composite beams. Journal of Sound and Vibration. 2000;237(5)819-836.

[2.100] Bassiouni, A.S, GadElrab, R.M, Elmahdy,T.H,. Dynamic analysis for laminated composite beams. Composite Structures. 1999;44(2-3)81-87.

[2.101] Kim W, Argento, Scott RA,. Free vibration of rotating tapered timoshenko shaft. Journal of Sound and Vibration. 1999;46(2)1225-1247.

[2.102] Patel BP, Ganapathi M, Touratier M. Nonlinear free vibration/post buckling analysis of laminates orthoropic beams/columns on a two parameter elastic foundation. Composite Structures. 1999;46(2)189-196.

[2.103] Yildirim V,. Rotary inertia, axial and shear deformation effects on the in-plane natural frequencies of the symmetric cross-ply laminated circular arches. Journal of Sound and Vibration. 1999;224(4)575-589.

[2.104] Hidenori M, Junja Y,. Dynamic response of plane anisotropic beams with shear deformation. Journal of Engineering Mechanics. 1997;123(12)1268-1275.

[2.105] Song SJ, Waas AM,. Effects of shear deformation on buckling and free vibration of laminated composite beams. Composite Structures. 1997;37(1)33-43.

[2.106] Farghaly SH, Gadelrab RM,. Free vibration of a stepped composite timoshenko cantilever beam. Composite Structures. 1995;187(5)886-896.

[2.107] Fein H,. Holographic analysis of the structural and operational dynamics of an advanced graphite-epoxy composite flight control structure. Proceeding - SPIE the International Society for Optical Engineering. 1998;3397179-186.

[2.108] Fein H,. Holographic interferometry applied to characterize the dynamic structure of an advanced graphite-epoxy polymer composite structure. Proceeding - SPIE the International Society for Optical Engineering. 1997;3010(0361-0748)258-265.

[2.109] He, S. Y. Chen,W.S., Chen ZL. A uniformizing method for the free vibration analysis of metal-piezoceramic composite thin plates. Journal of Sound and Vibration. 1998;217(2)261-281.

[2.110] Sundaresan, P., Singh, G. Rao, G.V. A simplified approach to investigate vibratory behaviour of thermally stressed laminated structures. Journal of Sound and Vibration. 1999;219(4)603-618.

[2.111] Wang S. Vibration of thin skew fibre reinforced composite laminates. Journal of Sound and Vibration. 1997;201(3)335-352.

[2.112] Cupia P. Calculation of natural frequencies of composite plates by the rayleigh -ritz method with orthogonal polynomials. Journal of Sound and Vibration. 1997;201(3)385-387.

[2.113] Messina A, Soldatos KP,. Ritz-type dynamic analysis of cross-ply laminated circular cylinders subjected to different boundary conditions. Journal of Sound and Vibration. 1999;227(4)749-768.

[2.114] Seeley CE, Chattopadhyay A. Modeling of adaptive composites including debonding. International Journal of Solids and Structures. 1999;36(12)1823-1843.

[2.115] Friswell MI, Inman DJ,. Hybrid damping treatments in thermal environments. Bristol: Smart Materials and Structures, IoP Publishing,; 1998.

226

[2.116] Trindade MA, Benjeddou A, Ohayon R,. Modeling of frequency-dependent viscoelastic materials for active-passive vibration damping. Journal of Vibration and Acoustics. 2000;122(2)169-174.

[2.117] Trindade MA, Benjeddou A, Ohayon R,. Finite element analysis of frequency- and temperature-dependent hybrid active-passive vibration damping. European Journal of Finite Elements. 2000;89-111.

[2.118] Van Rijn LPVM. Structural solution for a composite glider wing with suction boundary layer control for 100% laminar flow. Composites Part A:. 1997;28(12)1013-1018.

[2.119] Shiau LC, Wu TY,. Nonlinear flutter of laminated plates with in-plane force and transverse shear effects. Journal of Mechanics of Structures and Machines. 2001;29(1)121-142.

[2.120] Shiau, L. C. Hwang,S.T. Application of finite strip method to composite panel flutter analysis. Journal of Aircraft. 2000;37(4)740-742.

[2.121] Suleman A. Adaptive composites modelling and application in panel flutter and noise suppression. Computers and Structures. 2000;76(11)365-378.

[2.122] C. Jinsoo CY,. Supersonic flutter analysis of wings using an unsteady 3D panel method. Computers and Fluids. 2001;30(2)237-256.

[2.123] Balakrishnan AV. Subsonic flutter suppression using self-straining actuators. Journal of the Franklin Institure. 2001;338(2-3)149-170.

[2.124] Dewey H. Hodges, Mayuresh J. Patil, Seungmook Chae. Effect of thrust on bending-torsion flutter of wings. Journal of Aircraft. 2002;39(2)371-376.

[2.125] Kurnik W, Przybyowicz PM,. Stability of rotating cantilever columns under follower loads. In: Proceedings of the IX International Symposium on Dynamic Problems of Mechanics DINAME. Florianpolis, Santa Catarina, Brazil, 2001.

[2.126] Kurnik W., Przybylowicz PM. Active stabilisation of a piezoelectric fiber composite shaft subject to follower load. International Journal of Solids and Structures. 2003;40(19)5063-5079.

[2.127] De Rosa MA, Franciosi C. The influence of an intermediate support on the stability behaviour of cantilever beams subjected to follower forces. Journal of Sound and Vibration. 1990;137107-115.

[2.128] Hodges DH. Lateral-torsional flutter of a deep cantilever loaded by a lateral follower force at the tip. Journal of Sound and Vibration. 2001;247(1)175-183.

[2.129] H. J. Liu , Z.C. Yang , L.C. Zha . Semi-active flutter control by structural asymmetry. Journal of Sound and Vibration. 2000;229(12)199-205.

[2.130] Gern FH, Librescu L. Effects of externally mounted stores on aeroelasticity of advanced swept cantilevered aircraft wings. Aerospace Science and Technology. 2(5)321-333.

[2.131] Gern FH, Librescu L. Aeroelastic tailoring of composite wings exhibiting nonclassical effects and carrying external stores. Journal of Aircraft. 2000;37(6)1097-1104.

[2.132] Hu WBZ,L.C. Semiactive flutter control of wing:store system with electromagnetic friction damper. Journal of Sound and Vibration. 1997;200(5)625-630.

[2.133] Dowell EH, Ilgamov M. Studies in Nonlinear Aeroelasticity, Springer, New York, 1988.

[2.134] Lee BHK, Price SJ, Wong YS. Nonlinear aeroelastic analysis of airfoils: bifurcation and chaos. Progress in Aerospace Sciences. 1999;35;205-334.

[2.135] L. Librescu. Elastostatics and kinetics of anisotropic and heterogeneous shell-type structures. in: Aeroelastic Stability of Anisotropic Multilayered Thin Panels, Noordhoff International Publishers Leiden, The Netherlands, 1975, p. 106-158.

[2.136] Liviu Librescu, Gianfranco Chiocchia, Piergiovanni Marzocca. Implications of cubic physical/aerodynamic non-linearities on the character of the flutter instability boundary. International Journal of Non-Linear Mechanics. 2003;38(2)173-199.

[2.137] Chandiramani NK, Plaut RH, Librescu LI. Non-linear flutter of a buckled shear-deformable composite panel in a high-supersonic flow. International Journal of Non-Linear Mechanics. 1995;30(2)149-167.

[2.138] Oh IK, Lee I, Lee DM. Non-linear transient response of fluttering stiffened composite plates subject to thermal load. Journal of Sound and Vibration. 2001;245(4)715-736.

[2.139] Lee I, Roh, J. H. Oh,I.K. Aerothermoelastic phenomena of aerospace and composite structures. Journal of Thermal Stresses. 2003;26(6)525-546.

[2.140] Hagood, N.W., von Flotow,A.,. Damping of structural vibrations with piezoelectric materials and passive electrical networks. Journal of Sound and Vibration. 1991;146(2)243-68.

[2.141] Hollkamp JJ. Multimodal passive vibration suppression with piezoelectric materials and resonant shunts. Journal of Intelligent Materials, Systems and Structures. 1994;5(1)49-57.

[2.142] Zhou RC, Lai Z, Xue DY, Hauang JK, Mei C. Suppression of nonlinear panel flutter with piezoelectric actuators using finite element. AIAA Journal. 1995;33(6)1098-1105.

[2.143] Kim SJ, Han CH, Yun CY. Improvement of aeroelastic stability of hingeless helicopter rotor blade by passive piezoelectric damping. Proc. SPIE Smart Struct. Mater. Conf., Volume: 3672, (1999), pp. 1552-1561.

[2.144] Seong Hwan Moon Seung Jo Kim. Active and passive suppressions of nonlinear panel flutter using finite element method. AIAA Journal. 2001;39(11)2042-2050.

[2.145] Agnes G. Active/passive piezoelectric vibration suppression. Proc. SPIE Smart Structural Material Conference1994: Passive Damping, Conor D. Johnson (Ed.),. 1994;2193;24-34.

[2.146] Moon SH, Kim SJ. Suppression of nonlinear composite panel flutter with active/passive hybrid piezoelectric networks using finite element method. Composite Structures. 2003;59(4)525-533.

[2.147] Bauchau OA, Rodriguez J, Bottasso CL. Modeling of unilateral contact conditions with application to aerospace systems involving backlash, freeplay and friction. Mechanics Research Communications. 2001;28(5)571-599.

[2.148] Hall BD, Mook DT, Nayfeh AH, Preidikman S. Novel strategy for suppressing the flutter oscillations of aircraft wings. AIAA Journal. 2001;39(10)1843-1850.

[2.149] Patil MJ, Hodges DH, Cesnik CES. Characterizing the effects of geometrical nonlinearities on aeroelastic behavior of high-aspect-ratio wings. In Proceedings of the International Forum on Aeroelasticity and Structural Dynamics, Williamsburg, Virginia. 1999.

[2.150] Tang DM, Dowell EH. Experimental and theoretical study on aeroelastic response of high-aspect-ratio wings. AIAA Journal. 2001;391430-1441.

[2.151] Hall B, Preidikman S, Mook DT. A time-domain simulation for evaluating smart wing concepts for reducing gust loads. Proc. SPIE's Smart Structures and Materials 1999: Smart Structures and Integrated Systems, Norman M. Wereley; Ed.ASME Mechanics and Materials Conference, Blacksburg, Virginia,. 1999;3668;105-116.

[2.152] Bisplinghoff RL, Ashley H, Halfman RL. Aeroelasticity. New York: Dover Publications Inc; 1996.

[2.153] Strganac TW, Kim YI. Aeroelastic behavior of composite plates subject to damage growth. Journal of Aircraft. 1996;3368-73.

[2.154] Pidaparti, R. M. V. Chang, C.C. Finite element supersonic flutter analysis of skewed and cracked composite panels. Computers and Structures. 1998;69(2)265-270.

[2.155] Wei Z, Yam LH, Cheng L. Detection of internal delamination in multi-layer composites using wavelet packets combined with modal parameter analysis. Composite Structures. 2004;64(3-4)377-387.

[2.156] Lin KJ, Lu PJ, Tarn JQ. Flutter analysis of anisotropic panels with patched cracks. Journal of Aircraft. 1991;28(12)899-904.

[2.157] Shiau LC. Flutter of composite laminated beam plates with delamination. AIAA Journal. 1992;302;504-11.

[2.158] Pidaparti RMV. Free vibration and flutter of damaged composite panels. Composite Structures. 1997;38(1-4)477-481.

[2.159] M. Karpel . Design for active flutter suppression and gust alleviation using state-space aeroelastic modeling. Journal of Aircraft. 1982;19(3)221-227.

[2.160] Marzocca P, Librescu L, Chiocchia G. Aeroelastic response of 2-D lifting surfaces to gust and arbitrary explosive loading signatures. International Journal of Impact Engineering. 2001;25(1)41-65.

[2.161] Karpouzion G, Librescu L,. Nonclassical effects on divergence and flutter of anisotropic swept aircraft wings. AIAA Journal. 1996;34(4)786-794.

[2.162] Marzocca PL,L., Chiocchia G. Aeroelastic response of a 2-D airfoil in a compressible flow field and exposed to blast loading. Aerospace Science and Technology. 2002;6(4)259-272.

[2.163] Qin Z, Marzocca PL,L. Aeroelastic instability and response of advanced aircraft wings at subsonic flight speeds. Aerospace Science and Technology. 2002;6(3)195-208.

[2.164] Edwards JW, Ashley H, Breakwell JV. Unsteady aerodynamic modeling for arbitrary motions. AIAA Journal. 1979;365-374.

[2.165] T. Ueda, E.H. Dowell. Flutter analysis using nonlinear aerodynamic forces. Journal of Aircraft. 1984;21(2)101-109.

[2.166] Sparks Jr., D. W. Maghami, P.G. Neural networks for rapid design and analysis. AIAA-98-1779. 1998;Part 11-19.

[2.167] Lind Rick. Match-point solutions for robust flutter analysis. Journal of Aircraft. 2002;39(1)91-99.

[2.168] Roy ID, Eversman W. Adaptive flutter suppression of an unswept wing. Journal of Aircraft. 1996;33;775-783.

[2.169] Mam K. Adaptive non-linear control of a clamped rectangular plate with PZT patches. Journal of Sound and Vibration. 2003;264(4)835-850.

[2.170] Virk GS, Al-Dmour AS. Real-time vibration suppression in a flexible cantilever rig. Microprocessors and Microsystems. 1999;23(6)365-384.

Chapter 3

[3.1] J Njuguna, K Pielichowski. Recent developments in polyurethane-based conducting composites. Journal of Material Science. 2004;39(13)4081-4094.

[3.2] M. Gerard A. Chaubey, B. D. Malhotra. Application of conducting polymers to biosensors Biosens. Bioelectron. 2002;17(5)345-349.

[3.3] Z. Wirpsza, Poliuretany Chemia Technologia Zastosowanie (Wydawnictwo Naukowo-Techniczne, Warsaw, 1991) p. 101.

[3.4] Y. Z. Wang, Y. C. Hsu, R.R.Wu, H. M. Kao . Synthesis and structure properties of polyurethane based conducting copolymer I. 13 C NMR analysis Synth. Met. 2003;13(2)1561-1560.

[3.5] K. Pielichowski, J. Pielichowski, J.Iqbal, P.Gurtat. Polyaniline-based catalysts characterized by dynamic DSC Appl. Catal. A: Gen. 1997;161(1)25-28.

[3.6] Pielichowski KS,D. Morphological features and flammability of MDI/HMDI-based segmented polyurethanes containing 3-chloro-1,2-propanediol in the main chain. Polymer Degradation and Stability. 2003;80(2)327-331.

[3.7] G. P. Evans. Advances in Electrochemical Science and Engineering (Wiley-VCH, Weinheim, 1990) p. 1.

[3.8] Y. Cao, P. Smith, A.Heeger. Counter-ion induced processibility of conducting polyaniline and of conducting polyblends of polyaniline in bulk polymers. Synth. Met. 1992;48(1)91-97.

[3.9] Y. Cao, A. Andreatta, A.J.Heeger, P. Smith. Influence of chemical polymerization conditions on the properties of polyaniline. Polymer. 1989;30(12)2305-2311.

[3.10] C.D. Doyle . Kinetic analysis of thermogravimetric data. J. Appl. Polym. Sci. 1962;66;39.

[3.11] T. Ozawa . A new method of analyzing thermogravimetric data. Bull. Chem. Soc. Jpn. 1965;38;1881.

[3.12] H.L. Friedman . Kinetics of thermal degradation of char-forming plastics from thermogravimetry. J. Polym. Sci. 1965;C6;175.

[3.13] J.M. Criado, D. Dollimore, G.R. Heal. A critical study of the suitability of the Freeman and Carroll method for the kinetic analysis of Thermochim. Acta. 1982;54;159.

[3.14] J. Opfermann E. Kaisersberger. An advantageous variant of the Ozawa-Flynn-Wall analysis. Thermochim. Acta. 1992;203;167-175.

[3.15] J. Sestak J. Malek. Diagnostic limits of phenomenological models of heterogeneous reactions and thermal analysis kinetics. Solid State Ionics. 1993;63-65;245-254.

[3.16] W.P. Yang C.W. Macosko, S.T. Wellinghoff. Thermal degradation of urethanes based on 4,4'-diphenylmethane diisocyanate and 1,4-butanediol (MDI/BDO) polymer. 1986;27(8)1235-1240.

[3.17] Pielichowski K, Pielichowski JP, A study of the thermal properties of blends of poly(vinyl chloride) with novel epoxypropanecarbazole-based dyes by TGA/FTIR. J. Appl. Polym. Sci. 1998;67;1465.

[3.18] F. Cheng , Y. Wang. Microphase separation kinetics in segmented polyurethanes. J. Chromatgr. A. 2000;886;225.

[3.19] N. Grassie M. Zulfiqar, M. J. Guy. Thermal degradation of a series of polyester polyurethanes J. Polym. Sci., Polym. Chem. Ed. 1980;18(1)265-274.

[3.20] B. Chu, T. Gao, Y. Li, J. Wang,C.R.Desper C.A.Byrne. Microphase separation kinetics in segmented polyurethanes: Macromolecules. 1992;25(21)5724.

[3.21] M. Herrera, M. Wilhelm,G.Matuschek, A. Kettrup. Thermoanalytical and pyrolysis studies of nitrogen containing polymers. J. Anal. Appl. Pyrol. 2001;58/59;173.

[3.22] J. Chambers, J. Jiricny, C. Reese. The thermal decomposition of polyurethanes and polyisocyanurates Fire Mater. 1981;5; 4133.

[3.23] Njuguna, J. Pielichowski, K. Banerjee,J.R. Recent advances in polymer nanocomposites for aerospace applications. In the Proceedings of The First Seminar on Structure and Properties of Advanced Materials for Environmental Applications, under the auspices of EC Marie Curie Programme (FP 5), Cracow University of Technology, Kraków,. 2004;pp. 92-96.

[3.24] H.S.O. Chan, M.Y.B. Teo, E. Khor,C.N.Lim,. Thermal analysis of conducting polymers part I J. Therm. Anal. 1989;35(3)765-774.

[3.25] J. Sestak . Thermophysical Properties of Solids, Their Measurements and Theoretical Thermal Analysis, (Elsevier, Amsterdam, 1984).

[3.26] R.H. Baughman, J.F. Wolf, H. Eckhardt, L.W. Shacklette. The structure of a novel polymeric metal: Acceptor-doped polyaniline. Synth. Met. 1988;25(2)121-137.

[3.27] W. Fosong, T. Jinsong, W. Lixiang,Z.Hongfang M.Zhishen,. Study on the crystallinity of polyaniline Mol. Cryst. Liq. Cryst. 1988;160;175-185.

[3.28] Y.B. Moon, Y. Cao, P.Smith, A.J. Heeger. X-Ray scattering from crystalline polyaniline Polymer Communictions. 1989;30(7)196-199.

[3.29] M.E. Józefowicz, R. Laversanne, H.H.S. Javadi, A.J. Epstein, J.P. Pouget, X.Tang A.G.MacDiarmid,. Multiple lattice phases and polaron-lattice-spinless-defect competition in polyaniline. Physical Reviews B. 1989;39(17)12958-12961.

[3.30] R.W. Warfield B. Hartmann,. Corresponding states relationship for electrical-resistivity of glassy-polymers Polymer. 1980;2131.

[3.31] J. F. Masson R.St.J. Manley. Solid-state NMR of some cellulose/synthetic polymer blends Macromolecules. 1991;24;6670.

[3.32] S.Y. Kwak N. Nakayima,. Morphology and mechanical properties of blends of polycarbonate. Macromolecules. 1996;29;3521.

[3.33] J.A. Conklin,S.C. Huang, S.M. Huang, T.Wen, R.B.Kaner. Thermal properties of polyaniline and poly(aniline-co-o-ethylaniline). Macromolecules. 1995;28;6522.

[3.34] M.C. Gupta, S.S. Umare. Influence of copolymer composition on the transport properties of conducting copolymers: poly(aniline-co-o-anisidine) . Macromolecules. 1992;25;138-142.

[3.35] A.D. Borkar M.C. Gupta,. Electrical and optical properties of conducting copolymer: poly (aniline-co-n-ethylaniline) Industrial Journal of Chemistry. 1990;29A;631.

[3.36] F.P. Bradner, J.S. Shapiro. Analysis of the kinetics of the thermal decomposition of poly(1,6-bis-N-carbazolyl-2,4-hexadiyne) obtained using thermogravimetric analysis. Polymer. 1992;33(20)4366-4374.

[3.37] N.S. Allen M. Edge,. Fundamentals of Polymer Degradation and Stabilisation (Elsevier Applied Science, London, 1992).

[3.38] J.P. Pouget, M.E. Józefowicz, A.J. Epstein,X.Tang A.G.MacDiarmid. X-ray structure of polyaniline Macromolecules. 1991;24;779.

[3.39] T.S. Chen, T.S. Shieh, J.Y. Chui. Studies on the First DSC Endotherm of polyurethane hard segment based on 4,4'-diphenylmethane diisocyanate and 1,4-butanediol .Macromolecules. 1998;31(4)1312-1320.

[3.40] Chu B, Gao T, Li Y, Wang J, Desper CR, Catherine AB. Microphase separation kinetics in segmented polyurethanes: effects of soft segment length and structure. Macromolecules. 1992;25(21)5724-5729.

[3.41] H.S. Lee, S Yoo, S.W. Seo. Domain and segmental deformation behavior of thermoplastic elastomers using synchrotron SAXS and FTIR methods. J. Polymer Sciences: Part B: Polymer. Physics. 1999;37(22)3233-3245.

Chapter 4

[4.1] C. P.Chwang, C. D. Liu, S. W. Huang,D.Y.Chao, S. N. Lee . Synthesis and characterization of high dielectric constant polyaniline/polyurethane blends. Synthetic Metals. 2004;142(1-3)275-281.

[4.2] Yoon PJ, Han CD,. Effect of thermal history on the rheological behaviour of thermoplastic polyurethanes. Macromolecules. 2000;33(6)2171-2183.

[4.3] LeBaron PC, Pinnavaia TJ. Clay nanolayer reinforcement of a silicone elastomer. Chemistry of Materials. 2001;13(10)3760-5.

[4.4] Pielichowski K, Njuguna J. Thermal degradation of polymeric materials. Shawbury, Surrey, UK: RAPRA Technologies Limited; 2005.

[4.5] Njuguna JP, Pielichowski, K. Recent developments in polyurethane-based conducting composites. Journal of Material Science. 2004;39(13)4081-4094.

[4.6] Yang SM, Lee HL. Conductivity and morphology of the blend of polyaniline and water based polyurethane. Synth Met. 1999;102(1-3 pt 2)1226-1227.

[4.7] Y. Z. Wang, Y. C. Hsu,R.R.Wu, H. M. Kao . Synthesis and structure properties of polyurethane based conducting copolymer I. 13 C NMR analysis Synthetic Metals. 2003;13(2)1561-1560.

[4.8] J. E. Osterholm,J.Laakso P.Nyholm. Melt and solution processable poly(3-alkylthiophenes) and their blends. Synthetic Metals. 1989;28(1-2)435-444.

[4.9] H. Isotalo Ma, H. Stubb . Effects of humidity and heat on the conductivity of poly(3-alkylthiophenes) Synthetic Metals. 1993;55-57;3581.

[4.10] T. Kang, K. G. Neoh, K. L. TAN . Polyaniline: A polymer with many interesting intrinsic redox states. Progress in Polymer Sciences. 1998; 23:(2)277-324.

[4.11] N. Gospodinova L. Terlemezyan,. Conducting polymers prepared by oxidative polymerization: polyaniline. Prog. Polym. Sci. 1998;23(8)1443-1484.

[4.12] S. L. Shenoy, D. Cohen,C.Erkey, R. A. Weiss. Solvent-free process for preparing conductive elastomers by an in situ polymerization of pyrrole. Industrial Engineering Chemical Research. 2002;41(6)1484-1488.

[4.13] X. G. Li, M. R. Huang, W.Duan, Y. L.Yang. Novel multifunctional polymers from aromatic diamines by oxidative polymerizations. Chemistry Reviews. 2002;102(9)2925-3030.

[4.14] P. Banerjee. Electrically conductive interpenetrating network composites of polyaniline and carboxymethylcellulose. European Polymer Journal. 1998;34(10)1557-1561.

[4.15] E. Csahokev, G. Inzelt. In situ dc conductivity study of the redox transformations and relaxation of polyaniline films. Electroanal. Chem. 2000;482(2)168-177.

[4.16] E. Carone, L. D'ilario,A.Martinelli. New conducting thermoplastic elastomers. I. Synthesis and chemical characterization. Journal of Applied Polymer Sciences. 2002;83(4)857-867.

[4.17]   T. Jeevananda TS,. Synthesis and characterization of polyaniline filled PU/PMMA interpenetrating polymer networks. European Polymer Journal. 2003;39(3)569-578.

[4.18] I. Diaconu, P. Coman, T. Buruiana,E.Buruiana,. in Proceedings of the 10th International Symposium on Electrets (ISE 10) Delphi, Greece, September 1999, edited by A. A. Konsta, A. Vassilikou-Dova, K. Vartzeli-Nikaki (IEEE, Piscataway, NJ, USA, 1999) p. 493.

[4.19] K. Pielichowski, D. Slotwinska. Flame-resistant modified segmented polyurethanes with 3-chloro-1,2-propanediol in the main chain-thermoanalytical studies . Thermochimica Acta. 2004;410(1-2)79-86.

[4.20] N. Grassie , G.A. Perdomo-Mendoza . Thermal degradation of polyether-urethanes. III: Polyether-urethanes prepared from methylene bis(4-phenylisocyanate) and low molecular weight poly(ethylene glycols) Polymer Degradation and Stability,. 1985;10(3)267-286.

[4.21] N. Grassie , M. Zulfiqar. Thermal degradation of the polyurethane from 1, 4-butanediol and methylene bis (4-phenyl isocyanate). Journal of Polymer Science A. 1978;16(7)1563-1568.

[4.22] J. Choi, M. Chipara, B. Xu, C. S. Yang, B. Doudin,P.A.Dowben. Comparison of the pi-conjugated ring orientations in polyaniline and polypyrrole. Phys. Chem. Lett. 2001;343(3)193-200.

[4.23]   V. W. Srichatrapimuk, S.L.Cooper. Infrared thermal analysis of polyurethane block polymers J. Macromol. Sci., Phys. 1978;B15;267.

[4.24] R. J. Goddard, S. L. Cooper. Polyurethane cationomers with pendant trimethylammonium groups. 1. fourier transform infrared temperature studies. Macromolecules. 1995;28(5)1390.

Chapter 5

[5.1]   LeBaron PC, Wang Z, Pinnavaia TJ. Polymer-layered silicate nanocomposites: An overview. Applied Clay Sciences. 1999;15(1)11-29.

[5.2]   Sinha Ray S, Okamoto M. Polymer/layered silicate nanocomposites: A review from preparation to processing. Progress in Polymer Science (Oxford). 2003;28(11)1539-1641.

[5.3]   Rodlert M, Plummer CJG, Garamszegi L, Leterrier Y, Grunbaure HJM, Manson J-E. Hyperbranched polymer/montmorillonite clay nanocomposites. Polymer. 2004;45(3)949-60.

[5.4]   LeBaron PC, Pinnavaia TJ. Clay nanolayer reinforcement of a silicone elastomer. Chemistry of Materials. 2001;13(10)3760-5.

[5.5]   Rodlert M, Plummer CJG, Garamszegi L, Leterrier Y, Grunbauer HJM, Manson JE. Hyperbranched polymer/montmorillonite clay nanocomposites. Polymer. 2004;45(3)949-960.

[5.6] Kotsilkova R, Nesheva D, Nedkov I, Krusteva E, Stavrev S. Rheological, Electrical, and Microwave Properties of Polymers with Nanosized Carbon Particles. J Appl Polym Sci. 2004;92(4)2220-2227.

[5.7] Steuerman DW, Star A, Narizzano R, Choi H, Ries RS, Nicolini C, et al. Interactions between conjugated polymers and single-walled carbon nanotubes. Journal of Physical Chemistry B. 2002;106(12)3124-30.

[5.8] Wei Z, Yam LH, Cheng L. Detection of internal delamination in multi-layer composites using wavelet packets combined with modal parameter analysis. Composite Structures. 2004;64(3-4)377-387.

[5.9] Xiong J, Liu Y, Yang X, Wang X. Thermal and mechanical properties of polyurethane/montmorillonite nanocomposites based on a novel reactive modifier. Polymer Degradation and Stability. 2004;86(3)549-555.

[5.10] Alexandre M, Dubois P. Polymer-layered silicate nanocomposites: Preparation, properties and uses of a new class of materials. Materials Science and Engineering: R: Reports. 2000;28(1-2)1-63.

[5.11] Park SH, Sposito G. Do Montmorillonite Surfaces Promote Methane Hydrate Formation; Monte Carlo and Molecular Dynamics Simulations. The Journal of Physical Chemistry B. 2003;107(10)2281-2290.

[5.12] Ray SS, Okamoto K, Okamoto M. Structure-property relationship in biodegradable poly(butylene succinate)/layered silicate nanocomposites. Macromolecules. 2003;36(7)2355-2367.

[5.13] Njuguna J, Pielichowski K. Polymer nanocomposites for aerospace applications: Fabrication. Advanced Engineering Materials. 2004;6(4)193-203.

[5.14] Njuguna J, Pielichowski K. Polymer nanocomposites for aerospace applications: fabrication. Advanced Engineering Materials. 2004;6(4)193-203.

[5.15] Njuguna J, Pielichowski K. Polymer nanocomposites for aerospace applications: properties. Advanced Engineering Materials. 2003;5(11)769-778.

[5.16] Tien YI, Wei KH. Hydrogen bonding and mechanical properties in segmented montmorillonite/polyurethane nanocomposites of different hard segment ratios. Polymer. 2001;42(7)3213-21.

[5.17] Kashiwagi T, Harris Jr. RH, Zhang X, Briber RM, Cipriano BH, Raghavan SR, et al. Flame retardant mechanism of polyamide 6-clay nanocomposites. Polymer. 2004;45(3)881-891.

[5.18] Pielichowski K, Njuguna J. Thermal Degradation of Polymeric Materials. Shawbury, Surrey, UK: RAPRA Technologies Limited; 2005.

[5.19]   Uhl FM, Davuluri SP, Wong SC, Webster DC. Polymer films possessing nanoreinforcements via organically modified layered silicate. Chemistry of Materials. 2004;16(6)1135-1142.

[5.20]   Han B, Cheng A, Ji G, Wu S, Shen J. Effect of organophilic montmorillonite on polyurethane/montmorillonite nanocomposites. Journal of Applied Polymer Sciences. 2004;91(4)2536-2542.

[5.21]   Wang S, Hu Y, Zong R, Tang Y, Chen Z, Fan W. Preparation and characterization of flame retardant ABS/montmorillonite nanocomposite. Applied Clay Science. 2004;2549-55.

[5.22]   Pattanayak A, Jana SC. Properties of bulk-polymerized thermoplastic polyurethane nanocomposites. Polymer. 2005;46(10)3394-406.

[5.23]   Pattanayak A, Sadhan CJ. Synthesis of thermoplastic polyurethane nanocomposites of reactive nanoclay by bulk polymerization methods. Polymer. 2005;46(10)3275-88.

[5.24] Petrovic ZS, Cho YJ, Javni I, Magonov S, Yerina N, Schaefer DW, et al. Effect of silica nanoparticles on morphology of segmented polyurethanes. Polymer. 2004;45(12)4285-4295.

[5.25] Gleiter H. Nanocrystalline materials. Progress in Materials Science. 1989;33(4)223-315.

[5.26]   Leszczyńska A, Njuguna J, Pielichowski K, Banerjee JR. Polymer/montmorillonite nanocomposites with improved thermal properties: Part I. Factors influencing thermal stability and mechanisms of thermal stability improvement. Thermochimica Acta. 2007/2/1;453(2)75-96.

[5.27] Hlangothi SP, Krupa I, Djokovic V, Luyt AS. Thermal and mechanical properties of cross-linked and uncross-linked linear low-density polyethylene–wax blends. Polymer Degradation and Stability. 2003;79(1)53-59.

[5.28] Wu C, Wang X, Yang C, Geng Y, Liu F. Empirical garnet–muscovite geothermometry in metapelites. Lithos. 2002/5;62(1-2)1-13.

[5.29] Kostopoulos V, Tsotra P, Karapappas P, Tsantzalis S, Vavouliotis A, Loutas TH, et al. Mode I interlaminar fracture of CNF or/and PZT doped CFRPs via acoustic emission monitoring. Composites Science and Technology. 2007/4;67(5)822-828.

Chapter 6

[6.1] Di Taranto RA. Theory of vibratory bending of elastic and viscoelastic layered finite-length beams. Journal of Applied Mechanics. 1965;ASME 32881-886.

[6.2] Mead DJ, Markus S,. The Forced vibration of a three-layer, damped sandwich beam with arbitrary boundary conditions. Journal of Sound and Vibration. 1969;10163-175.

[6.3] Ahmed KH. Dynamic analysis of sandwich beams. Journal of Sound and Vibration. 1972;21263-276.

[6.4] Sisemore CL, Darvannes, C.M. Transverse vibration of elastic-viscoelastic-elastic sandwich beams: compression experimental and analytical study. journal of Sound and Vibration. 2002;252(1)155-167.

[6.5] Sainsbury MG, Zang,Q.J. The Galerkin element method applied to the vibration of damped sandwich beams. Comput. Struct. 1999;71239-256.

[6.6] Rao DK. Frequency and loss factors of sandwich beams with various boundary conditions. Journal of Mechanical Engineering Science. 1978;20(5)271-282.

[6.7] Banerjee JR. Free vibration of sandwich beams using dynamic stiffness method. Computers and Structures. 2003;81(18-19)1915-1922.

[6.8] Banerjee JR, Sobey, A.J. Dynamic stiffness formulation and free vibration analysis of a three-layered sandwich beam. International Journal of Solids and Structures. 2005;42(8)2181-2197.

[6.9] Wittrick WH, Williams FW. A general algorithm for computing natural frequencies of elastic structures. Q J Mech Appl Math. 1971;24263-84.

[6.10] Wittrick WH, Williams. An algorithm for computing critical buckling loads of elastic structures. Journal of Structural Mechanics. 1973;1497-518.

Chapter 7

[7.1] Weisshaar TA,. Aeroelastic tailoring of forward swept composite wings. Journal of Aircraft. 1981;18(8)669-676.

[7.2] Weisshaar TA, Foist BL,. Vibration tailoring of advanced composite lifting surfaces. Journal of Aircraft. 1985;22(2)141-147.

[7.3] Green JA,. Aeroelastic tailoring of swept high aspect ratio composite wings. Journal of Aircraft. 1987;24812-819.

[7.4] Chandra R, Stemple, Chopra I. Thin-walled composite beams under bending, torsional and extensional loads. Journal of Aircraft. 1990;27619-626.

[7.5] Hodges, D. H., Atilgan, A. R., Fulton, M. V., Refield,L.W. Free vibration analysis of composite beams. Journal of American Helicopter Society. 1991;3636-47.

[7.6] Smith EC, Chopra I,. Formulation and evaluation of an analytical model for composite box beams. Journal of American Helicopter Society. 1991;3623-35.

[7.7] Rehfield, L.W., Atilgan, A.R., Hodges,D.H.,. Structural modelling for multicell composite rotor blades. Proceedings of the 29th AIAA/ASME/ASCE/AHS/ASC Structures, Structural Dynamics and Materials Conference, AIAA paper 88-2250. 1988.

[7.8] Tsai SW, Hahn HT, Hahn HT. Introduction to composite materials. CRC Press; 1980.

[7.9] Weisshaar TA. Aeroelastic stability and performance characteristics of aircraft with advanced composite sweptforward wing structures. Air Force Flight Dynamics Laboratory, AFFDLTR-78-116, Sept, Wright-Petterson AFB, Ohio. 1978;.

[7.10] Timoshenko S, Goodier. Theory of Elasticity, McGraw-Hill, New York, 1956.

[7.11] Rehfield LW. Design analysis methodology for composite rotor blades. Proceedings of the Seventh DoD/NASA Conference on Fibrous Composites in Structural Design. 85-3094.

[7.12] Jesen, D.W., Crawley, E.F. Dugundji,J. Vibration of cantilevered graphite/epoxy plates with bending-torsion coupling. Journal of Reinforced Plastics and Compsites. 1982;1254-269.

[7.13] Cesnik CES, Hodges, Patil MJ,. Aeroelastic analysis of composite wings. Proceedings of the 37th AIAA/ASME/ASCE/AHS/ASC Structures, Structural Dynamics, and Materials Conference, Paper No. AIAA-96-1444-CP, 1113-1123. 1996.

[7.14] Rehfield, L.W., Atilgan, A.R., Hodges,D.H.,. Non-classical behaviour of thin-walled composite beams with closed cross-sections. Journal of the American Helicopter Society. 1990;35(2)42-50.

[7.15] Armanios EA, Badir AM,. Free vibration analysis of anisotropic thin-walled closed-section beams. AIAA Journal. 1995;33;1905-1910.

[7.16] Rehfield LW, Atilgan. On the buckling behaviour of thin-walled laminated composite open section beams", Proceedings of the 30th AIAA/ASME/ASCE/ AHS/ASC Structures, Structural Dynamics and Materials Conference, AIAA paper 89-1171. 1989.

Chapter 8

[8.1] Pandey, M., Kabir, M., Sherbourne,A. Flexural-torsional stability of thin-walled composite I-section beams. Composites Engineering. 1995;5;321-342.

[8.2] Bauld Jr. NR, Tzeng LS. Vlasov theory for fiber-reinforced beams with thin-walled open cross sections. International Journal of Solids and Structures. 1984;20;277-297.

[8.3] Volovoi VV, Hodges DH, Berdichevsky VL, Sutyrin V. Asymptotic theory for static behavior of elastic anisotropic I-beams. International Journal of Solids and Structures. 1998;36,1017-1043.

[8.4] Hodges DH, Peters DA,. Lateral-torsional buckling of cantilevered elastically coupled composite strip- and I-beams. International Journal of Solids and Structures. 2001;38(9)1585-1603.

[8.5] Chandrashekhara K, Bhatia K,. Active buckling control of smart composite plates-finite-element analysis. Smart Materials and Structure. 1993;2(1)31-39.

[8.6] Chase JG, Bhashyam S,. Optimal stabilization of plate buckling. Smart Materials and Structure. 1999;8(2)204-211.

[8.7] Meressi T, Paden B. Buckling control of a flexible beam using piezoelectric actuators. Journal of Guidance Control and Dynamics. 1993;16(5)977-980.

[8.8] Thompson SP, Loughlan J. The active buckling control of some composite column structure strips using piezoceramic actuators. Composite Structures. 1995;32(1-4)59-67.

[8.9] Sloss JM, Bruch JC, Sadek IS, Adali S,. Piezo patch sensor/actuator control of the vibrations of a cantilever under axial load. Composite Structures. 2003;62(3)423-428.

[8.10] Yang Y, Ju, Soh CK. Analytical and semi-analytical solutions for vibration control of a cantilevered column using a piezoelectric actuator. Journal of Smart Materials and Structures. 2003;12(2)193-203.

[8.11] Wang Q. On buckling of column structures with a pair of piezoelectric layers. Engineering Structures. 2002;24(2)199-205.

[8.12] Timoshenko SP, Gere JM. Theory of Elastic Stability, McGraw-Hill International Book Company, Singapore, 1961.

[8.13] Goodier JN,. Torsional and flexural buckling of thin-walled open section under compressive and bending loads. Journal of Applied Mechanics. 1942;9A103-A107.

[8.14] Pekoz TB, Winter G,. Torsional-flexural buckling of thin-walled sections under eccentric load. Journal of Structural Division, ASCE. 1969;95941-963.

[8.15] Hoff NJ, Goodier JN,. Torsional and flexural buckling of thin-walled open section under compressive and bending loads. Journal of Applied Mechanics. 1943;10Al1O-Alll.

[8.16] Barsoum RS, Gallagher RH,. Finite element analysis of torsional and torsional-flexural stability problems. International Journal for Numerical Methods in Engineering. 1970;2;335-352.

[8.17] Renton JD,. Stability of space frames by computer analysis. Journal of Structural Division, ASCE. 1962;8881-103.

[8.18] Renton JD,. A direct solution of the torsional-flexural buckling of axially loaded thin-walled bars. The Structural Engineer. 1960;38273-276.

[8.19] Wittrick WH, Williams FW. A general algorithm for computing natural frequencies of elastic structures. Q J Mech Appl Math. 1971;24263-84.

[8.20]   Wittrick WH, Williams. An algorithm for computing critical buckling loads of elastic structures. Journal of Structural Mechanics. 1973;1;497-518.

[8.21]   Wittrick WH, Williams FW,. Exact buckling and frequency calculation surveyed. Structural Engineering Journal, ASCE. 1983;109;169-187.

[8.22]   Wang C,. Differential quadrature analysis of deflection, buckling, and free vibration of beams with rectangular plates, PhD Thesis , Department of Aeronautics and Astronautics, MIT, Cambridge. 1986.

[8.23]   Nemeth MP,. Importance of anisotropy on buckling of compression loaded symmetric composite plates. AIAA Journal. 1986;24;1831-1835.

[8.24]   Rehfield LW, Atilgan. On the buckling behaviour of thin-walled laminated composite open section beams", Proceedings of the 30th AIAA/ASME/ASCE/ AHS/ASC Structures, Structural Dynamics and Materials Conference, AIAA paper 89-1171. 1989;.

[8.25]   Kapania RK,Raciti. Recent advances in analysis of laminated beams and plates part i: shear effects and buckling. AIAA Journal. 1989;27(7)923-934.

[8.26]   Hodges DH,. A review of composite rotor blade modeling. AIAA Journal. 1990;28561-565.

[8.27]   Mansfeild EH, Sobey AJ,. The fibre composite helicopter blade. Aeronautical Quarterly. 1979;30413-449.

[8.28]   Minguet PDJ. Experiments and analysis for composite blades under large deflection, Part I: Static behaviour, Part II: Dynamic behaviour. AIAA Journal. 1990;28;1573-1588.

[8.29]   Libove C,. Stresses and rate of twist in single cell thin walled beams with anisotropic walls. AIAA Journal. 1988;26(9)September, 1988.

[8.30]   Rehfield, L.W., Atilgan, A.R., Hodges,D.H.,. Non-classical behaviour of thin-walled composite beams with closed cross-sections. Journal of the American Helicopter Society. 1990;35(2)42-50.

[8.31]   Mansfeild EH, Sobey AJ. The fibre composite helicopter blade. Aeronautical Quarterly. 1979;30413-449.

[8.32]   Banerjee JR, Williams. Coupled bending torsional dynamic stiffness matrix for Timoshenko beam elements. Computers and Structures. 1992;42;301-310.

[8.33]   Fitch J,. Solving algebraic problems with REDUCE. Journal of Symbolic Computation. 1985;1211-227.

[8.34]   Rayna G,. REDUCE software for algebraic computation. Springer-Verlag, New York. 1986;.

[8.35] Przemieniecki JS,. Theory of Matrix Structural Analysis, McGraw Hill, New York.1968.

[8.36] Jesen, D.W. Crawley, E.F. Dugundji, J. Vibration of cantilevered graphite/epoxy plates with bending-torsion coupling. Journal of Reinforced Plastics and Compsites. 1982;1;254-269.

[8.37] Akesson B. Overall buckling in bending and torsion of rack structures, Thin-walled Structures edited by J. Rhodes and A.C. Walkers, Granada, London.1980.

Chapter 9

[9.1] Armanios EA, Badir AM,. Free vibration analysis of anisotropic thin-walled closed-section beams. AIAA Journal. 1995;33;1905-1910.

[9.2] Hodges, D. H., Atilgan, A. R., Fulton, M. V., Refield, L.W.,. Free vibration analysis of composite beams. Journal of American Helicopter Society. 1991;36;36-47.

[9.3] Shi G, Lam KY,. Finite element vibration analysis of composite beams based on higher-order beam theory. Journal of Sound and Vibration. 1999;219;707-721.

[9.4] Minguet PD,J. Experiments and analysis for composite blades under large deflection, Part I: Static behaviour, Part II: Dynamic behaviour. AIAA Journal. 1990;28;1573-1588.

[9.5] Wu XX, Sun CT,. Vibration analysis of laminated composite thin-walled beams using finite elements. AIAA Journal. 1991;29;736-742.

[9.6] Banerjee JR, Williams FW. Free vibration of composite beams- an exact method using symbolic computation. Journal of Aircraft. 1995;32;636-642.

[9.7] Weisshaar TA, Foist BL,. Vibration tailoring of advanced composite lifting surfaces. Journal of Aircraft. 1985;22(2)141-147.

[9.8] Weisshaar TA,. Aeroelastic tailoring of forward swept composite wings. Journal of Aircraft. 1981;18(8)669-676.

[9.9] Shirk, H.M., Hertz, T.J., Weisshaar, T.A.,. Aeroelastic tailoring-theory, practice and promise. Journal of Aircraft. 1986;23(1)6-18.

[9.10] Beltzer AI,. Enginering analysis via symbolic computation- a break through. Applied Mechanics Reviews. 1990;43;119-127.

[9.11] Banerjee JR. Explicit Analytical Expressions for Frequency Equation and Mode Shapes of Composite Beams. International Journal of Solids Structures. 2001;38;1813-1830.

[9.12] Jesen, D.W., Crawley, E.F. Dugundji,J. Vibration of cantilevered graphite/epoxy plates with bending-torsion coupling. Journal of Reinforced Plastics and Compsites. 1982;1;254-269.

[9.13] Cesnik CES, Hodges, Patil MJ,. Aeroelastic analysis of composite wings. Proceedings of the 37th AIAA/ASME/ASCE/AHS/ASC Structures, Structural Dynamics, and Materials Conference, Paper No. AIAA-96-1444-CP, 1113-1123. 1996.

[9.14] Chandra R, Stemple, Chopra I. Thin-Walled Composite Beams Under Bending, Torsional and Extensional Loads. Journal of Aircraft. 1990;27;619-626.

[9.15] Berdichevshy, V., Armanios, E. Badir,A.,. Theory of anisotropic thin-walled closed-cross-section beams. Composites Engineering. 1992;2;411-432.

[9.16] Minguet P. Static and dynamic behaviour of composite helicopter blades under large deflection. PhD Dissertation, Department of Aeronautics and Astronautics, Massachusetts Institute of Technology, TELAC Report 89-7A. 1989.

[9.17] Rayna G,. REDUCE software for algebraic computation. Springer-Verlag, New York. 1986.

[9.18] Smith EC, Chopra I,. Formulation and evaluation of an analytical model for composite box beams. Journal of American Helicopter Society. 1991;36;23-35.

[9.19] ICATS:. Modent Suite, Integrated Software for Structural Dynamics, (ICATS 1998-2000, Imperial College Consultants, London, UK).

[9.20] Njuguna, J., Su, H., Cheung,C.W., Banerjee J.R. The influence of ply orientation on the free vibration of composite beams. In UNSW 2002 Conference Proceedings, Sydney, Australia, Eds. Bandyopadhyay, N. Gowripalan, S. Rizkalla, ACUN-4. 2002;p.307-314.

Chapter 10

[10.1] Liviu Librescu, Gianfranco Chiocchia, Piergiovanni Marzocca. Implications of cubic physical/aerodynamic non-linearities on the character of the flutter instability boundary. International Journal of Non-Linear Mechanics. 2003;38(2)173-199.

[10.2] Bisplinghoff RL, Ashley H, Halfman RL. Aeroelasticity. New York: Dover Publications Inc; 1996.

[10.3] Ueda J, Dowell EH. Doublet-point method for supersonic unsteady lifting surfaces. AIAA Journal. 1984;22(2)179-186.

[10.4] Chen PC, Liu DD. A harmonic gradient method for unsteady supersonic flow calculations. Journal of Aircraft. 1985;22(5)371-379.

[10.5] Lottati I, Nissim E. Nonplanar, supersonic, three-dimensional, oscillatory, piecewise continuous-kernel function method. Journal of Aircraft. 1987;24(1)45-54.

[10.6] Cho J, Williams MH. S-plane aerodynamics of nonplanar lifting surfaces. Journal of Aircraft. 1993;30(4)433-438.

[10.7] Cesnik CES, Hodges, Patil MJ,. Aeroelastic analysis of composite wings. Proceedings of the 37th AIAA/ASME/ASCE/AHS/ASC Structures, Structural Dynamics, and Materials Conference, Paper No. AIAA-96-1444-CP, 1113-1123. 1996.;.

[10.8] Ho S, Nassef H, Pornsinsirirak N, Tai YC, Ho CM. Unsteady aerodynamics and flow control for flapping wing flyers. Progress in Aerospace Sciences. 2003;39(8)635-681.

[10.9] Lottati I. Flutter and divergence Aeroelastic characteristics for composite forward swept cantilevered wing. Journal of Aircraft. 1985;22;1001-1007.

[10.10] Banerjee JR, Williams FW. Free vibration of composite beams- an exact method using symbolic computation. Journal of Aircraft. 1995;32;636-642.

[10.11] Wittrick WH, Williams FW. A general algorithm for computing natural frequencies of elastic structures. Q J Mech Appl Math. 1971;242;63-84.

[10.12] Wittrick WH, Williams. An algorithm for computing critical buckling loads of elastic structures. Journal of Structural Mechanics. 1973;1;497-518.

[10.13] Banerjee JR. Use and capability of CALFUN-A program for calculation of flutter speed using normal modes. In: Anonymous June 27-131; Athens. 1984:121-31.

[10.14] Banerjee JR. Flutter characteristics of high aspect ratio tailless aircraft. J Aircr. 1984;21(9)733-736.

[10.15] Banerjee JR. Flutter modes of high aspect ratio tailless aircraft. Journal of Aircraft. 1988;25;473-476.

[10.16] Banerjee JR. Flutter sensitivity studies of high aspect ratio aircraft wings. Transaction os Built Enviroment. Elsevier Science Publishers Ltd. Essex, UK; 1993:373-387.

[10.17] Georghiades GA, Banerjee JR. Role of modal interchange on the flutter of laminated composite wings. Journal of Aircraft. 1998;35(1)157-161.

[10.18] Georghiades GA, Banerjee JR. Significance of wash-out on the flutter characteristics of composite wings. Journal of Aircraft. 1998;35(5)823-825.

[10.19] Georghiades GA, Guo SJ, Banerjee JR. Flutter characteristics of laminated composite wings. Journal of Aircraft. 1996;33(6)1204-1206.

[10.20] Sarigul-Klijn NO,S. Effect of aspect ratio and ply orientation on aeroelastic response of composite plates. Journal of Aircraft. 1998;35(4)657-659.

[10.21] Kim, D. H. Lee,I. Nonlinear flutter characteristics of composite missile wing in transonic/low-supersonic flows. Journal of Aircraft. 2002;39(5)889-892.

[10.22] Njuguna J. Dynamics of composite wings. 2001;MSc. Thesis.

[10.23] Njuguna, J., Su, H., Cheung,C.W.Banerjee J.R. The influence of ply orientation on the free vibration of composite beams. In UNSW 2002 Conference Proceedings, Sydney, Australia, Eds. Bandyopadhyay, N. Gowripalan, S. Rizkalla, ACUN-4. 2002;p.307-314.

[10.24] Khot NS. Design of composite smart wing to enhance roll maneuver. Proceedings of - The Iinternational Society for the Optical Engineers (SPIE). 1996;3321;436-446.

[10.25] Khot, N. S. Zweber,J.V. Design of Flutter Characteristics of Composite Wings Using Frequency Constraint Optimization. Journal of Aerospace Engineering. 2003;16(1)19.

[10.26] H. Su CWCJRB,. Free Vibration of Metallic and Composite Beams Exhibiting Bending-Torsion Coupling. Proceedings of the Ninth International Conference on Civil and Structural Engineering Computing, Paper 74. 2003.

[10.27] Guo SJ, Bannerjee, J. R. Cheung,C.W. The effect of laminate lay-up on the flutter speed of composite wings. Proceedings of the Institute of Mechanical Engineers Vol. 217 Part G: J. Aerospace Engineering. 2003;pp.115-122.

Appendix A

[A.1] Theodorsen T. General theory of aerodynamic instability and the mechanism of flutter. NACA Report No. 496, 1935.

[A.2] Bisplinghoff RL, Ashley H, Halfman RL. Aeroelasticity. New York: Dover Publications Inc; 1996.

[A.3] Fung YC. An Introduction to the Theory of Aeroelasticity. New York: Dover Publications; 2002.

Appendix A: Evaluation of generalised aerodynamic matrix

The generalised aerodynamic matrix is formed by applying the principle of virtual work. The aerodynamic strip theory based on Theodorsen expressions for unsteady lift moment [A.1] and the normal modes obtained from the finite element method are used when applying the principle of virtual work. The displacements considered are the vertical deflection (bending) $h(y)$, and the pitching rotation (torsion) $\alpha(y)$, of the elastic axis of the wing at a spanwise distance y from the root. Thus the displacement components of the i th mode ϕ_i are respectively $h_i(y)$ and $\alpha_i(y)$. If $q_i(y)$ $(i = 1,2,3,.....n)$ are the generalised coordinates, $h(y)$ and $\alpha(y)$ can be expressed as

$$h(y) = \sum_{i=1}^{n} h_i(y) q_i(t) \tag{A.1}$$

$$\alpha(y) = \sum_{i=1}^{n} \alpha_i(y) q_i(t) \tag{A.2}$$

Equations (A.1) and (A.2) can be written in matrix form as

$$\begin{bmatrix} h(y) \\ \alpha(y) \end{bmatrix} = \begin{bmatrix} h_1(y) & h_2(y) \cdots & h_n(y) \\ \alpha_1(y) & \alpha_2(y) \cdots & \alpha_n(y) \end{bmatrix} \begin{bmatrix} q_1 \\ q_2 \end{bmatrix} \tag{A.3}$$

If $L(y)$ and $M(y)$ are respectively, the unsteady lift and moment at a spanwise distance y from the root, the virtual work done (δW) by the aerodynamic forces is given by

$$\delta W = \sum_{i=1}^{n} (v) \int_0^s (L(y) h_i(y) + M(y) \alpha_i(y)) dy \tag{A.4}$$

where s is the semi-span (i.e. length) of the wing and n is the number of normal modes considered in the analysis.

Equation (A.6) can be written in matrix form as

$$\begin{bmatrix} \delta W_1 / \delta q_1 \\ \delta W_2 / \delta q_2 \\ \vdots \\ \delta W_n / \delta q_n \end{bmatrix} = \int_0^s \begin{bmatrix} h_1 & \alpha_1 \\ h_2 & \alpha_2 \\ \vdots & \vdots \\ h_n & \alpha_n \end{bmatrix} \begin{bmatrix} L(y) \\ M(y) \end{bmatrix} \tag{A.5}$$

The unsteady lift $L(y)$ and moment $M(y)$ in two dimensional flow given by Theodorsen [A.1] can be expressed as

$$\begin{bmatrix} L(y) \\ M(y) \end{bmatrix} = \begin{bmatrix} A_{11} & A_{12} \\ A_{21} & A_{22} \end{bmatrix} \begin{bmatrix} h(y) \\ \alpha(y) \end{bmatrix} \tag{A.6}$$

where

$$
\begin{aligned}
A_{11} &= -\pi\rho U^2 \left\{ -k^2 + 2C(k)ik \right\} \\
A_{12} &= -\pi\rho U^2 b \left[\left(a_h k^2 + ik \right) + 2C(k)\left(1 + ik(1/2 - a_h)\right) \right] \\
A_{21} &= -\pi\rho U^2 b \left\{ 2C(k)ik(1/2 + a_h) - k^2 a_h \right\} \\
A_{22} &= \pi\rho U^2 b^2 \left[2(1/2 + a_h)C(k)\left(1 + ik(1/2 - a_h)\right) + k^2/8 + k^2 a_h^2 + (a_h - 1/2)ik \right]
\end{aligned}
\tag{A.7}
$$

in Eqns (A.7), U, b, ρ, k, $C(k)$ and a_h are in the usual notation: the airspeed, semi-chord, density of air, reduced frequency parameter, Theodorsen function and elastic axis location from mid-chord, respectively (see Refs. [A.2, A.3].

Substituting Eqns (A.5) and (A.6) and using Eqn (A.3)

$$\begin{bmatrix} \delta W_1/\delta q_1 \\ \delta W_2/\delta q_2 \\ \vdots \\ \delta W_n/\delta q_n \end{bmatrix} = \int_0^s \begin{bmatrix} h_1 & \alpha_1 \\ h_2 & \alpha_2 \\ \vdots & \vdots \\ h_n & \alpha_n \end{bmatrix} \begin{bmatrix} A_{11} & A_{12} \\ A_{21} & A_{22} \end{bmatrix} \begin{bmatrix} h_1(y) & h_2 \cdots\cdots & h_n \\ \alpha_1(y) & \alpha_2 \cdots\cdots & \alpha_n \end{bmatrix} \begin{bmatrix} q_1 \\ q_2 \\ \vdots \\ q_n \end{bmatrix} dy = \begin{bmatrix} QF_{11} & QF_{12} & \cdots & QF_{nn} \\ QF_{21} & QF_{22} & \cdots & QF_{2n} \\ \cdots & \cdots & \cdots & \cdots \\ QF_{n1} & QF_{n2} & \cdots & QF_{nn} \end{bmatrix} \tag{A.8}$$

where $[QF_{21}]$ is the generalised aerodynamic matrix with

$$QF_{ij} = \int_0^s \left(A_{11} h_i h_j + A_{12} h_j \alpha_i + A_{22} \alpha_i \alpha_j \right) dy \tag{A.9}$$

The generalised aerodynamic matrix $[QF_{21}]$ is usually a complex matrix with each element having a real part and an imaginary part. This is as a consequence of the term A_{11}, A_{12} ... etc, in Equation (A.9). In contrast, the generalised mass and stiffness matrices are both real (and diagonal) matrices.

Appendix B: Non-dimensional Sandwich Beam Parameters Used in Eqs. (6.26)-(6.30)

$$a = -\frac{K_2 A_2 G_2 L^2}{h_2^{\,2}\left(E_1 A_1 + \dfrac{E_2 A_2}{3}\right)} + \frac{\left(\rho_1 A_1 + \dfrac{\rho_2 A_2}{3}\right)}{\left(E_1 A_1 + \dfrac{E_2 A_2}{3}\right)} L^2 \omega^2 \quad b = \frac{\dfrac{E_2 A_2}{6}}{\left(E_1 A_1 + \dfrac{E_2 A_2}{3}\right)}$$

$$c = \frac{k_2 A_2 G_2 L^2}{h_2^{\,2}\left(E_1 A_1 + \dfrac{E_2 A_2}{3}\right)} + \frac{\left(\dfrac{\rho_2 A_2}{6}\right)}{\left(E_1 A_1 + \dfrac{E_2 A_2}{3}\right)} L^2 \omega^2 \quad e = -\frac{\dfrac{k_2 A_2 G_2}{2h_2^{\,2}} L^2}{\left(E_1 A_1 + \dfrac{E_2 A_2}{3}\right)} + \frac{\left(\dfrac{\rho_2 A_2}{6}\right)}{\left(E_1 A_1 + \dfrac{E_2 A_2}{3}\right)} L^2 \omega^2$$

$$f = \frac{k_2 A_2 G_2 L}{h_2\left(E_1 A_1 + \dfrac{E_2 A_2}{3}\right)}$$

$$g = \frac{E_3 A_3 + \dfrac{E_2 A_2}{3}}{\left(E_1 A_1 + \dfrac{E_2 A_2}{3}\right)} \quad h = -\frac{k_2 A_2 G_2 L^2}{h_2^{\,2}\left(E_1 A_1 + \dfrac{E_2 A_2}{3}\right)} + \frac{\left(\rho_3 A_3 + \dfrac{\rho_2 A_2}{3}\right)}{\left(E_1 A_1 + \dfrac{E_2 A_2}{3}\right)} L^2 \omega^2$$

$$m = -\frac{\left(\dfrac{k_1 A_1 G_1 + h_1^{\,2} K_2 A_2 G_2}{4h_2^{\,2}}\right) L^2}{\left(E_1 A_1 + \dfrac{E_2 A_2}{3}\right) h_1^{\,2}} + \frac{\left(\rho_1 I_1 + \dfrac{\rho_2 A_2 h_1^{\,2}}{12}\right)}{\left(E_1 A_1 + \dfrac{E_2 A_2}{3}\right) h_1^{\,2}} L^2 \omega^2 \quad n = \frac{\left\{k_1 A_1 G_1 - \left(\dfrac{k_2 A_2 G_2 h_1}{2h_2}\right)\right\} L}{\left(E_1 A_1 + \dfrac{E_2 A_2}{3}\right) h_1}$$

$$p = \frac{E_3 I_3 + \left(\dfrac{E_2 A_2 h_3^{\,2}}{12}\right)}{\left(E_1 A_1 + \dfrac{E_2 A_2}{3}\right) h_3^{\,2}}$$

$$q = -\frac{\left\{\left(\dfrac{K_2 A_2 G_2 h_3^{\,2}}{4h_2^{\,2}}\right) + K_3 A_3 G_3\right\} L^2}{\left(E_1 A_1 + \dfrac{E_2 A_2}{3}\right) h_3^{\,2}} + \frac{\left\{\left(\dfrac{\rho_2 A_2 h_3^{\,2}}{12}\right) + \rho_3 I_3\right\}}{\left(E_1 A_1 + \dfrac{E_2 A_2}{3}\right) h_3^{\,2}} L^2 \omega^2 \quad r = \frac{\left\{\left(\dfrac{k_2 A_2 G_2 h_3}{2h_2}\right) - k_3 A_3 G_3\right\} L}{\left(E_1 A_1 + \dfrac{E_2 A_2}{3}\right) h_3} \quad s = \frac{k_1 A_1 G_1 + k_2 A_2 G_2 + k_3 A_3 G_3}{\left(E_1 A_1 + \dfrac{E_2 A_2}{3}\right)}$$

$$t = \frac{\left(\rho_1 A_1 + \rho_2 A_2 + \rho_3 A_3\right) L^2 \omega^2}{\left(E_1 A_1 + \dfrac{E_2 A_2}{3}\right)}$$

$$z = \frac{E_1 I_1 + \left(\dfrac{E_2 A_2 h_1^{\,2}}{12}\right)}{\left(E_1 A_1 + \dfrac{E_2 A_2}{3}\right) h_1^{\,2}}$$

Appendix C: Non-dimensional sandwich beam parameters used in Eqs. (6.33)

$$A_1 = (-4b^3g - 16b^3p - 16b^3z - 4b^3 + 16b^2gp + 4b^2gz + b^2g + 16b^2pz + 4b^2p + 16b^2z - 16gpz)$$

$$A_2 = ags + 4aps + 16asz$$

$$A_3 = -4as + 32cs - 32es - 16f^2 + 32fn - 32fr - 4gt - 4hs - 16ms - 16n^2$$
$$+ 32nr - 16pt - 16qs - 16r^2 - 16tz - 4t$$

$$A_4 = -2cg - 8cp - 8cz - 2c - eg - 4ep - 4ez - e + 4hp + hz + 0.25h + 4mp + 4m + 4qz + q$$

$$A_5 = fg + 36fp + 36fz + f + 4gn + 8gr - 16np - 8n + 16rz - 4r$$

$$A_6 = 4ms + 4n^2 - 16nr + 16pt + 16qs + 16r^2 + 4tz + t$$

$$A_7 = 4n^2p + 4n^2 - 4nr + 4ptz + pt + 4r^2z + r^2 + 4tz$$

$$A_8 = 4cgsz + cgs + 16cpsz + 4cps + 16egps + 16esz - 16f^2pz - 16fgnp$$
$$- 8fgrz + 8fnp + 16frz + 4gnr$$

$$A_9 = -16agpsz - 16f^2gpz - 16f^2pz - 16gmps - 16gn^2p - 16gptz - 16gqsz - 16gr^2z - 16hpsz$$

$$B_1 = -2ac - ae + 0.25ah + 4am + aq + 4c^2 + 16ce - 2ch - 8cm - 8cq - 20e^2$$
$$- eh - 4em - 4eq + hm + 4hq + 4mq$$

$$B_2 = -a + 8c - 8e - h - 4m - 4q$$

$$B_3 = af - 8an - 4ar - 24cf - 16cn + 16cr - 24ef + 112en - 112er + fh$$
$$+ 36fm + 36fq + 4hn + 8hr + 16mr - 16nq$$

$$B_4 = 0.25b^2gt + 4b^2n^2 - 4b^2nr + b^2pt + b^2r^2 + 4b^2tz + 0.5bcgs + 2bcps$$
$$+ 8besz + 4bfnp + 8bfrz + 2bgnr - 4f^2pz - 4gmps - 4gn^2p - 4gptz - 4gqsz - 4gr^2z - 4hpsz$$

$$B_5 = -2cgt - 8cn^2 + 8cnr - 8cpt - 8cr^2 - 8ctz - 2ct - egt - 4en^2 + 16enr$$
$$- 4ept - 4er^2 - 2etz - et + gmt + 4gqt + hn^2 - 4hnr + 4hpt + 4hr^2 + htz$$
$$+ 0.25ht + 4mpt + 4mr^2 + 4mt + 4n^2q + 4qtz + qt$$

$$B_6 = -cgs - 4cps - 4csz - cs - 2egs - 8eps - 8esz - 2es + 0.5f^2g + 6f^2p + 6f^2z + 0.5f^2 + 2fgn$$
$$+ 2fgr - 2fn - 2fr + 2gms + 2gn^2 - 4gnr + 2gtz + 0.5gt + 2hsz + 0.5hs + 8mps + 8n^2p$$
$$- 4nr + 8ptz + 2pt + 8qsz + 2qs + 8r^2z + 2r^2$$

$$B_7 = 12f^2p + 12f^2z + 2fgr - 8fnp - 2fn + 8frz - 4gnr + 8gpt + 8gqs + 8gr^2 + 8hps$$
$$+ 8ms + 8n^2 - 4nr + 8tz$$

$$B_8 = -4f^2mp - 4f^2qz - 2fgmr - 4fgnq - 4fhnp - 2fhrz + 4fmr + 2fnq + hnr$$

$$B_9 = cgsz + 0.25cgs + 4cpsz + cps - 8f^2pz - 4fgrz + 4fnp + 2gnr$$

$$C_1 = 16e^2 gps + 16e^2 sz - 32efgnp + 32efrz - 16f^2 gmp - 16f^2 gqz - 16f^2 hpz - 16f^2 mp$$
$$- 16f^2 qz - 16gmpt - 16gmqs - 16gmr^2 - 16gn^2 q - 16gqtz - 16hmps - 16hn^2 p - 16hptz$$
$$- 16hqsz - 16hr^2 z$$

$$C_2 = -2bct - bet + 0.25bht + 4bmt + bqt - c^2 s - 2ces + 0.5cf^2 - 2cfn - 2cfr$$
$$+ 0.5cgt + 0.5chs - 4cnr + 2cpt + 2cqs + 2cr^2 - 2efn + 8ems + 8en^2 - 4enr$$
$$+ 8etz + 8fmr + 4fnq + 2hnr$$

$$C_3 = 0.25c^2 gs + c^2 ps + 4cfnp + 2cgnr + 4e^2 sz + 8efrz - 4f^2 mp - 4f^2 qz - 4gmpt$$
$$- 4gmqs - 4gmr^2 - 4gn^2 q - 4gqtz - 4hmps - 4hn^2 p - 4hptz - 4hqsz - 4hr^2 z$$

$$C_4 = 4bct + 16bet - 2bht - 8bmt - 8bqt + 8ces - 2cf^2 - 4cfn + 4cfr - cgt - chs$$
$$- 4cms - 4cn^2 - 4cpt - 4cqs - 4cr^2 - 4ctz - ct + 8e^2 s - 8ef^2 - 2egt - 2ehs$$
$$- 8ems - 8en^2 + 16enr - 8ept - 8eqs - 8er^2 - 8etz - 2et + 0.5f^2 h + 6f^2 m + 6f^2 q$$
$$+ 2fhn + 2fhr + 2gmt + 2hms + 2hn^2 - 4hnr + 2htz + 0.5ht + 8mpt + 8mqs$$
$$+ 8mr^2 + 8n^2 q + 8qtz + 2qt$$

$$C_5 = -80b^2 e^2 t - 4b^2 eht - 16b^2 emt - 16b^2 eqt + 4b^2 hmt + 16b^2 hqt + 16b^2 mqt$$

$$C_6 = -16e^3 s - 2e^2 f^2 + 28e^2 fn - 28e^2 fr + 8e^2 nr + 12ef^2 m + 12ef^2 q$$
$$+ 2efhr + 8efmr - 8efnq + 8egqt - 4ehnr + 8ehpt + 8ehqs$$
$$+ 8ehr^2 + 8emt - 8f^2 mq - 4fhmr - 8fhnq$$

$$C_7 = -egs - 4eps - 4esz - es + 0.25f^2 g + f^2 p + f^2 z + 0.25f^2 + fgn$$
$$+ 4fnp - 4frz - fr + gms + gn^2 + gtz + 0.25gt + hsz + 0.25hs + 4mps$$
$$+ 4n^2 p + 4ptz + pt + 4qsz + qs + 4r^2 z + r^2$$

$$C_8 = 4ef^2 p + 4ef^2 z + 2efgr - 8efnp - 2efn + 8efrz - 4egnr - 4enr$$
$$- 8f^2 mp - 8f^2 qz - 4fgmr - 4fhrz + 4fnq + 2hnr$$

$$C_9 = ef^2 p + ef^2 z + egpt + egqs + egr^2 + ehps + ems + en^2 + etz - 2fgnq$$
$$- 2fhnp + 2fmr$$

$$D_1 = -16f^2 gmq - 16f^2 hmp - 16f^2 hqz - 16f^2 mq - 16gmqt - 16hmpt - 16hmqs$$
$$- 16hmr^2 - 16hn^2 q - 16hqtz$$

$$D_2 = -bc^2 t - 2bcet + 0.5bcht + 2bcqt + 8bemt - c^2 es + 0.25c^2 f^2 - c^2 fr$$
$$+ 0.25c^2 gt + 0.25c^2 hs + c^2 pt + c^2 qs + c^2 r^2 - 2cefn - 4cenr + 4cfnq$$
$$+ 2chnr + 4e^2 ms + 4e^2 n^2 + 4e^2 tz + 8efmr - 4f^2 mq - 4gmqt - 4hmpt$$
$$- 4hmqs - 4hmr^2 - 4hn^2 q - 4hqtz$$

$$D_3 = 8c^2 et - c^2 ht - 4c^2 mt - 4c^2 qt + 8ce^2 t - 2ceht - 8cemt - 8ceqt + 2chmt$$
$$+ 8cmqt - 16e^3 t + 8ehqt$$

$$D_4 = 4e^2s - 2ef^2 - 4efn + 4efr - egt - ehs - 4ems - 4en^2 - 4ept - 4eqs$$
$$- 4er^2 - 4etz - et + 0.25f^2h + f^2m + f^2q + fhn - 4fmr + 4fnq$$
$$+ gmt + hms + hn^2 + htz + 0.25ht + 4mpt + 4mqs + 4mr^2 + 4n^2q + 4qtz + qt$$

$$D_5 = -2e^2f^2 + 4e^2fn - 4e^2fr + 8e^2nr + 4ef^2m + 4ef^2q + 2efhr + 8efmr - 8efnq$$
$$- 4ehnr - 8f^2mq - 4fhmr$$

$$D_6 = -16e^4s + 32e^3fn - 32e^3fr + 16e^2f^2m + 16e^2f^2q + 16e^2gqt + 16e^2hpt$$
$$+ 16e^2hqs + 16e^2hr^2 + 16e^2mt - 32efhnq - 16f^2hmq - 16hmqt$$

$$D_7 = -4ac^2e + ac^2h + 4ac^2q + 16ae^2m - 16ahmq + 16c^2e^2 - 4c^2eh - 16c^2em$$
$$- 16c^2eq + 4c^2hm + 16c^2mq - 16e^4 + 16e^2hq$$

Appendix D: Application of Cramer's Rule for the Determination of Constants of Eqs. (6.39)

$$P_j = \dfrac{\begin{vmatrix} fr_j & (br_j^2+c) & (br_j^2+e) & -\frac{1}{2}(br_j^2+c) \\ -fr_j & (gr_j^2+h) & \frac{1}{2}(br_j^2+c) & -(br_j^2+e) \\ -nr_j & \frac{1}{2}(br_j^2+c) & (zr_j^2+m) & -\frac{1}{4}(br_j^2+c) \\ rr_j & -(br_j^2+e) & -\frac{1}{4}(br_j^2+c) & (pr_j^2+q) \end{vmatrix}}{\begin{vmatrix} (r_j^2+a) & (br_j^2+c) & (br_j^2+e) & -\frac{1}{2}(br_j^2+c) \\ (br_j^2+c) & (gr_j^2+h) & \frac{1}{2}(br_j^2+c) & -(br_j^2+e) \\ (br_j^2+e) & \frac{1}{2}(br_j^2+c) & (zr_j^2+m) & -\frac{1}{4}(br_j^2+c) \\ -\frac{1}{2}(br_j^2+c) & -(br_j^2+e) & -\frac{1}{4}(br_j^2+c) & (pr_j^2+q) \end{vmatrix}} \qquad T_j = \alpha_j T_j$$

$$Q_j = \dfrac{\begin{vmatrix} (r_j^2+a) & fr_j & (br_j^2+e) & -\frac{1}{2}(br_j^2+c) \\ (br_j^2+c) & -fr_j & \frac{1}{2}(br_j^2+c) & -(br_j^2+e) \\ (br_j^2+e) & -nr_j & (zr_j^2+m) & -\frac{1}{4}(br_j^2+c) \\ -\frac{1}{2}(br_j^2+c) & rr_j & -\frac{1}{4}(br_j^2+c) & (pr_j^2+q) \end{vmatrix}}{\begin{vmatrix} (r_j^2+a) & (br_j^2+c) & (br_j^2+e) & -\frac{1}{2}(br_j^2+c) \\ (br_j^2+c) & (gr_j^2+h) & \frac{1}{2}(br_j^2+c) & -(br_j^2+e) \\ (br_j^2+e) & \frac{1}{2}(br_j^2+c) & (zr_j^2+m) & -\frac{1}{4}(br_j^2+c) \\ -\frac{1}{2}(br_j^2+c) & -(br_j^2+e) & -\frac{1}{4}(br_j^2+c) & (pr_j^2+q) \end{vmatrix}} \qquad T_j = \beta_j T_j$$

$$R_j = \dfrac{\begin{vmatrix} (r_j^2+a) & (br_j^2+c) & fr_j & -\frac{1}{2}(br_j^2+c) \\ (br_j^2+c) & (gr_j^2+h) & -fr_j & -(br_j^2+e) \\ (br_j^2+e) & \frac{1}{2}(br_j^2+c) & -nr_j & -\frac{1}{4}(br_j^2+c) \\ -\frac{1}{2}(br_j^2+c) & -(br_j^2+e) & rr_j & (pr_j^2+q) \end{vmatrix}}{\begin{vmatrix} (r_j^2+a) & (br_j^2+c) & (br_j^2+e) & -\frac{1}{2}(br_j^2+c) \\ (br_j^2+c) & (gr_j^2+h) & \frac{1}{2}(br_j^2+c) & -(br_j^2+e) \\ (br_j^2+e) & \frac{1}{2}(br_j^2+c) & (zr_j^2+m) & -\frac{1}{4}(br_j^2+c) \\ -\frac{1}{2}(br_j^2+c) & -(br_j^2+e) & -\frac{1}{4}(br_j^2+c) & (pr_j^2+q) \end{vmatrix}} \qquad T_j = \gamma_j T_j$$

$$S_j = \frac{\begin{vmatrix} \left(r_j^{\,2}+a\right) & \left(br_j^{\,2}+c\right) & \left(br_j^{\,2}+e\right) & fr_j \\[4pt] \left(br_j^{\,2}+c\right) & \left(gr_j^{\,2}+h\right) & \frac{1}{2}\left(br_j^{\,2}+c\right) & -fr_j \\[4pt] \left(br_j^{\,2}+e\right) & \frac{1}{2}\left(br_j^{\,2}+c\right) & \left(zr_j^{\,2}+m\right) & -nr_j \\[4pt] -\frac{1}{2}\left(br_j^{\,2}+c\right) & -\left(br_j^{\,2}+e\right) & -\frac{1}{4}\left(br_j^{\,2}+c\right) & rr_j \end{vmatrix}}{\begin{vmatrix} \left(r_j^{\,2}+a\right) & \left(br_j^{\,2}+c\right) & \left(br_j^{\,2}+e\right) & -\frac{1}{2}\left(br_j^{\,2}+c\right) \\[4pt] \left(br_j^{\,2}+c\right) & \left(gr_j^{\,2}+h\right) & \frac{1}{2}\left(br_j^{\,2}+c\right) & -\left(br_j^{\,2}+e\right) \\[4pt] \left(br_j^{\,2}+e\right) & \frac{1}{2}\left(br_j^{\,2}+c\right) & \left(zr_j^{\,2}+m\right) & -\frac{1}{4}\left(br_j^{\,2}+c\right) \\[4pt] -\frac{1}{2}\left(br_j^{\,2}+c\right) & -\left(br_j^{\,2}+e\right) & -\frac{1}{4}\left(br_j^{\,2}+c\right) & \left(pr_j^{\,2}+q\right) \end{vmatrix}} \qquad T_j = \eta_j T_j$$

Appendix E: Personal profile

James Njuguna graduated with a Diploma in Aeronautical Engineering from Trans-Eastern Airlines Aviation College, Kenya and holds an MSc in Aeronautical Engineering form City University, London. He previously worked as an aircraft engineer for AIM-Air Services for four years. During 2003-04 while being a research student, he was awarded Marie Curie Fellowship by the Marie Curie Fellowship of the European Community Programme to work in the Department of Chemistry and Technology of Polymers, Cracow University of Technology, Poland for a year.   In 2005 he joined Cranfield University's on a highly prestigious Research Councils UK Academic Fellowship. He is an Associate Member of the Royal Aeronautical Society (AMRAes), a member of American Institute of Aeronautics and Astronautics (MAIAA), and an active member of the National Composites Network (UK). He also serves in Composties Centre's Safety Committee within the Materials Department at Cranfield University and also a member of Cranfield's Blended Learning User Group. In 2006, was elected to serve as a member of the Cranfield University Senate and Court for the period 2006-2009.

James teaches composite structures to Motorsport engineering students. In addition he is also involved in developing a research portfolio in motorsport structural engineering with the aim of developing his own research group. To enhance his teaching skills, he is currently pursuing a Post Graduate Certificate in Learning, Teaching and Assessment in Higher Education. The qualification will lead to a Certified Teacher in Higher Education.   His research interests are in composite structures, structural dynamics, aeroelasticity, vibration energy harvesting, and high performance polymer elastomers and nanocomposites. He has co-authored a textbook on polymers, *'The Thermal Degradation of Polymeric Materials, Rapra Technologies Ltd., Surrey, UK, 2005'*. He also holds a number of publications in international journals and established conferences (see list below).

Publications from this research

Books

K. Pielichowski and J. Njuguna, Thermal Degradation of Polymeric Materials. RAPRA Technologies Limited, Shawbury, Surrey, UK, 2005.

Book Chapter

K. Pielichowski, B. Janowski, J. Njuguna, J. Pielichowski, "Polyhedral oligomeric silsesquioxanes (POSS)-containing nanohybrid polymers" Advances in Polymer Sciences 2006; 201:225-296. (Book series)

Journal Papers

J. Njuguna, "Flutter prediction, suppression and control in aircraft composite wings as a design prerequisite" J. Stru. Contr. Health Monitor 2006: (Published online).

A. Leszczynska, J. Njuguna, K. Pielichowski, J.R. Banerjee, "Thermal stability of polymer/montmorillonite nanocomposites: Part I: Factors influencing thermal stability and mechanisms of thermal stability improvement". Themochimica Acta, 2007; 453(2)75-96.

A. Leszczynska, J. Njuguna, K. Pielichowski, J.R. Banerjee, "Polymer/clay (montmorillonite) nanocomposites with improved thermal properties: Part II: A review study on thermal stability of montmorillonite nanocomposites based on different polymeric matrixes", Themochimica Acta, 2007; 454; 1-22.

J. Njuguna, K. Pielichowski, "Polymer nanocomposites for aerospace applications: Fabrication", Adv. Eng. Mater. 2004; 6(4): 193-203.

J. Njuguna, K. Pielichowski, "Recent progress in polyurethane-based conducting composites", J. Mater. Sci. 2004; 39(13): 4081-4094.

J. Njuguna, K. Pielichowski, "Polymer nanocomposites for aerospace applications: Characterisation", Adv. Eng. Mater. 2004; 6(4): 204-210.

J. Njuguna, K. Pielichowski, "Polymer nanocomposites for aerospace applications: Properties", Adv. Eng. Mater. 2003; 5(11): 769-778.

Peer-reviewed conference papers

J.R. Banerjee, R. Morishima, M. Perera, C. Cheung, J. Njuguna, "Dynamic analysis of a three-layered sandwich beam using theory and experiment", 47th AIAA/ASME/ASCE/AHS/ASC Structures, Structural Dynamics, and Materials Conference, 1 - 4 May 2006, Newport, Rhode Island, USA

J. Njuguna, J.R. Banerjee, C.W. Cheung, "Theoretical and experimental modal analysis of laminated composite beams", 2nd International Seminar on Modern Polymeric Materials for Environmental Applications under the auspices of EC Marie Curie Programme (FP 5), Kraków, Kraków, March 23-25, 2006

K. Pielichowski, J. Njuguna, J.R. Banerjee, R. Alcock, C.W. Cheung, "Recent advances in segmented polyurethane nanocomposites", 2nd International Seminar on Modern Polymeric Materials for Environmental Applications under the auspices of EC Marie Curie Programme (FP 5), Kraków, Kraków, March 23-25, 2006

J. Njuguna, K. Pielichowski, J.R. Banerjee, "Recent advances in polymer nanocomposites for aerospace applications", 1st International Seminar on Modern Polymeric Materials for Environmental Applications under the auspices of EC Marie Curie Programme (FP 5), Kraków, December 16-18, 2004.

J. Njuguna, H. Su, C.W. Cheung, J. R. Banerjee, "The influence of ply orientation on the free vibration of laminated composite beams", In UNSW 2002 Conference Proceedings, Sydney, Australia, Eds. Bandyopadhyay, N. Gowripalan, S. Rizkalla, ACUN-4, p.307-314.

Other contributions

"United Kingdom Space Generation Forum report to the British National Space Centre on the topic of the review of the BNSC", January 2002, UK- Space Generation Forum.

J. Njuguna, J. R. Banerjee, J. R. Alcock and C.W. Cheung. Theoretical and experimental modal analysis of a three-layered sandwich beam. Poster presentation at the House of Commons Science Week (UK) on 15 March 2006.

Submitted papers

J. Njuguna, K. Pielichowski, "The role of advanced polymer materials in aerospace", Prog. Aero. Sci.: submitted.

J. Njuguna, "A review on static and dynamic analyses of actively/passively controlled composite structures" Applied Comp. Mater.: submitted.

K. Pielichowski, B. Janowski, J. Njuguna, "Novel properties of polyhedral oligomeric silsesquioxanes (POSS) nanocomposites", Chem. Mater. submitted

To be submitted

J. Njuguna, K. Pielichowski, "Recent advances in polyurethane elastomeric nanocomposites. Part I: Preparation" Prog. Poly. Sci..:

Synthesis and structure properties of polyurethane-based conducting thermoplastic elastomers

Side impact structures for world rallying cars – re-design considerations